Ministry of Education and Science of the Russian Federation
Saint Petersburg National Research University of Information
Technologies, Mechanics, and Optics

NANOSYSTEMS:

PHYSICS, CHEMISTRY, MATHEMATICS

2022, volume 13(1)

Наносистемы: физика, химия, математика

2022, том 13, № 1

N A N O
Ф&Х&М

NANOSYSTEMS:

PHYSICS, CHEMISTRY, MATHEMATICS

ADVISORY BOARD MEMBERS

Chairman: V.N. Vasiliev *(St. Petersburg, Russia)*,
V.M. Buznik *(Moscow, Russia)*; V.M. Ievlev *(Voronezh, Russia)*, P.S. Kop'ev*(St. Petersburg, Russia)*, N.F. Morozov *(St. Petersburg, Russia)*, V.N. Parmon *(Novosibirsk, Russia)*, A.I. Rusanov *(St. Petersburg, Russia)*,

EDITORIAL BOARD

Editor-in-Chief: I.Yu. Popov *(St. Petersburg, Russia)*

Section Co-Editors:
Physics – V.M. Uzdin *(St. Petersburg, Russia)*,
Material science – V.V. Gusarov *(St. Petersburg, Russia)*,
Chemistry – V.K. Ivanov *(Moscow, Russia)*,
Mathematics – I.Yu. Popov *(St. Petersburg, Russia)*.

Editorial Board Members:
V.M. Adamyan *(Odessa, Ukraine)*; O.V. Al'myasheva *(St. Petersburg, Russia)*; A.P. Alodjants *(Vladimir, Russia)*; S. Bechta *(Stockholm, Sweden)*; J. Behrndt *(Graz, Austria)*; M.B. Belonenko *(Volgograd, Russia)*; A. Chatterjee (*Hyderabad, India)*; A.V. Chizhov *(Dubna, Russia)*; A.N. Enyashin *(Ekaterinburg, Russia)*, P.P. Fedorov *(Moscow, Russia)*; E.A. Gudilin *(Moscow, Russia)*; H. Jónsson *(Reykjavik, Iceland)*; A.A. Kiselev *(Durham, USA)*; Yu.S. Kivshar *(Canberra, Australia)*; S.A. Kozlov *(St. Petersburg, Russia)*; P.A. Kurasov *(Stockholm, Sweden)*; A.V. Lukashin *(Moscow, Russia)*; I.V. Melikhov *(Moscow, Russia)*; G.P. Miroshnichenko *(St. Petersburg, Russia)*; I.Ya. Mittova *(Voronezh, Russia)*; Nguyen Anh Tien *(Ho Chi Minh, Vietnam)*; V.V. Pankov *(Minsk, Belarus)*; K. Pankrashkin *(Orsay, France)*; A.V. Ragulya *(Kiev, Ukraine)*; V. Rajendran *(Tamil Nadu, India)*; A.A. Rempel *(Ekaterinburg, Russia)*; V.Ya. Rudyak *(Novosibirsk, Russia)*; H.M. Sedighi (*Ahvaz, Iran*); D Shoikhet *(Karmiel, Israel)*; P Stovicek *(Prague, Czech Republic)*; V.M. Talanov *(Novocherkassk, Russia)*; A.Ya. Vul' *(St. Petersburg, Russia)*; A.V. Yakimansky (*St. Petersburg, Russia*), V.A. Zagrebnov *(Marseille, France)*.

Editors:
I.V. Blinova; A.I. Popov; A.I. Trifanov; E.S. Trifanova *(St. Petersburg, Russia)*,
R. Simoneaux *(Philadelphia, Pennsylvania, USA)*.

Address: ITMO University, Kronverkskiy pr., 49, St. Petersburg 197101, Russia.
Phone: +7(812)607-02-54, **Journal site:** http://nanojournal.ifmo.ru/,
E-mail: nanojournal.ifmo@gmail.com

AIM AND SCOPE

The scope of the journal includes all areas of nano-sciences. Papers devoted to basic problems of physics, chemistry, material science and mathematics inspired by nanosystems investigations are welcomed. Both theoretical and experimental works concerning the properties and behavior of nanosystems, problems of its creation and application, mathematical methods of nanosystem studies are considered.

The journal publishes scientific reviews (up to 30 journal pages), research papers (up to 15 pages) and letters (up to 5 pages). All manuscripts are peer-reviewed. Authors are informed about the referee opinion and the Editorial decision.

CONTENT

MATHEMATICS

PHYSICS

CHEMISTRY AND MATERIAL SCIENCE

NANOSYSTEMS:
PHYSICS, CHEMISTRY, MATHEMATICS

Cardone G., Durante T. *Nanosystems: Phys. Chem. Math.*, 2022, **13** (1), 5–11.
http://nanojournal.ifmo.ru
DOI 10.17586/2220-8054-2022-13-1-5-11

Original article

Asymptotic analysis of a planar waveguide perturbed by a non periodic perforation

Giuseppe Cardone[1,a], Tiziana Durante[2,b]

[1]Universita di Napoli "Federico II", Napoli, Italy
[2]University of Salerno, 84084 Fisciano (SA), Italy

[a]giuseppe.cardone@unina.it, [b]tdurante@unisa.it

Corresponding author: Giuseppe Cardone, giuseppe.cardone@unina.it

ABSTRACT We consider a general second order elliptic operator in a planar waveguide perforated by small holes distributed along a curve and subject to classical boundary conditions on the holes. Under weak assumptions on the perforation, we describe all possible homogenized problems.

KEYWORDS perforation, elliptic operator, unbounded domain, homogenization, norm resolvent convergence.

FOR CITATION Cardone G., Durante T. Asymptotic analysis of a planar waveguide perturbed by a non periodic perforation. *Nanosystems: Phys. Chem. Math.*, 2022, **13** (1), 5–11.

1. Introduction

In this paper, we consider a second order elliptic operator in a planar strip perforated along a curve which can be either infinite or finite and closed. The shapes and the distribution of the holes can be rather arbitrary and no periodicity is assumed. We impose on the boundary of the holes classical boundary conditions, i.e., Dirichlet, Neumann or Robin conditions: boundaries of different holes can be subject to different types of boundary conditions.

Our operator describes a quantum particle in a non-isotropic waveguide (the infinite strip) since the coefficients of the operator are variable. The perforation represents small defects distributed along a given line, while the conditions on the boundaries of the holes impose certain regime, for instance, the Dirichlet condition describes a wall and the particle can not pass through such boundary. Our aim is to describe all possible homogenized problems. In fact, the homogenization process describes the effective behavior of our model once the perforation becomes finer, while the type of resolvent convergence characterizes in which sense the perturbed model is close to the effective one. The results we will state, are proved in [1] .

Our first main result describes the homogenized problems depending on the geometry, sizes, and distribution of the holes as well as of the conditions on the boundary of the holes. The differential expression for the homogenized operator is the same as for the original operator, but with Dirichlet condition or delta-interaction or no condition on the reference curve along which the perforation is made. Our second main result is the norm resolvent convergence of the perturbed operator to the homogenized one and the estimates for the rates of convergence. In all cases except one the operator norm is that of the operators from L_2 into W_2^1, while in the exceptional case it is from L_2 into L_2. Nevertheless, in the latter case we show that by employing a special boundary corrector one can replace the norm by that of the operators acting from L_2 into W_2^1. Such kind of results on norm resolvent convergence are completely new for the domains perforated periodically along curves or manifolds, especially in view of the fact that we succeeded in studying the general non-periodic perforation with arbitrary boundary conditions.

Our technique is based on the variational formulations of the equations for the perturbed and the homogenized operators. We use no smoothing operator like in previous papers on the operators with rapidly oscillating coefficients. Instead, we write the integral identity for the difference of the perturbed and homogenized resolvents and then estimate the terms coming from the boundary conditions. It requires certain accurate estimates for various boundary integrals over holes and over the reference curve. The main difference of our technique with that in the previous works is the assumptions for the perforation. In previous works [2–8], the main assumption was the existence of an operator of continuation the holes for the functions defined outside as well as uniform estimates for this operator. In our work, we assume the solvability of a certain fixed boundary value problems for the divergence operator in the vicinity of the holes. We believe that our assumptions are not worse than the existence of the continuation operator, since we require just a solvability of certain boundary value problem while the existence of the continuation operator means the possibility to extend *each* function in a given Sobolev space.

The attention to the norm resolvent convergence started a new direction in the homogenization theory. It was found for the operators with fast periodically oscillating coefficients that their resolvents converge to the resolvents of the homogenized operators in the norm resolvent sense. This was a much stronger result in comparison with known classical results stating just a weak or a strong resolvent convergence. Results based on norm resolvent convergence were obtained by M.Sh. Birman, T.A. Suslina [9–14], V.V. Zhikov and S.E. Pastukhova [15–20], G. Griso [21, 22], and by C.E. Kenig,

F. Lin, Z. Shen [23,24]; see also other papers by these authors. Moreover, in the above cited works, the authors succeeded in establishing sharp estimates for the rates of convergence in the sense of various operator norms.

In view of the above described results, a natural question appeared: whether a similar norm resolvent convergence is valid for other types of the perturbations in the homogenization theory? This issue was studied recently for certain perturbations in the boundary homogenization.

In [25–33], [34–40] problems with frequent alternation of boundary conditions were treated. The norm resolvent convergence was proven for all possible homogenized problems as well as for both periodic and non-periodic alternations. Estimates for the rate of convergence were obtained. In periodic cases, certain asymptotic expansions for the spectra of perturbed operators were constructed.

In [41, 42], [43, Ch. III, Sec. 4], the norm resolvent convergence for problems with a fast periodically oscillating boundary was proven. The most general results were obtained in [41]. Namely, various geometries of oscillations as well as various boundary conditions on the oscillating boundary were considered. Estimates were obtained for the rate of norm resolvent convergence in the sense of various operator norms.

The norm resolvent convergence for periodic perforations was studied in [16,44,45] . In [44] the whole of a domain was perforated. The operator was described by the Helmholtz equation; on the boundaries of the holes the Dirichlet condition was imposed. The authors treated the case when the holes disappeared under the homogenization and made no influence for the homogenized operators. The norm resolvent convergence was proven; no estimates for the rate of convergence were found. In [16], an elliptic operator in a perforated domain was studied. Here, again, the whole of the domain was perforated. It was assumed that the sizes of the holes and the distances between them are of the same order of smallness. On the boundaries of the holes the Neumann condition was imposed. The norm resolvent convergence and the estimates for the rate of convergence were established.

One more interesting paper devoted to norm resolvent convergence is [19]. Here, the perturbation was defined by rescaling an abstract periodic measure. The main result is the description of the homogenized operator, the proof of the norm resolvent convergence, and the estimates for the rate of convergence. A general model of [19] covered various perturbations, including periodic perforation of the whole of a domain, provided the sizes of the holes and the distances between them are of the same smallness order.

2. Problem and main results

Let $x = (x_1, x_2)$ be the Cartesian coordinates in $\mathbb{R}^2$, $\Omega := \{x : 0 < x_2 < d\}$ be a horizontal strip of width $d > 0$. By γ, we denote a curve in Ω separated from $\partial\Omega$ by a fixed distance. Curve γ is supposed to be C^3-smooth and to have no self-intersections. We consider two cases assuming that γ is either an infinite curve or it is a finite closed curve. By s, we denote the arc length of γ, $s \in [-s_*, s_*]$, where s_* is either finite or $s_* = +\infty$. If curve γ is finite, we identify points $s = -s_*$ and $s = s_*$. By $\varrho = \varrho(s)$ we denote the vector function describing the curve γ. Since curve γ is C^3-smooth, then $\varrho \in C^3[-s_*, s_*]$; for an infinite curve by $[-s_*, s_*]$ we mean $\mathbb{R}$. The above assumptions for γ yield that this curve partitions domain Ω into two disjoint subdomains. The upper or exterior one is denoted by Ω_+ and the lower or interior subdomain is Ω_-. By $B_r(a)$ we denote the ball in $\mathbb{R}^2$ of radius r centered at a.

Let $\mathbb{M}^\varepsilon \subseteq \mathbb{Z}$ be some set, and $s_k^\varepsilon \in [-s_*, s_*]$, $k \in \mathbb{M}^\varepsilon$, be a set of points satisfying $s_k^\varepsilon < s_{k+1}^\varepsilon$. By ω_k, $k \in \mathbb{M}^\varepsilon$, we indicate a set of bounded domains in $\mathbb{R}^2$ having C^2-boundaries. We stress that these domains are not supposed to be simply connected. Denoting by ε a small positive parameter, we define:

$$\theta^\varepsilon := \theta_0^\varepsilon \cup \theta_1^\varepsilon, \quad \theta_i^\varepsilon := \bigcup_{k\in\mathbb{M}_i} \omega_k^\varepsilon, \quad i = 0, 1, \quad \omega_k^\varepsilon := \{x : \varepsilon^{-1}\eta^{-1}(\varepsilon)(x - y_k^\varepsilon) \in \omega_k\}, \quad y_k^\varepsilon := \varrho(s_k^\varepsilon),$$

where $\mathbb{M}_0^\varepsilon \cap \mathbb{M}_1^\varepsilon = \emptyset$, $\mathbb{M}_0^\varepsilon \cup \mathbb{M}_1^\varepsilon = \mathbb{M}^\varepsilon$, and $\eta = \eta(\varepsilon)$ is a some function satisfying the inequality $0 < \eta(\varepsilon) \leqslant 1$. We make the following assumptions.

(A1) There exist fixed numbers $0 < R_1 < R_2$, $b > 1$, $L > 0$ and points $x^k \in \omega_k$, $k \in \mathbb{M}^\varepsilon$, such that

$$B_{R_1}(x^k) \subset \omega_k \subset B_{R_2}(0), \quad |\partial\omega_k| \leqslant L \quad \text{for each} \quad k \in \mathbb{M}^\varepsilon,$$
$$B_{bR_2\varepsilon}(y_k^\varepsilon) \cap B_{bR_2\varepsilon}(y_i^\varepsilon) = \emptyset \quad \text{for each} \quad i, k \in \mathbb{M}^\varepsilon, \quad i \neq k,$$

and for all sufficiently small ε.

(A2) For b and R_2 in A1 and $k \in \mathbb{M}^\varepsilon$ there exists a generalized solution $X_k : B_{b_*R_2}(0) \setminus \omega_k \mapsto \mathbb{R}^2$, $b_* := (b + 1)/2$, to the boundary value problem:

$$\begin{gathered} \operatorname{div} X_k = 0 \quad \text{in} \quad B_{b_*R_2}(0) \setminus \omega_k, \\ X_k \cdot \nu = -1 \quad \text{on} \quad \partial\omega_k, \quad X_k \cdot \nu = \varphi_k \quad \text{on} \quad \partial B_{b_*R_2}(0), \end{gathered} \tag{2.1}$$

belonging to $L_\infty(B_{b_*R_2}(0) \setminus \omega_k)$ and bounded in the sense of this space uniformly in $k \in \mathbb{M}^\varepsilon$. Here, ν is the outward normal to $\partial B_{b_*R_2}(0)$ and to $\partial\omega_k$, while φ_k is a some function in $L_\infty(\partial B_{b_*R_2}(0))$ satisfying:

$$\int\limits_{\partial B_{b_*R_2}(0)} \varphi_k \, ds = |\partial\omega_k|. \tag{2.2}$$

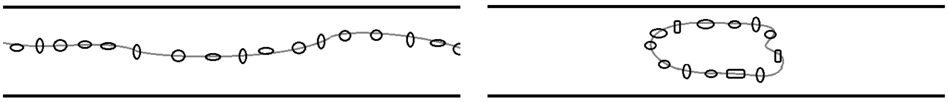

(a) Perforation along an infinite curve (b) Perforation along a closed curve

FIG. 1. Perforated domain

By $A_{ij} = A_{ij}(x)$, $A_i = A_i(x)$, $A_0 = A_0(x)$ we denote functions satisfying the conditions:

$$\begin{gathered} A_{ij}, A_i \in W^1_\infty(\Omega), \quad i,j = 1,2, \quad A_0 \in L_\infty(\Omega), \quad A_{ji} = A_{ji}, \\ \sum_{i,j=1}^{2} A_{ij} z_i z_j \geqslant c_2 |\xi|^2, \quad x \in \Omega, \quad z = (z_1, z_2) \in \mathbb{R}^2, \end{gathered} \tag{2.3}$$

where c_2 is a positive constant independent of x and ξ, and A_{ij}, A_0 are real-valued.

In the vicinity of γ we introduce local coordinates (s,τ), where τ is the distance to a point measured along the normal ν^0 to γ which is inward for Ω_-, and s, we remind, is the arc length of γ. Since the curvature of γ is uniformly bounded, the coordinates (s,τ) are well-defined for $|\tau| \leqslant \tau_0$, $s \in \mathbb{R}$, where τ_0 is a sufficiently small fixed positive number.

We denote by $\Omega^\varepsilon := \Omega \setminus \theta^\varepsilon$ our perforated domain, cf. Fig. 1. In this paper we study a singularly perturbed operator depending on ε which we denote as $\mathcal{H}^\varepsilon$. It is introduced by the differential expression

$$-\sum_{i,j=1}^{2} \frac{\partial}{\partial x_i} A_{ij} \frac{\partial}{\partial x_j} + \sum_{j=1}^{2} A_j \frac{\partial}{\partial x_j} - \frac{\partial}{\partial x_j} \overline{A_j} + A_0 \tag{2.4}$$

in Ω^ε subject to the Dirichlet condition on $\partial\Omega \cup \partial\theta^\varepsilon_0$ and to the Robin condition

$$\left(\frac{\partial}{\partial N^\varepsilon} + a \right) u = 0 \quad \text{on} \quad \partial\theta^\varepsilon_1, \qquad \frac{\partial}{\partial N^\varepsilon} := \sum_{i,j=1}^{2} A_{ij} \nu^\varepsilon_i \frac{\partial}{\partial x_j} + \sum_{j=1}^{2} \overline{A}_j \nu^\varepsilon_j,$$

where $\nu^\varepsilon = (\nu^\varepsilon_1, \nu^\varepsilon_2)$ is the inward normal to $\partial\theta^\varepsilon_1$, $a = a(x)$ is a function defined for $|\tau| < \tau_0$ and $a \in W^1_\infty(\{x : |\tau| < \tau_0\})$.

By $\mathfrak{a}^\varepsilon$ we denote the sesquilinear form:

$$\begin{aligned} \mathfrak{a}^\varepsilon(u,v) := &\sum_{i,j=1}^{2} \left(A_{ij} \frac{\partial u}{\partial x_j}, \frac{\partial v}{\partial x_i} \right)_{L_2(\Omega^\varepsilon)} + \sum_{j=1}^{2} \left(A_j \frac{\partial u}{\partial x_j}, v \right)_{L_2(\Omega^\varepsilon)} \\ &+ \sum_{j=1}^{2} \left(u, A_j \frac{\partial v}{\partial x_j} \right)_{L_2(\Omega^\varepsilon)} + (A_0 u, v)_{L_2(\Omega^\varepsilon)} \end{aligned} \tag{2.5}$$

in $L_2(\Omega^\varepsilon)$ on the domain $W^1_2(\Omega^\varepsilon)$. Rigorously, we introduce operator $\mathcal{H}^\varepsilon$ as the lower-semibounded self-adjoint operator in $L_2(\Omega^\varepsilon)$ associated with the closed lower-semibounded symmetric sesquilinear form $\mathfrak{h}^\varepsilon(u,v) := \mathfrak{a}^\varepsilon(u,v) + (au,v)_{L_2(\partial\theta^\varepsilon_1)}$ in $L_2(\Omega^\varepsilon)$ on $\mathring{W}^1_2(\Omega^\varepsilon, \partial\Omega \cup \partial\theta^\varepsilon_0)$. Hereafter, for any domain $Q \subset \mathbb{R}^2$ and any curve $S \subset Q$, by $\mathring{W}^1_2(Q,S)$, we denote the subspace of $W^1_2(Q)$ consisting of the functions with zero trace on S, and we let $\mathring{W}^1_2(Q) := \mathring{W}^1_2(Q, \partial Q)$. If else is not said, in what follows, all the differential operators are introduced in this way, i.e., they will be self-adjoint lower semibounded operators in $L_2(\Omega)$ or $L_2(\Omega^\varepsilon)$ associated with closed lower-semibounded symmetric sesquilinear form. For the sake of brevity, for each operator, we shall just write the differential expression with the boundary condition as well as the associated form.

Our main aim is to study the resolvent convergence and the spectrum's behavior of the operator $\mathcal{H}^\varepsilon$. To formulate our main results, we need additional notations.

By $\mathcal{H}^0_\mathrm{D}$ we denote the operator in $L_2(\Omega)$ with the differential expression (2.4) subject to the Dirichlet condition on γ and $\partial\Omega$. The associated form is $\mathfrak{h}^0_\mathrm{D}(u,v) := \mathfrak{a}(u,v)$ in $L_2(\Omega)$ on $\mathring{W}^1_2(\Omega, \partial\Omega \cup \gamma)$, where form $\mathfrak{a}$ is introduced by expression (2.5), where Ω^ε is replaced by Ω. By analogy with [46, Lem. 2.2], [47, Ch. IV, Sec. 2.2, 2.3], [48, Lem. 3.2] one can check that the domains of operator $\mathcal{H}^0_\mathrm{D}$ is given by the identity $\mathfrak{D}(\mathcal{H}^0_\mathrm{D}) = \mathring{W}^1_2(\Omega, \partial\Omega \cup \gamma) \cap W^2_2(\Omega \setminus \gamma)$. By i we denote the imaginary unit, and by $\|\cdot\|_{X\to Y}$ we denote the norm of an operator acting from a Banach space X to a Banach space Y.

Now, we are ready to formulate our first main result.

Theorem 2.1. *Let*

$$\varepsilon \ln \eta(\varepsilon) \to 0, \quad \varepsilon \to +0, \tag{2.6}$$

and suppose (A1), (A2), and

(A3) *There exists a constant* $R_3 > bR_2$ *such that*

$$\{x : |\tau| < \varepsilon b R_2\} \subset \bigcup_{k\in\mathbb{M}_0^\varepsilon} B_{R_3\varepsilon}(y_k^\varepsilon), \quad \omega_k^\varepsilon \subset B_{R_3\varepsilon}(y_k^\varepsilon) \quad \textit{for each} \quad k \in \mathbb{M}_0^\varepsilon.$$

Then, the estimate:

$$\|(\mathcal{H}^\varepsilon - \mathrm{i})^{-1} - (\mathcal{H}^0_{\mathrm{D}} - \mathrm{i})^{-1}\|_{L_2(\Omega)\to W_2^1(\Omega^\varepsilon)} \leqslant C\varepsilon^{\frac{1}{2}}\big(|\ln\eta(\varepsilon)|^{\frac{1}{2}} + 1\big) \tag{2.7}$$

holds true, where C *is a positive constant independent of* ε*.*

Let $\nu^0 = (\nu_1^0, \nu_2^0)$ and

$$\frac{\partial}{\partial N^0} := \sum_{i,j=1}^{2} A_{ij}\nu_i^0 \frac{\partial}{\partial x_j}.$$

By $[\cdot]_\gamma$ we indicate the jump of a function on γ, $[u]_\gamma = u\big|_{\tau=+0} - u\big|_{\tau=-0}$. Given a function $\beta = \beta(s)$ in $W_\infty^1(\gamma)$, we introduce operator $\mathcal{H}_\beta^0$ with differential expression (2.4) subject to the boundary conditions

$$[u]_\gamma = 0, \quad \left[\frac{\partial u}{\partial N^0}\right]_\gamma + \beta u\big|_\gamma = 0. \tag{2.8}$$

The associated form is $\mathfrak{h}_\beta^0(u,v) := \mathfrak{a}(u,v) + (\beta u, v)_{L_2(\gamma)}$ in $L_2(\Omega)$ on $\mathring{W}_2^1(\Omega)$. Again, by analogy with [46, Lem. 2.2], [47, Ch. IV, Sec. 2.2, 2.3], [48, Lem. 3.2], one can show that:

$$\mathfrak{D}(\mathcal{H}_\beta^0) = \{u \in \mathring{W}_2^1(\Omega) : u \in W_2^2(\Omega_\pm) \text{ and (2.8) is satisfied}\}.$$

If $\beta = 0$, instead of $\mathcal{H}_0^0$ we shall simply write $\mathcal{H}^0$. As one can see, in this case there is no boundary condition on γ and the domain of $\mathcal{H}^0$ is $\mathfrak{D}(\mathcal{H}^0) = \mathring{W}_2^1(\Omega) \cap W_2^2(\Omega)$.

In the next theorem, we deal with the case when the perturbed operator involves the Dirichlet condition at least on a part of $\partial\theta^\varepsilon$ but in contrast to (2.6), the function $\varepsilon \ln\eta(\varepsilon)$ converges either to a non-zero constant or to infinity.

Theorem 2.2. *Suppose (A1), (A2), let:*

$$\frac{1}{\varepsilon \ln \eta(\varepsilon)} \to -\rho, \quad \varepsilon \to +0, \tag{2.9}$$

and set $\mathbb{M}_0^\varepsilon$ *be non-empty. For* b *and* R_2 *in A1 and* $s \in \mathbb{R}$ *we denote:*

$$\alpha^\varepsilon(s) := \begin{cases} \dfrac{\pi}{bR_2}, & |s - s_k^\varepsilon| < bR_2\varepsilon, \quad k \in \mathbb{M}_0^\varepsilon, \\ 0, & \textit{otherwise}. \end{cases}$$

Suppose also that:

(A4) *There exists a function* $\alpha = \alpha(s)$ *in* $W_\infty^1(\gamma)$ *and a function* $\varkappa = \varkappa(\varepsilon)$, $\varkappa(\varepsilon) \to +0$, $\varepsilon \to +0$, *such that for all sufficiently small* ε *the estimate:*

$$\sum_{q\in\mathbb{Z}} \frac{1}{|q|+1}\left|\int_n^{n+\ell} \big(\alpha^\varepsilon(s) - \alpha(s)\big)\mathrm{e}^{-\frac{\mathrm{i}q}{2\pi\ell}(s-n)}\,ds\right|^2 \leqslant \varkappa^2(\varepsilon) \tag{2.10}$$

is valid, where $n = -s_*$, $\ell = 2s_*$, *if* γ *is a finite curve, and* $n \in \mathbb{Z}$, $\ell = 1$, *if* γ *is an infinite curve. In the latter case estimate (2.10) is supposed to hold uniformly in* n*.*

We denote:

$$\beta := \alpha\frac{(\rho+\mu)}{A_{11}A_{22} - A_{12}^2}, \quad \beta_0 := \alpha\frac{\rho}{A_{11}A_{22} - A_{12}^2}, \quad \mu(\varepsilon) := -\frac{1}{\varepsilon\ln\eta(\varepsilon)} - \rho.$$

Then the estimates:

$$\|(\mathcal{H}^\varepsilon - \mathrm{i})^{-1} - (\mathcal{H}_\beta^0 - \mathrm{i})^{-1}\|_{L_2(\Omega)\to L_2(\Omega^\varepsilon)} \leqslant C\big(\varepsilon^{\frac{1}{2}} + \varkappa(\varepsilon)\big) \tag{2.11}$$

$$\|(\mathcal{H}^\varepsilon - \mathrm{i})^{-1} - (\mathcal{H}_{\beta_0}^0 - \mathrm{i})^{-1}\|_{L_2(\Omega)\to L_2(\Omega^\varepsilon)} \leqslant C\big(\varepsilon^{\frac{1}{2}} + \varkappa(\varepsilon) + \mu(\varepsilon)\big) \tag{2.12}$$

hold true, where C *is a positive constant independent of* ε*. There exists an explicit function* W^ε *(see (6.5) in [1]) such that the estimate:*

$$\|(\mathcal{H}^\varepsilon - \mathrm{i})^{-1} - (1 - W^\varepsilon)(\mathcal{H}_\beta^0 - \mathrm{i})^{-1}\|_{L_2(\Omega)\to W_2^1(\Omega^\varepsilon)} \leqslant C\big(\varepsilon^{\frac{1}{2}} + \varkappa(\varepsilon)(\rho + \mu(\varepsilon))\big), \tag{2.13}$$

is valid, where C *is a positive constant independent of* ε*. If* $\rho = 0$, *the estimate*

$$\|(\mathcal{H}^\varepsilon - \mathrm{i})^{-1} - (\mathcal{H}^0 - \mathrm{i})^{-1}\|_{L_2(\Omega)\to W_2^1(\Omega^\varepsilon)} \leqslant C\big(\varepsilon^{\frac{1}{2}} + \mu^{\frac{1}{2}}(\varepsilon)\big) \tag{2.14}$$

holds true, where C *is a positive constant independent of* ε*.*

The next two theorems concern the case when $\mathbb{M}_0^\varepsilon$ is empty, i.e., the perturbed operator involves just the Robin condition on $\partial\theta^\varepsilon$.

Theorem 2.3. *Suppose (A1), (A1), let set $\mathbb{M}_0^\varepsilon$ be empty and either $a \equiv 0$ or $\eta(\varepsilon) \to 0$, $\varepsilon \to +0$. Then the estimate*

$$\|(\mathcal{H}^\varepsilon - \mathrm{i})^{-1} - (\mathcal{H}^0 - \mathrm{i})^{-1}\|_{L_2(\Omega)\to W_2^1(\Omega^\varepsilon)} \leqslant C\eta(\varepsilon)|\ln \eta(\varepsilon)|^{\frac{1}{2}}, \tag{2.15}$$

holds true, if $a \not\equiv 0$, $\eta \to +0$, and

$$\|(\mathcal{H}^\varepsilon - \mathrm{i})^{-1}f - (\mathcal{H}^0 - \mathrm{i})^{-1}f\|_{L_2(\Omega)\to W_2^1(\Omega^\varepsilon)} \leqslant C\varepsilon^{\frac{1}{2}}\eta(\varepsilon)(|\ln \eta(\varepsilon)|^{\frac{1}{2}} + 1), \tag{2.16}$$

if $a \equiv 0$. Here C is a positive constant independent of ε.

Theorem 2.4. *Suppose (A1), (A2), let $\eta = \mathrm{const}$, set $\mathbb{M}_0^\varepsilon$ be empty. For b and R_2 in (A1) we denote:*

$$\alpha^\varepsilon(s) := \begin{cases} \dfrac{|\partial\omega_k|\eta}{2bR_2}, & |s - s_k^\varepsilon| < bR_2\varepsilon, \quad k \in \mathbb{M}^\varepsilon, \\ \quad 0, & \textit{otherwise}. \end{cases}$$

Suppose also that:

(A5) *There exists a function $\alpha = \alpha(s)$ in $W_\infty^1(\gamma)$ and a function $\varkappa = \varkappa(\varepsilon)$, $\varkappa(\varepsilon) \to +0$, $\varepsilon \to +0$, such that for all sufficiently small ε the estimates (2.10) are valid.*

Then the estimate:

$$\|(\mathcal{H}^\varepsilon - \mathrm{i})^{-1} - (\mathcal{H}_{\alpha\mathrm{a}}^0 - \mathrm{i})^{-1}\|_{L_2(\Omega)\to W_2^1(\Omega^\varepsilon)} \leqslant C\big(\varepsilon^{\frac{1}{2}} + \varkappa(\varepsilon)\big), \tag{2.17}$$

holds true, where C is a positive constant independent of ε.

Let us discuss the main results. Assumption (A1) says that the sizes of holes are of the same order and there is a minimal distance between them. This is a very natural assumption for the perforation. At the same time, no periodicity for the perforation is assumed. Moreover, since set $\mathbb{M}^\varepsilon$ is arbitrary, we do not need to assume that it is infinite, and for instance, the number of holes can be finite. In the latter case, by choosing an appropriate set $\mathbb{M}^\varepsilon$, we can even get the situation when the distances between the holes are not small, but finite. In this situation one can still apply Theorems 2.2–2.4. Theorem 2.1 is valid only in the case when the holes with Dirichlet condition are distributed quite densely in order to satisfy Assumption A3.

Assumption (A2) is a restriction for the geometry of boundaries $\partial\omega_k$. We first stress that problem (2.1) can be rewritten to the Neumann problem for the Laplace equation by letting $X_k = \nabla V_k$. Then identity (2.2) is the solvability condition and this is the only restriction for φ_k we suppose. Problem (2.1) is solvable for each fixed k and it is solution belongs to $L_\infty(B_{b_* R_2}(0) \setminus \omega_k)$. And we assume that the norm $\|X_k\|_{L_\infty(B_{b_* R_2}(0)\setminus\omega_k)}$ is bounded uniformly in k.

According to Theorem 2.1, if the sizes of the holes are not too small (cf. (2.6)) and the holes with the Dirichlet condition are, roughly speaking, distributed "uniformly" (Assumption (A3)), the homogenized operator is subject to the Dirichlet condition on γ and we have the norm resolvent condition in the sense of the operator norm $\|\cdot\|_{L_2(\Omega)\to L_2(\Omega^\varepsilon)}$. As one can see, relation (2.6) admits the situation when the sizes of the holes are much smaller than the distances between them (for instance, $\eta(\varepsilon) = \varepsilon^\alpha$, $\alpha = const > 0$), but nevertheless the homogenized operator is still subject to the Dirichlet condition on γ. This phenomenon is close to a similar one for the operators with frequent alternation of boundary conditions, cf. [28, 29, 49].

If the function $\varepsilon \ln \eta(\varepsilon)$ goes to a constant or to infinity as $\varepsilon \to +0$ and there are holes with the Dirichlet condition, the homogenized operator has boundary condition (2.8) on γ, see Theorem 2.2. This boundary condition describes a delta-interaction on γ, see, for instance, [50, App. K, Sec. K.4.1], and the similar situation holds for the problems with frequent alternation of boundary conditions with the Dirichlet conditions on exponentially small parts of the boundary, cf. [26–28, 49]. The norm resolvent convergence holds in the sense of the operator norm $\|\cdot\|_{L_2(\Omega)\to L_2(\Omega^\varepsilon)}$ only. To improve the norm, one has either to employ the boundary corrector, see (2.13), or to assume additionally $\rho = 0$, see (2.14). We observe that according to Assumption (A4), coefficient β in boundary condition (2.8) for the homogenized operator depends only on the distribution of the points s_k^ε and there is no dependence on the geometries of the holes. There are also no special restrictions for part $\partial\theta_0^\varepsilon$ with the Dirichlet condition. For instance, the number of holes in $\partial\theta_0^\varepsilon$ can be finite or infinite and the distribution of this set can be very arbitrary.

If the perturbed operator has no Dirichlet condition on $\partial\theta^\varepsilon$, the homogenized operator has either condition (2.8) on γ (Theorem 2.4) or even no condition (Theorem 2.3). In both cases we again have the norm resolvent convergence in the operator norm $\|\cdot\|_{L_2(\Omega)\to W_2^1(\Omega^\varepsilon)}$. In Theorem 2.3 we need no additional restrictions thanks to the assumption $\eta(\varepsilon) \to +0$ or $a \equiv 0$. In Theorem 2.4 η is constant and because of this we introduce Assumption (A5). Its means that the lengths of $\partial\omega_k$ should be distributed rather smoothly to satisfy (2.10). We stress that the coefficient β in (2.8) for the homogenized operator depends both on the distribution of the holes and the sizes of their boundaries.

Let us also discuss assumptions (A4) and (A5). This is in fact the same assumption but adapted for two different cases. The sum in the left hand side of (2.10) is nothing but the norm in $W_2^{-\frac{1}{2}}(0, \ell)$. This estimate obviously holds true for a periodic perforation. As an example of a non-periodic perforation, we can mention the situation when we start with a strictly periodic perforation along an infinite curve but then we change the geometry and locations of a part of holes so that the total number of deformed holes associated with each segment $s \in (q, q + 1)$, $q \in \mathbb{Z}$, is relatively small in comparison with unchanged holes. Then inequality (2.10) is still true. Moreover, our conjecture is that Assumptions (A4) and (A5) can not be improved or omitted once we want to have a norm resolvent convergence.

About the sharpness of the estimates for the rate of convergences, we observe that many of these estimates are order sharp, i.e., the smallness order can not be improved. At the same time, the study of the sharpness is an independent problem that requires a completely different approach in comparison with the technique we employ in the proofs of Theorems 2.1–2.4. The sharpness of the estimates are proved in Section 8 of [1].

Our final main result describes the convergence of the spectrum of $\mathcal{H}^\varepsilon$.

Theorem 2.5. *Under the hypotheses of Theorems 2.1–2.4 the spectrum of perturbed operator $\mathcal{H}^\varepsilon$ converges to that of the corresponding homogenized operator. Namely, if λ is not in the spectrum of the homogenized operator, for sufficiently small ε, the same is true for the perturbed operator. And if λ is in the spectrum of the homogenized operator, for each ε, there exists λ_ε in the spectrum of the perturbed operator such that $\lambda_\varepsilon \to \lambda$ as $\varepsilon \to +0$.*

We note that this theorem is not implied immediately by Theorems 2.1–2.4. Despite these theorems state convergence of the perturbed resolvent to a homogenized one in the norm sense, the norm is ε-dependent. Nevertheless, this makes no serious troubles and in the proof of Theorem 2.5 it is proved a simple trick to overcome this difficulty.

References

[1] Borisov D., Cardone G., Durante T. Homogenization and uniform resolvent convergence for elliptic operators in a strip perforated along a curve. *Proc. R. Soc.Edingurgh Sect. A*, 2016, **146**(6), P. 115-1158.

[2] Belyaev A.G. Averaging of a mixed boundary value problem for the Poisson equation in a domain perforated along the boundary. *Russ. Math. Surv.*, 1990, **45**, P. 140.

[3] Chechkin G.A., Chechkina T.A., D'Apice C., De Maio U. Homogenization in domains randomly perforated along the boundary. *Discr. Cont. Dynam. Syst., Ser. B.*, 2009, **12**, P. 713–730.

[4] Chechkin G.A., Koroleva Yu.O., Meidell A., Persson L.-E. On the Friedrichs Inequality in a Domain Perforated Aperiodically along the Boundary. Homogenization Procedure. Asymptotics for Parabolic Problems. *Russ. J. Math. Phys.*, 2009, **16**, P. 1-16.

[5] Gómez D., Lobo M., Pérez M.E., Shaposhnikova T.A. Averaging of variational inequalities for the Laplacian with nonlinear restrictions along manifolds. *Appl. Anal.*, 2013, **92**, P. 218–237.

[6] Gómez D., Pérez M.E., Shaposhnikova T.A. On homogenization of nonlinear Robin type boundary conditions for cavities along manifolds and associated spectral problems. *Asymptot. Anal.*, 2012, **80**, P. 289–322.

[7] Lobo M., Oleinik O.A., Pérez M.E., Shaposhnikova T.A. On homogenizations of solutions of boundary value problems in domains, perforated along manifolds. *Ann. Sc. Norm. Super. Pisa Cl. Sci.*, 1997, **25**(4), P. 611–629.

[8] Lobo M., Oleinik O.A., Pérez M.E., Shaposhnikova T.A. On boundary-value problems in domains perforated along manifolds. *Russ. Math. Surv.*, 1997, **52**, P. 838–839.

[9] Birman M.Sh. On the averaging procedure for periodic operators in a neighborhood of an edge of an internal gap. *St. Petersburg Math. J.*, 2004, **15**, P. 507–513.

[10] Birman M.Sh., Suslina T.A. Homogenization with corrector term for periodic elliptic differential operators. *St. Petersburg Math. J.*, 2006, **17**, P. 897–973.

[11] Birman M.Sh., Suslina T.A. Homogenization with corrector for periodic differential operators. Approximation of solutions in the Sobolev class $H^1(\mathbb{R}^d)$. *St. Petersburg Math. J.*, 2007, **18**, P. 857–955.

[12] Suslina T.A. Homogenization with corrector for a stationary periodic Maxwell system. *St. Petersburg Math. J.*, 2008, **19**, P. 455–494.

[13] Suslina T.A. Homogenization in Sobolev class $H^1(\mathbb{R}^d)$ for periodic elliptic second order differential operators including first order terms. *St. Petersburg Math. J.*, 2011, **22**, P. 81–162.

[14] Suslina T.A., Kharin A.A. Homogenization with corrector for a periodic elliptic operator near an edge of inner gap. *J. Math. Sci.*, 2009, **159**, P. 264–280.

[15] Cardone G., Pastukhova S.E., Zhikov V.V. Some estimates for nonlinear homogenization. *Rend. Accad. Naz. Sci. XL Mem. Mat. Appl.*, 2005, **29**, P. 101–110.

[16] Pastukhova S.E. Some Estimates from Homogenized Elasticity Problems. *Dokl. Math.*, 2006, **73**, P. 102–106.

[17] Pastukhova S.E., Tikhomirov R.N. Operator Estimates in Reiterated and Locally Periodic Homogenization. *Dokl. Math.*, 2007, **76**, P. 548–553.

[18] Zhikov V.V. On operator estimates in homogenization theory. *Dokl. Math.*, 2005, **72**, P. 534–538.

[19] Zhikov V.V. Spectral method in homogenization theory. *Proc. Steklov Inst. Math.*, 2005, **250**, P. 85–94.

[20] Zhikov V.V. Some estimates from homogenization theory. *Dokl. Math.*, 2006, **73**, P. 96–99.

[21] Griso G. Error estimate and unfolding for periodic homogenization. *Asymptot. Anal.*, 2004, **40**, P. 269–286.

[22] Griso G. Interior error estimate for periodic homogenization. *C. R. Acad. Sci. Paris Ser. I Math.*, 2005, **340**, P. 251–254.

[23] Kenig C.E., Lin F., Shen Z. Convergence rates in L^2 for elliptic homogenization problems. *Arch. Rat. Mech. Anal.*, 2012, **203**, P. 1009–1036.

[24] Kenig C.E., Lin F., Shen Z. Periodic homogenization of green and neumann functions. *Comm. Pure Appl. Math.*, 2014, **67**, P. 1219–1262.

[25] Borisov D., Bunoiu R., Cardone G. Homogenization and asymptotics for a waveguide with an infinite number of closely located small windows. *J. Math. Sci.*, 2011, **176**, P. 774–785.

[26] Borisov D., Bunoiu R., Cardone G. On a waveguide with frequently alternating boundary conditions: homogenized Neumann condition. *Ann. Henri Poincaré*, 2010, **11**, P. 1591–1627.

[27] Borisov D., Bunoiu R., Cardone G. On a waveguide with an infinite number of small windows. *Compt. Rend. Math.*, 2011, **349**, P. 53–56.

[28] Borisov D., Bunoiu R., Cardone G. Waveguide with non-periodically alternating Dirichlet and Robin conditions: homogenization and asymptotics. *Z. Angew. Math. Phys.*, 2013, **64**, P. 439–472.

[29] Borisov D., Cardone G. Homogenization of the planar waveguide with frequently alternating boundary conditions. *J. Phys. A.*, 2009, **42**, id 365205.

[30] Borisov, D., Cardone, G.: Complete asymptotic expansions for the eigenvalues of the Dirichlet Laplacian in thin three-dimensional rods, ESAIM: COCV 17 (2011), 887-908.

[31] Borisov D., Cardone G. Planar waveguide with "twisted" boundary conditions. *Small width, J. Math. Phys.*, 2012, **53**, 023503.

[32] Borisov D., Cardone G. Spectra of operator pencils with small PT-symmetric periodic perturbation. *ESAIM: COCV*, 2020, **26**, 2019070.

[33] Borisov D., Cardone G., Checkhin G., Koroleva Yu. On elliptic operators with Steklov condition perturbed by Dirichlet condition on a small part of boundary. *Calc. Var. Part. Diff. Eq.*, 2021, **60**, P. 48.

[34] Cardone G., Khrabustovskyi A. Neumann spectral problem in a domain with very corrugated boundary, *J. Diff. Eq.*, 2015, **259**(6), P. 2333–2367.

[35] Cardone G., Khrabustovskyi A. δ'-interaction as a limit of a thin Neumann waveguide with transversal window. *J. Math. Anal. Appl.*, 2019, **473**(2), P. 1320–1342.

[36] Cardone G., Khrabustovskyi A. Spectrum of the Laplacian on a domain perturbed by small resonators, arXiv: 1808.05402.

[37] Cardone G., Minutolo V., Nazarov S.A. Gaps in the essential spectrum of periodic elastic waveguides. *Z. Angew. Math. Mech.*, 2009, **89**(9), P. 729–741.

[38] Cardone G., Nazarov S.A., Sokolowski. Asymptotics of solutions of the Neumann problem in a domain with closely posed components of the boundary. *Asympt. Anal.*, 2009, **62**, P. 41–88.

[39] Cardone G., Nazarov S.A., Taskinen J. Spectra of open waveguides in periodic media. *J. Functional Anal.*, 2015, **269**(8), P. 2328–2364.

[40] Aiyappan S., Cardone G., Perugia C., Prakash R. Homogenization of a nonlinear monotone problem in a locally periodic domain via unfolding method. *Nonlinear Analysis: Real World Applications*, 2022, **66**, 103537.

[41] Borisov D., Cardone G., Faella L., Perugia C. Uniform resolvent convergence for a strip with fast oscillating boundary. *J. Diff. Equ.*, 2013, **255**, P. 4378–4402.

[42] Nazarov S.A. Dirichlet problem in an angular domain with rapidly oscillating boundary: Modeling of the problem and asymptotics of the solution. *St. Petersburg Math. J.*, 2008, **19**, P. 297–326.

[43] Olejnik O.A., Shamaev A.S., Yosifyan G.A. Mathematical Problems in Elasticity and Homogenization. *Stud. Math. Appl.*, 1992, **26**. North-Holland, Amsterdam.

[44] Marchenko V.A., Khruslov E.Ya. *Boundary Value Problems in Domains with Fine-Grained Boundary*. Naukova Dumka, Kiev, 1974. (in Russian)

[45] Cardone G., Panasenko G.P., Sirakov Y. Asymptotic analysis and numerical modeling of mass transport in tubular structures. *Math. Models Meth. Appl. Sc.*, 2010, **20**(4), P. 1-25.

[46] Borisov D. Asymptotics for the solutions of elliptic systems with fast oscillating coefficients. *St. Petersburg Math. J.*, 2009, **20**, P. 175–191.

[47] Mikhajlov V.P. *Partial Differential Equations*. Mir Publishers, Moscow, 1978.

[48] Borisov D., Krejčiřık D. $\mathcal{PT}$-symmetric waveguide. *Integr. Equat. Oper. Th.*, 2008, **62**, P. 489–515.

[49] Chechkin G.A. Averaging of boundary value problems with singular perturbation of the boundary conditions. *Russ. Acad. Sci. Sb. Math.*, 1994, **79**, P. 191–220.

[50] Albeverio S., Gesztesy F., Høegh-Krohn R., Holden H. *Solvable models in quantum mechanics*, 2nd ed. AMS Chelsea Publishing, Providence, Rhode Island, 2005.

Submitted 28 January 2022; revised 31 January 2022; accepted 2 February 2022

Information about the authors:

Giuseppe Cardone – Universita di Napoli ”Federico II”, Dipartimento di Matematica e Applicazioni ”R. Caccioppoli”, Via Cintia, Napoli, Italy; giuseppe.cardone@unina.it

Tiziana Durante – University of Salerno, Department of Information and Electrical Engineering and Applied Mathematics, Via Ponte Don Melillo, 1, 84084, Fisciano (SA), Italy; tdurante@unisa.it

Conflict of interest: the authors declare no conflict of interest.

NANOSYSTEMS:
PHYSICS, CHEMISTRY, MATHEMATICS

Original article

Briet Ph. *Nanosystems:*
Phys. Chem. Math., 2022, **13** (1), 12–16.
http://nanojournal.ifmo.ru
DOI 10.17586/2220-8054-2022-13-1-12-16

A model of sheared nanoribbons

Ph. Briet

Aix Marseille Université, Université de Toulon, CNRS, CPT, Marseille France

briet@univ-tln.fr

PACS 35R45, 85Q10

ABSTRACT In this note, we investigate the spectral properties of the Dirichlet Laplacian defined on an infinite band subject to a "shearing". We give conditions for which the shear does not produce discret eigenvalue. In a second part we discuss the existence of discrete spectrum.

KEYWORDS Quantum waveguide, sheared band, Hardy inequality

FOR CITATION Briet Ph. A model of sheared nanoribbons. *Nanosystems: Phys. Chem. Math.*, 2022, **13** (1), 12–16.

1. Introduction

The purpose of this note is to describe some unexpected spectral properties due to geometric shearing in a two dimensional quantum waveguide. To this end, we introduce the following model. Let $f : \mathbb{R} \to \mathbb{R}$ such that:
$(\mathbf{h})$ *the derivative* $f' \in L^\infty_{loc}(\mathbb{R})$ *and has a limit* β *at infinity:* $f'(s) \to \beta$ *as* $|s| \to \infty$, $\beta \in \mathbb{R} \cup \{\pm\infty\}$.
If $\beta \in \mathbb{R}$, the deviation is denoted by $\varepsilon := f'(s) - \beta$. Let $d > 0$. Consider the domain in $\mathbb{R}^2$:

$$\Omega = \{(x, y) \in \mathbb{R}^2; x \in \mathbb{R}, f(x) < y < f(x) + d\}$$

The straight tube is denoted as $\Omega_0 = \mathbb{R} \times (0, d)$ $(f = 0)$.

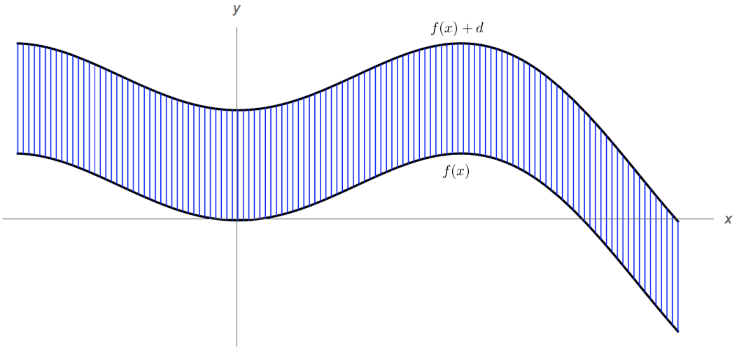

FIG. 1. Sheared nanoribbon

We are focusing on the spectral analysis of the "Dirichlet Laplacian" denoted by $-\Delta_D$ in $\mathrm{L}^2(\Omega)$ i.e. the self-adjoint operator in $\mathrm{L}^2(\Omega)$ defined from the quadratic form

$$\mathcal{Q}_D[\psi] = \int_\Omega |\nabla\psi(x, y)|^2 dxdy, \quad \psi \in \mathrm{H}^1_0(\Omega).$$

Here, we use standard notation for Sobolev space e.g. $\mathrm{H}^1_0(\Omega)$: H^1-norm closure of $C^\infty_0(\Omega)$, the H^1 norm is denoted by $\|\cdot\|_1$. For finite β it is convenient to use an appropriate change of variables:

$$(s, t) \in \Omega_0 \longrightarrow \mathcal{L}(s, t) = (s, f(s) + t) \in \Omega$$

The Laplace operator in the curvilinear coordinates $(s, t) \in \mathbb{R} \times (0, d)$ is given by:

$$H_f = -(\partial_s - f'\partial_t)^2 - \partial_t^2.$$

It is associated to the following quadratic form:

$$q[\varphi] = \|(\partial_s - f'\partial_t)\varphi\|^2 + \|\partial_t\varphi\|^2; \varphi \in \mathrm{Dom}(q) \tag{1}$$

By direct calculation or by using the following inequalities, [1]:

$$c_1\|\varphi\|_1^2 \leq q[\varphi] \leq c_2\|\varphi\|_1^2, \varphi \in C_0^\infty(\Omega_0), \tag{2}$$

for two constants $c_1, c_2 > 0$ we see that q is closed on $\mathrm{Dom}(q) = H_0^1(\Omega_0)$.

1.1. Related model

Our motivation for this work comes mainly from recent results about the spectral analysis of the Dirichlet Laplacian defined on a twisting tube in $\mathbb{R}^3$, [2]. Let $\omega \in \mathbb{R}^2$ an open bounded set of $\mathbb{R}^2$ and $\mathbf{\Omega_0} = \{(s, t_1, t_2) \in \mathbb{R}^3, s \in \mathbb{R}; (t_1, t_2) \in \omega\}$ the straight tube of section ω. Denoting by $\theta = \theta(s)$ the angle-rotation of ω at s around the longitudinal axis. In this natural coordinate system, the Laplace operator on $L^2(\mathbf{\Omega_0})$ reads as:

$$H_{\theta'} := -(\partial_s + \theta'(s)\partial_\varphi)^2 - \Delta_t,$$

where $\Delta_t := \partial_{t_1}^2 + \partial_{t_2}^2$, $\partial_\varphi := t_1\partial_{t_2} - t_2\partial_{t_1}$. The function θ is supposed to have a finite limit β at infinity, let $\varepsilon(s) := \theta'(s) - \beta$ be the deviation. For this model, if ε has a definite sign, the existence of discrete eigenvalues is implied by the condition $\beta\varepsilon < 0$, see [2,3]. On the other hand it is proved in [4] that $H_{\theta'}$ has no discrete spectrum if $\beta\varepsilon \geq 0$. This last result is proved for some β and ε but it is conjectured to be true for every $\beta \in \mathbb{R}$ and deviation ϵ s.t. $\beta\varepsilon \geq 0$, see [4]. This then leads us to introduce the following terminology, we will talk about *repulsive twisting* if $\beta\varepsilon \geq 0$ and the other cases as e.g. $\beta\varepsilon < 0$ correspond to *attractive twisting*. For related works see [5].

Similary in this note if β is finite, *repulsive shearing* means $\beta\varepsilon \geq 0$, while *attractive shearing* means $\beta\varepsilon < 0$.

The issues we address here are the following. We study first the localisation of the essential spectrum in section 2, this allows us to show that the spectrum is purely discrete for $\beta = \mp\infty$. Then in section 3 we prove the absence of discrete spectrum for repulsive shearing. Finally, we discuss the case of attractive shearing and the existence of discrete eigenvalues in the last section.

2. Essential spectrum

2.1. Finite limit

Let $E_1(\beta) = \left(1 + \beta^2\right) E_1$, where $E_1 = \left(\frac{\pi}{d}\right)^2$ is the first transverse mode: $-\partial_t^2\chi(t) = E_1\chi(t), \|\chi\|_{L^2(0,d)} = 1$. In fact $\chi(t) = \sqrt{\frac{2}{d}}\sin(\frac{\pi t}{d})$.

Theorem 2.1. *Suppose that* $\varepsilon(s) \to 0$ *as* $|s| \to \infty$. *Then*

$$\sigma_{ess}(H_f) = [E_1(\beta), +\infty]$$

To prove the Theorem 2.1 we use the following Weyl Criteria in a suitable form sense. We denote by $\mathrm{Dom}(q)^*$ the dual space equipped with the norm:

$$\|\cdot\|_{-1} := \sup_{\varphi \in \mathrm{Dom}(q), \|\varphi\|_1 = 1} |(\cdot, \varphi)| = \|(H_f + 1)^{-1/2} \cdot \|.$$

Then

Proposition 2.1. *Then* $\lambda \in \sigma_{ess}(H_f)$ *iff there exists* $(\varphi_n)_{n\in\mathbb{N}} \in C_0^\infty(\Omega_0)$, $\|\varphi_n\| = 1$, *s.t. the following conditions hold:*

i) supp$\varphi_n \subset \Omega_0 \setminus (-n, n) \times (0, d), \forall n \geq 1$

ii) $\|(H_f - \lambda)\varphi_n\|_{-1} \to 0$

For the proof of this proposition, see [1], we noticed that this type of result is reminiscent of the spectral analysis of N-body quantum systems see e.g. [6] and conversely in the context of multistratified media [7]. It is worth noting that here the smoothness of the deviation ε is not required.

Proof of the Theorem. First, we suppose $f' = \beta \in \mathbb{R}$, denote by H_β the corresponding operator, it is invariant with respect to the longitudinal translation, then by using standard argument of the integral direct decomposition of operators we obtain $\sigma(H_\beta) = \sigma_{ess}(H_\beta) = [E_1(\beta), +\infty]$, [3].
Let us show that $\sigma_{ess}(H_f) = \sigma_{ess}(H_\beta)$. We choose $\lambda \in \sigma_{ess}(H_f)$ and let $(\varphi_n)_{n\in\mathbb{N}}$ be a Weyl sequence in the sense of the proposition 2.1. We have

$$H_\beta\varphi_n = H_f\varphi_n + W\varphi_n;\ W\varphi_n = \big(- \partial_t\varepsilon\partial_s - \partial_s\varepsilon\partial_t + (2\beta\varepsilon + \varepsilon^2)\partial_t^2\big)\varphi_n$$

Then to prove that $\lambda \in \sigma_{ess}(H_\beta)$ it is sufficient to show that $\|W\varphi_n\|_{-1} \to 0$ as $n \to \infty$. Set $\varepsilon_n = esssup\{|\varepsilon(s)|; s \in (-\infty, -n) \cup (n, \infty)\}$. First consider

$$\|\partial_t\varepsilon\partial_s\varphi_n\|_{-1} = \sup_{\varphi \in \mathrm{Dom}(q), \|\varphi\|_1 = 1} |(\varepsilon\partial_s\varphi_n, \partial_t\varphi)|.$$

We have $\forall\varphi \in \mathrm{Dom}(q), \|\varphi\|_1 = 1$, $|(\varepsilon\partial_s\varphi_n, \partial_t\varphi)| \le \varepsilon_n\|\partial_s\varphi_n\|\|\partial_t\varphi\|$ and $\|\partial_s\varphi_n\| \le \|\partial_s(H_f + 1)^{-1/2}\|\|(H_f + 1)\varphi_n\|_{-1} < c$ for some constant $c > 0$. Therefore $\|\partial_t\varepsilon\partial_s\varphi_n\|_{-1} \to 0$ as $n \to \infty$.
By using the same arguments we also have $\|\partial_s\varepsilon\partial_t\varphi_n\|_{-1}$ and

$$\|\partial_t(2\beta\varepsilon + \varepsilon^2)\partial_t\varphi_n\|_{-1} \le const.\varepsilon_n\|\partial_t(H_f + 1)^{-1/2}\|\|(H_f + 1)\varphi_n\|_{-1} \to 0$$

as $n \to \infty$. This implies our claim. The reverse inclusion follows in a similar way. □

2.2. Infinite limit

We prove the following theorem.

Theorem 2.2. *Suppose that $f' \in L^\infty_{loc}(\mathbb{R})$ and $f' \to \pm\infty$. Then $\sigma_{ess}(H) = \emptyset$.*

In this note we give a slightly different proof of this theorem than the one in [1].

Proof. Let $R > 0$ and large, let $\Omega_R^{int} := \{x = (x, y) \in \Omega; |y| < R\}$ and $\Omega_R^{ext} := \{x = (x, y) \in \Omega; |y| > R\}$. Denote by q_{int} (resp. q_{ext}) the following quadratic form. Let $\mathrm{Dom}(q_{int}) = \{\psi = \varphi\lfloor_R^{\Omega_{int}}, \varphi \in \mathrm{Dom}(q)\}$ (resp. $\mathrm{Dom}(q_{ext}) = \{\psi = \varphi\lfloor_{\Omega_R^{ext}}, \varphi \in \mathrm{Dom}(q)\}$)and for $\psi \in \mathrm{Dom}(q_{int})$ (resp. $\psi \in \mathrm{Dom}(q_{ext})$,

$$q_{int}[\psi] = q[\psi](\text{resp. } \mathrm{q}_{\mathrm{ext}}[\psi] = \mathrm{q}[\psi]).$$

Then let H_{int} (resp. H_{ext}) be the associated self-adjoint operator in $L^2(\Omega_R^{int})$ (resp. $L^2(\Omega_R^{ext})$), the operator $H_{int} \oplus H_{ext}$ correspond to the operator H but defined by means of Neumann boundary conditions at $(x, y) \in \Omega, y = R$. Then from [8] we know that for every $\psi \in \mathrm{Dom}(q)$ the following inequality takes place, $(H\psi, \psi) \ge (H_{int} \oplus H_{ext}\psi, \psi)$ which implies

$$\inf \sigma_{ess}\,(H) \ge \inf \sigma_{ess}\,(H_{int} \oplus H_{ext})\,.$$

But the domain Ω_R^{int} is bounded so by standard arguments $\sigma_{ess}(H_{int}) = \emptyset$, [9]. Then

$$\inf \sigma_{ess}\,(H_{int} \oplus H_{ext}) = \sigma_{ess}(H_{ext}).$$

On the other hand $\forall\varphi \in \mathrm{Dom}(q_{ext})$, $\|\varphi\|_{L^2(\Omega_{ext})} = 1$ we have

$$(H_{ext}\varphi, \varphi) \ge (\partial_x^2 \otimes \mathbb{1}_y\varphi, \varphi).$$

For $y \in \mathbb{R}$, $|y| > R$, let $(u, v) \in \mathbb{R}^2$ be the solution of $f(u)+d = f(v) = y$, $|u|, |v| \to \infty$ as $y \to \infty$. By usual arguments then there exists $\xi \in (u, v)$ s.t. $d = |f(v) - f(u)| = |v - u||f'(\xi)|$ so $b(y) = \dfrac{d}{|f'(\xi)|} \to 0$ as $y \to \infty$.

This implies that

$$(\partial_x^2 \otimes \mathbb{1}_y\varphi, \varphi) = \int\limits_{|y|>R} dy \int\limits_u^v \partial_x^2\varphi\varphi \ge \left(\frac{\pi}{\sup_{|y|>R} b(y)}\right)^2 := i(R).$$

So $\inf \sigma_{ess}(H^{ext}) \ge i(R)$ for any $R > 0$ and large. But $i(R) \to \infty$ as $R \to \infty$, the theorem is proved. □

3. Hardy inequalities

Theorem 3.1 (repulsive shearing)**.** *Suppose $\beta \in \mathbb{R}$, $f' \in L^\infty_{loc}(\mathbb{R})$, $\varepsilon \neq 0$ and $\beta\varepsilon \ge 0$. Then there exists $c > 0$ s.t.*

$$-\Delta_D - E_1(\beta) \ge \frac{c}{1 + s^2}, \tag{3}$$

holds in the quadratic form sense in $L^2(\Omega)$.

Remark 3.1.
- *The theorem implies the non-existence of bound states for the system.*
- *Because of the presence of positive term in the r.h.s, the result is stable by adding a small perturbation.*
- *If $\varepsilon = 0$, simple arguments show that the theorem cannot be true, [4].*

Sketch of proof. The proof of the Theorem follows the same lines as in [1]. The key point is given by the following identity. Let $\psi \in C_0^\infty(\Omega_0)$, χ denoting the first transverse mode, then

$$q[\psi] - E_1(\beta)\|\psi\|^2 = \|\partial_s\psi - \varepsilon\partial_t\psi - \beta\chi\partial_t(\chi^{-1}\psi)\|^2 + \|\chi\partial_t(\chi^{-1}\psi)\|^2 + \int\limits_{\Omega_0} \beta\varepsilon\left(E_1(\beta) + (\frac{\chi'}{\chi})^2\right)|\psi|^2. \tag{4}$$

This comes from the ground state decomposition i.e. by choosing $\psi(s, t) = \chi(t)\phi(s, t)$, $\phi \in C_0^\infty(\Omega_0)$ (see [9]) in the formula (1). Notice that by (4), since the r.h.s. is positive if $\beta\varepsilon \ge 0$ then the associated operator $H_{f'}$ has no spectrum below $E_1(\beta)$.

Let I be an real interval s.t. essinf$\{|\varepsilon|\} > 0$ on I and $\Omega_0^I = I \times (0, d)$. Denoting by:

$$\tilde{q_I}[\psi] := \|\partial_s\psi - \varepsilon\partial_t\psi - \beta\chi\partial_t(\chi^{-1}\psi)\|^2_{L^2(\Omega_0^I)} + \|\chi\partial_t(\chi^{-1}\psi)\|^2_{L^2(\Omega_0^I)}$$

$\mathrm{Dom}(\tilde{q_I}) = \{\psi\lfloor_{\Omega_0^I}, \psi \in H_0^1(\Omega_0)\}$. It is shown in [1] that $\tilde{q_I}$ is a closed quadratic form and:

$$\lambda_I = \inf_{\psi \in \mathrm{Dom}(q_I), \psi \neq 0_{\mathcal{H}_I}} \frac{\tilde{q}_I[\psi]}{\|\psi\|^2_{\mathcal{H}_I}} > 0.$$

Hence this gives a a local Hardy inequality i.e.:

$$q[\psi] - E_1\|\psi\|^2 \geq \int\limits_{\Omega_0} \beta\varepsilon\left(E_1(\beta) + (\frac{\chi'}{\chi})^2\right)|\psi|^2 + \lambda_I\|\mathbb{I}_I\psi\|^2. \tag{5}$$

We now finish the proof of the theorem. We can check that if $\varepsilon(s_0) \neq 0$ that

$$Q[\psi] := \|\partial_s\psi - \varepsilon\partial_t\psi - \beta\chi\partial_t(\chi^{-1}\psi -)\alpha\frac{\chi}{s-s_0}\phi\|^2,\ \alpha = \frac{1}{2(1+\beta^2)}; \forall\psi \in C_0^\infty(\Omega_0 \setminus \{s_0\}).$$

satisfies the estimate:

$$0 \leq Q[\psi] \leq \|\partial_s\psi - \varepsilon\partial_t\psi - \beta\chi\partial_t(\chi^{-1}\psi)\|^2 + \|\chi\partial_t(\chi^{-1}\psi)\|^2 - \frac{1}{4(1+\beta^2)}\|\frac{\psi}{s-s_0}\|^2$$

and then:

$$\frac{1}{4(1+\beta^2)}\|\frac{\psi}{s-s_0}\|^2 \leq \|\partial_s\psi - \varepsilon\partial_t\psi - \beta\chi\partial_t(\chi^{-1}\psi)\|^2 + \|\chi\partial_t(\chi^{-1}\psi)\|^2. \tag{6}$$

Let $\psi \in C_0^\infty(\Omega_0, \mathbb{R})$ and η be the following function:

$$\eta(s) = \begin{cases} 1, & |s-s_0| > l; \\ -\frac{1}{l}(s-s_0), & s \in (s_0 - l, s_0)\,; \\ \frac{1}{l}(s-s_0), & s \in (s_0, s_0 + l)\,. \end{cases}$$

Set $\Omega_l := (s_0 - l, s_0 + l) \times (0, d)$. By using the decomposition, $\psi = \eta\psi + (1-\eta)\psi$, evidently we have,

$$\int\limits_{\Omega_0} \frac{|\psi|^2}{1+(s-s_0)^2} \leq\ 2(\int\limits_{\Omega_0} \frac{|\eta\psi|^2}{(s-s_0)^2} + \int\limits_{\Omega_l} |\psi|^2). \tag{7}$$

We use (6) to estimate the first term of the r.h.s. of (7). Then

$$\begin{aligned} \int\limits_{\Omega_0} \frac{|\eta\psi|^2}{(s-s_0)^2} &\leq 8(1+\beta^2)\left(\|\partial_s\eta\psi - \eta\varepsilon\partial_t\psi - \beta\eta\chi\partial_t(\chi^{-1}\psi)\|^2 + \|\eta\chi\partial_t(\chi^{-1}\psi)\|^2\right) \\ &\leq 8(1+\beta^2)\left(\|\partial_s\psi - \varepsilon\partial_t\psi - \beta\chi\partial_t(\chi^{-1}\psi)\|^2 + \|\beta\chi\partial_t(\chi^{-1}\psi)\|^2\right) + \|\eta'\psi\|^2) \\ &\leq 8(1+\beta^2)\left(q[\psi] - E_1(\beta)\|\psi\|^2 + \|\eta'\psi\|^2)\right). \end{aligned}$$

Hence, we get:

$$\int\limits_{\Omega_0} \frac{|\psi|^2}{1+(s-s_0)^2} \leq 16(1+\beta^2)(q[\psi] - E_1(\beta)\|\psi\|^2) + 2(8(1+\beta^2)\frac{1}{l^2} + 1)\int\limits_{\Omega_l} |\psi|^2. \tag{8}$$

Combining this last inequality with (5), we obtain (3) for such a vector ψ. But (3) can be extended for all vector $\psi \in \mathrm{Dom}(q)$ and the theorem is proved.

4. Discrete spectrum

Theorem 4.1 (Attractive shearing)**.** *Suppose that ε satisfies $\varepsilon^2 + 2\beta\varepsilon \in L^1(\mathbb{R})$ and either*

$$\int\limits_{\mathbb{R}} (\varepsilon^2 + 2\beta\varepsilon) < 0 \tag{9}$$

or

$$\varepsilon \in W^1_{loc}(\mathbb{R}), \varepsilon \neq 0, \varepsilon \neq -2\beta \textit{ and } \int\limits_{\mathbb{R}} (\varepsilon^2 + 2\beta\varepsilon) = 0. \tag{10}$$

Then $\sigma_d(H_f) \neq \emptyset$.

Proof. i) follows from the following : Let $\psi_n(s,t) = \varphi_n(s)\chi(t); n \in \mathbb{N}$ where $(\varphi_n)_{n\in\mathbb{N}}$ is a suitable mollification of the identity on $\mathbb{R}$ then from (4),

$$q[\psi_n] - E_1(\beta)\|\psi_n\|^2 =$$

$$\|\partial_s\psi_n - f'\partial_t\psi_n - \varepsilon\chi'\varphi_n\|^2 + \|\chi\partial_t\phi_n\|^2 + \int\limits_{\Omega_0} \beta\varepsilon\left(E_1(\beta) + (\frac{\chi'}{\chi})^2\right)|\psi_n|^2 =$$

$$\|\varphi_n'\|^2_{L^2(\mathbb{R})} + E_1(\beta)\int\limits_{\mathbb{R}} (\varepsilon^2 + 2\beta\varepsilon)|\varphi_n|^2 ds$$

$$\to E_1(\beta)\int\limits_{\mathbb{R}} (\varepsilon^2 + 2\beta\varepsilon) ds \quad \text{as} \quad n \to \infty.$$

Then the condition (9), implies, for n large enough that $q[\psi_n] - E_1(\beta)\|\psi_n\|^2 < 0$.

ii) follows in a similar way by choosing a slightly different sequence of test functions,

$$\psi_{n,\delta}(s,t) = \chi(t)(\varphi_n(s) + \delta t\xi(s)); n \in \mathbb{N}, \delta > 0$$

where $\xi \in C_0^\infty((-n,n))$ and $\delta > 0$ is chosen in a suitable way.

Remark 4.1. *The assumptions* (9) *and* (10) *of the theorem are clearly not satisfied for repulsive shearing. They require no positive deviation and of course the condition* $\varepsilon < 0$ *is too strong.*

□

References

[1] Briet P., Abdou-Soimadou H., Krejčiřík D. Spectral analysis of sheared nanoribbons. *Z. Angew. Math. Phys.*, 2019, **70**(2), 18 pp.

[2] Exner P., Kovarik H. Spectrum of the Schrödinger operator in a periodically twisted tube. *Lett. Math. Phys.*, 2005, **73**, P. 183–192.

[3] Briet P., Raikov G., Kovarik H., Soccorsi E. Eigenvalue asymptotics in a twisted waveguide. *Comm. P.D.E.*, 2009, **34**(8).

[4] Briet P., Hammedi H., Krejčiřík D. Hardy inequality in a globally twisted waveguide. *Lett. Math. Phys.*, 2015, **105**, P. 939–958.

[5] Briet P., Hammedi H. Twisted waveguide with a Neumann window. Functional Analysis and Operator Theory for Quantum Physics : The Pavel Exner Anniversary Volume, European Mathematical Society, P. 161–175, 2017, EMS Series of Congress Reports, Eur. Math. Soc., Zürich, 2017.

[6] Deift P., Hunziker W, Simon B., Vock E. Pointwise bounds on eigenfunctions and wave packets in N-body quantum systems IV. *Commun. Math. Phys.*, 1978, **64**, 1–34.

[7] Dermenjian Y., Durand D., Iftimie V. Spectral analysis of an acoustic multistratified perturbed cylinder. *Commun. P.D.E.*, 1998, **23**(1-2), P. 141–169.

[8] Reed M., Simon B. *Methods of Modern Mathematical Physics, I: Functional Analysis*, Academic Press, New York-London, 1972.

[9] Davies E.B. *Heat Kernel and Spectral Theory*. Univ. Press, Cambridge, 1989.

[10] Krejčiřík D.D., Lu Z.Z. Location of the essential spectrum in curved quantum layers. *J.M.P.*, 2014, **55**, 13 pp.

Submitted 7 January 2022; accepted 9 January 2022

Information about the authors:

Ph. Briet – Aix Marseille Université, Université de Toulon, CNRS, CPT, Marseille France; briet@univ-tln.fr

Conflict of interest: the author declare no conflict of interest.

NANOSYSTEMS:
PHYSICS, CHEMISTRY, MATHEMATICS

Original article

Zagrebnov V.A. *Nanosystems: Phys. Chem. Math.*, 2022, **13** (1), 17–23.
http://nanojournal.ifmo.ru
DOI 10.17586/2220-8054-2022-13-1-17-23

Comments on the Chernoff estimate

Valentin A. Zagrebnov

Institut de Mathématiques de Marseille, 13453 Marseille, France

Valentin.Zagrebnov@univ-amu.fr

PACS 02.30.Sa, 02.30.Tb

ABSTRACT The Chernoff $\sqrt{n}$-Lemma is revised. This concerns two aspects: a re-examination of the Chernoff estimate in the strong operator topology and the operator-norm estimate for quasi-sectorial contractions. Applications to the Lie-Trotter product formula approximation C_0-semigroups are also discussed.

KEYWORDS Chernoff lemma, Semigroup theory, Product formula, Convergence rate.

ACKNOWLEDGEMENTS The strong convergence with the rate (c) (see, Section 3) was established for the first time by T. Möbus and C. Rouzé in [1, Lemma 4.2] by the method, which is different to that in our Lemma 3.1. I am thankful to Tim Möbus for useful correspondences and, in particular, for attracting my attention to an inconsistency in [2, Lemma 2.1], which is corrected in the present paper. These Comments are based on my lecture delivered on the *Pierre Duclos Workshop* (20-22 September 2021) at National Research University ITMO, Russian Federation. I am grateful to Prof. Igor Yu. Popov for invitation.

FOR CITATION Zagrebnov V.A. Comments on the Chernoff estimate. *Nanosystems: Phys. Chem. Math.*, 2022, **13** (1), 17–23.

1. Introduction

Recall that the Chernoff $\sqrt{n}$-Lemma [3, Lemma 2] is one of a key tool in the theory of semigroup approximations, see e.g. [4, Chapter III, Section 5]. For the reader's convenience and for motivation of the present comments, we show this lemma below.

Lemma 1.1. *Let bounded operator C on a Banach space $\mathfrak{X}$ ($C \in \mathcal{L}(\mathfrak{X})$) be a contraction, i.e., $\|C\| \leq 1$. Then, $\{e^{t(C-\mathbb{1})}\}_{t\geq 0}$ is a norm-continuous contraction semigroup on $\mathfrak{X}$ and one has the estimate:*

$$\|(C^n - e^{n(C-\mathbb{1})})x\| \leq \sqrt{n}\, \|(C-\mathbb{1})x\| \ , \tag{1.1}$$

for all $x \in \mathfrak{X}$ and $n \in \mathbb{N}$.

Proof. To prove the inequality (1.1) we use the representation:

$$C^n - e^{n(C-\mathbb{1})} = e^{-n} \sum_{m=0}^{\infty} \frac{n^m}{m!}(C^n - C^m) \ . \tag{1.2}$$

To proceed we insert:

$$\|(C^n - C^m)x\| \leq \left\|(C^{|n-m|} - \mathbb{1})x\right\| \leq |m-n|\|(C-\mathbb{1})x\| \ , \tag{1.3}$$

into (1.2) to obtain by the Cauchy-Schwarz inequality the estimate:

$$\begin{aligned} &\|(C^n - e^{n(C-\mathbb{1})})x\| \leq \|(C-\mathbb{1})x\|\, e^{-n} \sum_{m=0}^{\infty} \frac{n^m}{m!}|m-n| \leq \\ &\{\sum_{m=0}^{\infty} e^{-n}\frac{n^m}{m!}|m-n|^2\}^{1/2}\|(C-\mathbb{1})x\| \ . \ x \in \mathfrak{X} \ , \end{aligned} \tag{1.4}$$

Note that the sum in the right-hand side of (1.4) can be calculated explicitly. This gives the value n, which yields (1.1). ☐

The aim of the present comments is to revise the Chernoff $\sqrt{n}$-Lemma in two directions. First, we modify the $\sqrt{n}$-estimate (1.1) for contractions. Then, we apply two new estimates for the proof of the Chernoff product formula for *strongly continuous* semigroups (C_0-semigroups) in the *strong* operator topology, see Section 2 and Section 3.

Second, we use the idea of the *probabilistic approach* to the estimate in strong operator topology (Section 2) to uplift it to the *operator-norm* estimate for a special class of contractions: the *quasi-sectorial* contractions, see Section 4.

2. Revised $\sqrt{n}$-Lemma and Chernoff product formula

We start by a technical lemma. It is a *revised* version of the Chernoff $\sqrt{n}$-Lemma 1.1. Our *variational* estimate (2.1) in $\sqrt[3]{n}$-Lemma 2.1 and the *probabilistic approach* are, in a certain sense, more flexible than (1.1). Indeed, the scheme of the proof will be used later (Section 4) for uplifting the convergence of the Chernoff and the Lie-Trotter product formulae to the *operator-norm* topology.

Lemma 2.1. ($\sqrt[3]{n}$ -Lemma) *Let C be a contraction on a Banach space $\mathfrak{X}$. Then, $\{e^{t(C-\mathbb{1}}\}_{t\geq 0}$ is a norm-continuous contraction semigroup on $\mathfrak{X}$ and one has the estimate:*

$$\|(C^n - e^{n\,(C-\mathbb{1})})\,x\| \leq \frac{n}{\epsilon_n^2}\,2\,\|x\| + \epsilon_n\,\|(\mathbb{1}-C)\,x\,\|\,, \qquad n \in \mathbb{N}\setminus\{0\}\,, \tag{2.1}$$

for all $x \in \mathfrak{X}$ and $\epsilon_n > 0$. For the optimal value of the parameter ϵ_n :

$$\epsilon_n^* := \left(\frac{4\,n\,\|x\|}{\|(\mathbb{1}-C)\,x\,\|}\right)^{1/3}, \tag{2.2}$$

on the right-hand side of (2.1)*, we obtain the estimate:*

$$\|(C^n - e^{n\,(C-\mathbb{1})})\,\| \leq \frac{3}{2}\,\sqrt[3]{n}\,\|2\,(\mathbb{1}-C)\,\|^{2/3}\,, \tag{2.3}$$

which is the $\sqrt[3]{n}$ -Lemma.

Proof. Since operator C is bounded and $\|C\| \leq 1$, the operator $(\mathbb{1}-C)$ is the generator of a norm-continuous contraction semigroup:

$$\|\,e^{\,t(C-\mathbb{1})}\,\| \leq e^{-t}\left\|\sum_{m=0}^{\infty}\frac{t^m}{m!}C^m\right\| \leq 1\,. \tag{2.4}$$

In order to prove estimate (2.1), we use the representation:

$$C^n - e^{n(C-\mathbb{1})} = e^{-n}\sum_{m=0}^{\infty}\frac{n^m}{m!}(C^n - C^m)\,. \tag{2.5}$$

Then, we *split* the sum (2.5) into two parts: the *central* part for $|m-n| \leq \epsilon_n$ and the *tails* for $|m-n| > \epsilon_n$. Optimisation of the *splitting* parameter ϵ_n in (2.1) yields the best estimate and thus the optimal value of $\delta \in \mathbb{R}$.

For evaluation of the *tails*, we use the *Tchebychëv inequality*. Let $X_n \in \mathbb{N}_0$ be the *Poisson random variable* with the *rate* parameter n, that is, with the probability distribution $\mathbb{P}\{X_n = m\} = n^m e^{-n}/m!$. Then, one gets for the expectation: $\mathbb{E}(X_n) = n$, and for the variance: $\text{Var}(X_n) := \mathbb{E}((X_n - \mathbb{E}(X_n))^2) = n$. That being so, the Tchebychëv inequality yields

$$\mathbb{P}\{|X_n - \mathbb{E}(X_n)| > \epsilon\} \leq \frac{\text{Var}(X_n)}{\epsilon_n^2}\,, \ \text{ for any } \ \epsilon_n > 0. \tag{2.6}$$

Note that although for any $x \in \mathfrak{X}$ there is an evident bound: $\|(C^n - C^m)\,x\| \leq 2\,\|x\|$, for estimating (2.5) we shall also use below inequalities:

$$\begin{aligned}\|(C^{\,n} - C^{\,m})\,x\| &= \|C^{\,n-k}(C^k - C^{\,m-n+k})\,x\| \\ &\leq |m-n|\;\|C^{\,n-k}(\mathbb{1}-C)\,x\|, \quad k = 0,1,\ldots,n\,.\end{aligned} \tag{2.7}$$

Then by $\|C\| \leq 1$ and by the Tchebychëv inequality (2.6) we obtain the estimate for *tails*:

$$\begin{aligned}&e^{-n}\sum_{|m-n|>\epsilon_n}\frac{n^m}{m!}\|(C^n - C^m)\,x\| \leq e^{-n}\sum_{|m-n|>\epsilon_n}\frac{n^m}{m!}\cdot\,2\,\|x\| \\ &= \ \mathbb{P}\{|X_n - \mathbb{E}(X_n)| > \epsilon_n\}\cdot\,2\,\|x\| \leq \frac{n}{\epsilon_n^2}\,2\,\|x\|\,.\end{aligned} \tag{2.8}$$

To evaluate the *central* part of the sum (2.5), when $|m-n| \leq \epsilon_n$, note that by virtue of (2.7):

$$\begin{aligned}\|(C^n - C^m)x\| &\leq |m-n|\;\|C^{n-[\epsilon_n]}\,(\mathbb{1}-C)x\| \\ &\leq \epsilon_n\,\|(\mathbb{1}-C)\,x\|.\end{aligned} \tag{2.9}$$

Then we obtain:

$$e^{-n}\sum_{|m-n|\leq\epsilon_n}\frac{n^m}{m!}\,\|(C^n - C^m)\,x\| \leq \epsilon_n\,\|(\mathbb{1}-C)\,x\|\,, \quad x \in \mathfrak{X}\,, \tag{2.10}$$

for $n \in \mathbb{N}\setminus\{0\}$. Estimate (2.10), together with (2.8), yield (2.1) for all $u \in \mathfrak{X}$ and $\epsilon_n > 0$.

Minimising the estimate (2.1) with respect to parameter $\epsilon_n > 0$ one obtains the optimal value for ϵ_n^* (2.2) and

$$\frac{n}{\epsilon_n^{*\,2}}\, 2\,\|x\| + \epsilon_n^* \,\|(\mathbb{1} - C)\,x\,\| = \frac{3}{2}\,\sqrt[3]{n}\,(4\,\|x\|)^{1/3}\,\|(\mathbb{1} - C)\,x\,\|^{2/3}\,, \tag{2.11}$$

for all $x \in \mathfrak{X}$ and $n \in \mathbb{N} \setminus \{0\}$. As a consequence, (2.1) and (2.11) yield (2.3), which is the $\sqrt[3]{n}$ -Lemma. □

Theorem 2.2. (Chernoff product formula) *Let $\Phi : t \mapsto \Phi(t)$ be a function from $\mathbb{R}_0^+$ to contractions on $\mathfrak{X}$ such that $\Phi(0) = \mathbb{1}$. Let $\{U_A(t)\}_{t\geq 0}$ be a contraction C_0-semigroup, and let $D \subset \operatorname{dom}(A)$ be a core of the generator A.*

If the function $\Phi(t)$ has a strong right-derivative $\Phi'(+0)$ at $t = 0$ (that is, $\Phi'(+0)x$ exists for any $x \in \operatorname{dom}(\Phi'(+0))$) and if

$$\Phi'(+0)\,x := \lim_{t\to+0} \frac{1}{t}(\Phi(t) - \mathbb{1})\,x = -\,A\,x\,,$$

for all $x \in D$, then

$$\lim_{n\to\infty} [\Phi(t/n)]^n\,x = U_A(t)\,x\,, \tag{2.12}$$

for all $t \in \mathbb{R}_0^+$ and $x \in \mathfrak{X}$.

Proof. Consider the bounded approximations $\{A_n(s)\}_{n\geq 1}$ of generator A:

$$A_n(s) := \frac{\mathbb{1} - \Phi(s/n)}{s/n}\,, \quad s \in \mathbb{R}^+\,, \quad n \in \mathbb{N}\,. \tag{2.13}$$

Note that these operators are m-accretive: $\|(A_n(s) + \zeta\mathbb{1})^{-1}\| \leq (\mathrm{Re}(\zeta))^{-1}$ for $\mathrm{Re}(\zeta) > 0$ and for any $n \in \mathbb{N}$. By $\|\Phi(t)\| \leq 1$ together with (2.13) we obtain $\|e^{-t\,A_n(s)}\| \leq 1$, but also

$$\lim_{n\to\infty} A_n(s)\,x = A\,x\,, \tag{2.14}$$

for all $x \in D$ and any $s \in \mathbb{R}^+$. Then, given that $D = \operatorname{core}(A)$, by virtue of the *Trotter-Neveu-Kato* generalised strong convergence theorem (see, e.g., [5, Theorem 3.17] or [4, Chapter III, Theorem 4.8]) one obtains

$$\lim_{n\to\infty} e^{-t\,A_n(s)}\,x = U_A(t)\,x\,, \quad x \in \mathfrak{X}\,, \quad t \in \mathbb{R}_0^+\,. \tag{2.15}$$

This is the strong and uniform in t and in s convergence (2.15) of contractive approximants $\{e^{-t\,A_n(s)}\}_{n\geq 1}$ for $t \in [0,\tau]$ and $s \in (0, s_0]$.

Now, by Lemma 2.1 for contraction $C := \Phi(t/n)$ we obtain owing to (2.3) that:

$$\begin{aligned} &\|[\Phi(t/n)]^n\,x - e^{-t\,A_n(t)}\,x\| = \|([\Phi(t/n)]^n - e^{n(\Phi(t/n)-\mathbb{1})})\,x\| \\ &\leq \frac{3}{2}\,\sqrt[3]{n}\,(4\,\|x\|)^{1/3}\,\|(\mathbb{1} - \Phi(t/n))\,x\,\|^{2/3}\,, \quad x \in \mathfrak{X}\,. \end{aligned} \tag{2.16}$$

Since by (2.14) one gets for any $x \in D$ and uniformly on $(0, t_0]$:

$$\lim_{n\to\infty} \sqrt[3]{n}\,\|\,(\mathbb{1} - \Phi(t/n))\,x\,\|^{2/3} = \lim_{n\to\infty} t^{2/3}\,n^{-1/3}\,\|A_n(t)\,x\|^{2/3} = 0\,, \tag{2.17}$$

equations (2.16) and (2.17) provide uniformly on $(0, t_0]$:

$$\lim_{n\to\infty} \|\,[\Phi(t/n)]^n\,x - e^{-t\,A_n(t)}\,x\| = 0, \quad x \in D\,. \tag{2.18}$$

Then, (2.15) and (2.18) yield uniformly in $t \in [0, t_0]$ limit:

$$\lim_{n\to\infty} [\Phi(t/n)]^n\,x = U_A(t)\,x\,, \quad x \in D\,. \tag{2.19}$$

Note that by *density* of D and by the *uniform* estimate $\|\,[\Phi(t/n)]^n\,x - e^{-t\,A_n(t)}x\| \leq 2\,\|x\|$ the convergence in (2.18) can be extended to all $x \in \mathfrak{X}$. Indeed, it is known that on the *bounded* subsets of $\mathcal{L}(\mathfrak{X})$ the topology of *point-wise* convergence on a *dense* subset $D \subset \mathfrak{X}$ coincides with the *strong* operator topology, see, e.g., [6, Chapter III, Lemma 3.5]. As a consequence, limit (2.18) being extended to $x \in \mathfrak{X}$ and limit (2.15) yield (2.12). □

The limit (2.12) is called the *Chernoff product formula* in the *strong* operator topology for contractive C_0-semigroup $\{U_A(t)\}_{t\geq 0}$.

Proposition 2.3. [3] (Lie-Trotter product formula) *Let A, B and C be generators of contraction C_0-semigroups on $\mathfrak{X}$. Suppose that algebraic sum:*

$$Cx = Ax + Bx\,, \tag{2.20}$$

is valid for all $x \in D$, where domain $D = \operatorname{core}(C)$. Then, the semigroup $\{U_C(t)\}_{t\geq 0}$ can be approximated on $\mathfrak{X}$ in the strong operator topology by the Lie-Trotter product formula:

$$e^{-tC}\,x = \lim_{n\to\infty} (e^{-tA/n} e^{-tB/n})^n\,x\,, \quad x \in \mathfrak{X}\,, \tag{2.21}$$

for all $t \in \mathbb{R}_0^+$ *and* $C := \overline{(A+B)}$*, which is closure of the sum (2.20).*

Proof. Let us define the contraction $\mathbb{R}_0^+ \ni t \mapsto \Phi(t)$, $\Phi(0) = \mathbb{1}$, by:

$$\Phi(t) := e^{-tA} e^{-tB} \ . \tag{2.22}$$

Note that if $x \in D$, then derivative

$$\Phi'(+0)x = \lim_{t \to +0} \frac{1}{t} (\Phi(t) - \mathbb{1})\, x = -(A+B)\, x \ . \tag{2.23}$$

Now, we are in position to apply Theorem 2.2. This yields (2.21) for $C := \overline{(A+B)}$. □

Corollary 2.4. *Extension of the strongly convergent Lie-Trotter product formula of Proposition 2.3 to quasi-bounded and holomorphic semigroups follows through verbatim.*

3. Revision of the Chernoff estimate

In this section, we show a one more Chernoff-type estimate (3.1), which is of a different nature than the variational estimate (2.1) ($\sqrt[3]{n}$-Lemma 2.1). In fact, it is a kind of *improvement* of the original Chernoff estimate (1.1) ($\sqrt{n}$-Lemma 1.1).

Lemma 3.1. *Let* $C \in \mathcal{L}(\mathfrak{X})$ *be contraction on a Banach space* $\mathfrak{X}$*. Then* $\{e^{t(C-\mathbb{1})}\}_{t \geq 0}$ *is a norm-continuous contraction semigroup on* $\mathfrak{X}$ *and the following estimate:*

$$\|(C^n - e^{n(C-\mathbb{1})})\, x\| \leq \frac{n}{2} \left(\|(C-\mathbb{1})^2\, x\| + \frac{e^2}{3}\, \|(C-\mathbb{1})^3\, x\|\right) , \tag{3.1}$$

holds for all $n \in \mathbb{N}$ *and* $x \in \mathfrak{X}$*.*

Proof. The first assertion is proven in Lemma 2.1, see (2.4).

To prove inequality (3.1) we use the *telescopic* representation:

$$C^n - e^{n(C-\mathbb{1})} = \sum_{k=0}^{n-1} C^{n-k-1}\, (C - e^{(C-\mathbb{1})})\, e^{k(C-\mathbb{1})} \ . \tag{3.2}$$

To proceed we exploit that operator $C \in \mathcal{L}(\mathfrak{X})$ is bounded and therefore:

$$C - e^{(C-\mathbb{1})} = -\frac{1}{2}\, (\mathbb{1} - C)^2 - (\mathbb{1} - C)^3 \sum_{m=3}^{\infty} \frac{(-1)^m}{m!}\, (\mathbb{1} - C)^{m-3} \ , \tag{3.3}$$

Owing to $\|C\| \leq 1$ one obtains the estimate:

$$\| \sum_{m=3}^{\infty} \frac{1}{m!}\, (\mathbb{1} - C)^{m-3} \| \leq \frac{1}{6}\, e^{\|\mathbb{1} - C\|} \leq \frac{e^2}{6} \, . \tag{3.4}$$

Then on account of (3.2) - (3.4) and (2.4) we obtain inequality (3.1). □

Corollary 3.2. (Chernoff product formula) *Let* $\Phi : t \mapsto \Phi(t)$ *be a function from* $\mathbb{R}_0^+$ *to contractions on* $\mathfrak{X}$ *such that* $\Phi(0) = \mathbb{1}$*, which satisfies conditions of Theorem* 2.2*. Then*

$$\lim_{n \to \infty} \|([\Phi(t/n)]^n - e^{n(\Phi(t/n) - \mathbb{1})})\, x\| = 0 \, , \quad x \in \mathfrak{X} \, , \tag{3.5}$$

and one gets the product formula (2.12).

Proof. On account of (3.1) we obtain estimate

$$\begin{aligned} &\|([\Phi(t/n)]^n - e^{n(\Phi(t/n) - \mathbb{1})})\, x\| \leq \\ &\frac{t^2}{2n} \left(\left\| \frac{n^2}{t^2}\, (\mathbb{1} - \Phi(t/n))^2\, x \right\| + \frac{e^2}{3}\, \frac{t}{n}\, \left\| \frac{n^3}{t^3} (\mathbb{1} - \Phi(t/n))^3\, x \right\| \right) , \quad x \in \mathfrak{X} \, . \end{aligned} \tag{3.6}$$

Note that by (2.14) we have on the dense set $D = \mathrm{core}(A)$ for any $t \in \mathbb{R}^+$:

$$\lim_{n \to \infty} \frac{n}{t}\, (\mathbb{1} - \Phi(t/n))\, x = A\, x \ , \quad x \in D \, . \tag{3.7}$$

Given that generator A of contractive C_0-semigroup is *accretive*, for $\mathrm{Re}(\zeta) > 0$ the range of resolvent: $\mathrm{ran}((A + \zeta\mathbb{1})^{-1}) = \mathfrak{X}$. As a consequence (cf. [6, Chapter III, Problem 2.9]), domains $\mathrm{dom}(A^2) \supset \mathrm{dom}(A^3)$ are *dense* in $\mathfrak{X}$ and limit (3.7) provides:

$$\lim_{n \to \infty} (A_n(t))^2\, x = A^2\, x \ , \quad \lim_{n \to \infty} (A_n(t))^3\, x = A^3\, x \ , \quad x \in D \subset \mathrm{dom}(A^3), \tag{3.8}$$

where $A_n(t) = (t/n)^{-1}\, (\mathbb{1} - \Phi(t/n))$.

By virtue of estimate (3.6) and (3.8), we obtain:

$$\lim_{n\to\infty} \|([\Phi(t/n)]^n - e^{n(\Phi(t/n)-\mathbb{1})})\, x\| = 0\,, \quad x \in D\,. \tag{3.9}$$

Then similarly to concluding arguments in Theorem 2.2 (that on the *bounded* subsets of $\mathcal{L}(\mathfrak{X})$ the topology of *point-wise* convergence on a *dense* subset $D \subset \mathfrak{X}$ coincides with the *strong* operator topology) the limit (3.9) can be extended to $x \in \mathfrak{X}$.

Now, given that $D = \mathrm{core}(A)$, by virtue of the *Trotter-Neveu-Kato* theorem we obtain the limit (2.15), and owing to (3.9) for $x \in \mathfrak{X}$, we deduce *Chernoff product formula* (2.12). □

Resuming the Chernoff $\sqrt{n}$-inequality: (1.1), and its variety: (2.1) and (3.1), we conclude that due to the terms with $\|(C-\mathbb{1})\, x\|$ all of them control only the *strong* convergence of the product formulae. The *rates*: $R_n(t)$, of these converges *conditioned* to $x \in D$ have the following asymptotic form for $t > 0$ and large $n \in \mathbb{N}$:
(a) For (1.1): $R_n(t) = 1/\sqrt{n}\, \|A_n(t)\, x\|$.
(b) For (2.1): $R_n(t) = 1/\sqrt[3]{n}\, \|A_n(t)\, x\|^{2/3}$.
(c) For (3.1): $R_n(t) = 1/n\, \|A_n(t)^2\, x\|$.

Remark 3.3. None of these three methods has an evident straightforward extension that could ensure the *operator-norm* convergence of the Chernoff product formula. In the next Section 4 we show that a relatively sophisticated method (cf.(b)) based on the Tchebychëv inequality (Section 2) is *a fortiori* more accurate to allow *uplifting* the convergence of the Chernoff product formula to the operator-norm topology for *quasi-sectorial* contractions on a Hilbert space.

4. Quasi-sectorial contractions and $(\sqrt[3]{n})^{-1}$-Theorem

Definition 4.1. [7] A contraction C on the Hilbert space $\mathfrak{H}$ is called *quasi-sectorial* with semi-angle $\alpha \in [0, \pi/2)$ with respect to the vertex at $z = 1$, if its numerical range $W(C) \subseteq D_\alpha$. Here

$$D_\alpha := \{z \in \mathbb{C} : |z| \le \sin\alpha\} \cup \{z \in \mathbb{C} : |\arg(1-z)| \le \alpha \text{ and } |z-1| \le \cos\alpha\}. \tag{4.1}$$

We comment that $D_{\alpha=\pi/2} = \mathbb{D}$ (unit disc) and recall that a *genera*l contraction C satisfies condition: $W(C) \subseteq \mathbb{D}$.

Note that if operator C is a quasi-sectorial contraction, then $\mathbb{1} - C$ is an m-sectorial operator with vertex $z = 0$ and semi-angle α. Then for C the limits: $\alpha = 0$ and $\alpha = \pi/2$, correspond respectively to self-adjoint and to standard contractions whereas for $\mathbb{1} - C$ they give a non-negative self-adjoint and an m-accretive (bounded) operators.

For $\lambda > 0$ the resolvent $(A + \lambda\,\mathbb{1})^{-1}$ of an m-sectorial operator A, with semi-angle $\alpha \in [0, \alpha_0]$, $\alpha_0 < \pi/2$, and vertex at $z = 0$, gives an example of the quasi-sectorial contraction.

Proposition 4.2. [7, 8] *If C is a quasi-sectorial contraction on a Hilbert space $\mathfrak{H}$ with semi-angle $0 \le \alpha < \pi/2$, then*

$$\|C^n(\mathbb{1} - C)\| \le \frac{K_\alpha}{n+1}\,, \; n \in \mathbb{N}\,. \tag{4.2}$$

The property (4.2) implies that the quasi-sectorial contractions belong to the class of so-called *Ritt's* operators [9]. This allows one to go beyond the $\sqrt[3]{n}$ -Lemma 2.1 to the $(\sqrt[3]{n})^{-1}$-Theorem and from estimates in the strong operator topology to the operator-norm topology.

Theorem 4.3. ($(\sqrt[3]{n})^{-1}$-Theorem) *Let C be a quasi-sectorial contraction on $\mathfrak{H}$ with numerical range $W(C) \subseteq D_\alpha$, $0 \le \alpha < \pi/2$. Then*

$$\left\|C^n - e^{n(C-\mathbb{1})}\right\| \le \frac{M_\alpha}{n^{1/3}}\,, \;\; n \in \mathbb{N}\,, \tag{4.3}$$

where $M_\alpha = 2K_\alpha + 2$ and K_α is defined by (4.2).

Proof. With help of inequality (4.2) we can improve the estimate of the *central* part of the sum (2.5) in Lemma 2.1. Note that on account of (2.7) we obtain by (4.2) and $\|C\| \le 1$:

$$\|C^n - C^m\| \le |m-n|\, \|C^{n-[\epsilon_n]}(\mathbb{1} - C)\| \le \epsilon_n\, \frac{K_\alpha}{n - [\epsilon_n] + 1}\,, \tag{4.4}$$

cf. (2.9). Here $\epsilon_n := n^{\delta+1/2}$ for $\delta < 1/2$, which makes sense for the estimate (2.8) of *tails*, and $[\epsilon_n]$ is the *integer* part of $\epsilon_n \ge |m-n|$. Then owing to (4.4) the *central* part has the estimate:

$$e^{-n} \sum_{|m-n|\le\epsilon_n} \frac{n^m}{m!}\, \|(C^n - C^m)\, x\| \le \epsilon_n\, \frac{K_\alpha}{n - [\epsilon_n] + 1}\, \|x\|\,, \quad x \in \mathfrak{X}\,, \quad n \in \mathbb{N}\,. \tag{4.5}$$

As a consequence, (2.8) and (4.5) yield instead of (2.3) (or (1.1)) the *operator-norm* estimate:

$$\left\|C^n - e^{n(C-\mathbb{1})}\right\| \le \frac{2}{n^{2\delta}} + \epsilon_n\, \frac{K_\alpha}{n - [\epsilon_n] + 1}\,, \; n \in \mathbb{N}\,. \tag{4.6}$$

Let $n_0 \in \mathbb{N}$ satisfies inequality: $2\,(\epsilon_{n_0} - 1) \leq n_0$. Then (4.6) gives

$$\left\| C^n - e^{n(C-\mathbb{1})} \right\| \leq \frac{2}{n^{2\delta}} + \frac{2K_\alpha}{n^{1/2-\delta}} \ , \ n > n_0 \ . \tag{4.7}$$

The estimate $M_\alpha / n^{1/3}$ of the Theorem 4.3 results from the *optimal* choice of the value: $\delta = 1/6$, in (4.7). □

Similar to $(\sqrt[3]{n})$-Lemma, the $(\sqrt[3]{n})^{-1}$-Theorem is the first step in developing the *operator-norm* approximation formula à la Chernoff. To this end one needs an operator-norm analogue of Theorem 2.2. Since the last includes the Trotter-Neveu-Kato strong convergence theorem, we need the *operator-norm* extension of this assertion for quasi-sectorial contractions.

Proposition 4.4. [7] *Let $\{X(s)\}_{s>0}$ be a family of m-sectorial operators in a Hilbert space $\mathfrak{H}$ such that for some $0 < \alpha < \pi/2$ and any $s > 0$ the numerical range $W(X(s)) \subseteq S_\alpha$. Let X_0 be an m-sectorial operator defined in a closed subspace $\mathfrak{H}_0 \subseteq \mathfrak{H}$, with $W(X_0) \subseteq S_\alpha$. Then the two following assertions are equivalent:*

$$(a) \qquad \lim_{s \to +0} \left\| (\zeta\mathbb{1} + X(s))^{-1} - (\zeta\mathbb{1} + X_0)^{-1} P_0 \right\| = 0 \ , \ \textit{for} \ \zeta \in S_{\pi-\alpha} \ ,$$

$$(b) \qquad \lim_{s \to +0} \left\| e^{-tX(s)} - e^{-tX_0} P_0 \right\| = 0 \ , \ \textit{for} \ t > 0 \ .$$

Here P_0 denotes the orthogonal projection from $\mathfrak{H}$ onto $\mathfrak{H}_0$ and $S_\alpha = \{z \in \mathbb{C} : |\arg(z)| \leq \alpha\}$ is a sector in complex plane $\mathbb{C}$ with semi-angle α and vertex at $z = 0$.

Now $(\sqrt[3]{n})^{-1}$-Theorem 4.3 and Proposition 4.4 yield a desired generalisation of the operator-norm approximation formula:

Proposition 4.5. [7] *Let $\{\Phi(s)\}_{s\geq 0}$ be a family of uniformly quasi-sectorial contractions on a Hilbert space $\mathfrak{H}$, i.e. such that there exists $0 \leq \alpha < \pi/2$ and $W(\Phi(s)) \subseteq D_\alpha$, for all $s \geq 0$. Let*

$$X(s) := (\mathbb{1} - \Phi(s))/s \ , \tag{4.8}$$

and let X_0 be a closed operator with non-empty resolvent set, defined in a subspace $\mathfrak{H}_0 \subseteq \mathfrak{H}$. Then, the family $\{X(s)\}_{s>0}$ converges, when $s \to +0$, in the uniform resolvent sense to the operator X_0 if and only if

$$\lim_{n \to \infty} \left\| \Phi(t/n)^n - e^{-tX_0} P_0 \right\| = 0 \ , \quad \text{for} \ t > 0 \ . \tag{4.9}$$

Here, P_0 denotes the orthogonal projection onto the subspace $\mathfrak{H}_0$.

Let A be an m-sectorial operator with semi-angle $0 < \alpha < \pi/2$ and with vertex at $z = 0$, which means that numerical range $W(A) \subseteq S_\alpha = \{z \in \mathbb{C} : |\arg(z)| \leq \alpha\}$. Then, $\{\Phi(t) := (\mathbb{1} + tA)^{-1}\}_{t\geq 0}$ is the family of quasi-sectorial contractions, i.e., $W(\Phi(t)) \subseteq D_\alpha$. Let $X(s) := (\mathbb{1} - \Phi(s))/s$, $s > 0$, and $X_0 := A$. Then, $X(s)$ converges when $s \to +0$, to X_0 in the uniform resolvent sense with the asymptotic

$$\|(\zeta\mathbb{1} + X(s))^{-1} - (\zeta\mathbb{1} + X_0)^{-1}\| = s \left\| \frac{A}{\zeta\mathbb{1} + A + \zeta s A} \cdot \frac{A}{\zeta\mathbb{1} + A} \right\| = O(s),$$

for any $\zeta \in S_{\pi-\alpha}$, since we have the estimate:

$$\left\| \frac{A}{\zeta\mathbb{1} + A + \zeta s A} \cdot \frac{A}{\zeta\mathbb{1} + A} \right\| \leq \left(1 + \frac{|\zeta|}{\mathrm{dist}\,(\zeta(1 + s\zeta)^{-1}, -S_\alpha)}\right) \left(1 + \frac{|\zeta|}{\mathrm{dist}(\zeta, -S_\alpha)}\right) \ .$$

Therefore, the family $\{\Phi(t)\}_{t\geq 0}$ satisfies the conditions of Proposition 4.5. This implies the operator-norm approximation of the exponential function , i.e. the semigroup for m-sectorial generator, by the powers of resolvent (*the Euler approximation formula*):

Corollary 4.6. [8,10] *If A is an m-sectorial operator in a Hilbert space $\mathfrak{H}$, with semi-angle $\alpha \in (0, \pi/2)$ and with vertex at 0, then*

$$\left\| (\mathbb{1} + tA/n)^{-n} - e^{-tA} \right\| \leq \frac{L_\alpha}{n} \ , \quad t \in S_{\pi/2-\alpha} \ , \tag{4.10}$$

for $n \in \mathbb{N}$.

5. Conclusion

Summarising we note that for the quasi-sectorial contractions instead of *divergent* (for $n \to \infty$) Chernoff's estimate (1.1), we find the estimate (4.7) which converges for $n \to \infty$ to zero in the *operator-norm* topology. Note that the rate $O(1/n^{1/3})$ of this convergence is obtained with help of the Poisson representation and the Tchebychëv inequality in the spirit of the proof of Lemma 2.1, and which is not optimal.

The estimate $M/n^{1/3}$ in the $(\sqrt[3]{n})^{-1}$-Theorem 4.3 can be improved by a more refined lines of reasoning. For example, by scrutinising our probabilistic arguments one can find a more precise Tchebychëv-type bound for probability of *tails*. This improves the estimate (4.7) to the rate $O(\sqrt{\ln(n)/n})$, see [11], but again only for *quasi-sectorial* contractions providing due to Proposition 4.2 the *operator-norm* contrôl (4.5) of the *central* part.

On the other hand, a careful analysis of localisation the *numerical range* of quasi-sectorial contractions [8, 10], generated in a Hilbert space $\mathfrak{H}$ by m-sectorial operators with semi-angle $\alpha \in (0, \pi/2)$, permits one to uplift the operator-norm estimate in Corollary 4.6 to the ultimate optimal α-dependent rate $O(1/n)$, [10, Theorem 4.1].

We note that with help of the *spectral representation*, one can easily obtain in (4.7) the optimal rate $O(1/n)$ of the operator-norm convergence for *self-adjoint* contractions C. This is a particular case of the quasi-sectorial contraction for $\alpha = 0$, cf. [7, Remark 3.2]. This also concerns the optimal rate of convergence $O(1/n)$ for the self-adjoint Euler approximation formula (4.10) for $A = A^* \geq 0$, which is $m($sectorial operator for $\alpha = 0$.

References

[1] Möbus T., Rouzé C. Optimal convergence rate in the quantum Zeno effect for open quantum systems in infinite dimensions. arXiv:2111.13911v2 [quant-ph], 2021, 1–27.

[2] Zagrebnov V.A. Comments on the Chernoff $\sqrt{n}$-lemma. In: *Functional Analysis and Operator Theory for Quantum Physics* (The Pavel Exner Anniversary Volume), European Mathematical Society, Zürich, 2017, P. 565–573.

[3] Chernoff P.R. Product formulas, nonlinear semigroups and addition of un- bounded operators. *Mem. Amer. Math. Soc.*, 1974, **140**, P. 1–121.

[4] Engel K.-J., Nagel R. *One-parameter Semigroups for Linear Evolution Equations*. Springer-Verlag, Berlin, 2000.

[5] Davies E.B. *One-parameter Semigroups*. Academic Press, London, 1980.

[6] Kato T. *Perturbation Theory for Linear Operators*. (Corrected Printing of the Second Edition). Springer-Verlag, Berlin Heidelberg, 1995.

[7] Cachia V., Zagrebnov V.A. Operator-Norm Approximation of Semigroups by Quasi-sectorial Contractions. *J. Fuct. Anal.*, 2001, **180**, P. 176–194.

[8] Zagrebnov V.A. Quasi-sectorial contractions. *J. Funct. Anal.*, 2008, **254**, P. 2503–2511.

[9] Ritt R.K. A condition that $\lim_{n\to\infty} T^n = 0$. *Proc. Amer. Math. Soc.*, 1953, **4**, P. 898–899.

[10] ArlinskiĭYu., Zagrebnov V. Numerical range and quasi-sectorial contractions. *J. Math. Anal. Appl.*, 2010, **366**, P.33–43.

[11] Paulauskas V. On operator-norm approximation of some semigroups by quasi-sectorial operators. *J. Funct. Anal.*, 2004, **207**, P. 58–67.

Submitted 7 January 2022; accepted 9 January 2022

Information about the authors:

V.A. Zagrebnov – Institut de Mathématiques de Marseille - AMU CMI - Technopôle Château-Gombert 39 rue F. Joliot Curie, 13453 Marseille, France; Valentin.Zagrebnov@univ-amu.fr

Conflict of interest: the author declare no conflict of interest.

NANOSYSTEMS:
PHYSICS, CHEMISTRY, MATHEMATICS

Mikhaylov A.S., Mikhaylov V.S. *Nanosystems: Phys. Chem. Math.*, 2022, **13** (1), 24–29.
http://nanojournal.ifmo.ru
DOI 10.17586/2220-8054-2022-13-1-24-29

Original article

On the construction of de Branges spaces for dynamical systems associated with finite Jacobi matrices

Alexander S. Mikhaylov[1,2,a], Victor S. Mikhaylov[1,b]

[1]St. Petersburg Department of V. A. Steklov Institute of Mathematics of the Russian Academy of Sciences, 191023 St. Petersburg, Russia
[2]St. Petersburg State University, 199034 St. Petersburg, Russia

[a]mikhaylov@pdmi.ras.ru, [b]vsmikhaylov@pdmi.ras.ru

Corresponding author: Alexander S. Mikhaylov, mikhaylov@pdmi.ras.ru

ABSTRACT We consider dynamical systems with boundary control associated with finite Jacobi matrices. Using the method previously developed by the authors, we associate with these systems special Hilbert spaces of analytic functions (de Branges spaces).

KEYWORDS Boundary control method, Krein equations, Jacobi matrices, de Branges spaces

ACKNOWLEDGEMENTS A. S. Mikhaylov and V. S. Mikhaylov were partly supported by Volkswagen Foundation project "From Modeling and Analysis to Approximation".

FOR CITATION Mikhaylov A.S., Mikhaylov V.S. On the construction of de Branges spaces for dynamical systems associated with finite Jacobi matrices. *Nanosystems: Phys. Chem. Math.*, 2022, **13** (1), 24–29.

1. Introduction

For a given sequence of positive numbers $\{a_0, a_1, \dots, a_{N-1}\}$ (in what follows we assume $a_0 = 1$) and real numbers $\{b_1, b_2, \dots, b_N\}$, we denote by A the finite Jacobi matrix given by:

$$A = \begin{pmatrix} b_1 & a_1 & 0 & 0 & 0 & \dots \\ a_1 & b_2 & a_2 & 0 & 0 & \dots \\ \dots & \dots & \dots & \dots & \dots & \dots \\ \dots & \dots & \dots & a_{N-2} & b_{N-1} & a_{N-1} \\ \dots & \dots & \dots & \dots & a_{N-1} & b_N \end{pmatrix}. \tag{1}$$

Let $u = (u_1, \dots, u_N) \in \mathbb{R}^N$ and $T > 0$ be fixed. With the matrix A we associate the dynamical system:

$$\begin{cases} u_{tt}(t) - Au(t) = F(t), \quad t > 0, \\ u(0) = u_t(0) = 0, \end{cases} \tag{2}$$

where the vector function $F(t) = (f(t), 0, \dots, 0)$, $f \in L_2(0, T)$ is interpreted as a *boundary control*. The solution of (2) is denoted by u^f. With the system (2), we associate the *response operator* acting by the rule:

$$\left(R^T f\right)(t) = u_1^f(t), \quad 0 < t < T. \tag{3}$$

The forward and inverse problems for the system (2) and for the special case of this system, the finite Krein-Stieltjes string, were the subjects of [1, 2], where, as a main tool, we used the Boundary control method [3, 4]. In this paper, we would like to demonstrate one more application of the Boundary control method, namely the construction of the de Banges space associated with (2).

De Branges spaces play an important role in the inverse spectral theory of first order canonical systems, see for example [5–7]. In [8, 9], the authors shows how to use the Boundary control method to associate de Branges spaces with different dynamical systems. Note that our approach differs from the classical one and potentially admits theallows generalization to multidimensional systems. The algorithm proposed in [8,9] is as follows: fixing some finite time $t = T$, one denotes by $\mathcal{F}^T$ the set of controls acting on the time interval $(0, T)$ and introduces the *reachable set* of the dynamical system at this time:

$$U^T := \{u^f(T) \,|\, f \in \mathcal{F}^T\}.$$

Then, one applies the Fourier transform $\mathbb{F}$ associated with the operator A to elements from U^T and get a linear manifold $\mathbb{F}U^T$. Then. this linear manifold is equipped with the norm defined by the *connecting operator*, which resulted in the de

Branges space associated with the initial dynamical system. In the models considered in [8,9], models the dynamical systems have different properties in with respect to the *boundary controllability*: the system associated with the Schrödinger operator is exactly controllable from the boundary,; the system associated with the one-dimensional Dirac operator is not controllable, but the controllability restores after some trick associated with doubling the state of the system, ; the discrete system associated with a finite Jacobi matrix is boundary controllable, but the time in the model considered was discrete, see also [10] for the case of semi-infinite matrix. The peculiarity of the system (2) is the lack of the boundary controllability, and in opposite to all systems considered in [9, 10], the speed of the wave propagation in (2) is infinite. Nevertheless we will show that the method from [8, 8] works, and using it, one can construct de Branges space associated with A.

In the second section, we provide the necessary information on for the solution of the forward and inverse problems for (2) from [2]. In the third section, we remind the reader of some useful definitions and construct the de Branges space associated with (2).

2. Dynamical system, forward problem, Krein equations

The following Cauchy problem for the difference equation:

$$\begin{cases} a_1\phi_2+b_1\phi_1=\lambda\phi_1, \\ a_n\phi_{n+1}+a_{n-1}\phi_{n-1}+b_n\phi_n=\lambda\phi_n, \quad n=2,\dots,N, \\ \phi_1=1, \end{cases} \tag{4}$$

determines the set of polynomials $\{1,\phi_2(\lambda),\dots,\phi_N(\lambda),\phi_{N+1}(\lambda)\}$. Let $\lambda_1,\dots,\lambda_N$ be the roots of the equation $\phi_{N+1}(\lambda)=0$, it is known [11] that they are real and distinct. We denote by $(\cdot,\cdot)$ the scalar product in $\mathbb{R}^N$ and introduce the vectors and the coefficients by the rules:

$$\varphi(\lambda)=\begin{pmatrix}\phi_1(\lambda)\\ \cdot\\ \cdot\\ \phi_N(\lambda)\end{pmatrix},\quad \varphi_k=\begin{pmatrix}\phi_1(\lambda_k)\\ \cdot\\ \cdot\\ \phi_N(\lambda_k)\end{pmatrix},\quad \rho_k=(\varphi_k,\varphi_k)\,,\quad k=1,\dots,N.$$

Thus, φ_k are non-normalized eigenvectors of A, corresponding to eigenvalues λ_k:

$$A\varphi_k=\lambda_k\varphi_k,\qquad k=1,\dots,N.$$

We call by *spectral data* and *the spectral function* ρ the following objects:

$$\{\lambda_i,\rho_i\}_{i=1}^N\,,\quad \rho(\lambda)=\sum_{\{k:\lambda_k<\lambda\}}\frac{1}{\rho_k}.$$

The standard application of the Fourier method yields:

Lemma 1. *The solution to (2) admits the spectral representation:*

$$u^f(t)=\sum_{k=1}^N h_k(t)\varphi_k,\quad u^f(t)=\int_{-\infty}^{\infty}\int_0^t S(t-\tau,\lambda)f(\tau)\,d\tau\varphi(\lambda)\,d\rho(\lambda), \tag{5}$$

where:

$$h_k(t)=\frac{1}{\rho_k}\int_0^t f(\tau)S_k(t-\tau)\,d\tau,$$

$$S(t,\lambda)=\begin{cases}\dfrac{\sin\sqrt{\lambda}t}{\sqrt{\lambda}}, & \lambda>0,\\ \dfrac{\operatorname{sh}\sqrt{|\lambda|}t}{\sqrt{|\lambda|}}, & \lambda<0,\\ t, & \lambda=0,\end{cases}\qquad S_k(t)=S(t,\lambda_k).$$

We introduce the *outer space* of the system (2), the space of controls: $\mathcal{F}^T:=L_2(0,T;\mathbb{C})$ with the scalar product $f,g\in\mathcal{F}^T$, $(f,g)_{\mathcal{F}^T}=\int_0^T f(t)\overline{g(t)}\,dt$. The *response operator* $R^T:\mathcal{F}^T\mapsto\mathcal{F}^T$ is introduced by the formula (3).

Making use of (5) implies the representation formula for R^T:

$$\left(R^T f\right)(t) = u_1^f(t) = \sum_{k=1}^N h_k(t) = \int_0^t r(t-s)f(s)\,ds,$$

where:

$$r(t) = \sum_{k=1}^N \frac{1}{\rho_k} S_k(t),$$

is called a *response function*. Note that the operator R^T is a natural analog of a dynamic Dirichlet-to-Neumann operator [4] in continuous, and [9, 12, 13] in discrete cases.

The *inner space* of (2), i.e. the space of states is $\mathcal{H}^N := \mathbb{C}^N$, indeed for any $T > 0$ and $f \in \mathcal{F}^T$, we have that $u^f(T) \in \mathcal{H}^N$. The scalar product in $\mathcal{H}^N$ is given by:

$$(a, b)_{\mathcal{H}^N} = \sum_{k=1}^N a_k \overline{b_k}.$$

The *control operator* $W^T : \mathcal{F}^T \mapsto \mathcal{H}^N$ is introduced by the rule:

$$W^T f = u^f(T).$$

Due to (5), we have that $W^T f = \sum_{k=1}^N h_k(T)\varphi_k$. In [1, 2], the authors used real inner and outer spaces, but in the complex case all the results are valid as well.

We introduce the subspace:

$$\mathcal{F}_1^T = \operatorname{Lin}\left\{S_k(T-t)\right\}_{k=1}^N,$$

where we assume complex coefficients in the span. The following lemma establishes the boundary controllability of (2):

Lemma 2. *The operator W^T maps $\mathcal{F}_1^T$ onto $\mathcal{H}^N$ isomorphically.*

The *connecting operator* $C^T : \mathcal{F}^T \mapsto \mathcal{F}^T$ is defined by the rule $C^T := \left(W^T\right)^* W^T$, so by the definition for $f, g \in \mathcal{F}^T$, one has:

$$\left(C^T f, g\right)_{\mathcal{F}^T} = \left(u^f(T), u^g(T)\right)_{\mathcal{H}^N} = \left(W^T f, W^T g\right)_{\mathcal{H}^N}. \tag{6}$$

It is crucial in the Boundary control method that C^T can be expressed in terms of inverse data:

Theorem 1. *The connecting operator admits the representation in terms of dynamic inverse data:*

$$\left(C^T f\right)(t) = \frac{1}{2}\int_0^T \int_{|t-s|}^{2T-s-t} r(\tau)\,d\tau f(s)\,ds,$$

and in terms of spectral inverse data:

$$\left(C^T f\right)(t) = \int_0^T \sum_{k=1}^N \frac{1}{\rho_k} S_k(T-t) S_k(T-s) f(s)\,ds. \tag{7}$$

Remark 1. *The formula (7) implies that $\mathcal{F}_1^T = C^T \mathcal{F}^T$, so $\mathcal{F}_1^T$ is completely determined by inverse data.*

2.1. Krein equations

By $f_k^T \in \mathcal{F}_1^T$, we denote the controls, driving the system (2) to prescribed *special states*:

$$d_k \in \mathcal{H}^N,\ d_k = (0, \dots, 1, \dots, 0), \quad k = 1, \dots, N.$$

It is important that such a controls can be found as the solutions to the Krein equations:

Theorem 2. *The control f_1^T can be found as the solution to the following equation:*

$$\left(C^T f_1^T\right)(t) = r(T-t), \quad 0 < t < T. \tag{8}$$

The controls f_k^T, $k = 2, \dots, N$ satisfy the system:

$$\begin{cases} -\left(C^T f_1^T\right)'' = b_1 C^T f_1^T + a_1 C^T f_2^T, \\ -\left(C^T f_k^T\right)'' = a_{k-1} C^T f_{k-1}^T + b_k C^T f_k^T + a_k C^T f_{k+1}^T, \quad k = 2, \dots, N-1, \\ -\left(C^T f_N^T\right)'' = a_{N-1} C^T f_{N-1}^T + b_N C^T f_N^T. \end{cases} \tag{9}$$

3. De Branges space for A

Here, we provide the information on de Branges spaces in accordance with [5,7]. The entire function $E:\mathbb{C}\mapsto\mathbb{C}$ is called a *Hermite-Biehler function* if $|E(z)|>|E(\overline{z})|$ for $z\in\mathbb{C}_+$. We use the notation $F^{\#}(z)=\overline{F(\overline{z})}$. The *Hardy space* H_2 is defined by: $f\in H_2$ if f is holomorphic in $\mathbb{C}^+$ and $\sup\limits_{y>0}\int_{-\infty}^{\infty}|f(x+iy)|^2\,dx<\infty$. Then, the *de Branges space* $B(E)$ consists of entire functions such that:

$$B(E):=\left\{F:\mathbb{C}\mapsto\mathbb{C},\ F\text{ entire},\ \frac{F}{E},\frac{F^{\#}}{E}\in H_2\right\}.$$

The space $B(E)$ with the scalar product:

$$[F,G]_{B(E)}=\frac{1}{\pi}\int\limits_{\mathbb{R}}F(\lambda)\overline{G(\lambda)}\frac{d\lambda}{|E(\lambda)|^2},$$

is a Hilbert space. For any $z\in\mathbb{C}$, the *reproducing kernel* is introduced by the relation:

$$J_z(\xi):=\frac{\overline{E(z)}E(\xi)-E(\overline{z})\overline{E(\overline{\xi})}}{2i(\overline{z}-\xi)}. \tag{10}$$

Then,

$$F(z)=[J_z,F]_{B(E)}=\frac{1}{\pi}\int\limits_{\mathbb{R}}J_z(\lambda)\overline{F(\lambda)}\frac{d\lambda}{|E(\lambda)|^2}.$$

We observe that a Hermite–Biehler function $E(\lambda)$ defines J_z by (10). The converse is also true [5,6]:

Theorem 3. *Let X be a Hilbert space of entire functions with reproducing kernel such that:*

1) *For any $\omega\in\mathbb{C}$ the point evaluation is a bounded functional, i.e. $|f(\omega)|\leqslant C_\omega\|f\|_X$,*
2) *if $f\in X$ then $f^{\#}\in X$ and $\|f\|_X=\|f^{\#}\|_X$,*
3) *if $f\in X$ and $\omega\in\mathbb{C}$ such that $f(\omega)=0$, then $\dfrac{z-\overline{\omega}}{z-\omega}f(z)\in X$ and $\left\|\dfrac{z-\overline{\omega}}{z-\omega}f(z)\right\|_X=\|f\|_X$,*

then X is a de Branges space based on the function:

$$E(z)=\sqrt{\pi}(1-iz)J_i(z)\|J_i\|_X^{-1},$$

where J_z is a reproducing kernel.

In the space $L_{2,\rho}(\mathbb{R})$ we take the subspace spanned on the first N polynomials generated by (4):

$$L_N:=\operatorname{Lin}\{\phi_1(\lambda),\dots,\phi_N(\lambda)\}.$$

Note that $\phi_1(\lambda),\dots,\phi_N(\lambda)$ are mutually orthogonal in $L_{2,\rho}(\mathbb{R})$, see [11]. By $P_N:L_{2,\rho}(\mathbb{R})\to L_{2,\rho}(\mathbb{R})$ we denote the orthogonal projector in $L_{2,\rho}(\mathbb{R})$ onto L_N acting by the rule:

$$P_Na=\sum_{k=1}^{N}(a,\phi_k)_{L_{2,\rho}(\mathbb{R})}\phi_k(\lambda),\quad a\in L_{2,\rho}(\mathbb{R}).$$

We introduce the Fourier transformation $\mathbb{R}^N\mapsto L_{2,\rho}(\mathbb{R})$ by the formula:

$$(Fb)(\lambda)=\sum_{k=1}^{N}b_k\phi_k(\lambda),\quad b=(b_1,\dots,b_N)\in\mathbb{R}^N.$$

Note that F is an unitary map between $\mathbb{R}^N$ and L_N, and:

$$b_k=(Fb(\lambda),\phi_k(\lambda))_{L_{2,\rho}(\mathbb{R})}.$$

In accordance with the general approach proposed in [8,9], we consider the *reachable set* of the dynamical system (2):

$$U^T:=W^T\mathcal{F}^T=\left\{u^f(T)\,|\,f\in\mathcal{F}^T\right\}.$$

By the Lemma 2 we know that:

$$U^T=W^T\mathcal{F}_1^T.$$

Then, for any $f\in\mathcal{F}^T$ we can evaluate:

$$\left(Fu^f(T)\right)(\lambda)=\sum_{k=1}^{N}\int\limits_{\mathbb{R}}\int\limits_0^T S_k(T-\tau,\beta)f(\tau)\,d\tau\phi_k(\beta)\,d\rho(\beta)\phi_k(\lambda)=P_N\int\limits_0^T S(T-\tau,\cdot)f(\tau)\,d\tau.$$

We introduce the linear manifold of Fourier images of the reachable set:

$$B_N := FU^T = \operatorname{Lin}\{\phi_1, \dots, \phi_N\},$$

thus, B_N is a set of polynomials with complex coefficients of the degree not grater than $N-1$.

The metric in B_N is introduced by the following rule: for $H, G \in B_N$, such that $H = P_N \int_0^T S(T-\tau,\cdot)h(\tau)\,d\tau$, $G = P_N \int_0^T S(T-\tau,\cdot)g(\tau)\,d\tau$, where $h, g \in \mathcal{F}_1^T$ we set:

$$(H,G)_{B^T} := \left(C^T h, g\right)_{\mathcal{F}^T}.$$

On the other hand, for $h, g \in \mathcal{F}_1^T$ we can evaluate using the definition of C^T and Fourier transformation:

$$\begin{aligned}(H,G)_{B^T} = (C^T h, g)_{\mathcal{F}^T} = (u^h(T), u^g(T))_{\mathcal{H}^N} = \int\limits_{\mathbb{R}} \left(Fu^h(T)\right)(\lambda)\left(Fu^h(T)\right)(\lambda)\,d\rho(\lambda)\\ = \int\limits_{\mathbb{R}} \left(P_N \int\limits_0^T S(T-\tau,\cdot)h(\tau)\,d\tau\right)(\lambda)\left(P_N \int\limits_0^T S(T-\tau,\cdot)g(\tau)\,d\tau\right)(\lambda)\,d\rho(\lambda)\\ = \int\limits_{\mathbb{R}} H(\lambda)G(\lambda)\,d\rho(\lambda),\end{aligned}$$

We note that for the systems considered in [8, 9] it was a certain option in the choosing of the measure $d\rho(\lambda)$ in the above calculations. Due to the infinite speed of wave propagation in (2), we do not have this option here.

We set *the special control problem* for the system (2): to find a control $j_z \in \mathcal{F}_1^T$ which drives (2) to the prescribed state:

$$u_k^{j_z}(T) = \overline{\phi_k(z)}, \quad k = 1, \dots, N.,$$

at time $t = T$. Due to Theorem 2, such a control exists and is unique in $\mathcal{F}_1^T$. Then, for such a control, we can evaluate:

$$\left(C^T j_z, g\right)_{\mathcal{F}^T} = \left(u^g(T), u^{j_z}(T)\right)_{\mathcal{H}^N} = \sum_{k=1}^N u_k^g(T)\phi_k(z) = \left(Fu^g(T)\right)(z).$$

Thus, for:

$$J_z(\lambda) := \left(Fu^{j_z}(T)\right)(\lambda)$$

and $G(\lambda) = \left(Fu^g(T)\right)(\lambda)$, we have that:

$$\left(J_z, G\right)_{B_N} = \left(C^T j_z, g\right)_{\mathcal{F}^T} = G(z).$$

In other words, $J_z(\lambda)$ is a reproducing kernel in B_N.

To show that B_N is a de Branges space, we use the Theorem 3, all three conditions of which are trivially satisfied: indeed, for $G \in B_N$ such that $G = P_N \int_0^T S(T-\tau,\cdot)g(\tau)\,d\tau$, where $g \in \mathcal{F}_1^T$ we can evaluate:

$$\begin{aligned}|G(z)| = |(J_z, G)_{B_N}| = \left|\left(C^N j_z, g\right)_{\mathcal{F}^N}\right|\\ \leqslant \|\left(C^T\right)^{\frac{1}{2}} j_z\|_{\mathcal{F}^N} \|\left(C^N\right)^{\frac{1}{2}} g\|_{\mathcal{F}^N} = \|\left(C^N\right)^{\frac{1}{2}} j_z\|_{\mathcal{F}^N} \|G\|_{B_N}.\end{aligned}$$

Clearly $G^{\#}$, being a polynomial is entire and:

$$\|G^{\#}\|_{B_N} = \left(\int\limits_{-\infty}^{\infty} \overline{\overline{G(\overline{\mu})}}\,\overline{G(\overline{\mu})}\,d\rho(\mu)\right)^{1/2} = \|G\|_{B_N}.$$

When $\omega \in \mathbb{C}$ such that $F(\omega) = 0$, then $\dfrac{z-\overline{\omega}}{z-\omega}F(z)$ is an entire function and:

$$\left\|\frac{z-\overline{\omega}}{z-\omega}G(z)\right\|_{B_N} = \left(\int\limits_{-\infty}^{\infty} \overline{\frac{z-\overline{\omega}}{z-\omega}G(z)}\,\frac{z-\overline{\omega}}{z-\omega}G(z)\,d\rho(z)\right)^{1/2} = \|G\|_{B_N}.$$

Thus, B_N is a de Branges space.

References

[1] Mikhaylov A.S., Mikhaylov V.S. Dynamic inverse problem for a Krein–Stieltjes string. *Applied Mathematics Letters*, 2019, **96**, P. 195–210.

[2] Mikhaylov A.S., Mikhaylov V.S. Inverse dynamic problem for finite Jacobi matrices. *Journal of Inverse and Ill-Posed problems*, 2021, **29**(4), P. 611–628.

[3] Belishev M.I. Boundary control and inverse problems: a one-dimensional version of the boundary control method. *Zap. Nauchn. Sem. S.-Peterburg. Otdel. Mat. Inst. Steklov. (POMI)*, 2008, **354**, P. 19–80 (in Russian); English translation: *J. Math. Sci. (N. Y.)*, 2008, **155**(3), P. 343–378.

[4] Belishev M.I. Recent progress in the boundary control method. *Inverse Problems*, 2007, **23**(5), P. R1–R67.

[5] Louis de Branges. *Hilbert space of entire functions*. Prentice-Hall, NJ, 1968.

[6] Dym H., McKean H.P. *Gaussian processes, function theory, and the inverse spectral problem*. Academic Press, New York etc., 1976.

[7] Romanov R.V. Canonical systems and de Branges spaces http://arxiv.org/abs/1408.6022.

[8] Mikhaylov A.S., Mikhaylov V.S. Inverse dynamic problems for canonical systems and de Branges spaces. *Nanosystems: Physics, Chemistry, Mathematics*, 2018, **9**(2), P. 215–224.

[9] Mikhaylov A.S., Mikhaylov V.S. Boundary Control method and de Branges spaces. Schrödinger operator, Dirac system, discrete Schrödinger operator. *Journal of Mathematical Analysis and Applications*, 2018, **460**(2), P. 927–953.

[10] Mikhaylov A.S., Mikhaylov V.S. Hilbert spaces of functions associated with Jacobi matrices. *IEEE Proceedings of Days on Diffraction*, 2021.

[11] Akhiezer N.I. *The classical moment problem*. Oliver and Boyd, Edinburgh, 1965.

[12] Mikhaylov A.S., Mikhaylov V.S. Dynamic inverse problem for Jacobi matrices. *Inverse Problems and Imaging*, 2019, **13**(3), P. 431–447.

[13] Mikhaylov A.S., Mikhaylov V.S. Inverse problem for dynamical system associated with Jacobi matrices and classical moment problems. *Journal of Mathematical Analysis and Applications*, 2020, **487**(1).

[14] Belishev M.I. Boundary control in reconstruction of manifolds and metrics (the BC method). *Inverse Problems*, 1997, **13**(5), P. R1–R45.

Submitted 25 December 2021; accepted 31 December 2021

Information about the authors:

A. S. Mikhaylov – St. Petersburg Department of V. A. Steklov Institute of Mathematics of the Russian Academy of Sciences, 7, Fontanka, 191023 St. Petersburg, Russia; St. Petersburg State University, St.Petersburg State University, 7/9 Universitetskaya nab., St. Petersburg, 199034 Russia; ORCID 0000-0002-0257-496X; mikhaylov@pdmi.ras.ru

V. S. Mikhaylov – St. Petersburg Department of V. A. Steklov Institute of Mathematics of the Russian Academy of Sciences, 7, Fontanka, 191023 St. Petersburg, Russia; ORCID 0000-0002-4727-2041; vsmikhaylov@pdmi.ras.ru

Conflict of interest: the authors declare no conflict of interest.

NANOSYSTEMS:
PHYSICS, CHEMISTRY, MATHEMATICS

Original article

Sabirov K.K., Yusupov J.R., et al. *Nanosystems: Phys. Chem. Math.*, 2022, **13** (1), 30–35.
http://nanojournal.ifmo.ru
DOI 10.17586/2220-8054-2022-13-1-30-35

Networks with point-like nonlinearities

K. K. Sabirov[1], J. R. Yusupov[2,3,a], Kh. Sh. Matyokubov[4], H. Susanto[5], D. U. Matrasulov[6]

[1]Tashkent University of Information Technologies, 100200, Tashkent, Uzbekistan
[2]Yeoju Technical Institute in Tashkent, 100121, Tashkent, Uzbekistan,
[3]National University of Uzbekistan, 100174, Tashkent, Uzbekistan
[4]Urgench State University, 220100, Urgench, Uzbekistan,
[5]Khalifa University, 127788, Abu Dhabi, UAE,
[6]Turin Polytechnic University in Tashkent, 100095, Tashkent, Uzbekistan

[a]j.yusupov@ytit.uz

Corresponding author: J. R. Yusupov, j.yusupov@ytit.uz

PACS 03.75.Lm, 05.45.Yv, 05.45.-a

ABSTRACT We study static nonlinear waves in networks described by a nonlinear Schrödinger equation with point-like nonlinearities on metric graphs. Explicit solutions fulfilling vertex boundary conditions are obtained. Spontaneous symmetry breaking caused by bifurcations is found.

KEYWORDS metric graphs, point-like nonlinearity, NLSE, spontaneous symmetry breaking bifurcations

FOR CITATION Sabirov K.K., Yusupov J.R., Matyokubov Kh.Sh., Susanto H., Matrasulov D.U. Networks with point-like nonlinearities. *Nanosystems: Phys. Chem. Math.*, 2022, **13** (1), 30–35.

1. Introduction

Modeling wave and particle transports in branched structures is an important problem with applications in many subjects of contemporary physics, such as optics, condensed matters, complex molecules, polymers and fluid dynamics. Mathematical treatment of such problems is reduced to solving different partial differential equations (PDEs) on so-called metric graphs. These are set of one-dimensional bonds, with assigned lengths. The connection rule of the bonds is called topology of the graph and is described in terms of the adjacency matrix [1, 2]. Linear and nonlinear wave equations on metric graphs attracted much attention recently and they are becoming a hot topic [3–29].

Solving wave equations on metric graphs requires imposing boundary conditions at the branching points (graph vertices). In the case of linear evolution equations, e.g., for the linear Schrödinger equation, the main requirement for such boundary conditions is that they should keep self-adjointness of the problem [30], while for nonlinear PDEs, one needs to use other fundamental conservation laws (e.g., energy, norm, momentum, charge, etc) for obtaining vertex boundary conditions [5, 15, 18]. Energy and norm conservation were used to derive vertex boundary conditions for the nonlinear Schrödinger equation (NLSE) on metric graphs in [5], where exact solutions were obtained and the integrability of the problem was shown under certain constraints. In [15], a similar study was done for the sine-Gordon equation on metric graphs. Soliton solutions of a nonlinear Dirac equation on metric graphs have been obtained in [18]. Static solitons in networks were studied in the Refs. [7–11] by solving stationary nonlinear Schrödinger equations on metric graphs. A model for transparent nonlinear networks was proposed recently in [22]. Earlier, transparent quantum graphs were studied in [20, 21, 23]. Modeling nonlinear waves and solitons in branched structures and networks provides a powerful tool for tunable wave, particle, heat and energy transport in different practically important systems, such as branched optical fibers, carbon nanotube networks, branched polymers and low-dimensional functional materials.

Here, we consider a Schrödinger equation with a point-like nonlinearity on metric graphs. NLSE with point-like nonlinearity can be implemented in dual-core fiber Bragg gratings as well as in the ordinary fibers [33] and Bose-Einstein condensates confined in double-well traps [34, 35]. A similar problem on a line with double-delta type nonlinearity was considered earlier in [31, 32], where explicit solutions were derived. On the basis of numerical analysis, it was shown that symmetric states are stable up to a spontaneous symmetry breaking bifurcation point. From a fundamental viewpoint, it would be interesting to see the difference between solutions of the problem on the line and networks, as the topology of a network may cause additional effects. Here, we use the methods of [31] to obtain explicit solutions of our problem. Degenerate spontaneous symmetry breaking bifurcations are also obtained.

The paper is organized as follows: in the next section formulation of the problem for metric star graph and the derivation of the vertex boundary conditions are presented. In Section 3 we obtain exact analytical solutions of the problem and formulate constraints for integrability. Numerical results and analysis of bifurcation are also presented in this section. Finally, Section 4 presents some concluding remarks.

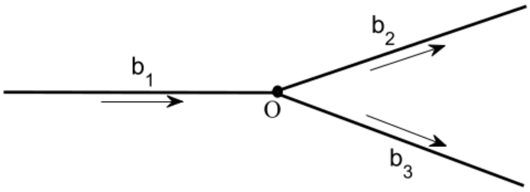

FIG. 1. Metric star graph

2. Vertex boundary conditions

Consider a metric star graph consisting of three semi-infinite bonds, $b_1 \sim (-\infty;0)$, $b_3 \sim (0;+\infty)$, $b_3 \sim (0;+\infty)$ (see, Fig. 1). On each bond of this graph the NLSE with variable nonlinearity coefficient, $g_j(x)$ can be written as

$$i\frac{\partial\psi_j}{\partial t} = -\frac{1}{2}\frac{\partial^2\psi_j}{\partial x^2} + g_j(x)|\psi_j|^2\psi_j, \tag{1}$$

where $j = 1, 2, 3$ denotes the bond number.

To solve Eq. (1), one needs to impose vertex boundary conditions (VBC), which can be derived, e.g., from norm and energy conservations laws. The norm and energy are given respectively by:

$$N = \sum_{j=1}^{3}\int_{b_j} |\psi_j(x)|^2 dx, \tag{2}$$

and:

$$H = \frac{1}{2}\sum_{j=1}^{3}\int_{b_j}\left(\left|\frac{\partial\psi_j}{\partial x}\right|^2 + g_j(x)|\psi_j|^4\right)dx. \tag{3}$$

From $\dot{N} = 0$ and $\dot{H} = 0$ and using $\psi_1, \dfrac{\partial\psi_1}{\partial x} \to 0$ as $x \to -\infty$ and $\psi_{2,3}, \dfrac{\partial\psi_{2,3}}{\partial x} \to 0$ as $x \to +\infty$, we obtain the following vertex boundary conditions (at $x = 0$):

$$\mathrm{Im}\left(\psi_1\frac{\partial\psi_1^*}{\partial x}\right) = \mathrm{Im}\left(\psi_2\frac{\partial\psi_2^*}{\partial x}\right) + \mathrm{Im}\left(\psi_3\frac{\partial\psi_3^*}{\partial x}\right), \tag{4}$$

$$\mathrm{Re}\left(\frac{\partial\psi_1}{\partial t}\frac{\partial\psi_1^*}{\partial x}\right) = \mathrm{Re}\left(\frac{\partial\psi_2}{\partial t}\frac{\partial\psi_2^*}{\partial x}\right) + \mathrm{Re}\left(\frac{\partial\psi_3}{\partial t}\frac{\partial\psi_3^*}{\partial x}\right). \tag{5}$$

Thus, both energy and current conservation give rise to nonlinear vertex boundary conditions. However, the VBC given by Eqs. (4) and (5) can be fulfilled if the following two types of the linear relations at the vertices are imposed:

Type I:

$$\begin{cases} \alpha_1\psi_1|_{x=0} = \alpha_2\psi_2|_{x=0} = \alpha_3\psi_3|_{x=0}, \\ \dfrac{1}{\alpha_1}\dfrac{\partial\psi_1}{\partial x}\Big|_{x=0} = \dfrac{1}{\alpha_2}\dfrac{\partial\psi_2}{\partial x}\Big|_{x=0} + \dfrac{1}{\alpha_3}\dfrac{\partial\psi_3}{\partial x}\Big|_{x=0}, \end{cases} \tag{6}$$

and

Type II:

$$\begin{cases} \dfrac{1}{\alpha_1}\psi_1|_{x=0} = \dfrac{1}{\alpha_2}\psi_2|_{x=2} + \dfrac{1}{\alpha_3}\psi_3|_{x=0}, \\ \alpha_1\dfrac{\partial\psi_1}{\partial x}\Big|_{x=0} = \alpha_2\dfrac{\partial\psi_2}{\partial x}\Big|_{x=0} = \alpha_3\dfrac{\partial\psi_3}{\partial x}\Big|_{x=0}, \end{cases} \tag{7}$$

where $\alpha_1, \alpha_2, \alpha_3$ are real constants, which will be determined below. In the following we will focus on VBC of type I, as it looks more physical. In the next section we obtain exact analytical solutions of Eq. (1) for the VBCs given by Eq. (6) and derive a constraint, which provides integrability of the problem.

3. Exact solutions and bifurcations

Detailed treatment of Eq. (1) on a line was done in [31], where an exact solution was obtained for the localized nonlinearity given by:

$$g(x) = -\frac{1}{a\sqrt{\pi}}\left[e^{-\frac{(x+1)^2}{a^2}} + e^{-\frac{(x-1)^2}{a^2}}\right].$$

Here, we will consider the same type of nonlinearity given on each bond of the star graph presented in Fig. 1. Our prescription for solving Eq. (1) for the vertex boundary conditions (6) and (7) was developed in our previous works (see, e.g., the Refs. [5, 6, 9, 17–20]). Briefly, it can be described as follows: Having known solution of a given evolution equation on a line, we require that it should fulfill the vertex boundary conditions given on a graph. Of course, this cannot be achieved in the general case. Therefore, one needs to find constraints that ensure fulfilling vertex boundary conditions by the solution of the evolution equation (Eq. (1) in our case) on a line. Usually, such constraints are given in terms of the parameters appearing in the evolution equation and vertex boundary conditions [5,6,9]. Here, for solving the problem given by Eqs. (1) and (6), we find a solution on each bond and fulfill the vertex boundary conditions.

Consider the star graph presented in Fig. 1, whose bonds are assigned localized nonlinearities given by the following expressions:

$$
\begin{aligned}
g_1(x) &= -\frac{\beta_1}{a\sqrt{\pi}} e^{-\frac{(x+c_1)^2}{a^2}},\\
g_j(x) &= -\frac{\beta_j}{a\sqrt{\pi}} e^{-\frac{(x-c_j)^2}{a^2}},\ j=2,3
\end{aligned}
$$

where $c_j > 0$ for $j = 1, 2, 3$. For this specific form of $g_j(x)$, the space and time variables in Eq. (1) can be separated, that yields (at $a \to 0$):

$$
\begin{aligned}
&-\mu\phi_1 + \frac{1}{2}\phi_1'' + \beta_1\delta(x+c_1)\phi_1^3 = 0,\\
&-\mu\phi_j + \frac{1}{2}\phi_j'' + \beta_j\delta(x-c_j)\phi_j^3 = 0,\ \ j=2,3.
\end{aligned}
\tag{8}
$$

The solution of Eqs. (8) without the vertex boundary conditions can be written as:

$$
\begin{aligned}
\phi_1(x) &= \begin{cases} \dfrac{A_1}{\sqrt{\beta_1}} e^{\sqrt{2\mu}(x+c_1)}, & x < -c_1,\\[2mm] \dfrac{B_{11}}{\sqrt{\beta_1}} e^{\sqrt{2\mu}(x+c_1)} + \dfrac{B_{12}}{\sqrt{\beta_1}} e^{-\sqrt{2\mu}(x+c_1)}, & -c_1 < x \le 0, \end{cases}\\
\phi_j(x) &= \begin{cases} \dfrac{A_{j1}}{\sqrt{\beta_j}} e^{\sqrt{2\mu}(x-c_j)} + \dfrac{A_{j2}}{\sqrt{\beta_j}} e^{-\sqrt{2\mu}(x-c_j)}, & 0 \le x < c_j,\\[2mm] \dfrac{B_j}{\sqrt{\beta_j}} e^{-\sqrt{2\mu}(x-c_j)}, & x > c_j. \end{cases} ,\ \ j=2,3.
\end{aligned}
\tag{9}
$$

Fulfilling the VBCs (6) by solutions (9) leads to

$$
\begin{aligned}
&\frac{\alpha_1}{\sqrt{\beta_1}}(B_{11}e^{\sqrt{2\mu}c_1} + B_{12}e^{-\sqrt{2\mu}c_1}) = \frac{\alpha_2}{\sqrt{\beta_2}}(A_{21}e^{-\sqrt{2\mu}c_2} + A_{22}e^{\sqrt{2\mu}c_2}) = \frac{\alpha_3}{\sqrt{\beta_3}}(A_{31}e^{-\sqrt{2\mu}c_3} + A_{32}e^{\sqrt{2\mu}c_3}),\\
&\frac{1}{\alpha_1\sqrt{\beta_1}}(B_{11}e^{\sqrt{2\mu}c_1} - B_{12}e^{-\sqrt{2\mu}c_1}) = \frac{1}{\alpha_2\sqrt{\beta_2}}(A_{21}e^{-\sqrt{2\mu}c_2} - A_{22}e^{\sqrt{2\mu}c_2}) + \frac{1}{\alpha_3\sqrt{\beta_3}}(A_{31}e^{-\sqrt{2\mu}c_3} - A_{32}e^{\sqrt{2\mu}c_3}).
\end{aligned}
\tag{10}
$$

Furthermore, for the sake of simplicity we consider the case when $c_1 = c_2 = c_3 = c$. Choosing parameters A and B to fulfill the relations will yield:

$$
A_{j1} = B_{11}e^{2\sqrt{2\mu}c},\quad B_{12} = B\cdot B_{11}e^{2\sqrt{2\mu}c},\quad A_{j2} = B\cdot B_{11},\quad B \neq \pm 1,\quad j=2,3.
$$

From the first equation of (10), we get:

$$
\frac{\alpha_1}{\alpha_{2,3}} = \frac{\sqrt{\beta_1}}{\sqrt{\beta_{2,3}}},\quad \frac{1}{\alpha_1\sqrt{\beta_1}} = \frac{1}{\alpha_2\sqrt{\beta_2}} + \frac{1}{\alpha_3\sqrt{\beta_3}}.
$$

These equations lead to the constraint given by:

$$
\frac{1}{\beta_1} = \frac{1}{\beta_2} + \frac{1}{\beta_3}.
\tag{11}
$$

Eq. (11) presents a constraint that provides fulfilling the vertex boundary conditions (6) by the solution (9). Furthermore, from the continuity of the solution $\phi_j(x)$ we have

$$
\begin{aligned}
A_1 &= B_{11}\left(1 + Be^{2\sqrt{2\mu}c}\right),\\
B_j &= B_{11}(e^{2\sqrt{2\mu}c} + B),\quad j=2,3.
\end{aligned}
$$

For the jump $\Delta(\phi_1')|_{x=-c} = -2\beta_1\left(\phi_1|_{x=-c}\right)^3$ we can find:

$$
B_{11} = \pm\sqrt{\frac{\sqrt{2\mu}Be^{2\sqrt{2\mu}c}}{\left(1 + Be^{2\sqrt{2\mu}c}\right)^3}}.
\tag{12}
$$

For the jump $\Delta(\phi_j')|_{x=c} = -2\beta_j\left(\phi_j|_{x=c}\right)^3$, $j=2,3$ we can find:

$$B_{11} = \pm\sqrt{\frac{\sqrt{2\mu}e^{2\sqrt{2\mu}c}}{\left(e^{2\sqrt{2\mu}c}+B\right)^3}}. \tag{13}$$

Equating (12) and (13) we obtain:

$$B = \frac{\left(e^{2\sqrt{2\mu}c} \pm \sqrt{e^{4\sqrt{2\mu}c}-4}\right)^3}{8}, \tag{14}$$

where $\mu \geq \dfrac{\ln^2 2}{8c^2}$.

Now we consider the cases, when the nonlinearities appear on two and one bonds only. Similarly as the above, one can obtain solutions for these cases. For the star graph with nonlinearities appearing in two bonds we have the following stationary NLSE on each bond b_j ($b_1 \sim (-\infty;0]$, $b_{2,3} \sim [0;+\infty)$) of the star graph

$$\begin{gathered}
-\mu\phi_1 + \frac{1}{2}\phi_1'' + \beta_1\delta(x+c_1)\phi_1^3 = 0,\ \ c_1>0\\
-\mu\phi_2 + \frac{1}{2}\phi_2'' + \beta_2\delta(x-c_2)\phi_2^3 = 0,\ \ c_2>0\\
-\mu\phi_3 + \frac{1}{2}\phi_3'' = 0.
\end{gathered} \tag{15}$$

The solution of this equations without the vertex boundary conditions can be written as:

$$\begin{aligned}
\phi_1(x) &= \begin{cases} \dfrac{A_1}{\sqrt{\beta_1}}e^{\sqrt{2\mu}(x+c_1)}, & x<-c_1,\\ \dfrac{B_{11}}{\sqrt{\beta_1}}e^{\sqrt{2\mu}(x+c_1)} + \dfrac{B_{12}}{\sqrt{\beta_1}}e^{-\sqrt{2\mu}(x+c_1)}, & -c_1<x\leq 0,\end{cases}\\
\phi_2(x) &= \begin{cases} \dfrac{A_{21}}{\sqrt{\beta_2}}e^{\sqrt{2\mu}(x-c_2)} + \dfrac{A_{22}}{\sqrt{\beta_2}}e^{-\sqrt{2\mu}(x-c_2)}, & 0\leq x<c_2,\\ \dfrac{B_2}{\sqrt{\beta_2}}e^{-\sqrt{2\mu}(x-c_2)}, & x>c_2,\end{cases}\\
\phi_3(x) &= \frac{B_3}{\sqrt{\beta_3}}e^{-\sqrt{2\mu}x}, \qquad x\geq 0.
\end{aligned} \tag{16}$$

Similarly, for the case when the nonlinearity appears in a single bond of the star graph, we have the solution:

$$\begin{aligned}
\phi_1(x) &= \begin{cases} \dfrac{A_1}{\sqrt{\beta_1}}e^{\sqrt{2\mu}(x+c_1)}, & x<-c_1,\\ \dfrac{B_{11}}{\sqrt{\beta_1}}e^{\sqrt{2\mu}(x+c_1)} + \dfrac{B_{12}}{\sqrt{\beta_1}}e^{-\sqrt{2\mu}(x+c_1)}, & -c_1<x\leq 0,\end{cases}\\
\phi_j(x) &= \frac{A_j}{\sqrt{\beta_j}}e^{-\sqrt{2\mu}x},\ j=2,3,\ \ x\geq 0.
\end{aligned} \tag{17}$$

Again, requiring fulfilling the vertex boundary conditions (6) by the solutions (16) and (17), one can obtain constraints (in terms of parameters β_j) ensuring that (16) and (17) are the solution of the problem on graph.

The above analytical solution (9) is obtained under the assumption that the constraint (11) is satisfied. In the following, we solve Eq. (8) numerically both for the case when the constraint in Eq. (11) is fulfilled and broken. The point nonlinearity in Eq. (8) is represented by the Gaussian function with $c = 3$ and $a = 0.1$. In the following, we only limit ourselves with positive solutions.

In Fig. 2, we plot two possible solutions for the case when the sum rule given by Eq. (11) is fulfilled. The first panel shows a solution when all the bonds are excited by the delta nonlinearity, while in the second one (b), only the first and the second bonds have point-like excitations. Using the configuration in the limit $\mu\to\infty$ as our code, we represent solutions in panels (a) and (b) as $[1,1,1]$ and $[1,1,0]$, respectively.

In Fig. 3(a), we present bifurcation diagrams of the solutions in Fig. 2. We obtain that the two configurations in Fig. 2 are connected with each other, with $[1,1,1]$ as the main branch and $[1,1,0]$ as a bifurcating solution through a pitchfork bifurcation with the configuration $[0,0,1]$. We therefore observe a spontaneous symmetry breaking bifurcation. It is particularly interesting to note that the bifurcation is quite degenerate in the sense that we obtain both a subcritical as well as a supercritical bifurcation emerging from the same point. We also obtain several other solutions bifurcating from the same bifurcation point, which are all indicated in Fig. 3(a).

We have considered a different case when all the nonlinearity coefficients are the same, i.e., without loss of nonlinearity $\beta_j = 1$. In this case, the condition (11) is not satisfied. We plot the bifurcation diagram of the positive solutions in Fig. 3(b), where now we obtain that all the asymmetric solutions merge into two branches only, which bifurcate from the same point.

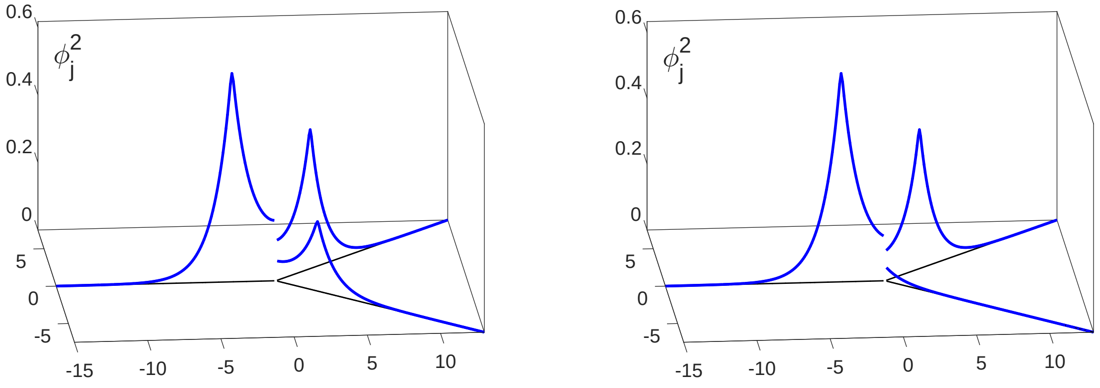

(a) (b)

FIG. 2. Two possible solutions are plotted. Here, $\beta_1 = 2/3$, $\beta_2 = 1$, and $\beta_3 = 2$ satisfying the condition for conserved norm and energy, and $\mu = 0.1$. The solution in panel (a) is denoted by configuration $[1,1,1]$ and in panel (b) by $[1,1,0]$.

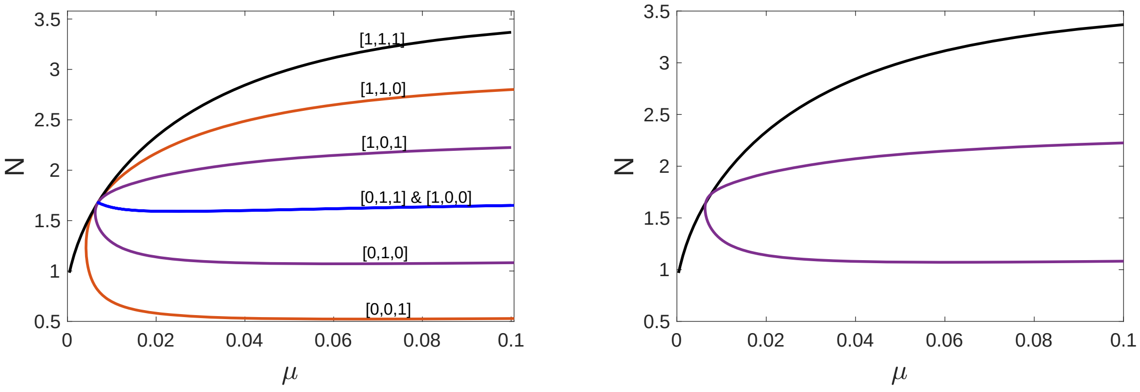

(a) (b)

FIG. 3. (a) Bifurcation diagram of solutions in Fig. 2. (b) The same diagram, but for $\beta_j = 1$, $j = 1, 2, 3$.

4. Conclusions

In this paper we studied nonlinear Schrödinger equation with localized nonlinearities on metric graphs. Exact solutions are obtained and their stability is analyzed by exploring the bifurcations for the case of point-like (varying) nonlinearity that has the form of a delta-well. Exact analytical solutions of the problem were obtained for different cases of point excitations, determined by the presence of a delta-well on different bonds. The constraint providing existence of such analytical solutions are derived in the form of simple sum rule written in terms of the bond nonlinearity coefficients. Numerical solutions of the problem are also obtained both for integrable and non-integrable cases. Bifurcations of the solutions are studied in terms of chemical potential μ using the numerical solutions. The model considered in this paper is relevant for different practically important problems such as BEC in branched traps, Bragg gratings in branched fibers, etc. Extension of the treatment to other graph topologies is rather straightforward, provided the graph contains arbitrary subgraph, which is connected to three or more outgoing semi-infinite bonds.

References

[1] Kottos T., Smilansky U. Periodic Orbit Theory and Spectral Statistics for Quantum Graphs. *Ann.Phys.*, 1999, **274**(1), P. 76–124.

[2] Exner P., Kovarik H. *Quantum waveguides*. Springer, 2015.

[3] Susanto H., van Gils S. Semifluxons with a hump in a $0 - \pi$ Josephson junction. *Physica C*, 2004, **408**, P. 579.

[4] Susanto H., van Gils S., Doelman A., Derks G. Analysis on the stability of Josephson vortices at tricrystal boundaries: A $3\phi_0/2$-flux case. *Phys. Rev. B*, 2004, **69**, 212503.

[5] Sobirov Z., Matrasulov D., Sabirov K., Sawada S., Nakamura K. Integrable nonlinear Schrödinger equation on simple networks: Connection formula at vertices. *Phys. Rev. E*, 2010, **81**, 066602.

[6] Sobirov Z., Matrasulov D., Sawada S., Nakamura K. Transport in simple networks described by an integrable discrete nonlinear Schrödinger equation. *Phys.Rev.E*, 2011, **84**, 026609.

[7] Adami R., Cacciapuoti C., Finco D., Noja D. Fast Solitons on Star Graphs. *Rev. Math. Phys.*, 2011, **23**, 409.
[8] Adami R., Cacciapuoti C., Finco D., Noja D. Stationary states of NLS on star graphs. *Europhys. Lett.*, 2012, **100**, 10003.
[9] Sabirov K.K., Sobirov Z.A., Babajanov D., Matrasulov D.U. Stationary nonlinear Schrödinger equation on simplest graphs. *Phys.Lett. A*, 2013, **377**, P. 860.
[10] Noja D. Nonlinear Schrödinger equation on graphs: recent results and open problems. *Philos. Trans. R. Soc. A*, 2014, **372**, 20130002.
[11] Adami R., Cacciapuoti C., Noja D. Stable standing waves for a NLS on star graphs as local minimizers of the constrained energy. *J. Diff. Eq.*, 2016, **260**, 7397.
[12] Caputo J.-G., Dutykh D. Nonlinear waves in networks: Model reduction for the sine-Gordon equation. *Phys. Rev. E*, 2014, **90**, 022912.
[13] Uecker H., Grieser D., Sobirov Z., Babajanov D., Matrasulov D. Soliton transport in tubular networks: Transmission at vertices in the shrinking limit. *Phys. Rev. E*, 2015, **91**, 023209.
[14] Noja D., Pelinovsky D., Shaikhova G. Bifurcations and stability of standing waves in the nonlinear Schrödinger equation on the tadpole graph. *Nonlinearity*, 2015, **28**, 2343.
[15] Sobirov Z., Babajanov D., Matrasulov D., Nakamura K., Uecker H. Sine-Gordon solitons in networks: Scattering and transmission at vertices. *EPL*, 2016, **115**, 50002.
[16] Kairzhan A., Pelinovsky D.E. Spectral stability of shifted states on star graphs. *J. Phys. A: Math. Theor.*, 2018, **51**, 095203.
[17] Sabirov K.K., Rakhmanov S., Matrasulov D., Susanto H. The stationary sine-Gordon equation on metric graphs: Exact analytical solutions for simple topologies. *Phys. Lett. A*, 2018, **382**, 1092.
[18] Sabirov K.K., Babajanov D.B., Matrasulov D.U., Kevrekidis P.G. Dynamics of Dirac solitons in networks. *J. Phys. A: Math. Gen.*, 2018, **51**, 435203.
[19] Sabirov K.K., Akromov M., Otajonov Sh.R., Matrasulov D.U. Soliton generation in optical fiber networks. *Chaos, Solitons & Fractals*, 2020, **133**, 109636.
[20] Yusupov J.R., Sabirov K.K., Ehrhardt M., Matrasulov D.U. Transparent quantum graphs. *Phys. Let. A*, 2019, **383**, P. 2382–2388.
[21] Aripov M.M., Sabirov K.K., Yusupov J.R. Transparent vertex boundary conditions for quantum graphs: Simplified approach. *Nanosystems: Phys., Chem., Math.*, 2019, **10**(5), P. 505–510.
[22] Yusupov J.R., Sabirov K.K., Ehrhardt M., Matrasulov D.U. Transparent nonlinear networks. *Phys. Rev. E*, 2019, **100**, 032204.
[23] Yusupov J.R., Sabirov K.K., Asadov Q.U., Ehrhardt M., Matrasulov D.U. Dirac particles in transparent quantum graphs: Tunable transport of relativistic quasiparticles in branched structures. *Phys. Rev. E*, 2020, **101**(6), 062208.
[24] Yusupov J.R., Matyokubov Kh.Sh., Sabirov K.K. Particle transport in a network of quantum harmonic oscillators. *NANOSYSTEMS: Phys., Chem., Math.*, 2020, **11**(2), P. 145–152.
[25] Sabirov K.K., Yusupov J.R., Matyokubov Kh.Sh. Dynamics of polarons in branched conducting polymers. *Nanosystems: Phys., Chem., Math.*, 2020, **11**(2), P. 183–188.
[26] Sabirov K.K., Yusupov J., Jumanazarov D., Matrasulov D. Bogoliubov de Gennes equation on metric graphs. *Phys. Lett. A*, 2018, **382**, 2856.
[27] Babajanov D., Matyoqubov H., Matrasulov D. Charged solitons in branched conducting polymers. *J. Chem. Phys.*, 2018, **149**, 164908.
[28] Yusupov J.R., Matyokubov Kh.Sh., Sabirov K.K., Matrasulov D.U. Exciton dynamics in branched conducting polymers: Quantum graphs based approach. *Chem. Phys.*, 2020, **537**, 110861.
[29] Noja D., Rolando S., Secchi S. Standing waves for the NLS on the double-bridge graph and a rational-irrational dichotomy. *J. Diff. Eqn.*, 2019, **266**, P. 147.
[30] Kostrykin V., Schrader R. Kirchhoff's rule for quantum wires. *J. Phys. A: Math. Gen.*, 1999, **32**, P. 595.
[31] Mayteevarunyoo T., Malomed B.A., Dong G. Spontaneous symmetry breaking in a nonlinear double-well structure. *Phys. Rev. A*, 2008, **78**, 053601.
[32] Brazhnyi V.A., Malomed B.A. Spontaneous symmetry breaking in Schrödinger lattices with two nonlinear sites. *Phys. Rev. A*, 2011, **83**, 053844.
[33] Mak W.C.K., Malomed B.A., Chu P.L. Solitary waves in coupled nonlinear waveguides with Bragg gratings. *J. Opt. Soc. Am. B*, 1998, **15**, 1685.
[34] Gubeskys A., Malomed B.A. Symmetric and asymmetric solitons in linearly coupled Bose-Einstein condensates trapped in optical lattices. *Phys. Rev. A*, 2007, **75**, 063602.
[35] Matuszewski M., Malomed B.A., Trippenbach M. Spontaneous symmetry breaking of solitons trapped in a double-channel potential. *Phys. Rev. A*, 2007, **75**, 063621.

Submitted 24 June 2021; revised 30 December 2021; accepted 1 February 2022

Information about the authors:

K. K. Sabirov – Tashkent University of Information Technologies, 108 A.Temur Str., 100200, Tashkent Uzbekistan

J. R. Yusupov – Yeoju Technical Institute in Tashkent,156 U.Nasyr Str., 100121, Tashkent, Uzbekistan; National University of Uzbekistan, 4 Universitet Str., 100174, Tashkent, Uzbekistan; j.yusupov@ytit.uz

Kh. Sh. Matyokubov – Urgench State University, 14 H. Olimjon Str., 220100, Urgench, Uzbekistan

H. Susanto – Khalifa University, Abu Dhabi Campus, PO Box 127788, Abu Dhabi, UAE

D. U. Matrasulov – Turin Polytechnic University in Tashkent, 17 Niyazov Str., 100095, Tashkent, Uzbekistan

Conflict of interest: the authors declare no conflict of interest.

NANOSYSTEMS:
PHYSICS, CHEMISTRY, MATHEMATICS

Original article

Yuldashev T.K., Fayziev A.K. *Nanosystems: Phys. Chem. Math.*, 2022, **13** (1), 36–44.
http://nanojournal.ifmo.ru
DOI 10.17586/2220-8054-2022-13-1-36-44

On a nonlinear impulsive system of integro-differential equations with degenerate kernel and maxima

Tursun K. Yuldashev[1,a], Aziz K. Fayziev[2,b]

[1]National University of Uzbekistan, Tashkent, Uzbekistan
[2]Tashkent State Technical University, Tashkent, Uzbekistan

[a]tursun.k.yuldashev@gmail.com, [b]fayziyev.a@inbox.ru

Corresponding author: Tursun K. Yuldashev, tursun.k.yuldashev@gmail.com

ABSTRACT A nonlocal boundary value problem for a system of ordinary integro-differential equations with impulsive effects, degenerate kernel and maxima is investigated. The boundary value problem is given by the integral condition. The method of successive approximations in combination with the method of compressing mapping is used. The existence and uniqueness of the solution of the boundary value problem are proved. The continuous dependence of the solution on the right-hand side of the boundary value condition is shown.

KEYWORDS impulsive integro-differential equations, nonlocal condition, successive approximations, existence and uniqueness, continuous dependence of solution

FOR CITATION Yuldashev T.K., Fayziev A.K. On a nonlinear impulsive system of integro-differential equations with degenerate kernel and maxima. *Nanosystems: Phys. Chem. Math.*, 2022, **13** (1), 36–44.

1. Introduction

Many problems in modern sciences, technology and economics are described by differential equations, the solutions of which are functions with first kind discontinuities at fixed or non-fixed times. Such differential equations are called differential equations with impulse effects [1–8]. As is known, in recent years the interest in the study of differential equations with nonlocal boundary conditions has increased (see, for example, [9–17]). In particular, in [15] a physical situation in which a non-metallic conductor is in contact with a perfect conductor is studied. In [16], the problems of mathematical models in reaction-diffusion systems are considered. In [17], the nonlocal conditions are used in the theory of phase transitions.

In [18–24] the problems of solvability for some type of integro-differential equations with degenerate kernel were considered. Also, a lot of publications of studying on differential equations with impulsive effects, describing many natural and technical processes, are appearing [25–35].

In this paper, we investigate a nonlocal boundary value problem for a system of first order Fredholm integro-differential equations with impulsive effects, degenerate kernel and nonlinear maxima. The questions of the existence and uniqueness of the solution to the boundary value problem, as well as the continuous dependence of the solution on the right-hand side of the boundary condition, are investigated. In [36], it is justified that the theoretical study of differential equations with maxima is relevant.

We consider the following system of Fredholm integro-differential equations:

$$x'(t) = \lambda \int\limits_0^T H(t,s)x(s)ds + f\big(t, x(t), \max\{x(\tau)|\tau \in [h_1; h_2]\}\big), \tag{1}$$

for $t \in [0,T]$, $t \neq t_i$, $i = 1,2,...,p$ with nonlocal boundary value conditions:

$$Ax(0) + \int\limits_0^T K(t)x(t)dt = B, \tag{2}$$

and impulsive effect:

$$x\left(t_i^+\right) - x\left(t_i^-\right) = I_i\left(x\left(t_i\right)\right), \quad i = 1,2,...,p, \tag{3}$$

where $H(t,s) = \sum\limits_{k=1}^{m} a_k(t)b_k(s)$, $0 = t_0 < t_1 < ... < t_p < t_{p+1} = T$, $A \in \mathbb{R}^{n\times n}$, $K(t) \in \mathbb{R}^{n\times n}$ are given matrix and $\det Q \neq 0, Q = A + \int\limits_0^T K(t)\,dt$, $f : [0,T] \times \mathbb{R}^n \times \mathbb{R}^n \to \mathbb{R}^n$, $I_i : \mathbb{R}^n \to \mathbb{R}^n$ are given functions; $0 < h_1 < h_2 < t$,

$h_j = h_j(t, x(t)), j = 1, 2$, λ is real nonzero parameter, $x\left(t_i^+\right) = \lim\limits_{h\to 0^+}(x_i + h)$, $x\left(t_i^-\right) = \lim\limits_{h\to 0^-}(t_i - h)$ are right-sided and left-sided limits of function $x(t)$ at the point $t = t_i$, respectively. Every system of functions $\{a_k(t)\}_{k=1}^m$ and $\{b_k(s)\}_{k=1}^m$ are linearly independent.

2. Reduction to an integral equation

Here are some notations that will be used below. We denote by $C\left([0, T], \mathbb{R}^n\right)$ the Banach space, which consists of continuous functions $x(t) \in \mathbb{R}^n$ on the segment $[0, T]$ with the norm:

$$\|x\| = \sqrt{\sum_{j=1}^{n} \max_{t\in[0,T]} |x_j(t)|}.$$

Since we consider the integro-differential equation (1) with impulsive effect at the points t_i, $i = 1, 2, ..., p$, use the following linear space:

$$PC\big([0, T], \mathbb{R}^n\big) = \big\{x : [0, T] \to \mathbb{R}^n; x(t) \in C\big((t_i, t_{i+1}], \mathbb{R}^n\big), i = 1, ..., p\big\},$$

where $x\left(t_i^+\right)$ and $x\left(t_i^-\right)$ $(i = 0, 1, ..., p)$ exist and bounded; $x\left(t_i^-\right) = x\left(t_i\right)$.

It is obvious, that the linear space $PC\left([0, T], \mathbb{R}^n\right)$ is Banach space with the following norm:

$$\|x\|_{PC} = \max\left\{\|x\|_{C((t_i,t_{i+1}])}, \quad i = 1, 2, ..., p\right\}.$$

Formulation of problem. To find the function $x(t) \in PC\left([0, T], \mathbb{R}^n\right)$, which for all $t \in [0, T]$, $t \neq t_i$, $i = 1, 2, ..., p$ satisfies the integro-differential equation (1), nonlocal integral condition (2) and for $t = t_i$, $i = 1, 2, ..., p$, $0 < t_1 < t_2 < ... < t_p < T$ satisfies the limit condition (3).

Let the function $x(t) \in PC\left([0, T], \mathbb{R}^n\right)$ is a solution of the problem (1)–(3). Then we rewrite the Fredholm integro-differential equation (1) as:

$$x'(t) = \lambda \int_0^T \sum_{k=1}^{m} a_k(t)b_k(s)x(s)ds + f\big(t, x(t), \max\left\{x(\tau)|\tau \in [h_1; h_2]\right\}\big).$$

By the designation:

$$c_k = \int_0^T b_k(s)x(s)ds,$$

the last integro-differential equation we rewrite in the following form:

$$x'(t) = \lambda \sum_{k=1}^{m} a_k(t)c_k + f\big(t, x(t), \max\left\{x(\tau)|\tau \in [h_1; h_2]\right\}\big).$$

Then, by integration of the last equation on the interval $t \in (0, t_{i+1}]$, we obtain:

$$\int_0^t \left[\lambda \sum_{k=1}^{m} a_k(s)c_k + f(s, x(s), \cdot)\right] ds =$$

$$= \int_0^t x'(s)ds = \left[x\left(t_1\right) - x\left(0^+\right)\right] + \left[x\left(t_2\right) - x\left(t_1^+\right)\right] + ... + \left[x\left(t\right) - x\left(t_i^+\right)\right] =$$

$$= -x\left(0\right) - \left[x\left(t_1^+\right) - x\left(t_1\right)\right] - \left[x\left(t_2^+\right) - x\left(t_2\right)\right] - ... - \left[x\left(t_i^+\right) - x\left(t_i\right)\right] + x\left(t\right).$$

Taking into account the integral condition (2) in the last equality, we obtain:

$$x(t) = x(0) + \int_0^t \left[\lambda \sum_{k=1}^{m} a_k(s)c_k + f(s, x(s), \cdot)\right] ds + \sum_{0<t_i<t} I_i\left(x\left(t_i\right)\right). \tag{4}$$

Let the function $x(t) \in PC\left([0,T], \mathbb{R}^n\right)$ in (4), satisfies the boundary value conditions (2):

$$\left[A + \int\limits_0^T K(t)dt\right] x(0) =$$
$$= B - \int\limits_0^T K(t) \int\limits_0^t \left[\lambda \sum_{k=1}^m a_k(s)c_k + f(s, x(s), \cdot)\right] dsdt - \int\limits_0^T K(t) \sum_{0<t_i<t} I_i\left(x\left(t_i\right)\right) dt. \tag{5}$$

Since $\det Q \neq 0$, from the equality (5) we have:

$$x(0) = Q^{-1}\left[B - \int\limits_0^T K(t) \int\limits_0^t \left[\lambda \sum_{k=1}^m a_k(s)c_k + f(s, x(s), \cdot)\right] dsdt - \int\limits_0^T K(t) \sum_{0<t_i<t} I_i\left(x\left(t_i\right)\right) dt\right]. \tag{6}$$

Substituting the equality (6) into representation (4), we obtain:

$$x(t) = Q^{-1}\left[B - \int\limits_0^T K(t) \int\limits_0^t \left[\lambda \sum_{k=1}^m a_k(s)c_k + f(s, x(s), \cdot)\right] dsdt - \int\limits_0^T K(t) \sum_{0<t_i<t} dt\right] +$$
$$+ \int\limits_0^t f(s, x(s), \cdot) ds + \sum_{0<t_i<t} I_i\left(x\left(t_i\right)\right). \tag{7}$$

Since the following equalities hold:

$$\int\limits_0^T K(t) \int\limits_0^t \left[\lambda \sum_{k=1}^m a_k(s)c_k + f(s, x(s), \cdot)\right] dsdt = \int\limits_0^T \int\limits_t^T K(s)ds \left[\lambda \sum_{k=1}^m a_k(t)c_k + f(t, x(t), \cdot)\right] dt,$$

$$\int\limits_0^T K(t) \sum_{0<t_i<t} I_i\left(x\left(t_i\right)\right) dt = \sum_{0<t_i<T} \int\limits_{t_i}^T K(t)dt I_i\left(x\left(t_i\right)\right),$$

from presentation (7) we obtain:

$$x(t) = Q^{-1}B - Q^{-1} \int\limits_0^T \int\limits_t^T K(s)ds \left[\lambda \sum_{k=1}^m a_k(t)c_k + f(t, x(t), \cdot)\right] dt -$$
$$- Q^{-1} \sum_{0<t_i<t} \int\limits_{t_i}^T K(t)dt I_i\left(x\left(t_i\right)\right) + \int\limits_0^t \left[\lambda \sum_{k=1}^m a_k(s)c_k + f(s, x(s), \cdot)\right] ds + \sum_{0<t_i<t} I_i\left(x\left(t_i\right)\right). \tag{8}$$

Let us make some simplifications in representation (8). Then the following equalities hold:

$$\int\limits_0^t \left[\lambda \sum_{k=1}^m a_k(s)c_k + f(s, x(s), \cdot)\right] ds - Q^{-1} \int\limits_0^T \int\limits_t^T K(s)ds \left[\lambda \sum_{k=1}^m a_k(t)c_k + f(t, x(t), \cdot)\right] dt =$$
$$= Q^{-1} \int\limits_0^t \left(A + \int\limits_0^\theta K(s)ds\right) \left[\lambda \sum_{k=1}^m a_k(\theta)c_k + f(\theta, x(\theta), \cdot)\right] d\theta -$$
$$- Q^{-1} \int\limits_0^T \int\limits_t^T K(s)ds \left[\lambda \sum_{k=1}^m a_k(\theta)c_k + f(\theta, x(\theta), \cdot)\right] d\theta; \tag{9}$$

$$\sum_{0<t_i<t} I_i\left(x\left(t_i\right)\right) - Q^{-1} \sum_{0<t_i<T} \int\limits_{t_i}^T K(t)dt I_i\left(x\left(t_i\right)\right) =$$
$$= Q^{-1} \sum_{0<t_i<t} \left(A + \int\limits_0^{t_i} K(t)dt\right) I_i\left(x\left(t_i\right)\right) - \sum_{t<t_{i+1}<T} Q^{-1} \int\limits_{t_i}^T K(t)dt I_i\left(x\left(t_i\right)\right). \tag{10}$$

Taking into account (9) and (10), from the presentation (8) we obtain the following integral equation:

$$x(t)=Q^{-1}B+\sum_{0<t_i<t}G\left(t_i\right)I_i\left(x\left(t_i\right)\right)+\lambda\sum_{k=1}^{m}\int\limits_0^T G(s)a_k(s)c_k ds+\int\limits_0^T G(t,s)f(s,x(s),\cdot)ds, \tag{11}$$

for $t\in\left(t_i,t_{i+1}\right], i=0,1,...,p$, where:

$$G(t)=\begin{cases}Q^{-1}\left(A+\int\limits_0^t K(s)ds\right), & 0\le s\le t,\\ -Q^{-1}\int\limits_t^T K(s)ds, & t<s\le T.\end{cases}$$

Substituting the equation (11) into designation:

$$c_k=\int\limits_0^T b_k(s)x(s)ds,$$

we obtain the following linear system of algebraic equations (LSAE):

$$c_k+\lambda\sum_{j=1}^{m}c_{kj}\Phi_{kj}=\Psi_{1k}+\Psi_{2k}\left(f,I_i\right), \quad k=\overline{1,m}, \tag{12}$$

where:

$$\Phi_{kj}\left(f,I_i\right)=\int\limits_0^T b_k(s)\int\limits_0^T G(\theta)a_j(\theta)d\theta ds, \quad \Psi_{1k}=Q^{-1}B\int\limits_0^T b_k(s)ds,$$

$$\Psi_{2k}\left(f,I_i\right)=\int\limits_0^T b_k(s)\Big[\int\limits_0^T G(\theta)f\big(\theta,x(\theta),\max\left\{x(\tau)|\tau\in[h_1;h_2]\right\}\big)d\theta+\sum_{0<t_i<t}G\left(t_i\right)I_i\left(x\left(t_i\right)\right)\Big]ds,$$

$$k=\overline{1,m},\ h_l=h_l(t,x(\theta)),\ l=1,2. \tag{13}$$

The LSAE (12) is uniquely solvable for any finite right-hand side, if the following Fredholm condition is satisfied:

$$\Delta_k(\lambda)=\begin{vmatrix}1+\lambda\Phi_{k11} & \lambda\Phi_{k12} & ... & \lambda\Phi_{k1m}\\ \lambda\Phi_{k21} & 1+\lambda\Phi_{k22} & ... & \lambda\Phi_{k2m}\\ ... & ... & ... & ...\\ \lambda\Phi_{km1} & \lambda\Phi_{km2} & ... & 1+\lambda\Phi_{kmm}\end{vmatrix}\ne 0. \tag{14}$$

Consider such regular values of parameter λ, for which condition (14) is satisfied. Then, solving LSAE (12), we obtain:

$$c_k=\frac{\Delta_{1k}(\lambda)}{\Delta(\lambda)}+\frac{\Delta_{2k}\left(\lambda,f,I_i\right)}{\Delta(\lambda)}, \tag{15}$$

where:

$$\Delta_{lk}(\lambda)=\begin{vmatrix}1+\lambda\Phi_{11} & ... & \lambda\Phi_{1(i-1)} & \Psi_{l1} & \lambda\Phi_{1(i+1)} & ... & \lambda\Phi_{1m}\\ \lambda\Phi_{21} & ... & \lambda\Phi_{2(i-1)} & \Psi_{l2} & \lambda\Phi_{2(i+1)} & ... & \lambda\Phi_{2m}\\ ... & ... & ... & ... & ... & ... & ...\\ \lambda\Phi_{m1} & ... & \lambda\Phi_{m(i-1)} & \Psi_{lm} & \lambda\Phi_{m(i+1)} & ... & 1+\lambda\Phi_{mm}\end{vmatrix}, \quad l=1,2. \tag{16}$$

Substituting equality (15) into representation (11), we obtain the following new presentation of solution:

$$x(t)=\Theta(t;x)\equiv\chi_0+\lambda\sum_{k=1}^{m}\left[\frac{\Delta_{1k}(\lambda)}{\Delta(\lambda)}+\frac{\Delta_{2k}\left(\lambda,f,I_i\right)}{\Delta(\lambda)}\right]\chi_{1k}+$$

$$+\int\limits_0^T G(s)f\big(s,x(s),\max\left\{x(\tau)|\tau\in[h_1;h_2]\right\}\big)ds+\sum_{0<t_i<t}G\left(t_i\right)I_i\left(x\left(t_i\right)\right), \tag{17}$$

where:

$$\chi_0 = Q^{-1}B, \quad \chi_{1k} = \int_0^T G(s)a_k(s)ds, \quad k = \overline{1,m}, \; h_l = h_l(t, x(s)), \; l = 1, 2.$$

3. The questions of one value solvability

Theorem. Suppose the following conditions are fulfilled:
1) For all $t \in [0,T]$, $x, y \in \mathbb{R}^n$ holds:

$$|f(t, x_1, y_1) - f(t, x_2, y_2)| \leq M_1(t)\,|x_1 - x_2| + M_2(t)\,|y_1 - y_2|\,;$$

2) For all $t \in [0,T]$, $x \in \mathbb{R}^n$ holds:

$$|h_j(t, x_1) - h_j(t, x_2)| \leq M_{3j}(t)\,|x_1 - x_2|\,, j = 1, 2;$$

3) For all $x \in \mathbb{R}^n, i = 0, 1, ..., p$ holds:

$$|I_i(x_1) - I_i(x_2)| \leq m_i\,|x_1 - x_2|\,;$$

4) $\rho = S_1 + S_2 < 1$, where:

$$S_1 = |\lambda| \sum_{k=1}^{m} |\chi_{1k}| \cdot \left|\bar{\Delta}_{2k}(\lambda)\right| \int_0^T |G(s)|\,[M_1(s) + M_2(s)\,(1 + M_f\,(M_{31}(s) + M_{32}(s)))]\,ds,$$

$$S_2 = |\lambda| \sum_{k=1}^{m} |\chi_{1k}| \cdot \left|\bar{\Delta}_{2k}(\lambda)\right| \sum_{i=1}^{p} |G(t_i)|\,m_i,$$

$$\bar{\Delta}_{2k}(\,\lambda) = \begin{vmatrix} 1+\lambda\Phi_{11} & ... & \lambda\Phi_{1(i-1)} & \bar{\Psi}_{21} & \lambda\Phi_{1(i+1)} & \cdots & \lambda\Phi_{1m} \\ \lambda\Phi_{21} & ... & \lambda\Phi_{2(i-1)} & \bar{\Psi}_{22} & \lambda\Phi_{2(i+1)} & \cdots & \lambda\Phi_{2m} \\ \cdots & \cdots & \cdots & \cdots & \cdots & \cdots & \cdots \\ \lambda\Phi_{m1} & ... & \lambda\Phi_{m(i-1)} & \bar{\Psi}_{2m} & \lambda\Phi_{m(i+1)} & \cdots & 1+\lambda\Phi_{mm} \end{vmatrix},$$

$$\bar{\Psi}_{2k} = \int_0^T b_k(s)ds.$$

Then, the nonlocal boundary value problem (1)–(3) has a unique solution $x(t) \in PC\,([0,T], \mathbb{R}^n)$ for the regular values of parameter λ. This solution can be found from the following iterative process:

$$\begin{cases} x^j(t) = \Theta(t; x^{j-1}), & j = 1, 2, 3, ... \\ x^0(t) = \chi_0 = Q^{-1}B, & t \in (t_i, t_{i+1}), i = 0, 1, 2, ..., p. \end{cases} \tag{18}$$

Moreover, for this solution the following estimate is true:

$$\|x_1(t) - x_2(t)\|_{PC} \leq (1-\rho)^{-1}\left\|Q^{-1}\right\| \cdot \|B_1 - B_2\|\,.$$

Proof. We consider the following operator:

$$\Theta : PC\,([0,T]; \mathbb{R}^n) \to PC\,([0,T] \times \mathbb{R}^n)\,,$$

defined by the right-hand side of integral equation (11). Obviously, the fixed point of the operator Θ is the unique solution to the boundary value problem (1)–(3). Using the principle of contracting operators, we show that the operator Θ defined by equation (17), has a unique fixed point.

For the zero approximation from (18) we easily obtain that:

$$\left\|x^0(t)\right\| \leq \left\|Q^{-1}B\right\| < \infty. \tag{19}$$

For the first difference from approximation (18) we have the estimate:

$$\left\|x^1(t)-x^0(t)\right\| \le |\lambda| \sum_{k=1}^{m} \left[\left|\frac{\Delta_{1k}(\lambda)}{\Delta(\lambda)}\right| + \left|\frac{\Delta_{2k}\left(\lambda, f, I_i\right)}{\Delta(\lambda)}\right|\right] |\chi_{1k}| +$$

$$+\int_0^T |G(s)| \cdot \left|f\left(s, x^0(s), \max\left\{x^0(\tau)|\tau \in \left[h_1^0; h_2^0\right]\right\}\right)\right| ds + \sum_{i=1}^{p} |G(t_i)| \cdot \left|I_i\left(x^0(t_i)\right)\right| \le$$

$$\le |\lambda| \sum_{k=1}^{m} \left[\left|\frac{\Delta_{1k}(\lambda)}{\Delta(\lambda)}\right| + \left|\frac{\Delta_{2k}\left(\lambda, f^0, I_i^0\right)}{\Delta(\lambda)}\right|\right] |\chi_{1k}| + S\left(M_f + m_I\right) < \infty, \quad (20)$$

where:

$$f^0 = \int_0^T G(t) f\left(t, x^0(t), \max\left\{x^0(\tau)|\tau \in \left[h_1^0; h_2^0\right]\right\}\right) dt,$$

$$I_i^0 = I_i\left(x^0\left(t_i\right)\right), \quad S = \int_0^T |G(s)|\, ds + \sum_{i=1}^{p} |G(t_i)|,$$

$$M_f = \max_{t \in [0,T]} \left|f\left(t, Q^{-1}B, Q^{-1}B\right)\right|, \quad m_I = \max_{i \in \{1,2,\ldots,p\}} \left|I_i\left(Q^{-1}B\right)\right|.$$

Then, by virtue of the conditions of the theorem and (13), (16), for arbitrary $t \in (t_i, t_{i+1}]$ we have:

$$\left|x^j(t) - x^{j-1}(t)\right| \le |\lambda| \sum_{k=1}^{m} \left|\frac{\left|\Delta_{2k}\left(\lambda, f^{j-1}, I_i^{j-1}\right) - \Delta_{2k}\left(\lambda, f^{j-2}, I_i^{j-2}\right)\right|}{\Delta(\lambda)}\right| |\chi_{1k}| +$$

$$+\int_0^T |G(s)| \cdot \left|f\left(s, x^{j-1}(s), \max\left\{x^{j-1}(\tau)|\tau \in \left[h_1^{j-1}; h_2^{j-1}\right]\right\}\right) - f\left(s, x^{j-2}(s), \max\left\{x^{j-2}(\tau)|\tau \in \left[h_1^{j-2}; h_2^{j-2}\right]\right\}\right)\right| ds +$$

$$+\sum_{i=1}^{p} |G(t_i)| \cdot \left|I_i\left(x^{j-1}(t_i)\right) - I_i\left(x^{j-2}(t_i)\right)\right| \le$$

$$\le |\lambda| \sum_{k=1}^{m} |\chi_{1k}| \cdot \left|\bar{\Delta}_{2k}(\lambda)\right| \int_0^T |G(s)| \cdot \left[M_1(s) \cdot \left|x^{j-1}(s) - x^{j-2}(s)\right| +\right.$$

$$+ M_2(s) \cdot \left| \max\left\{x^{j-1}(\tau)|\tau \in \left[h_1^{j-1}; h_2^{j-1}\right]\right\} - \max\left\{x^{j-2}(\tau)|\tau \in \left[h_1^{j-2}; h_2^{j-2}\right]\right\} \right|\left.\right] ds +$$

$$+ |\lambda| \sum_{k=1}^{m} |\chi_{1k}| \cdot \left|\bar{\Delta}_{2k}(\lambda)\right| \cdot \sum_{i=1}^{p} |G(t_i)| \cdot m_i \cdot \left|x^{j-1}(t_i) - x^{j-2}(t_i)\right| + \int_0^T |G(s)| \cdot \left[M_1(s) \cdot \left|x^{j-1}(s) - x^{j-2}(s)\right| +\right.$$

$$+ M_2(s) \cdot \left| \max\left\{x^{j-1}(\tau)|\tau \in \left[h_1^{j-1}; h_2^{j-1}\right]\right\} - \max\left\{x^{j-2}(\tau)|\tau \in \left[h_1^{j-2}; h_2^{j-2}\right]\right\} \right|\left.\right] ds +$$

$$+ \sum_{i=1}^{p} |G(t_i)| \cdot m_i \cdot \left|x^{j-1}(t_i) - x^{j-2}(t_i)\right|, \quad (21)$$

where $h_l^j = h_l(t, x^j(t))$, $l = 1, 2$ and:

$$\bar{\Delta}_{2k}(\ \lambda) = \begin{vmatrix} 1+\lambda\Phi_{11} & \ldots & \lambda\Phi_{1(i-1)} & \bar{\Psi}_{21} & \lambda\Phi_{1(i+1)} & \ldots & \lambda\Phi_{1m} \\ \lambda\Phi_{21} & \ldots & \lambda\Phi_{2(i-1)} & \bar{\Psi}_{22} & \lambda\Phi_{2(i+1)} & \ldots & \lambda\Phi_{2m} \\ \ldots & \ldots & \ldots & \ldots & \ldots & \ldots & \ldots \\ \lambda\Phi_{m1} & \ldots & \lambda\Phi_{m(i-1)} & \bar{\Psi}_{2m} & \lambda\Phi_{m(i+1)} & \ldots & 1+\lambda\Phi_{mm} \end{vmatrix},$$

$$\bar{\Psi}_{2k} = \int_0^T b_k(s) ds.$$

By virtue of third condition of the theorem, we have:

$$\begin{aligned}
&\left|\max\left\{x^{j-1}(\tau)|\tau\in\left[h_1^{j-1};h_2^{j-1}\right]\right\}-\max\left\{x^{j-2}(\tau)|\tau\in\left[h_1^{j-2};h_2^{j-2}\right]\right\}\right|\le\\
&\qquad\le\left|\max\left\{x^{j-1}(\tau)|\tau\in\left[h_1^{j-1};h_2^{j-1}\right]\right\}-\max\left\{x^{j-2}(\tau)|\tau\in\left[h_1^{j-1};h_2^{j-1}\right]\right\}\right|+\\
&\qquad+\left|\max\left\{x^{j-2}(\tau)|\tau\in\left[h_1^{j-1};h_2^{j-1}\right]\right\}-\max\left\{x^{j-2}(\tau)|\tau\in\left[h_1^{j-2};h_2^{j-2}\right]\right\}\right|\le\\
&\le\left|x^{j-1}(t)-x^{j-2}(t)\right|+M_f\left[\left|h_1\left(t,x^{j-1}(t)\right)-h_1\left(t,x^{j-2}(t)\right)\right|+\left|h_2\left(t,x^{j-1}(t)\right)-h_2\left(t,x^{j-2}(t)\right)\right|\right]\le\\
&\qquad\qquad\le\left(1+M_f\left(M_{31}(t)+M_{32}(t)\right)\right)\left|x^{j-1}(t)-x^{j-2}(t)\right|.
\end{aligned}\tag{22}$$

Substituting the estimate (22) into (21), we obtain:

$$\left\|x^j(t)-x^{j-1}(t)\right\|_{PC}\le\rho\cdot\left\|x^{j-1}(t)-x^{j-2}(t)\right\|_{PC},\tag{23}$$

where $\rho=S_1+S_2$ and:

$$S_1=|\lambda|\sum_{k=1}^m|\chi_{1k}|\cdot\left|\bar\Delta_{2k}(\lambda)\right|\int\limits_0^T|G(s)|\cdot\left[M_1(s)+M_2(s)\left(1+M_f\left(M_{31}(s)+M_{32}(s)\right)\right)\right]ds,$$

$$S_2=|\lambda|\sum_{k=1}^m|\chi_{1k}|\cdot\left|\bar\Delta_{2k}(\lambda)\right|\sum_{i=1}^p|G(t_i)|\cdot m_i.$$

According to the last condition of the theorem, $\rho<1$. Therefore, from the estimate (23) we have:

$$\left\|x^j(t)-x^{j-1}(t)\right\|_{PC}<\left\|x^{j-1}(t)-x^{j-2}(t)\right\|_{PC}.\tag{24}$$

It follows from (24) that the operator Θ on the right-hand side of (17) is contracting. According to fixed point principle, taking into account estimates (19), (20) and (24), we conclude that the operator Θ has a unique fixed point. Consequently, the nonlocal boundary value problem (1)–(3) has a unique solution $x(t)\in PC\left([0,T],\mathbb{R}^n\right)$.

Now, let us show the continuous dependence of the solution to the boundary value problem (1)–(3) on the right-hand side of condition (2). Let $B_1,B_2\in\mathbb{R}^n$ are two different constants and $x_1(t),x_2(t)\in PC\left([0,T],\mathbb{R}^n\right)$ are corresponding solutions of the problem (1)–(3). Then, we have:

$$\begin{aligned}
&x_1(t)-x_2(t)=Q^{-1}\left[B_1-B_2\right]+\lambda\sum_{k=1}^m\frac{\Delta_{2k}\left(\lambda,f_1,I_{1i}\right)-\Delta_{2k}\left(\lambda,f_2,I_{2i}\right)}{\Delta(\lambda)}\chi_{1k}+\\
&\quad+\int\limits_0^T G(s)\cdot\left|f\left(s,x_1(s),\max\left\{x_1(\tau)|\tau\in\left[h_1^1;h_2^1\right]\right\}\right)-f\left(s,x_2(s),\max\left\{x_2(\tau)|\tau\in\left[h_1^2;h_2^2\right]\right\}\right)\right|ds+\\
&\qquad\qquad+\sum_{i=1}^P G(t_i)\left[I_i(x_1(t_i))-I_i(x_2(t_i))\right],
\end{aligned}\tag{25}$$

where $h_j^k=h_j(t,x_k(t))$, $j,k=1,2$. Now, using the first two conditions of the theorem, from (25) we obtain:

$$\begin{aligned}
&|x_1(t)-x_2(t)|\le Q^{-1}\left[B_1-B_2\right]+|\lambda|\sum_{k=1}^m\left|\frac{\left|\Delta_{2k}\left(\lambda,f_1,I_{1i}\right)-\Delta_{2k}\left(\lambda,f_2,I_{2i}\right)\right|}{\Delta(\lambda)}\right||\chi_{1k}|+\\
&+\int\limits_0^T|G(s)|\cdot\left[M_1(s)\cdot|x_1(s)-x_2(s)|+M_2(s)\cdot\left|\max\left\{x_1(\tau)|\tau\in\left[h_1^1;h_2^1\right]\right\}-\max\left\{x_2(\tau)|\tau\in\left[h_1^2;h_2^2\right]\right\}\right|\right]ds+\\
&\qquad\qquad+\sum_{i=1}^p|G(t_i)|\cdot m_i\cdot|x_1(t_i)-x_2(t_i)|.
\end{aligned}$$

Hence, as in the case of estimation process for (23), we obtain:

$$\|x_1(t)-x_2(t)\|_{PC}\le\left\|Q^{-1}\right\|\|B_1-B_2\|+\rho\cdot\|x_1(t)-x_2(t)\|_{PC}.$$

Since $\rho<1$, from the last inequality, it follows that:

$$\|x_1(t)-x_2(t)\|_{PC}\le(1-\rho)^{-1}\left\|Q^{-1}\right\|\cdot\|B_1-B_2\|.$$

If we put $\|B_1-B_2\|<\delta$ and $\varepsilon=(1-\rho)^{-1}\left\|Q^{-1}\right\|\cdot\delta$, then, from the last inequality, we obtain $\|x_1(t)-x_2(t)\|_{PC}<\varepsilon$. The theorem is proved.

4. Conclusion

The theory of differential equations plays an important role in solving applied problems. Especially, nonlocal boundary value problems for differential equations with impulsive actions have many applications in mathematical physics, mechanics and technology, in particular in nanotechnology.

In this paper, we investigated the system of first order Fredholm integro-differential equations (1) with nonlocal boundary value condition (2) and with condition (3) of impulsive effects for $t = t_i$ $i = 1, 2, ..., p$, $0 < t_1 < t_2 < ... < t_p < T$. The kernel of integro-differential equation (1) is degenerate. The nonlinear right-hand side of this equation consists of the construction of nonlinear maxima. The questions of the existence and uniqueness of the solution of the boundary value problem (1)–(3) are studied. The continuous dependence of the solution on the right-hand side of the boundary condition was proved.

The results obtained in this work will allow us in the future to investigate nonlocal boundary value problems for the heat equation and the wave equation with impulsive actions. We hope that our work will stimulate the study of various boundary value problems for partial differential and integro-differential equations with impulsive actions.

References

[1] Benchohra M., Henderson J., Ntouyas S.K. *Impulsive differential equations and inclusions*. Contemporary mathematics and its application. Hindawi Publishing Corporation, New York, 2006.

[2] Boichuk A.A., Samoilenko A.M. *Generalized inverse operators and Fredholm boundary-value problems*. Utrecht, Brill, 2004.

[3] Boichuk A.A., Samoilenko A.M. *Generalized inverse operators and Fredholm boundary-value problems (2nd ed.)*. Walter de Gruyter GmbH, Berlin–Boston, 2016. 314 p.

[4] Islomov B.I., Abdullaev A.A. On a problem for an elliptic type equation of the second kind with a conormal and integral condition. *Nanosystems: Physics, Chemistry, Mathematics*, 2018, **9** (3), P. 307–318.

[5] Lakshmikantham V., Bainov D.D., Simeonov P.S. *Theory of impulsive differential equations*. World Scientific, Singapore, 1989. 434 p.

[6] Perestyk N.A., Plotnikov V.A., Samoilenko A.M., Skripnik N.V. *Differential equations with impulse effect: multivalued right-hand sides with discontinuities*. DeGruyter Stud. **40**, Math. Walter de Gruter Co., Berlin, 2011.

[7] Samoilenko A.M., Perestyk N.A. *Impulsive differential equations*. World Sci., Singapore, 1995.

[8] Halanay A., Veksler D. *Qualitative theory of impulsive systems*. Mir, Moscow, 1971. 309 p. (in Russian).

[9] Assanova A. An integral-boundary value problem for a partial differential equation of second order. *Turkish J. of Mathematics*, 2019, **43** (4), P. 1967–1978.

[10] Assanova A.T. On the solvability of nonlocal problem for the system of Sobolev-type differential equations with integral condition. *Georgian Mathematical J.*, 2021, **28** (1), P. 49–57.

[11] Assanova A.T., Imanchiyev A.E., Kadirbayeva Zh.M. A nonlocal problem for loaded partial differential equations of fourth order. *Bulletin of the Karaganda university – Mathematics,* 2020, **97** (1), P. 6–16.

[12] Assanova A.T., Tokmurzin Z.S. A nonlocal multipoint problem for a system of fourth-order partial differential equations. *Eurasian Math. J.*, 2020, **11** (3), P. 8–20.

[13] Minglibayeva A.B., Assanova A.T. An existence of an isolated solution to nonlinear two-point boundary value problem with parameter. *Lobachevskii J. of Mathematics*, 2021, **42** (3), P. 587–597.

[14] Yuldashev T.K. Nonlinear optimal control of thermal processes in a nonlinear inverse problem. *Lobachevskii J. of Mathematics*, 2020, **41** (1), P. 124–136.

[15] Gianni R. Equation with nonlocal boundary condition. *Mathematical Models and Methods in Applied Sciences*, 1993, **3** (6), P. 789–804.

[16] Pao C.V. Numerical solutions of reaction-diffusion equations with nonlocal boundary conditions. *J. of Computational and Applied Mathematics*, 2001, **136** (1–2), P. 227–243.

[17] Giacomin G., Lebowitz J.L. Phase segregation dynamics in particle systems with long range interactions, I. Macroscopic limits. *J. of Statist. Phys.*, 1997, **87**, P. 37–61.

[18] Yuldashev T.K. Nonlocal mixed-value problem for a Boussinesq-type integrodifferential equation with degenerate kernel. *Ukrainian Mathematical J.*, 2016, **68** (8), P. 1278–1296.

[19] Yuldashev T.K. Determination of the coefficient and boundary regime in boundary value problem for integro-differential equation with degenerate kernel. *Lobachevskii J. of Mathematics*, 2017, **38** (3), P. 547–553.

[20] Yuldashev T.K. Nonlocal boundary value problem for a nonlinear Fredholm integro-differential equation with degenerate kernel. *Differential equations*, 2018, **54** (12), P. 1646–1653.

[21] Yuldashev T.K. Spectral features of the solving of a Fredholm homogeneous integro-differential equation with integral conditions and reflecting deviation. *Lobachevskii J. of Mathematics*, 2019, **40** (12), P. 2116–2123.

[22] Yuldashev T.K. On inverse boundary value problem for a Fredholm integro-differential equation with degenerate kernel and spectral parameter. *Lobachevskii J. of Mathematics*, 2019, **40** (2), P. 230–239.

[23] Yuldashev T.K. On the solvability of a boundary value problem for the ordinary Fredholm integrodifferential equation with a degenerate kernel. *Computational Mathematics and Math. Physics*, 2019, **59** (2), P. 241–252.

[24] Yuldashev T.K. On a Volterra type fractional integro-differential equation with degenerate kernel. *AIP Conference Proceedings*, 2021, **2365**, 020016.

[25] Annamalai Anguraj, Mani Mallika Arjunan. Existence and uniqueness of mild and classical solutions of impulsive evolution equations. *Elect. J. of Differential Equations*, 2005, **2005** (111), P. 1–8.

[26] Ashyralyev A., Sharifov Y.A. Existence and uniqueness of solutions for nonlinear impulsive differential equations with two–point and integral boundary conditions. *Advances in Difference Equations*, 2013, **2013** (173).

[27] Ashyralyev A., Sharifov Y.A. Optimal control problems for impulsive systems with integral boundary conditions. *Elect. J. of Differential Equations*, 2013, **2013** (80), P. 1–11.

[28] Bin L., Xinzhi L., Xiaoxin L. Robust global exponential stability of uncertain impulsive systems. *Acta Mathematika Scientia*, 2005, **25** (1), P. 161–169.

[29] Ji Sh., Wen Sh. Nonlocal cauchy problem for impulsive differential equations in Banach spaces. Intern. *J. of Nonlinear Science*, 2010, **10** (1), P. 88–95.

[30] Li M., Han M. Existence for neutral impulsive functional differential equations with nonlocal conditions. *Indagationes Mathematcae*, 2009, **20** (3), P. 435–451.

[31] Mardanov M.J., Sharifov Ya.A., Molaei H.H. Existence and uniqueness of solutions for first-order nonlinear differential equations with two-point and integral boundary conditions. *Electr. J. of Differential Equations*, 2014, **2014** 259), P. 1–8.

[32] Sharifov Ya.A. Optimal control problem for systems with impulsive actions under nonlocal boundary conditions. *Vestnik Samarskogo Gosudarstvennogo Tekhnicheskogo Universiteta. Seria: Fiziko-matematicheskie nauki*, 2013, **4** (33), P. 34–45 (in Russian).

[33] Sharifov Ya.A. Optimal control for systems with impulsive actions under nonlocal boundary conditions. *Russian Mathematics (Izv. VUZ)*, 2013, **57** (2), P. 65–72.

[34] Sharifov Y.A., Mammadova N.B. Optimal control problem described by impulsive differential equations with nonlocal boundary conditions. *Differential equations*, 2014, **50** (3), P. 403–411.

[35] Sharifov Y.A. Conditions optimality in problems control with systems impulsive differential equations with nonlocal boundary conditions. *Ukrainain Math. J.*, 2012, **64** (6), P. 836–847.

[36] Yuldashev T.K. Limit value problem for a system of integro-differential equations with two mixed maxima. *Vestnik Samarskogo Gosudarstvennogo Tekhnicheskogo Universiteta. Seria: Fiziko-matematicheskie nauki*, 2008, **1** (16), P. 15–22 (in Russian).

Submitted 28 November 2021; revised 26 December 2021; accepted 28 December 2021

Information about the authors:

Tursun K. Yuldashev – National University of Uzbekistan, Universitet street, 4, NUUz, Tashkent, 100174, Uzbekistan; ORCID 0000-0002-9346-5362; tursun.k.yuldashev@gmail.com

Aziz K. Fayziev – Tashkent State Technical University, Universitet street, 2, TSTU, Tashkent, 100174, Uzbekistan; ORCID 0000-0001-6798-3265; fayziyev.a@inbox.ru

Conflict of interest: the authors declare no conflict of interest.

NANOSYSTEMS:
PHYSICS, CHEMISTRY, MATHEMATICS

Original article

Belonenko M.B., Konobeeva N.N. *Nanosystems: Phys. Chem. Math.*, 2022, **13** (1), 45–49.
http://nanojournal.ifmo.ru
DOI 10.17586/2220-8054-2022-13-1-45-49

Two-dimensional non-topological solutions of Maxwell's equations in a medium of strained carbon nanotubes with impurities

Mikhail B. Belonenko[a], Natalia N. Konobeeva[b]

Volgograd State University, Volgograd, Russia

[a]belonenko@volsu.ru, [b]yana_nn@volsu.ru

Corresponding author: Mikhail B. Belonenko, belonenko@volsu.ru

PACS 42.65.Tg, 61.72.-y, 73.63.Fg

ABSTRACT In this work, we investigate the few-cycle optical pulses with Gauss and Bessel profile in strained carbon nanotubes with impurities. We consider a multi-level impurity in which the energy levels are well separated from the conduction and valence bands of carbon nanotubes. The effect of the impurity parameters on the electromagnetic pulse is analyzed. Also, we investigate the influence of the value of the mechanical stretching on the few-cycle pulse shape.

KEYWORDS carbon nanotubes, impurities, mechanical tension, few-cycle pulse

ACKNOWLEDGEMENTS Authors thank the Ministry of Science and Higher Education of the Russian Federation for the numerical modeling support under the government task (0633-2020-0003).

FOR CITATION Belonenko M.B., Konobeeva N.N. Two-dimensional non-topological solutions of Maxwell's equations in a medium of strained carbon nanotubes with impurities. *Nanosystems: Phys. Chem. Math.*, 2022, **13** (1), 45–49.

1. Introduction

Few-cycle optical pulses have a great practical potential in the development of nonlinear optics devices [1, 2]. Such pulses include those that contain only a few oscillations of the electromagnetic field. Pulses with Gaussian [3] and Bessel [4] cross sections are of great interest. The first (Gaussian beam) is most commonly used in lasers. The second has a number of unusual properties, one of which is diffractionlessness [5].

Note that the medium in which pulse propagates has a great influence on its behavior. From this point of view, media containing carbon nanotubes [6] are very attractive due to their stabilizing effect, including on pulses with the Bessel cross section [7]. It should be said, that the presence of impurities in CNTs has a significant effect on the pulse evolution, which is shown in many works [8, 9]. There are several models for accounting for the impurities. The simplest of them is the Anderson model [10], which takes into account only the hybridization of electronic subsystems. Another is the strong electron-electron model [11], in which the Fermi velocity depends on the electron energy in a logarithmic manner. And, the third model considered in this work is the multi-level impurity model [12], in which transitions between the CNT conduction band and impurity levels are possible.

At the same time, the question related to the influence of a strong acoustic field remains unexplored. In Ref. [13] the authors study the effect of external deformations in the one-dimensional case. In this work, we study the dynamics of 2D few-cycle optical pulse in a dielectric medium with impurity CNTs under the action of an acoustic field.

2. Model and basic equations

The electron spectrum for zigzag carbon nanotubes $(n,0)$, taking into account the impurity $\varepsilon_{imp}(p,s)$, has the following form [12]:

$$\begin{gathered}\varepsilon_{imp}(p,s)=0.5\left(R+Q+\sqrt{(R-Q)^2-4\left(2D\cdot\Delta(p,s)-\Delta(p,s)^2-D^2\right)}\right),\\ R=-\sum_{j=1}^{4}\frac{|\alpha_{1,j}|^2}{W_j},\quad Q=-\sum_{j=1}^{4}\frac{|\alpha_{2,j}|^2}{W_j},\quad D=\sum_{j=1}^{4}\frac{\alpha_{1,j}\alpha^*_{2,j}}{W_j}.\end{gathered}\tag{1}$$

Here R, Q determine the transitions of an electron between impurity levels and sublattices of nanotubes, D describes interlattice transitions in CNTs, W_j is the energy of an electron localized at the j-th impurity level, $\alpha_{i,j}$ is the quantity equals to the hopping integral related to the concentration of impurities between the site of the sublattice of the nanotube i and the impurity level j. We restrict ourselves to the consideration of four levels, since, as the level number increases, its contribution to the impurity parameters decreases. $\Delta(p,s)$ is the dispersion law for electrons of carbon nanotubes in the absence of impurity [14]:

$$\Delta\left(p,s\right)=\gamma\sqrt{1+4\cos\left(ap\right)\cos\left(\frac{\pi}{n}s\right)+4\cos^{2}\left(\frac{\pi}{n}s\right)}, \tag{2}$$

where $\gamma\approx 2$ eV, $a=3b/2\hbar$, $b=0.142$ nm is the distance between neighboring atoms in carbon nanotube with quasi-momentum (p,s), and p is the momentum component along the CNT axis, $s=0,..,n$.

Due to the distance between CNTs exceeds their diameter is about in 10 times, we can neglect the interaction between the tubes. We consider the geometry of our problem, in which the wave vector is perpendicular to the CNT array and the electric field strength vector $\mathbf{E}$ is co-directional the nanotube axis.

The acoustic field is due to the stress field, which appears due to the deformation field. It can be taken into account in the framework of the gauge theory. This field is determined by the vector potential $\mathbf{A}'$, which changes the momentum of electrons in a medium containing an array of carbon nanotubes. All interatomic bonds in CNTs under stress are nonequivalent; therefore, the neighboring hopping integrals may not coincide. We can consider CNTs as a rolled sheet of graphene and write down all the equations for it. Further, we should write the periodic boundary conditions. Then, the gauge vector potential has the form: $\mathbf{A}'=(A'_z,A'_x)$ [15]:

$$\begin{aligned}A'_x&=\frac{(\gamma_2+\gamma_3-2\gamma_1)}{2},\\A'_z&=\frac{\sqrt{3}\,(\gamma_3-\gamma_2)}{2},\end{aligned} \tag{3}$$

where $\gamma_{1,2,3}$ is the modulation of hopping integrals due to displacements of carbon atoms.

The contributions of the electromagnetic field and lattice deformations are reduced to the sum of the corresponding vector potentials (the electromagnetic field of the pulse and the gauge) [16]:

$$\begin{gathered}\frac{\partial^2 A}{\partial x^2}+\frac{\partial^2 A}{\partial z^2}-\frac{\varepsilon}{c^2}\frac{\partial^2 A}{\partial t^2}+4\pi j\left(A+A'/e\right)=0,\\A'=\chi\frac{\beta\gamma u_{zz}}{a}\cdot(1+\mu),\end{gathered} \tag{4}$$

where ε is the dielectric constant of the medium, β is the electronic Gruneisen parameter, which determines the change in the frequency of lattice vibrations with a change in the volume of the system [17] (for CNT we can take $\beta\approx 2$), $\mu=0.19$ is the Poisson's coefficient for carbon nanotubes [18], χ is the parameter depending on the characteristics of the chemical bond in the substance, which can be set for CNTs equal to 1, u_{zz} is the longitudinal component of the strain tensor, j is the current density, which is determined as:

$$j=2e\sum_{s=1}^{n}\int\limits_{BZ}v\left(p,s\right)\cdot f\left(p,s\right)dp, \tag{5}$$

where e is the electron charge, $v\left(p,s\right)=\partial\varepsilon_{imp}\left(p,s\right)/\partial p$, $f(p,s)$ is the Fermi distribution function, BZ means integration over the first Brillouin zone. Carrying out standard calculations of the current density for CNTs, we obtain the effective equation for the vector potential of the electric field:

$$\begin{aligned}&\frac{\partial^2 A}{\partial x^2}+\frac{\partial^2 A}{\partial z^2}-\frac{\varepsilon}{c^2}\frac{\partial^2 A}{\partial t^2}+\frac{4en_0\gamma_0 a}{c}\sum_{q=1}^{\infty}b_q\sin\left(\frac{aq\left(eA+A'\right)}{c}\right)=0,\\&b_q=\frac{1}{N_F}\sum_s a_{sq}\int\limits_{BZ}dp\cdot\cos\left(pq\right)\frac{\exp\left(-\varepsilon_{imp}\left(p,s\right)/k_BT\right)}{1+\exp\left(-\varepsilon_{imp}\left(p,s\right)/k_BT\right)},\\&a_{sq}=\int\limits_{BZ}dp\cdot\cos\left(pq\right)\cdot\varepsilon_{imp}\left(p,s\right),\end{aligned} \tag{6}$$

where n_0 is the electron concentration, k_B is the Boltzmann constant, T is the temperature, a_{sq} are the coefficients in the expansion of the electron dispersion law (1) in a Fourier series, N_F is the normalization constant for the Fermi distribution.

The initial condition with a Gaussian (7a) and a Bessel (7b) transverse profile is chosen in the following form:

$$\begin{aligned}A\left(x,z,0\right)&=Q_0\cdot\exp\left(-\frac{x^2}{l_x^2}-\frac{z^2}{l_z^2}\right),\\\frac{dA\left(x,z,0\right)}{dt}&=\frac{2\cdot z\cdot v\cdot Q_0}{l_z^2}\cdot\exp\left(-\frac{x^2}{l_x^2}-\frac{z^2}{l_z^2}\right),\end{aligned} \tag{7a}$$

$$\begin{gathered}A\left(x,z,0\right)=Q_0\cdot\exp\left(-\frac{z^2}{l_z^2}\right)\exp\left(-\frac{x}{l}\right),\\ \frac{dA\left(x,z,0\right)}{dt}=\frac{2\cdot z\cdot \upsilon\cdot Q_0}{l_z^2}\cdot J_0\left(\left|\frac{x}{l_x}\right|\right)\exp\left(-\frac{z^2}{l_z^2}\right)\exp\left(-\frac{x}{l}\right),\end{gathered}\tag{7b}$$

where Q_0 is the initial amplitude of the electromagnetic pulse, l_x, l_z is the width of the pulse along the x and z-axis, υ is the pulse velocity along OZ, l is the cutoff parameter for Bessel function. All values are given here already in dimensionless form.

3. Main results and discussion

Equation (6) is solved numerically [19] with the following system parameters: CNT of the "zigzag" type $(7,0)$, $\varepsilon=4$, $T=293$ K, $\upsilon=0.9$ (in units of the light speed).

The evolution of the electromagnetic field during its propagation in a medium with impurity carbon nanotubes under the action of an acoustic field is shown in Figs. 1 and 2 for the Gaussian and Bessel profiles, respectively.

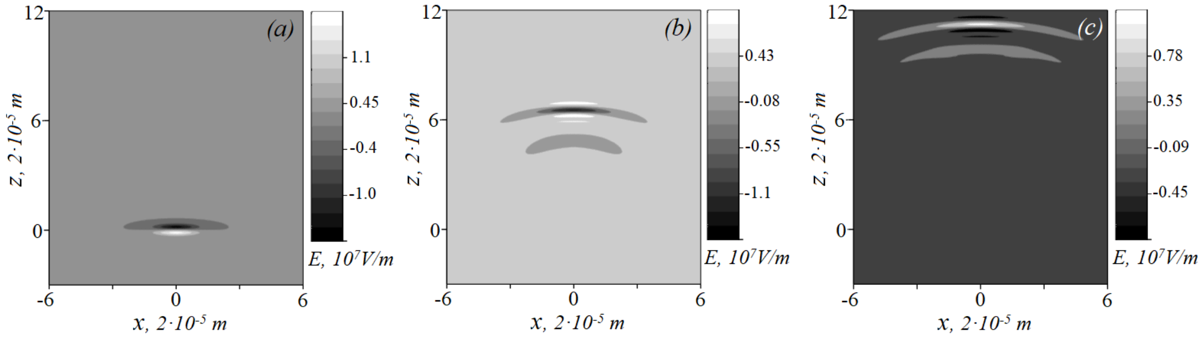

FIG. 1. Pulse evolution with a Gaussian profile ($u_{zz}=0.1$): a) $t=0$; b) $t=7$; c) $t=12$. The time unit corresponds to $2\cdot 10^{-14}$ s

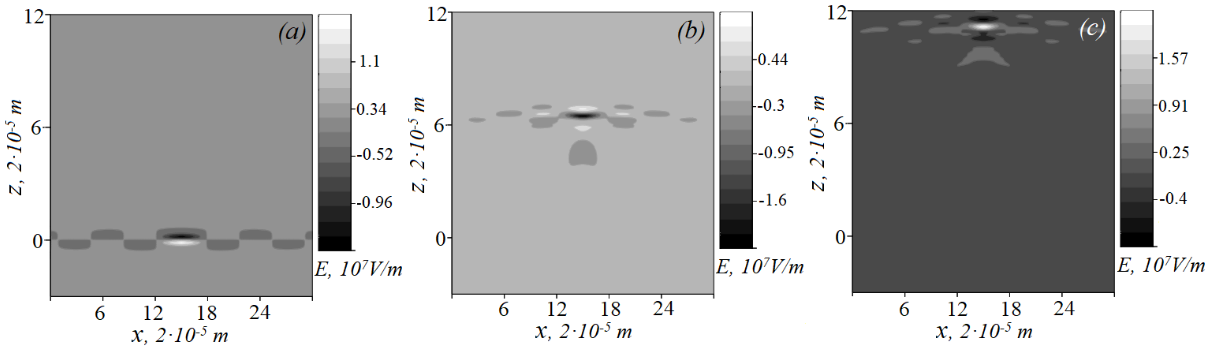

FIG. 2. Pulse evolution with a Bessel profile ($u_{zz}=0.1$): a) $t=0$; b) $t=7$; c) $t=12$. The time unit corresponds to $2\cdot 10^{-14}$ s

From the above dependencies, we can say that the pulse propagates about 10 of its wavelengths regardless of the cross-sectional shape. Therefore, it moves stably even under the action of deformation. Although the fields are assumed to be strong, there is no significant change in the character of the pulse propagation with a Bessel profile. It should be noted, that for the same values of the initial pulse amplitude with a Gaussian profile, a noticeable decrease in the diffraction effect is observed, which is associated with the nonlinear properties of the medium. Note that in both cases (Figs. 1, 2) a "tail" appears behind the main pulse, which is clearly visible on the following Figs. 3 and 4. Figs. 1 and 2 show only a part of the computational domain for clarity of the behavior of the main pulse.

The dependence of the shape of the electromagnetic pulse on the magnitude of the acoustic field is shown in Fig. 3.

It can be seen, that the mechanical load on the CNT has a greater effect on the pulse with a transverse Gaussian profile as compared to the Bessel pulse, even in the case of small values of the u_{zz}. This can be associated with the pulse with a transverse Bessel cross section and has the property of immunity from diffraction. Note that the mechanical tension on the CNT changes the dispersion law of electrons in the CNT, and, therefore, changes the form of the nonlinearity of the medium. As before, nonlinearity has a stronger effect on the Gaussian pulse dynamics.

Next, we investigate the effect of impurities in strained CNTs on the pulse propagation process (Fig. 4).

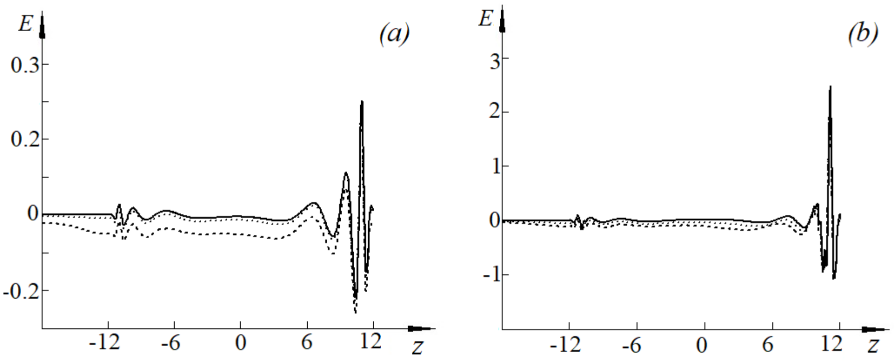

FIG. 3. The dependence of the electric field strength E (longitudinal section at the pulse center: $t = 12$, $D = 0.1\gamma$) on the coordinate z for different longitudinal components of the strain tensor: a) Gaussian profile: the solid curve corresponds to $u_{zz} = 0$, the dotted curve – $u_{zz} = 0.01$, the dashed curve – $u_{zz} = 0.05$; b) Bessel profile: the solid curve corresponds to $u_{zz} = 0$, the dotted curve – $u_{zz} = 0.05$, the dashed curve – $u_{zz} = 0.1$. The z-unit corresponds to $2 \cdot 10^{-5}$ m, along the E-axis – 10^7 V/m, in time – $2 \cdot 10^{-14}$ s

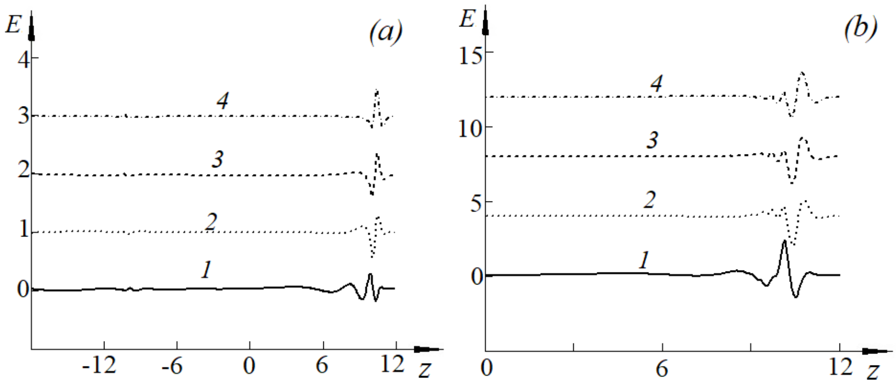

FIG. 4. The dependence of the electric field strength E (longitudinal section at the pulse center: $t = 12$, $u_{zz} = 0.01$) on the coordinate z for the different impurity parameters ($D = -R = -Q$): (a) Gaussian profile – for clarity, each i-th curve is shifted up by $(i - 1)$ units; (b) Bessel profile – for clarity, each i-th curve is shifted up by $4(i - 1)$ units: curve 1 corresponds to $D = 0$ (no impurity), curve 2 – $D = 0.3\gamma$, curve 3 – $D = 0.5\gamma$, curve 4 – $D = 1.0\gamma$. The unit along the z-axis corresponds to $2 \cdot 10^{-5}$ m, along the E-axis E – 10^7 V/m, in time – $2 \cdot 10^{-14}$ s

It can be seen from the given dependencies that the impurity parameters allows us to not only change the shape, but also the pulse amplitude. We also note that for pulses of both cross sections (Gaussian and Bessel), pulse inversion is observed when impurity carbon nanotubes are introduced into the medium (curves 2–4).

4. Conclusion

Let us formulate the main results from the work:

1. There is a localized pulse propagation in dielectric medium with impurity carbon nanotubes under mechanical strain. Dispersive broadening of pulses during propagation can be compensated for by selecting the appropriate parameters of the acoustic field and impurity.
2. For a pulse with a transverse Gaussian profile, the effect of the acoustic field is more pronounced than for a pulse with a Bessel profile.
3. It is observed, that due to the impurity introduction, it is possible to control the amplitude and shape of few-cycle optical pulse with different profiles.

References

[1] Goorjian P.M., Agrawal G.P. Computational modeling of ultrashort pulse propagation in semiconductor materials. *Quantum Optoelectronics*, 1997, **9**, P. 95–97.

[2] Kozlov S.A., Samartsev V.V. *Fundamentals of Femtosecond Optics*. Woodhead Publishing, Cambridge, 2013, 273 p.

[3] Bauer C., Freeman R., et al. Gaussian pulses. *J. of Magnetic Resonance*, 1969, **58** (3), P. 442–457.

[4] Khonina S.N., Kazanskiy N.L., Karpeev S.V., Butt M.A. Bessel Beam: significance and applications – A Progressive Review. *Micromachines*, 2020, **11** (11), 997.

[5] Simon D.S. Bessel beams, self-healing, and diffraction-free propagation. In *A Guided Tour of Light Beams*, Morgan & Claypool Publishers, London, 2016, P. 1–15.

[6] Iijima S. Helical microtubules of graphitic carbon. *Nature*, 1991, **354**, P. 56–58.

[7] Belonenko M.B., Dvuzhilov I.S., Nevzorova Y.V. Two-dimensional extremely short optical pulses with a Bessel cross section in inhomogeneous medium of carbon nanotubes. *Optics and Spectroscopy*, 2016, **121** (5), P. 739–743.

[8] Konobeeva N.N., Polunina A.A., Belonenko M.B. Three-dimensional extremely short optical pulses in graphene with coulomb impurities with taking into account inhomogeneity. *Nanosystems: Phys., Chem., Math.*, 2016, **7** (6), P. 936–940.

[9] Fedorov E.G., Konobeeva N.N., Belonenko M.B. Two-dimensional electromagnetic breathers in an array of nanotubes with multilevel impurities. *Russ. J. Phys. Chem. B*, 2014, **8** (3), P. 409–415.

[10] Anderson P.W. Localized magnetic states in metals. *Phys. Rev.*, 1961, **124**, P. 41–53.

[11] Kotov V.N., Pereira V.M., Uchoa B. Polarization charge distribution in gapped graphene: Perturbation theory and exact diagonalization analysis. *Phys. Rev. B*, 2008, **78**, 075433.

[12] Zhukov A.V., Bouffanais R., et al. Influence of multi-level impurities on the dynamics of ultrashort electromagnetic pulses in carbon nanotubes. *EPL*, 2014, **106**, 37005.

[13] Lyapkosova O.S., Lebedev N.G., Belonenko M.B. Extremely short optical pulses in strained graphene in terms of the gauge theory. *Physics of the Solid State*, 2013, **55** (12), P. 2602–2607.

[14] Eletskii A.V. Carbon nanotubes. *Physics-Uspekhi*, 1997, **40** (9), P. 899–924.

[15] Vozmediano M.A.H., Katsnelson M.I., Guinea F. Gauge fields in graphene. *Phys. Rep.*, 2010, **496**, P. 109–148.

[16] Konobeeva N.N., Skvortsov D.S. Modeling of two-dimensional light bullets propagation in an array of carbon nanotubes taking into account the mechanical tension and magnetic field. *Mathematical physics and computer simulation*, 2020, **23** (3), P. 36–44.

[17] Sanditov D.S., Mantatov V.V., Darmaev M.V., Sanditov B.D. On the Grüneisen parameter for crystals and glasses. *Techn. Phys.*, 2009, **54**, P. 385–388.

[18] Rafii-Tabar H. *Computation physics of carbon nanotubes*. Cambridge University Press, Cambridge, 2008, 493 p.

[19] Strikwerda J. *Finite difference schemes and PDE*. SIAM, Philadelphia, 2004, 447 p.

Submitted 16 November 2021; revised 27 December 2021; accepted 28 December 2021

Information about the authors:

Mikhail B. Belonenko – Volgograd State University, University avenue, 100, Volgograd, 400062, Russia;
ORCID 0000-0003-2003-3793; belonenko@volsu.ru

Natalia N. Konobeeva – Volgograd State University, University avenue, 100, Volgograd, 400062, Russia;
ORCID 0000-0002-6043-9555; yana_nn@volsu.ru

Conflict of interest: the authors declare no conflict of interest.

NANOSYSTEMS:
PHYSICS, CHEMISTRY, MATHEMATICS

Rosol A.H.A., Dimyati K., et al. *Nanosystems: Phys. Chem. Math.*, 2022, **13** (1), 50–55.
http://nanojournal.ifmo.ru
DOI 10.17586/2220-8054-2022-13-1-50-55

Original article

Gold nanoparticles PVA thin film as Q-switcher in neodymium doped fiber laser cavity

Ahmad Haziq Aiman Rosol[1,2], Kaharudin Dimyati[1,2], Nur Farhanah Zulkipli[2], Retno Apsari[2], Moh Yasin[2], Sulaiman Wadi Harun[1,a]

[1]University of Malaya, 50603 Kuala Lumpur, Malaysia
[2]Airlangga University, Surabaya, Indonesia

[a]swharun@um.edu.my

Corresponding author: Sulaiman Wadi Harun, swharun@um.edu.my

PACS 42.82.Gw, 42.81.-i, 42.55.Wd

ABSTRACT A gold nanoparticle-based saturable absorber (SA) was successfully employed in Neodymium-doped fiber laser (NDFL) cavity for pulse generation via a Q-switching mechanism for the first time. The SA device was made by mixing the gold nanoparticles into PVA solution before being dried to form a thin film was included into the NDFL cavity, which was optimized to obtain Q-switched pulses centered at wavelength of 1089 nm. The pulse rate of the laser rose from 37.37 to 49.60 kHz while the pulse width fell from 4.82 to 3.84 μs as the 808 nm pump laser was raised from 98 to 144 mW. At the highest input pump power of 144 mW, the maximum output power and pulse energy was achieved at 0.52 mW and 10.48 nJ, respectively. The developed Q-switched laser has numerous applications including, material micromachining, communication, sensing, etc.

KEYWORDS neodymium doped fiber laser, gold nanoparticles, plasmonic

ACKNOWLEDGEMENTS This work was supported by the Airlangga University Research Grant (2021) and the University of Malaya (Grant No ST036-2020)

FOR CITATION Rosol A.H.A., Dimyati K., Zulkipli N.F., Apsari R., Yasin M., Harun S.W. Gold nanoparticles PVA thin film as Q-switcher in neodymium doped fiber laser cavity. *Nanosystems: Phys. Chem. Math.*, 2022, **13** (1), 50–55.

1. Introduction

Current Q-switched fiber lasers have received many researchers' attention, owing to their potential applications in numerous areas including telecommunication, material processing, medical diagnostics, spectroscopy, and optical sensing [1–3]. Conventionally, these lasers were realized using an active method employing external modulators [4]. In comparison with this method, the passive method using saturable absorber (SA) is less complicated while offering many advantages in terms of price, practicality, simplicity, and compactness [5]. In Q-switching, the SA is directly added into a laser cavity to generate short pulses due to the modulation of cavity loss and produce short pulses. When the laser intensity reaches the saturation power of the SA, the cavity loss is suddenly decreased, thus allowing more photons to be transmitted, leading to the production of a sequence of pulse train within the oscillator. To date, various nanomaterials such as single-wall carbon nanotubes [6], graphene [6], topological insulators [7, 8], and transition metal dichalcogenides [9–12] have been investigated and reported as SA. These materials have common advantages of wide absorption, ultrafast response time, and large third-order nonlinearity [13]. For example, Niu et al. proposed the employment of tin disulfide (SnS_2), which has a bandgap value of 2.24 eV as a Q-switcher. The laser successfully produced a short pulse with a maximum repetition rate of 233 kHz and minimum pulse width of 0.51 μs at 1532.7 nm [14].

Additionally, noble metal nanoparticles have also gained attention for SA applications owing to their close-lying energy bands, which allow a free electron to move. The energy filled the electron on the conduction band till it stimulated the plasmonic resonance to the surface as the photons interact with metal nanoparticles [15]. The metal nanoparticles could also be employed for pulse generation owing to the broadband absorption induced by the surface plasmon resonance and ultrafast response time [16–18]. For instance, Muhammad et al. demonstrated Q-switched erbium-doped fiber laser (EDFL) by using copper nanoparticles as saturable absorbers [19]. In another work, Ahmad et al. reported Q-switched pulse generation using gold nanoparticles obtained through thermal deposition method whereby maximum pulse width of 4.25 μs was realized [20]. All the reported works are carried out in 1.55 μm region based on the EDFLcavity.

More recently, interest in Q-switched neodymium-doped fiber laser (NDFL) operating in wavelength region around 1 μm is also increasing. NDFL can produce lasing in 1060 nm wavelength region through four-level transition of $^4F_{3/2} \rightarrow {}^4I_{11/2}$. Until recently, most Q-switched fiber lasers at around 1060 nm were achieved using an ytterbium-doped fiber laser. In this paper, a Q-switched NDFL operating at 1060 nm was demonstrated using the gold nanoparticles (GNPs) as SA.

The SA was fabricated by embedding the GNPs into the PVA by drop-casting method to form a SA thin film. This was then added into the NDFL cavity to modulate loss for generation of short pulse.

2. SA fabrication and characterizations

Figure 1 shows the fabrication process flow of GNPs based thin film using sodium borohydride ($NaBH_4$), gold (III) chloride trihydrate ($HAuCl_4 \cdot 3H_2O$), poly (sodium 4-styrenesulfonate) (PSSS), and tri-sodium citrate (TSC) liquids. All chemicals and solvents were used as received without further purification. At first, the GNPs were made using a $NaBH_4$ reduction method. 3 mL of $NaBH_4$, 3 mL PSSS and 50 mL TSC were poured into a beaker containing 1000 mL deionized water (with the resistivity of 18 MΩ) while stirring at 450 rpm. Then, 50 mL $HAuCl_4$ (5 mM, in water) was slowly dropped into the mixture in a rate of $\sim$ 2 mL/min with continuous stirring followed by the addition of the excess amount of TSC (20 mL). After that the mixture was left for 5 minutes to allow the reaction among the chemicals to complete before it was continued with a centrifugation process for cleaning purposes. We mixed the prepared GNPs solution with PVA liquid to prepare a SA thin film. The PVA liquid was obtained by dissolving PVA powder into distilled water. The powder was completely dissolved after a thorough stirring process at high temperature of 145 °C. The GNPs PVA mixture was then slowly stirred for about 2 hours to obtain an homogenous suspension solution, which was then used to prepare the thin film. It was poured and spread onto a petri dish before it was left to dry at room temperature for about 48 hours. The dried thin film was peeled so that it can be integrated into the laser cavity for the Q-switching experiment.

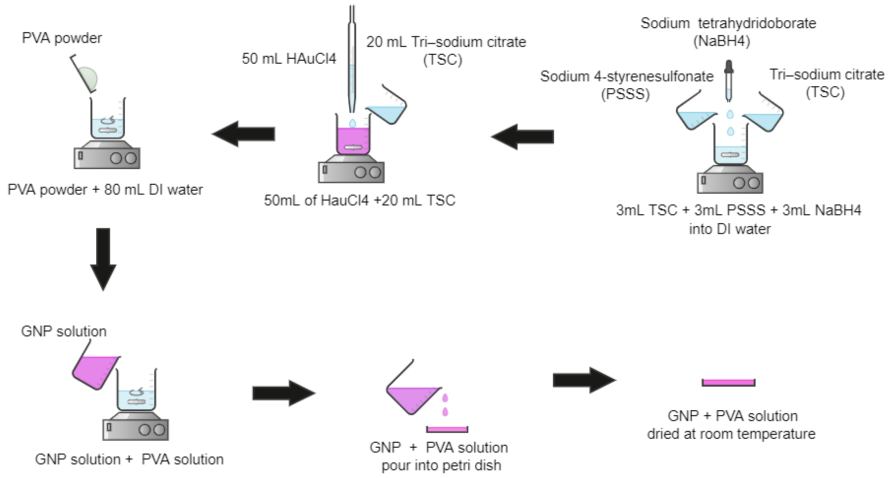

FIG. 1. Fabrication step for GNPs thin film

The non-linear absorption of the thin film was then investigated using a balanced twin-detector measurement technique. The light pulses from a homemade mode-locked fiber laser operating at pulse width of 1.3 ps and repetition rate of 2.5 MHz was used in the measurement. The non-linear absorption curve was obtained by comparing the peak power of the laser before and after the thin film. As shown in Fig. 2(a), the absorption reduces with the increase of input optical intensity. This indicates that the fabricated SA film has an excellent saturable absorption property, which could be used for pulse generation. The modulation depth, non-saturable absorption and saturable intensity of the film are obtained as 13.6 %, 47.2 %, and 0.5 MW/cm^2 respectively. It is worth noting that we have not observed any nonlinear response from pure PVA film, confirming that the saturable absorption property was solely originated from the GNPs. The linear optical absorption profile was also examined for this SA using a white light source and optical spectrum analyzer (OSA). Fig. 2(b) shows the absorbance spectrum of the GNPs PVA film, which was measured within a wavelength range from 1000 to 1300 nm. As shown in the figure, the absorption of about 5 dB was obtained at wavelength of 1080 nm.

3. Cavity configuration

The schematic diagram of the proposed laser setup is illustrated in Fig. 3. It used the newly developed GNPs PVA thin film as Q-switcher. An 11 m long Nd-doped fiber (NDF) with a peak absorption of 8.5 dB/m at 810 nm was employed as the laser active medium for the operation at 1080 nm region. The Nd-doped active fiber has a numerical aperture of 0.18 and a cutoff wavelength of 990 nm. We employed a single mode fiber (SMF) coupled 808 nm laser diode with the maximum power of $\sim$ 250 mW as the pump source. The SMF has a cutoff wavelength of 780 nm and core/clad diameter of 4.4/125 μm. The pump light was launched into the ring NDFL cavity via an 808/1064 wavelength division multiplexer. A polarization-insensitive isolator is incorporated into the NDFL cavity to provide unidirectional operation. An 80/20 optical coupler is employed to extract 20 % of the generated laser for measurement. The total cavity length

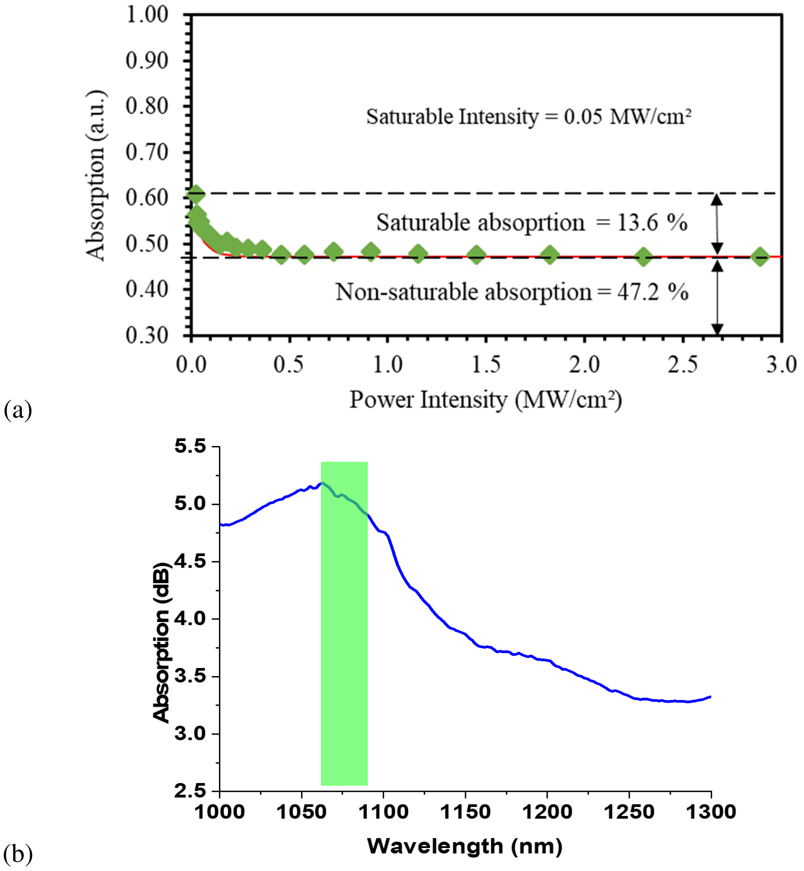

FIG. 2. (a) The non-linear and (b) linear absorption properties of GNPs thin film

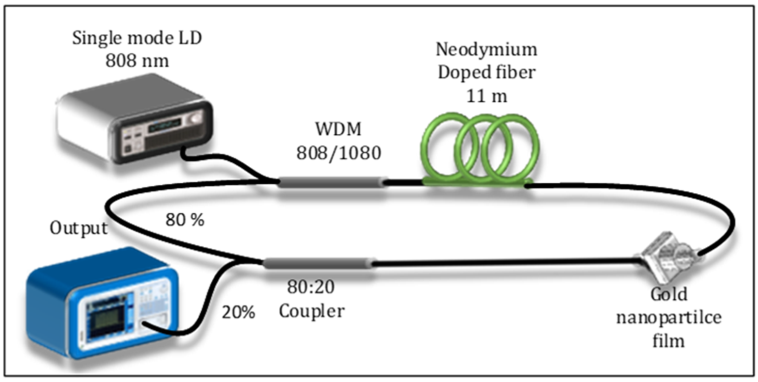

FIG. 3. The illustration of NDFL configuration

was about 13.5 m. The output pulses of the passively Q-switched fiber laser were characterized by a fast-speed InGaAs photodetector, 350 MHz digital oscilloscope (GWINSTEK, GDS-3352), 7.8 GHz spectrum analyzer (Anritsu), power meter (PM100D-S122C), and optical spectrum analyzer (OSA, AQ6317).

4. Result and discussion

In this experiment, a self-starting Q-switched pulse train was realized as the pump power was raised above the threshold of 98 mW. The output pulse train of the laser was presented for three different pump powers of 98, 121 and 144 mW as shown in Figs. 4(a,b and c), respectively. The pulse train has a peak-to-peak spacing (or pulse period) of 26.75, 22.53 and 20.16 μs, which corresponds to a repetition rate of 37.37, 44.38 and 49.6 kHz, respectively. The pulse period reduces with the pump power due to the Q-switching effect, which is dependent on the saturation of the SA. An increase of pump intensity improves the gain in the cavity and thus it saturates the SA within a shorter time. This leads to faster bleaching of the GNPs SA, resulting in the reduction of the pulse period. This is a typical trend for a passively Q-switched lasers.

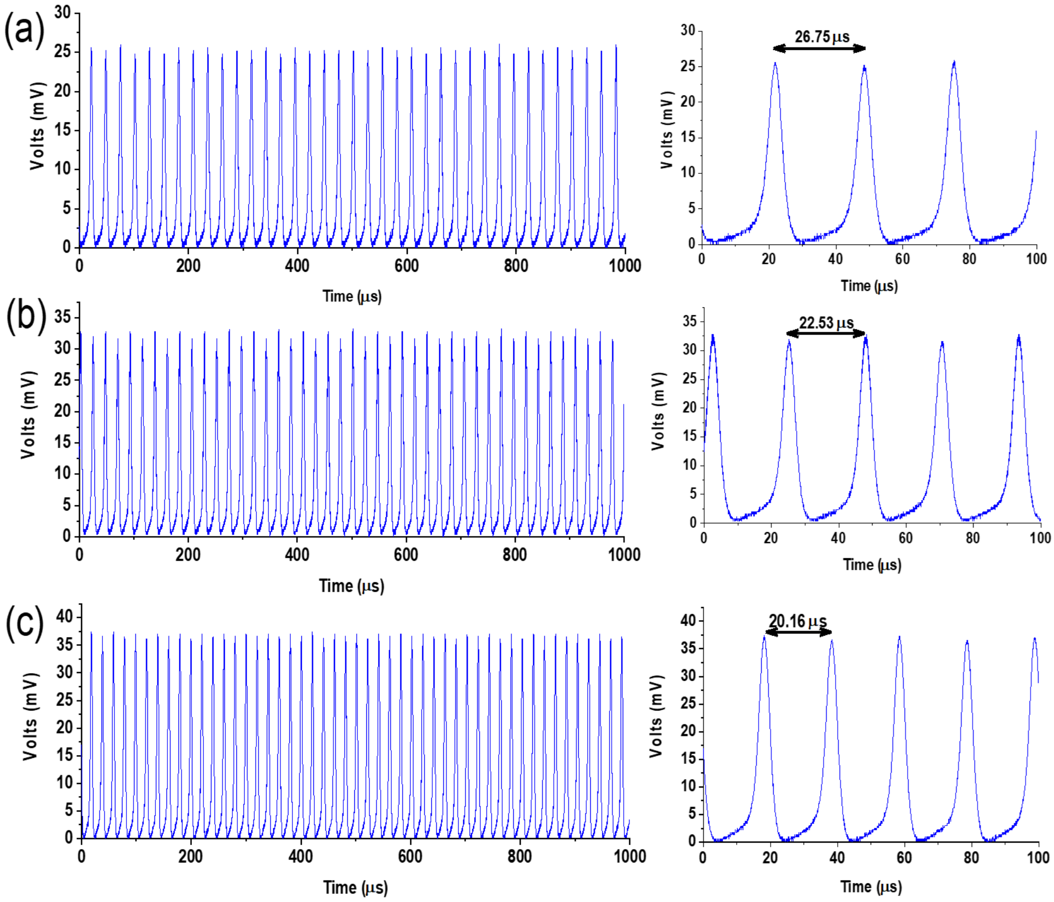

FIG. 4. The pulse train of the Q-switched NDFL with AuNPs PVA film-based SA at three different pump powers of (a) 98 mW; (b) 121 mW and (c) 144 mW

Figure 5(a) displays the typical output spectral characteristic of the Q-switched NDFL at the pump power of 98 mW. As shown in the figure, the central wavelength of the Q-switched operation is at approximately 1089 nm which is due to Nd ions transition from $^4F_{3/2}$ to $^4F_{11/2}$ in four level laser system. Fig. 5(b) shows the RF spectrum of the pulse train at 144 mW pump power. The fundamental frequency was recorded at 49.6 kHz with a SNR of 50 dB, indicating the stability of the Q-switched laser. As the pump power was increased, the rise time and fall time of the Q-switched pulse become concurrently shorter [21] and this leads to the increase of repetition rate. As shown in Fig. 5(c), the repetition rate varied from 37.37 to 49.60 kHz and the pulse width changed from 4.82 to 3.84 μs as the applied pump power increased from 98 to 144 mW. However, the pulse train was unstable when the applied pump power was greater than 144 mW. This is most probably due to the rapid bleaching of the AuNPs SA under the high pump power. As shown in Fig. 5(d), the variation of average output power, single pulse energy and peak power against the pump power shows a generally rising trend. The maximum output power, pulse energy and peak power was achieved at 0.52 mW, 10.48 nJ and 2.73 mW at the highest input pump power of 144 mW. It is worthy to note that the GNP SA could also be used to generate mode-locked pulses operating in the picosecond regime. However, a slight modification of the NDFL cavity is required to enhance the nonlinear effect as well as to balance the group velocity dispersion.

5. Conclusion

A Q-switched laser has been successfully shown in NDFL cavity using the newly developed GNPs PVA thin film as a SA device. The Q-switched pulses were successfully produced, and they operate at central wavelength of 1089 nm with maximum repetition rate of 49.6 kHz. The minimum pulse width, maximum pulse energy and maximum peak power of the Q-switched NDFL were obtained at about 3.84 μs, 10 nJ and 2.75 mW respectively. The experimental results suggest that GNPs are a favorable material for Q-switching application in 1-micron region.

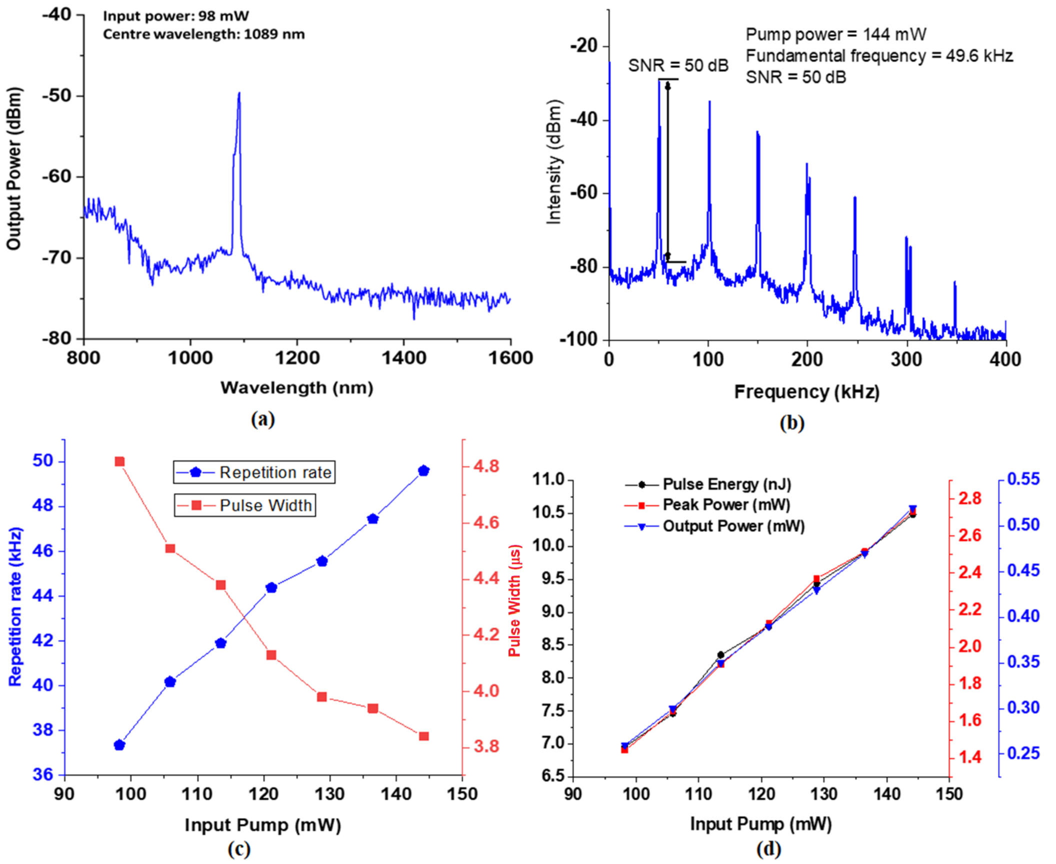

FIG. 5. The output pulse characteristics (a) Optical wavelength spectrum (b) RF spectrum (c) repetition rate and pulse width versus pump power and (d) output power, pulse energy and peak power against pump power

References

[1] Wang X., Cui Y., et al. Recent advances in the functional 2D photonic and optoelectronic devices. *Advanced Optical Materials*, 2019, **7**, 1801274.

[2] Yefet S., Pe'er A. A review of cavity design for Kerr lens mode-locked solid-state lasers. *Applied Sciences*, 2013, **3**, P. 694–724.

[3] Fermann M.E., Hartl I. Ultrafast fiber laser technology. *IEEE J. of Selected Topics in Quantum Electronics*, 2009, **15**, P. 191–206.

[4] Jeon M.-Y., Lee H.K., et al. Harmonically mode-locked fiber laser with an acousto-optic modulator in a Sagnac loop and Faraday rotating mirror cavity. *Optics Communications*, 1998, **149**, P. 312–316.

[5] Wang X.-D., Luo Z.-C., et al. Microfiber-based gold nanorods as saturable absorber for femtosecond pulse generation in a fiber laser. *Applied Physics Letters*, 2014, **105**, 161107.

[6] Li X., Wu K., et al. Single-wall carbon nanotubes and graphene oxide-based saturable absorbers for low phase noise mode-locked fiber lasers. *Scientific Reports*, 2016, **6**, 25266.

[7] Luo Z.-C., Liu M., et al. 2 GHz passively harmonic mode-locked fiber laser by a microfiber-based topological insulator saturable absorber. *Optics letters*, 2013, **38**, P. 5212–5215.

[8] Haris H., Harun S., et al. Passively Q-switched Erbium-doped and Ytterbium-doped fibre lasers with topological insulator bismuth selenide (Bi_2Se_3) as saturable absorber. *Optics & Laser Technology*, 2017, **88**, P. 121–127.

[9] Xia H., Li H., et al. Ultrafast erbium-doped fiber laser mode-locked by a CVD-grown molybdenum disulfide (MoS 2) saturable absorber. *Optics Express*, 2014, **22**, P. 17341–17348.

[10] Yan P., Liu A., et al. Passively mode-locked fiber laser by a cell-type WS 2 nanosheets saturable absorber. *Scientific Reports*, 2015, **5**, 12587.

[11] Niu K., Sun R., et al Passively mode-locked Er-doped fiber laser based on SnS 2 nanosheets as a saturable absorber. *Photonics Research*, 2018, **6**, P. 72–76.

[12] Zhang H., Ma P., et al. Palladium selenide as a broadband saturable absorber for ultra-fast photonics. *Nanophotonics*, 2020, **9** (8), P. 2557–2567.

[13] Sobon G. Mode-locking of fiber lasers using novel two-dimensional nanomaterials: graphene and topological insulators. *Photonics Research*, 2015, **3**, P. A56–A63.

[14] Niu K., Chen Q., et al. Passively Q-switched erbium-doped fiber laser based on SnS 2 saturable absorber. *Optical Materials Express*, 2017, **7**, P. 3934–3943.

[15] Gurudas U., Brooks E., et al. Saturable and reverse saturable absorption in silver nanodots at 532 nm using picosecond laser pulses. *J. of Applied Physics*, 2008, **104**, 073107.

[16] Kang Z., Xu Y., et al. Passively mode-locking induced by gold nanorods in erbium-doped fiber lasers. *Applied Physics Letters*, 2013, **103**, 041105.

[17] Jiang T., Xu Y., et al Passively Q-switching induced by gold nanocrystals. *Applied Physics Letters*, 2012, **101**, 151122.

[18] Kang Z., Guo X., et al. Gold nanorods as saturable absorbers for all-fiber passively Q-switched erbium-doped fiber laser. *Optical Materials Express*, 2013, **3**, P. 1986–1991.

[19] Muhammad A., Ahmad M., et al. Q-switching pulse operation in 1.5-μm region using copper nanoparticles as saturable absorber. *Chinese Phys. Lett.*, 2017, **34**, 034205.

[20] Ahmad M., Muhammad A., et al. Gold nanoparticle based saturable absorber for Q-switching in 1.5 μm laser application. *Laser Phys.*, 2017, **27**, 115101.

[21] Chen Y., Zhao C., et al. Large energy, wavelength widely tunable, topological insulator Q-switched erbium-doped fiber laser. *IEEE J. of Selected Topics in Quantum Electronics*, 2013, **20**, P. 315–322.

Submitted 2 December 2021; revised 12 December 2021; accepted 13 December 2021

Information about the authors:

Ahmad Haziq Aiman Rosol – Department of Electrical Engineering, University of Malaya, 50603 Kuala Lumpur, Malaysia; Department of Engineering, Faculty of Advanced Technology and Multidiscipline, Airlangga University, Surabaya, Indonesia; haziqaiman1992@gmail.com

Kaharudin Dimyati – Department of Electrical Engineering, University of Malaya, 50603 Kuala Lumpur, Malaysia; Department of Engineering, Faculty of Advanced Technology and Multidiscipline, Airlangga University, Surabaya, Indonesia; kaharudin@um.edu.my

Nur Farhanah Zulkipli – Department of Physics, Faculty of Science and Technology, Airlangga University, Surabaya, Indonesia; nurfarhanahzulkipli@yahoo.com

Retno Apsari – Department of Physics, Faculty of Science and Technology, Airlangga University, Surabaya, Indonesia; retna-a@fst.unair.ac.id

Moh Yasin – Department of Physics, Faculty of Science and Technology, Airlangga University, Surabaya, Indonesia; yasin@fst.unair.ac.id

Sulaiman Wadi Harun – Department of Electrical Engineering, University of Malaya, 50603 Kuala Lumpur, Malaysia; swharun@um.edu.my

Conflict of interest: the authors declare no conflict of interest.

NANOSYSTEMS:
PHYSICS, CHEMISTRY, MATHEMATICS

Rai R.K., Botet R.S. *Nanosystems:*
Phys. Chem. Math., 2022, **13** (1), 56–61.
http://nanojournal.ifmo.ru
DOI 10.17586/2220-8054-2022-13-1-56-61

Original article

Near-field optical patterns of dielectric nanoparticles deposited on a metallic surface

Rakesh K. Rai[1,a], Robert S. Botet[2,b]

[1]B. R. A. Bihar University, Muzaffarpur, India
[2]Université Paris-Saclay, Orsay, France

[a]rakesh2273@gmail.com, [b]robert.botet@u-psud.fr

Corresponding author: Rakesh K. Rai, rakesh2273@gmail.com

PACS 78.67.Sc, 78.67.Bf

ABSTRACT Spatial structures of electromagnetic near-fields generated by plasmonic resonances are studied through numerical simulations. Resonances can appear in silver nanoplates onto which nanoparticles of various shapes are deposited. For forthcoming biophysical applications, nanoparticles are considered here as irregular aggregates of grains made of DNA material. The Discrete Dipole Approximation technique is used to calculate the electromagnetic field profiles. In certain controlled physical situations, the plasmonic pattern appears to be the glowing anti-shadow of the deposited nanoparticle, and such a pattern locally produces strong increase in the electromagnetic fields. Even when the nanoparticle size is much smaller than the wavelength, fine (sub-wavelength) details of the anti-shadow are directly related to the shape of the nanoparticle. These observations should result in a better understanding of the Surface-Enhanced Raman Scattering process and an improvement in nanocharacterization techniques.

KEYWORDS light scattering, discrete dipole approximation, DNA materials, nanoparticles

FOR CITATION Rai R.K., Botet R.S. Near-field optical patterns of dielectric nanoparticles deposited on a metallic surface. *Nanosystems: Phys. Chem. Math.*, 2022, **13** (1), 56–61.

1. Introduction

Recent interest in the study of local electromagnetic fields near nanoobjects resulted from new developments in nanofabrication [1–3] and nanocharacterization techniques [1, 4] along with near-field scanning microscope improvements [5]. It is now clear that nanostructure shapes affect the various optical properties, hence the need to precisely study the scattering properties of non-spherical nanoparticles (NPs) in relation to their possible irregular shapes.

Electromagnetic fields near to and far from the scattering object may exhibit very different spatial distributions as well as magnitudes, even if both fields are linked together. In particular, due to coherence effect and/or plasmon oscillations, the field inside and near the nanoparticles (NPs) is often locally enhanced in comparison to the incident field. For example, Raman intensity scattered from pyridine adsorbed onto the roughened surface of noble metal (Ag, Cu or Au), is greatly enhanced [6, 7]. This Surface Enhanced Raman Spectroscopy (SERS) is essentially explained by plasmon resonance coupled to a correlated nanoscale roughness of the metallic surface. Roughness can result either of electrochemical treatment from a smooth metallic surface [6, 7] or from metallic NPs deposition on a smooth metallic surface [8, 9].

Particle detection requires EM scattering spots as intense as possible, whereas particle characterization calls for shape recognition from the observed EM scattering pattern. In this context, a novel research topic is the formation of intense sub-diffraction limited-field localization region – the photonic nanojet – in the shadow region (forward direction) of particular dielectric nanoparticles [10]. Such a nanojet depends strongly on the shape of the particle. However, this approach is, for the moment, restricted to particles made of homogeneous material with very simple shapes [11].

An efficient and versatile tool to calculate electromagnetic near-fields is the Discrete Dipole Approximation (DDA), in which the target under investigation is represented by an arrangement of identical small polarizable points (dipoles) on nodes of a simple cubic lattice, and covering the target geometry [12, 13]. The most popular corresponding numerical code is generically named: DDSCAT, and is available on Draine's website [14]. In the version DDSCAT 7.3, the electric field intensity near the scattering particles and inside it, is calculated for any arbitrary particle shape made of any dielectric material. This free software provides a valuable tool to study the distribution of the scattered electric field in the space near the particle. Hereafter, using the DDSCAT 7.3 code, we compute the electric field distribution near and inside Nps of different shapes but of same volume and made of the same dielectric material. That way, all the Nps have the same equivalent radius (that is the radius of the sphere of same volume), and only their shapes are changed. We focus our discussion on the 'electric enhancement factor', $Q = |E_{loc}/E_{inc}|^2$, here defined as the ratio between the intensity of the local scattered electric field, E_{loc}, and the intensity of the incident field, E_{inc}. For the small (*i.e.* size parameter $\ll 1$) NPs, the enhancement factor is proportional to the squared polarizability, α^2, with $\alpha \propto (\epsilon_p - 1)/(\epsilon_p + 2)$ and ϵ_p is the dielectric constant of the particle. The largest values of Q are obtained close to the Fröhlich resonance frequencies for which the dielectric constant $\epsilon_p \simeq -2$ [15]. In this case, the global enhancement factor is proportional to the volume of the small particle, then it does not depend on the definite shape of the NP. We will see below that, when the size parameter is of order 1 or larger, the largest values of Q depend on the NP shape.

In a previous study, it was observed that monodispered polystyrene NPs deposited on gold nanoplates could be detected by surface plasmon resonance [16]. Also, single stranded DNA associated with Ag nanoparticles were detected using silver film as base [17]. The present study consists of theoretical investigation of enhancement in near electric field of single nanoparticle of dielectric material aggregates in different shapes. We consider here two kinds of NPs, either isolated or deposited on a silver base, and we compare the electromagnetic near-field patterns in both cases. When the particle is deposited on a metallic surface, the enhanced electric field is clearly related to its outline, thus allowing nanocharacterization of the deposited NPs.

2. Method and calculation

Significant increase in the electric near-field is known for fractal metallic NPs over regular surface [18]. Although such very irregular particle shapes are of interest, we consider here two alternative kinds of shapes to keep the discussion simple:

(1) irregular compact-shape particle generated using the Reaction-Limited Particle-Cluster Aggregation model (RPCA) [19]. In this model, the NP is made by successive aggregation of monomers placed randomly on the surface of the aggregate. In a statistical average, the NP is homogeneous and its shape is spherical. (see Fig. 1, left);

(2) particle generated using a combination of Reaction-Limited Cluster-Cluster Aggregation model (RCCA) [20] for the core and Reaction-Limited Particle-Cluster Aggregation model (RPCA) [19] for the mantle, in a volume core/mantle ratio equal to 1:4. In the RCCA model, the particle is made by successive aggregation of clusters randomly sticking together, leading to a fractal core (fractal dimension = 2) of the actual NP. In a second step, the fractal arms of the RCCA cluster are made more dense by RPCA aggregation. This kind of particle is used to model insterstellar particles in an astrophysical context [21]. Details of the building process and examples are given in [22].

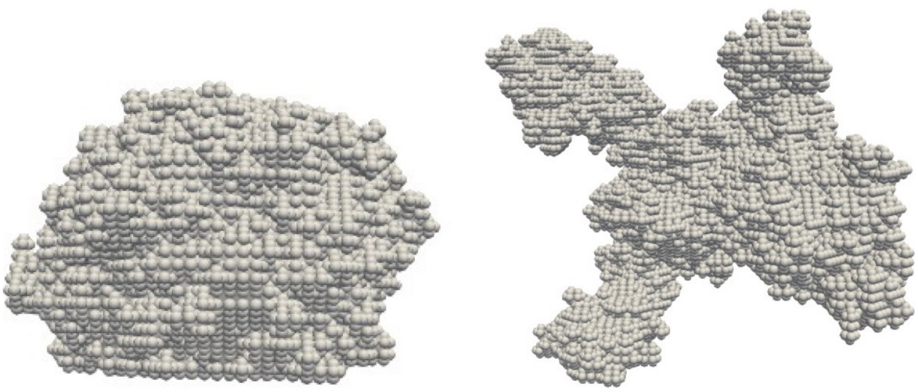

FIG. 1. Irregular compact RPCA and core-mantle particles, used in the calculations (see description in Section 2). On these figures, each small sphere represents an individual electromagnetic dipole used in the DDA method for the calculation of electromagnetic scattering.

Theoretical calculations for light scattering enhancement have been done using: 1) Discrete Dipole Approximation (DDA) method with the Clausius-Mossotti relation corrected by lattice dispersion relation and 3^{rd} order radiative term [23] or: 2) Finite-Difference Time-Domain (FDTD) method apart from Mie theory estimates [8]. The FDTD method is used to calculate local enhancement for different non-spherical shapes for combination of dielectric and noble metals [24].

Dipole discretization required by DDSCAT code is realized using the same number of dipoles for all the particles. The values of the refractive index depend on the material (here, DNA molecule or bulk silver) and they are taken from standard available data. The wavelength of the incident light is fixed here to the value 0.354 μm because it is close to a Frölich frequency for silver.

3. Results and discussion

3.1. Isolated DNA material aggregates

The refractive index of aggregates of DNA materials is $1.64+i1.47\times10^{-5}$ at the incident electromagnetic wavelength 0.354 μm. The electromagnetic wave propagates along the x-direction (see Figs. 2 and 3). Such water soluble DNA material was allowed to be deposited on the nickel surface to form DNA film and then refractive index of the film of this DNA material was determined [25]. We use here this refractive index in the calculations.

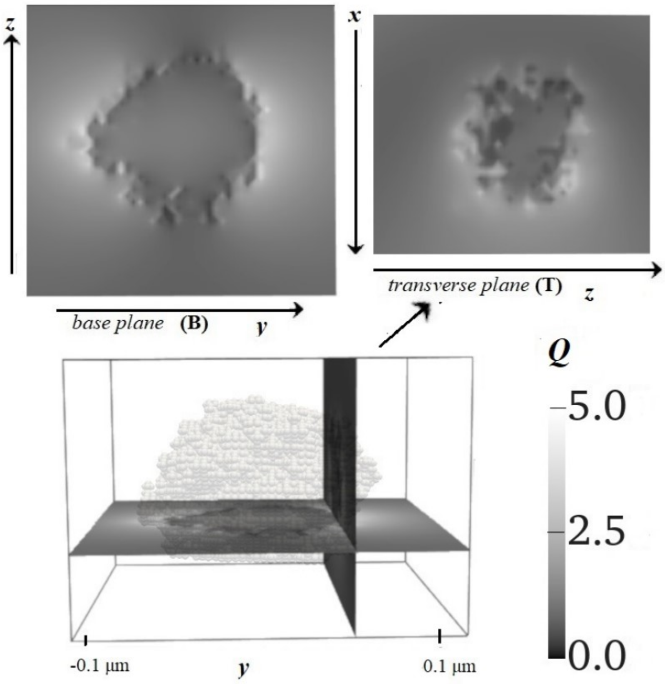

FIG. 2. Distribution of the local electric enhancement factor ($Q = |E_{loc}/E_{inc}|^2$) near and inside an irregular compact aggregate of DNA material. The electromagnetic wave is linearly polarized along the z-direction. The spatial scale in both figures is in μm. The enhanced factor, Q, is of order 5.

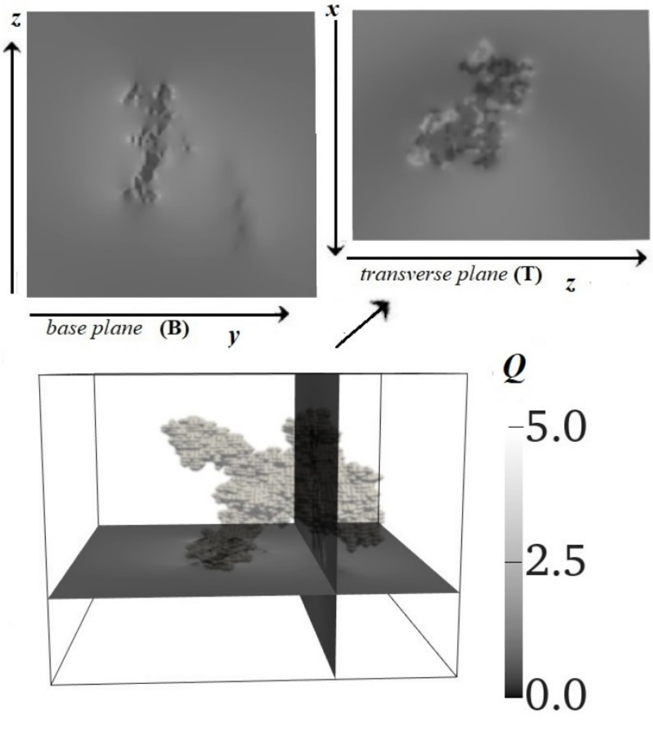

FIG. 3. Distribution of the local electric enhancement factor ($Q = |E_{loc}/E_{inc}|^2$) near and inside of a coated fractal NP of effective radius 0.06μm made of DNA material. The incident electromagnetic wavelength is 0.354 μm and the EM wave propagates along the x-direction. It is polarized along the z-direction. The spatial scale in both figures is in μm. The enhanced factor, Q, is of order 5.

- The isolated irregular compact (RPPA) particle
  On the top of Fig. 2, the electric enhancement factor, $Q = |E_{loc}/E_{inc}|^2$, is plotted inside and around the DNA aggregates' spheres of effective radius $a = 0.06$ μm for the electromagnetic wavelength $\lambda = 0.354$ μm. The value of the size parameter $x = 2\pi a/\lambda$ is then close to 1. The calculations are performed for an electromagnetic wave incident along the x-axis. The total number of dipoles representing the RPPA particle of DNA aggregates is 10012. To show more clearly the enhancement, two planes are considered in which base plane is perpendicular to the incident EM radiation.
- The isolated random coated fractal particle
  The RPCA-RCCA combination (see [22] for details and examples) generating a coated fractal particle made of 9908 dipoles, yields a very different electric field magnitude distribution (see Fig. 3), as it does not show any resemblance with the previous profile seen in Fig. 2. The values of the enhancement factor, Q are nearly the same. It is clear here that the intensity distribution depends on the shape of the particle.

3.2. Nanoparticles of DNA material deposited on a silver substrate

We now consider the same two particles as in Fig. 1 deposited on a silver base. The DDSCAT calculations are considerably heavier than the case of a free particle because we have to manage the electromagnetic response of the whole silver substrate. Therefore, for this part of the study, we placed the same DNA material NPs as before on the silver nano-plate of dimensions $300 \times 300 \times 50$ nm. This silver nanoplate is represented by $66 \times 66 \times 11$ (47916) dipoles. The graphical results are shown on Figs. 4 and 5.

Some important conclusions can be drawn from these profiles:

- Particles deposited on silver substrate exhibit a much larger electric enhancement of the near-field electric intensity compared to the case of the isolated particles. The mean value of this enhancement reaches a factor $\simeq 90$ for the particles in this case.
- The electric field pattern of the dielectric particle deposited on the silver substrate exhibits a glowing anti-shadow in the near-field region along the forward direction (Fig. 4), instead of the ordinary dark shadow as it is the case when there is no silver base. This anti-shadow is the result of plasmon resonance in the metallic base in the vicinity of the NP.

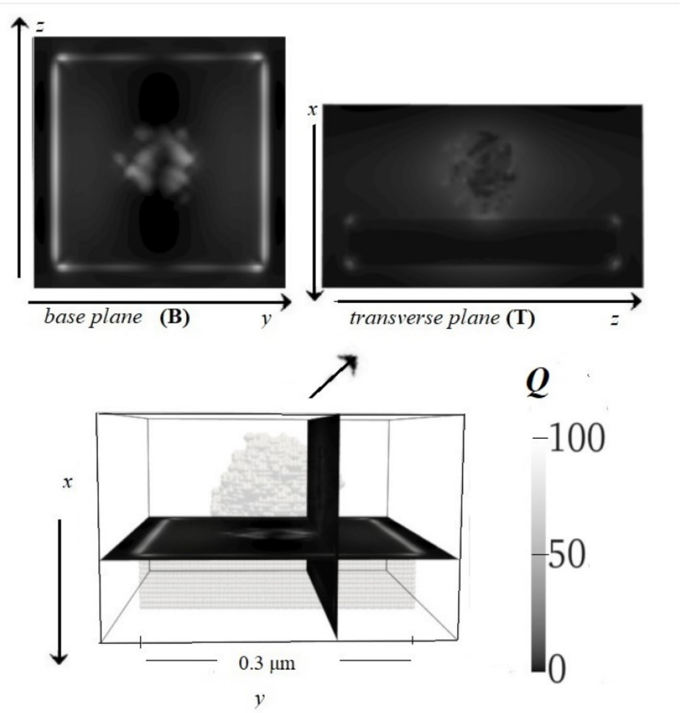

FIG. 4. Distribution of the local electric enhancement factor, ($Q = |E_{loc}/E_{inc}|^2$), for an irregular compact NP made of DNA material on a silver base. The glowing 'anti-shadow' appears as the enhanced brightness in the shadow position (that is near-field in the forward scattering direction) . Unlike the case of the isolated particles, the electric field intensity of the anti-shadow is significantly larger (more than 90 times larger).

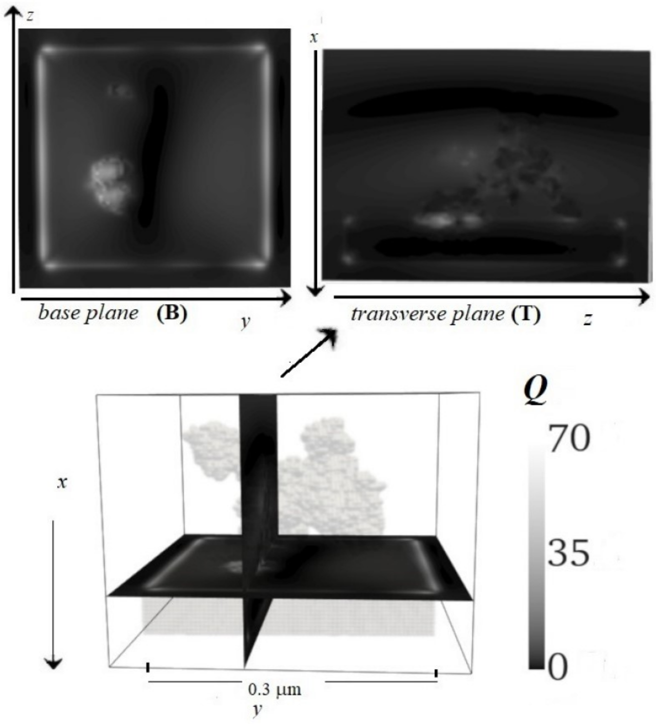

FIG. 5. Distribution of the local electric enhancement factor, ($Q = |E_{loc}/E_{inc}|^2$), for an irregular coated-fractal NP of DNA material on the silver base. Similarly to the irregular compact NP (Fig. 4), the electric field intensity of the anti-shadow part is here more than 70 times larger than the intensity of the incident field.

- Anti-shadow pattern is present for both the irregular compact and the coated fractal NP, but their geometrical structures are different. Thus, one can conclude that the shape of the anti-shadow pattern depends on the geometrical shape of the NPs.

These conclusions may be important for applications, either for nanocharacterization of NPs or for NPs detection. Indeed, using a simple protocol, definite information about the morphology of a single NP can be deduced from experimental analysis of its anti-shadow pattern, when the particle is deposited on a silver base at a wavelength close to Frölich frequency. Let us be more precise. We do not know any way to inverse mathematically the near-field pattern of the electromagnetic field scattered by a single particle to rebuild its exact geometrical shape. This fundamental flaw is shared with other domains of NP characterization, e.g. Small-Angle X-ray Scattering (SAXS) analysis [26]. However, the same technical method as in SAXS can be used, that is:

(1) generate various possible models of particles (e.g. through computer simulations);
(2) calculate the near-field anti-shadow for particles of each model deposited on a silver base (we showed that DDSCAT numerical code can be used efficiently to complete this task);
(3) experimentally measure the anti-shadow patterns generated by real NPs adsorbed onto the silver substrate and compare them to the models. The experimental part of the latter task could be done using Scanning Near-field Optical Microscope (SNOM) (e.g. [27]).

We have seen that two particles of different shapes exhibited very different anti-shadow patterns, then the protocol proposed above is expected to be sensitive to the particle shape.

4. Conclusion

In this article, we presented numerical calculations of light scattering by nanometer-sized dielectric particles deposited on a metal substrate, and we showed that the definite shape of the particle has a strong effect in the resulting near-field profile at a sub-wavelength scale. Actually, different shapes were seen to leave their own imprints on a silver base as particular anti-shadows, that is of strongly enhanced (glowing) local fields generated by surface plasmons. Therefore, the silver nanoplate serves as a base to detect enhancement in the local EM field around the dielectric material. Characterization of NP shapes can, in principle, be extracted from such anti-shadow images, even if only by comparing Scanning Near-field Optical Microscope images with anti-shadows calculated from relevant particle models. If the size of the NP is too small to use such scanning technique, the very large enhancement of the field intensity allows one to consider direct detection of the glowing anti-shadow as the signature of the NP deposited on the silver base.

References

[1] Pana X., Medina-Ramirez I., Mernaugh R., Liu J. Nanocharacterization and bactericidal performance of silver modified titania photocatalyst. *Colloids and Surfaces B: Biointerfaces*, 2010, **77**, P. 82–89.

[2] Gates B.D., Xu Q., et al. New approaches to nanofabrication: molding, printing, and other techniques. *Chem. Rev.*, 2005, **105**, P. 1171–1196.

[3] Biswas A., Bayer I.S., et al. Advances in top-down and bottom-up surface nanofabrication: techniques, applications & future prospects. *Advances in Colloid and Interface Science*, 2012, **170**, P. 2–27.

[4] Gillet J.-N., Meunier M. General Equation for Size Nanocharacterization of the Core-Shell Nanoparticles by X-ray Photoelectron Spectroscopy. *J. Phys. Chem. B*, 2005, **109**, P. 8733–8737.

[5] Betzig E., Trautman J.K. Near-Field Optics: Microscopy, Spectroscopy, and Surface Modification Beyond the Diffraction Limit. *Science*, 1992, **257**, P. 189–195.

[6] Jeanmaire D.L., Van Duyne R.P. Surface raman spectroelectrochemistry: Part I. Heterocyclic, aromatic, and aliphatic amines adsorbed on the anodized silver electrode. *J. of Electroanalytical Chemistry and Interfacial Electrochemistry*, 1977, **84**, P. 1–20.

[7] Albrecht M.G., Creighton J.A. Anomalously intense Raman spectra of pyridine at a silver electrode. *J. Am. Chem. Soc.*, 1977, **99**, P. 5215–5217.

[8] Schatz G.C., Young M.A., Van Duyne R.P. Electromagnetic mechanism of SERS. In: Kneipp K., Moskovits M. & Kneipp H.(Eds.) Surface-Enhanced Raman Scattering – Physics and Applications. Topics Apl. Phys., 2006, **103**, P. 19–46.

[9] Stiles P.L., Dieringer J.A., Shah N.C., Van Duyne R.P. Surface-enhanced Raman spectroscopy. *Annu. Rev. Anal. Chem.*, 2008, **1**, P. 601–626.

[10] Zhu J., Goddard L.L. All-dielectric concentration of electromagnetic fields at the nanoscale: the role of photonic nanojets. *Nanoscale Adv.*, 2019, **1**, P. 4615–4643.

[11] Jia Y., Li R., Zhuanga W., Liang J. Photonic nanojet generated by a spheroidal particle illuminated by a vector Bessel beam. *Results in Optics*, 2021, **4**, 100106.

[12] Purcell E.M., Pennypacker C.R. Scattering and absorption of light by nonspherical dielectric grains. *Astrophys. J.*, 1973, **186**, P. 705–714.

[13] Draine B.T. The discrete-dipole approximation and its application to interstellar graphite grains. *Astrophys. J.*, 1988, **333**, P. 848–872.

[14] Draine B.T. The Discrete Dipole Approximation for Scattering and Absorption of Light by Irregular Particles. URL: https://www.astro.princeton.edu/˜draine/DDSCAT.7.3.html.

[15] Anderson M.S. Enhanced infrared absorption with dielectric nanoparticles. *Appl. Phys. Lett.*, 2003, **83**, P. 2964–2966.

[16] Zybin A., Kuritsyn Y.A., et al. Real-time Detection of Single Immobilized Nanoparticles by Surface Plasmon Resonance Imaging. *Plasmonics*, 2009, **5** (1), P. 31–35.

[17] Braun G., Lee S.J., et al. Surface-Enhanced Raman Spectroscopy for DNA Detection by Nanoparticle Assembly onto Smooth Metal Films. *J. Am. Chem. Soc.*, 2007, **129**, P. 6378–6379.

[18] Shalaev V.M., Botet R., Mercer J., Stechel E.B. Optical properties of self-affine thin films. *Phys. Rev. B*, 1996, **54**, P. 8235–8242.

[19] Jullien R., Botet R. *Aggregation and Fractal Aggregates*. World Scientific Publishing, Singapore, 1987, 130 p.

[20] Meakin P., Jullien R. The effects of restructuring on the geometry of clusters formed by diffusion-limited, ballistic, and reaction-limited cluster-cluster aggregation. *J. Chem. Phys.*, 1988, **89**, P. 246–250.

[21] Rai R.K., Rastogi S., Botet R. Effect of grain shape on extinction using effective medium theory. *Asian J. of Physics*, 2015, **24**, P. 1097–1103.

[22] Rai R.K., Botet R.S. *Monthly Notices of the Royal Astron. Society*, 2014, **444**, P. 303–312.

[23] Draine B.T., Goodman J. Beyond Clausius-Mossotti – Wave propagation on a polarizable point lattice and the discrete dipole approximation. *Astrophys. J.*, 1993, **405**, P. 685–697.

[24] Abdulhalim I. Coupling configurations between extended surface electromagnetic waves and localized surface plasmons for ultrahigh field enhancement. *Nanophotonics*, 2018, **7** (12), P. 1891–1916.

[25] Inagaki T., Hamm R.N., Arakawa E.T. Optical and dielectric properties of DNA in the extreme ultraviolet, *The J. of Chemical Physics*, 1974, **61**, P. 4246–4250.

[26] Pedersen J.S. Analysis of small-angle scattering data from colloids and polymer solutions: modeling and least-squares fitting. *Advances in Colloid and Interface Science*, 1997, **70**, P. 171–210.

[27] Oshikane Y., Kataoka T., et al. Observation of nanostructure by scanning near-field optical microscope with small sphere probe. *Science and Technology of Advanced Materials*, 2007, **8**, P. 181–185.

Submitted 11 December 2021; revised 22 December 2021; accepted 23 December 2021

Information about the authors:

Rakesh K. Rai – RLSY College (Bettiah), B. R. A. Bihar University, Muzaffarpur, India; ORCID 0000-0003-4368-5276; rakesh2273@gmail.com

Robert S. Botet – Université Paris-Saclay, Laboratoire de Physique des Solides, CNRS UMR8502 , 91405 Orsay, France; ORCID 0000-0002-8515-111X; robert.botet@u-psud.fr

Conflict of interest: the authors declare no conflict of interest.

Availability of data and material: The numerical calculations were performed on PC. The data are available free of charge on request from the authors.

Code availability: To realize this work, we used the softwares: DDSCAT, PARAVIEW and MAYAVI which are freely available.

NANOSYSTEMS:
PHYSICS, CHEMISTRY, MATHEMATICS

Original article

Kuchko A.V., Smirnov A.V. *Nanosystems: Phys. Chem. Math.*, 2022, **13** (1), 62–70.
http://nanojournal.ifmo.ru
DOI 10.17586/2220-8054-2022-13-1-62-70

Iterative method of reconstructing the size distribution function of spherical nanoparticles based on the intensity of the small-angle X-ray scattering including the interference contribution to the intensity

Artem V. Kuchko[a], Alexander V. Smirnov[b]

ITMO University, St. Petersburg, Russia

[a]artemkav@gmail.com, [b]smirnav_2@mail.ru

Corresponding author: Artem V. Kuchko, artemkav@gmail.com

PACS 61.10.Eq, 61.43.Gt, 61.46.+w

ABSTRACT It has been shown that for systems of polydisperse spherical particles the interference distortions of the scattering intensity significantly affect the result of reconstructing the particle size distribution when the volume fraction of the scattering substance is higher than 10 %. We have developed an iterative method that reconstructs the size distribution function from the small-angle X-ray scattering intensity with interference distortions. The efficiency of this method is confirmed based on simulated scattering intensities and experimentally measured intensities of samples with a volume fraction of a scattering substance up to 40 %.

KEYWORDS small-angle X-ray scattering, polydisperse nanoparticle system, interference contribution, volume fractions distribution, statistical regularization method, iterative methods

FOR CITATION Kuchko A.V., Smirnov A.V. Iterative method of reconstructing the size distribution function of spherical nanoparticles based on the intensity of the small-angle X-ray scattering including the interference contribution to the intensity. *Nanosystems: Phys. Chem. Math.*, 2022, **13** (1), 62–70.

1. Introduction

Materials composed of particles whose sizes range from 1 to 100 nm are widely used in the production of new materials [1–5]. One method that provides direct information about the size, morphology, and structure of nanoparticles is small-angle X-ray scattering (SAXS) [6]. When it comes to particles of a particular shape, this method makes it possible to determine the particle size distribution [7, 8]. One of the significant limitations of the SAXS method is the initial section intensity distortion caused by interference from the individual particles [6, 9].

In most cases, the task of reconstructing a size distribution function (SDF) based on the scattering intensity is resolved without taking into account interference contributions [10–14]. The authors have previously developed a statistical regularization method (SRM) [8] representing the Bayesian approach to reconstructing the volume fraction distribution function (VFDF), which is a variant of SDF. This method is also used for highly sparse systems, since in such systems interference contributions to the scattering intensity are extremely negligible. Sparse systems are those systems whose volume fraction φ of the scattering substance does not exceed several percent. Such systems include, for example, powder suspension in a liquid, or a highly diluted powder component as a constituent of a composite material [15].

Nevertheless, when directly examining powder samples, the volume fraction φ of the scattering substance can represent a significant value. For zirconium dioxide as an example, the density of the powder substance itself equals $\rho_0 \cong 6.0$ g/cm^3 [16], while the bulk density of the powder sample can amount to $\rho \cong (1.2...2.5)$ g/cm^3. In such a sample, the volume fraction $\varphi = \rho/\rho_0$ may range from 20 – 40 %. In this case, disregarding the interference contributions in determining the size distribution, as discussed in Section 2, can lead to significant distortions in the reconstruction of a distribution function.

Speaking of spherical particles, Pederson [17] made what is possibly the only successful attempt to solve the problem of particle size distribution using the SAXS intensity including interparticle interference contributions. The basis of the solution proposed in that work represents a nonlinear least square method for selecting coefficients in the B-spline distribution function expansion. The approach suggested in [17] employs local monodisperse approximation (LMA), which simplifies calculating scattering intensity in comparison to a more precise method [18], based on the Percus–Yevick approach.

Still, LMA poses constraints on the distribution features of scattering inhomogeneities in the system that is being examined. These constraints, as follows from [17], are not critical for the system in which the values of scattering inhomogeneities change in space slowly enough, as can be seen, for instance, in solid solutions. At the same time, though, the LMA conditions are hardly ever met when investigating less ordered systems – powders, for example.

This paper suggests an alternative approach to the task of SDF reconstruction based on the intensity with regard to interference contributions. This approach is based on employing an analytical expression of the intensity of SAXS [18] for the system comprised of spherical particles of different sizes. Such expression can be found in the Percus–Yevick approach. Within the framework of the suggested approach, we propose an iterative procedure that simultaneously reconstructs both the volume fraction distribution function of radii of gyration and the corresponding structure factor.

In Section 2, we evaluate the degree of the distortion of the VFDF – reconstructed disregarding interference contributions – dependent on the φ volume fraction of the scattering substance for the typical model distribution, and we describe the proposed iterative procedure for reconstructing the VFDF based on the SAXS intensity. In Section 3, we explain the necessary preliminary procedure for processing the experimental SAXS curves of powder samples. In Section 4, we present the results of applying the iterative procedure for reconstructing VFDF from SAXS intensities calculated based on the model VFDF for different values of φ. In this section,we also present the results of applying the iterative procedure to the experimental intensities of powders composed of ZrO_2+Y_2O_3 with different component ratios.

2. Theory

2.1. Errors of reconstructing distribution function,disregarding interference distortions of the scattering intensity

Using a model distribution as an example, we shall estimate the error in reconstructing the particle size distribution when the reconstruction procedure disregards interference distortions of the scattering intensity. We have chosen the following form for the volume fraction distribution function as model one:

$$f(R_g) = R_g^{k-1} \frac{e^{-R_g/\theta}}{\theta^k \Gamma(k)}, \tag{1}$$

in which R_g is radius of gyration, $k = 6$, $\theta = 2.5$, and $\Gamma(k)$ is the Euler gamma function. Similar distributions can, for example, be observed using electron microscopy on zirconium dioxide nanopowder obtained under hydrothermal conditions [14, 19, 20]. The distribution (1) coincides with the distribution used in the development of SRM [8].

For a chaotic system of spherical particles with a hard sphere interaction potential and a discrete set of radii, formulae for calculating the intensity $I(q)$ as a function of the scattering vector modulus q for a given value φ are described in [18]. Formulae for calculating the scattering intensity for a continuous SDF, obtained by generalizing from those derived in [18] are given in the Appendix.

For distribution (1), assuming that scattering density of the particle material equals 1, the intensity was calculated for volume fraction values $\varphi = 10^{-6}$, and values of from 0.05 and 0.4 at 0.05 intervals (see the first row of Table 1). Instances of the intensity graphs are given in Fig. 1(a). There is an obvious discrepancy between the scattering intensity curves for low values of a scattering vector, where interference contributions are most notable.

TABLE 1. Relative difference (4) between the reconstructed VFDF f_+ and the actual f for different values of the scattering substance volume fraction φ. Functions f_+ were reconstructed disregarding interference contributions.

φ	10^{-6}	0.05	0.1	0.15	0.2	0.25	0.3	0.35	0.4
$\delta\,(f, f_+)$, %	0.85	9.6	20	32	44	57	71	84	98

To characterize the contribution of interparticle interference in the scattering intensity, a structure factor is traditionally introduced. It is defined by the following formula:

$$S(q) = \frac{I(q)}{I_0(q)}. \tag{2}$$

Here, $I_0(q)$ denotes scattering intensity obtained by summing the scattering intensities of the individual particles. For spherical particles whose radii of gyration range between $R_{g\,\min}$ and $R_{g\,\max}$, the intensity total is (see [8]):

$$I_0(q) = \int\limits_{R_{g\,\min}}^{R_{g\,\max}} f\left(R_g\right) \Phi\left(\sqrt{\frac{5}{3}} \cdot q \cdot R_g\right) V\left(\sqrt{\frac{5}{3}} \cdot R_g\right) dR_g. \tag{3}$$

Here, $\Phi(x) = \left(3\dfrac{\sin x - x\cos x}{x^3}\right)^2$ and $V(R) = \dfrac{4}{3}\pi R^3$ is the volume of a sphere of radius R. Fig. 1(b) shows graphs of structure factors that correspond to scattering intensities represented in Fig. 1(a). For the minimal value of $\varphi = 10^{-6}$, the structure factor is practically indistinguishable from 1.

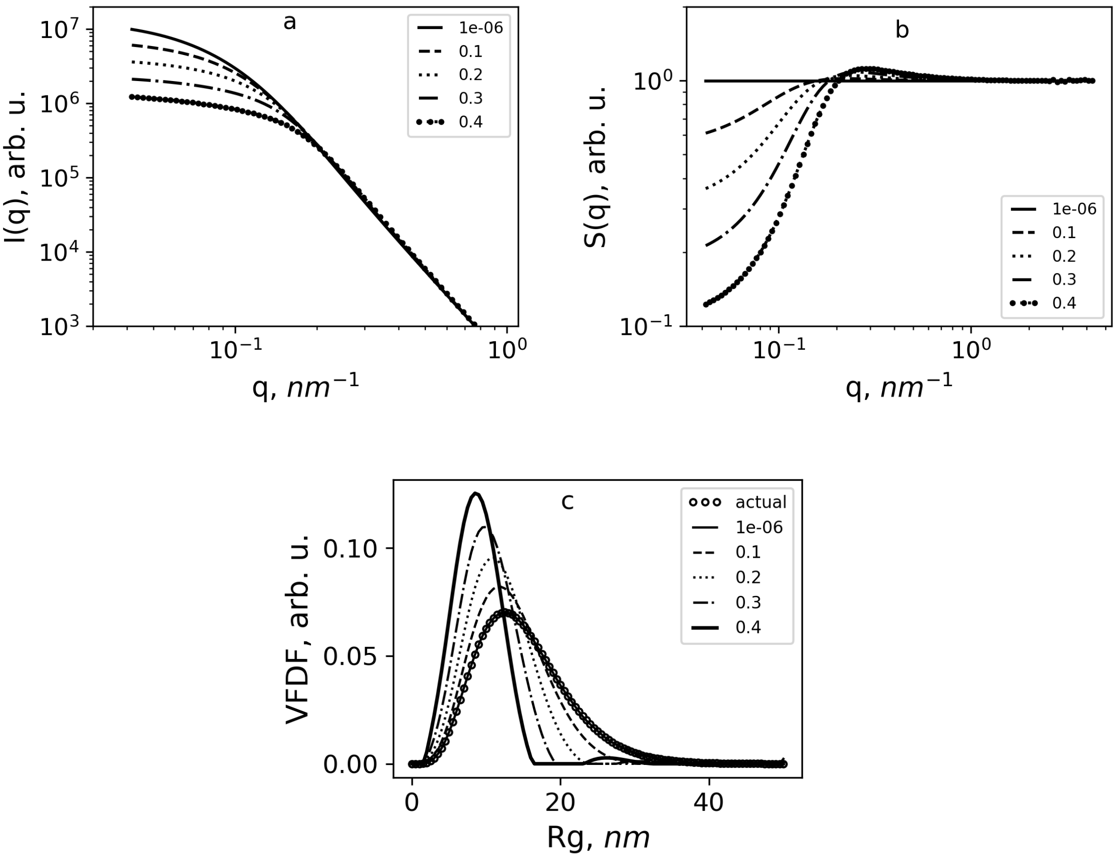

FIG. 1. Analysis results for spherical particle systems with model distribution (1) for different values of φ: a) scattering intensity $I(q)$; b) structure factor $S(q)$; c) actual VFDF and VFDF f_+ reconstructed from intensity $I(q)$, disregarding interference contributions. Values of φ are given in the legend. For easier comparison, the $I(q)$ graphs in Fig. 1(a) were normalized to the same intensity value at the maximum value of the scattering vector modulus

For every scattering intensity value φ without interference contributions, we have used SRM to find the most probable distribution $f_+\left(R_g\right)$. The subscript “+” indicates that negative values in the distributions obtained were substituted by zeros.

Normalized functions f_+ reconstructed from the intensity values in Figure 1a are given in Fig. 1(c). This figure clearly shows that the increase in the scattering substance volume fraction leads to considerable distortions of the reconstructed distribution – to the tapering of the distribution support and to the shift of the maximum to the lower radius of gyration values.

For quantitative comparison between the obtained functions f_+ and the actual distribution function f we use the relative difference:

$$\delta\left(f, f_+\right) = \frac{\|f - f_+\|}{\|f\|}. \tag{4}$$

Here, $\|\ldots\|$ represents the norm of function set by the following formula:

$$\|f\| = \sqrt{\int_{R_{\min}}^{R_{\max}} \left(f\left(R_g\right)\right)^2 dR_g}. \tag{5}$$

Values $\delta\left(f, f_+\right)$ for the function f_+ obtained for different values of φ are given in Table 1. It can be seen that already at the value $\varphi \geq 0.1$ the reconstruction error becomes significant – it represents several tens of percent.

For calculations that include interference contributions to the scattering intensity in a polydisperse spherical particle system, we have devised a script in the Python 3.7 programming language, using libraries numpy, scipy, and matplolib. The script is available at [https://gist.github.com/sp_intens_vrija]. As input data, the procedure takes the normalized particle number distribution function for radii, which is reconstructed together with VFDF.

2.2. Iterative method of reconstructing the distribution function including the interference contributions to the scattering intensity

The graphs in Fig. 1(c) show that as the scattering substance volume fraction grows, the reconstructed distribution function f_+ monotonically changes, but at the same time, the support of the function overlaps to a considerable extent with the support of the actual distribution function (1). It is safe to assume that the structure factor calculated based on f_+ will be similar to the structure factor corresponding to the actual function (1), and the initial intensity "corrected" with the inclusion of the structure factor obtained based on f_+ will be similar to the scattering intensity without interference contributions. What follows is the proposed iterative restoring procedure, based on these considerations.

The distribution $f_+^{(1)}$ obtained by SRM from the initial scattering indicatrix $I_{src}(q)$ is the first approximation for the sought distribution function.

The iterative procedure cycle involves the following steps:

(1) Based on the distribution $f_+^{(i)}$ (where i is the index of current iteration) and the given volume fraction φ of scattering substance, we calculate the scattering intensity $I^{(i)}(q)$ with the interference contributions, as well as the one $I_0^{(i)}(q)$ without these contributions.

(2) We calculate the structure factor:

$$S^{(i)}(q) = \frac{I^{(i)}(q)}{I_0^{(i)}(q)}. \tag{6}$$

(3) We calculate the approximate scattering intensity without interference contributions:

$$I_{iter}^{(i)}(q) = \frac{I_{src}(q)}{S^{(i)}(q)}. \tag{7}$$

(4) Based on $I_{iter}^{(i)}(q)$, we calculate $f_+^{(i+1)}$ using SRM.

It should be emphasized that in the third step of each iteration the numerator of the formula (7) is always the initial scattering indicatrix $I_{src}(q)$.

In the Results section, we will show that for the value of $\varphi = 0.4$, solutions $f_+^{(i)}$ "oscillate" around the actual function f_{src}, but without approaching it. This effect is suppressed by introducing the distribution function intermediate averaging in several subsequent steps. Therefore, for $\varphi > 0.3$, we use a modified iterative procedure, in which after several steps we calculate an average distribution function, which is used as an initial one in the subsequent iterations.

Convergence of the iterative procedure is controlled by a decrease in the relative difference $\delta\left(f_+^{(i-1)}, f_+^{(i)}\right)$ between the results of the two consecutive iterations as the number i of the iterations increases.

Cross-platform application SAXSEV 2.1. [21], which employs a Bayesian approach in reconstructing VFDF, was supplemented with a module that launches the recovery of VFDF in the iterative mode. The last version available at https://github.com/artemus-tech/SAXSEV.

3. Preliminary processing of experimental SAXS curves of powder samples

To test the iterative method, we utilized SAXS curves of powder samples composed of ZrO_2+Y_2O_3 synthesized under hydrothermal conditions [22]. These samples had a wide variety of component ratios: the mass fraction of yttrium oxide varied from 3 to 44 %. They were characterized by a significant difference in the average size of nanoparticles.

For these samples (see example in Fig. 2(a)), the shape of experimental SAXS curves differed noticeably from the theoretical one presented in Fig. 1(a). Firstly, for small values of q, and the measured intensity increases sharply as q decreases. This increase is probably due to the presence of agglomerates of large particles in the sample. Secondly, for large values of q, Porod's Law does not apply because of the presence of intraparticle heterogeneities at the atomic level, since the scattering of these heterogeneities makes a permanent contribution to the intensity [23].

These features complicate the direct application of the described iterative procedure, making the preliminary processing of experimental intensities necessary. We shall discuss this processing on the example of the typical scattering intensity (sample with the yttrium mass fraction of 10 %).

To eliminate a constant contribution for large values of q, classical methodology was used [24]. For large values of q, the main non-oscillating contribution to the scattering intensity behaves in this manner:

$$I(q) = A_0 + \frac{A_1}{q^4}. \tag{8}$$

It follows from this formula that the dependence $I \cdot q^4$ vs. q^4 is close to linear, and the coefficient A_0 is the slope of this dependence. After subtracting the obtained value A_0 from the intensity, we obtain the intensity $I'(q) = I(q) - c_0$, which, for the large values of q, behaves like $\sim q^{-4}$ (Porod's Law). The range in which the linear $I \cdot q^4$ vs. q^4 dependence approximation runs lies between the value q_1, at which deviations from the Porod's Law are still not discernible, and the maximum value q_2 (see Fig. 2(a)).

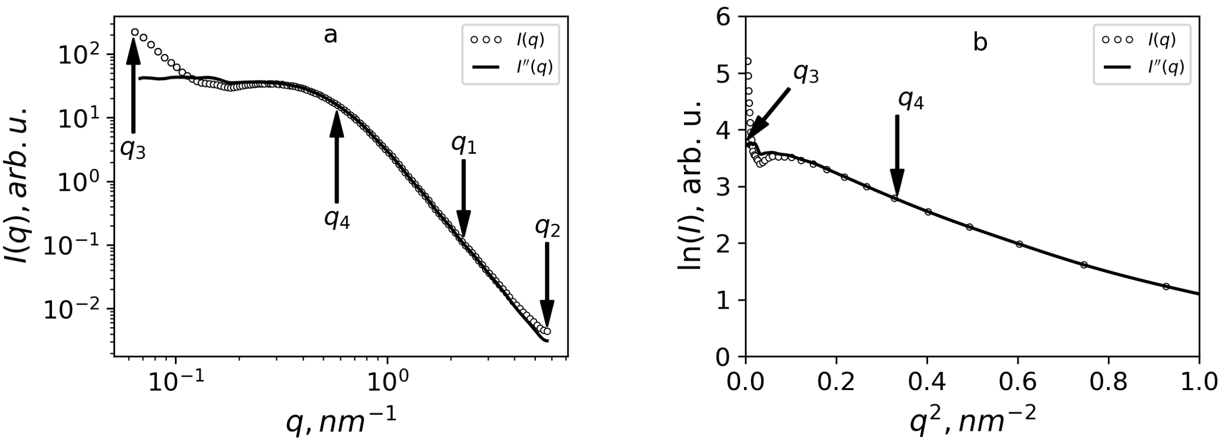

FIG. 2. Experimental intensity $I(q)$ SAXS of the powder sample composed of ZrO_2+Y_2O_3 (mass fraction of yttrium oxide amounts to 10 %) and the intensity $I''(q)$ obtained after preliminary processing: a) Intensities in the whole experimental range; b) Initial section of the graphs $\ln(I)$ vs. q^2. The indicated ranges (q_1, q_2), (q_3, q_4) are used to eliminate contributions of atomic-scale and large-scale inhomogeneities, respectively

In the initial section, intensity $I'(q)$ as well as $I(q)$ rises sharply, and its log-log plot is similar to the linear one. Such behavior gives evidence of a fractal-type distribution of the scattering density in the scale of relatively large sizes corresponding to small values of q. Structure factor for volume fractal looks like this [25]:

$$S_f(q, D, \xi, r_0) = 1 + \frac{D \cdot \Gamma(D-1)}{(qr_0)^D \left[1 + (q\xi)^{-2}\right]^{(D-1)/2}} \sin\left[(D-1)\arctan(q\xi)\right]. \tag{9}$$

On the other hand, when there is no fractal distortion, the scattering intensity logarithm $\ln(I)$ in the initial section (for sufficiently small values of q) is supposed to be a linear function of q^2 [26]. If we denote the intensity without fractal distortion as $I''(q)$, then:

$$\ln(I''(q)) = a + bq^2. \tag{10}$$

Intensity $I'(q)$can be represented as a product of a fractal structure factor (9) and undistorted intensity $I''(q)$: $I'(q) = S_f(q, D, \xi, r_0) \cdot I''(q)$, and its logarithm can be expressed with the formula (10):

$$\ln(I'(q)) = \ln(S_f(q, D, \xi, r_0)) + a + bq^2. \tag{11}$$

To extract $I''(q)$, it is necessary to find optimal parameter values D, ξ, r_0, a, b in the formula (11). These values have been obtained by minimization of the following estimating function:

$$\Delta(D, \xi, r_0, a, b) = \sum_{i=1}^{M} \left[\ln(I'(q_i)) - \left(\ln(SF(q_i, D, \xi, r_0)) + a + bq_i^2\right)\right]^2. \tag{12}$$

Here, the summation is performed on the initial M points in the argument range from the initial value q_3 to q_4, which is an approximate section boundary of the linear $\ln(I)$ dependence of q^2 (see Fig. 2(b)). Using the structure factor (9) with the optimal values for parameters $D^{opt}, \xi^{opt}, r_0^{opt}$, we can finally obtain the undistorted intensity:

$$I''(q) = \frac{I'(q)}{S_f\left(q, D^{opt}, \xi^{opt}, r_0^{opt}\right)}. \tag{13}$$

Figure 2(a) represents the primary experimental intensity $I(q)$ and the reduced intensity $I''(q)$ when the mass fraction of yttrium oxide equals 10 %.

The described preliminary processing procedure was used for all experimental intensities.

4. Results

4.1. Using the iterative procedure for VFDF reconstruction based on the model intensities of SAXS

The iterative procedure described above was tested for VFDF (1) for scattering substance volume fraction $\varphi = 0.1, 0.2, 0.3$, and 0.4. We can see in Fig. 3 for different values of φ the behavior of relative differences in VFDF $\delta\left(f_+^{(i-1)}, f_+^{(i)}\right)$ that were obtained after the $(i-1)$-th and i-th iterations, as well as the relative difference $\delta\left(f_{src}, f_+^{(i)}\right)$ between the actual VFDF and the result of the i-th iteration.

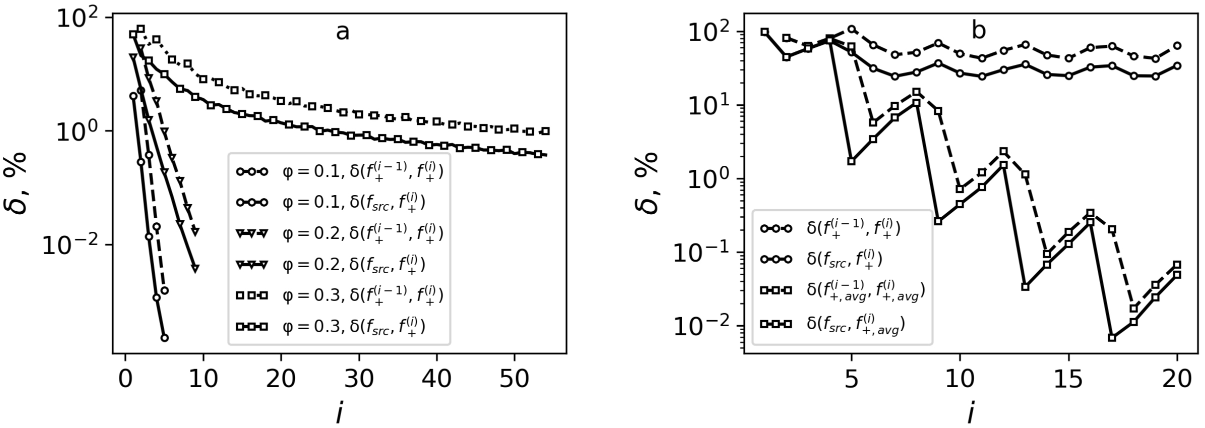

FIG. 3. Dependence of relative VFDF differenceson the number of iterations: a) for $\varphi = 0.1, 0.2, 0.3$ with no intermediate averaging; b) for $\varphi = 0.4$ with no intermediate averaging and with averaging after every fourth iteration following the previous four iterations. VFDFs, obtained using a modified iterative procedure with intermediate averaging, are marked with a subscript "avg"

As it can be seen in Fig. 3(a), for the value $\varphi \leq 0.3$ the iterative procedure converges to the actual distribution function without intermediate averaging. As the number of iterations increases, both relative differences $\delta\left(f_+^{(i-1)}, f_+^{(i)}\right)$ and $\delta\left(f_{src}, f_+^{(i)}\right)$ decrease practically monotonically. If the intermediate averaging is not employed, for the value of $\varphi = 0.4$ (see Fig. 3(b)), as the number of iterations increases, both functions $\delta\left(f_+^{(i-1)}, f_+^{(i)}\right)$ and $\delta\left(f_{src}, f_+^{(i)}\right)$ – oscillate, while their minima do not fall off below 20 %. Intermediate averaging after four consecutive iterations improves the convergence significantly. Fig. 3 also shows that the relative differences between the results of the $(i-1)$-th and the i-th iterations are always larger than the relative difference between the results of the i-th iteration and the actual distribution function.

Table 2 shows the iteration numbers at which the relative differences $\delta\left(f_+^{(i-1)}, f_+^{(i)}\right)$ reach a value less than 1 %; it also shows the corresponding value $\delta\left(f_{src}, f_+^{(i)}\right)$.

TABLE 2. Iteration number i, at which the relative difference $\delta\left(f_+^{(i-1)}, f_+^{(i)}\right)$ diminishes to below 1 %. The last column shows the relative difference between the actual distribution and the result of the i-th iteration.

φ	i	$\delta\left(f_+^{(i-1)}, f_+^{(i)}\right)$, %	$\delta\left(f_{src}, f_+^{(i)}\right)$, %
0.1	3	0.38	0.014
0.2	5	0.96	0.18
0.3	51	0.98	0.42
0.4	3·4+2*	0.094	0.068

*Three complete cycles with intermediate averaging after four iterations + two iterations

4.2. Application of the iterative method for VFDF reconstruction from experimental scattering intensities

Since the volume substance fraction in experimental samples is close to $\varphi = 0.4$, we have used a modified iterative procedure. This procedure results in a considerably rapid convergence: after repeating five cycles consisting of four iterations with intermediate averaging of the results, the relative difference $\delta\left(f_+^{(i-1)}, f_+^{(i)}\right)$ for all samples was less than 0.1 %. The dependence of this relative difference on the number of iterations is represented in Fig. 4(a).

Figure 4(b) shows the normalized reconstructed VFDFs in experimental samples with the scattering substance volume fraction $\varphi = 0.4$ using a modified iterative procedure. Fig. 4(c) facilitates the comparison of the calculated intensities based on VFDFs (Fig. 4(b)) with primary experimental ones. When calculating intensities in Fig. 4(c), parameters c_0, D, ξ, and r_0 calculated in the preliminary processing stage (see Section 3) were utilized.

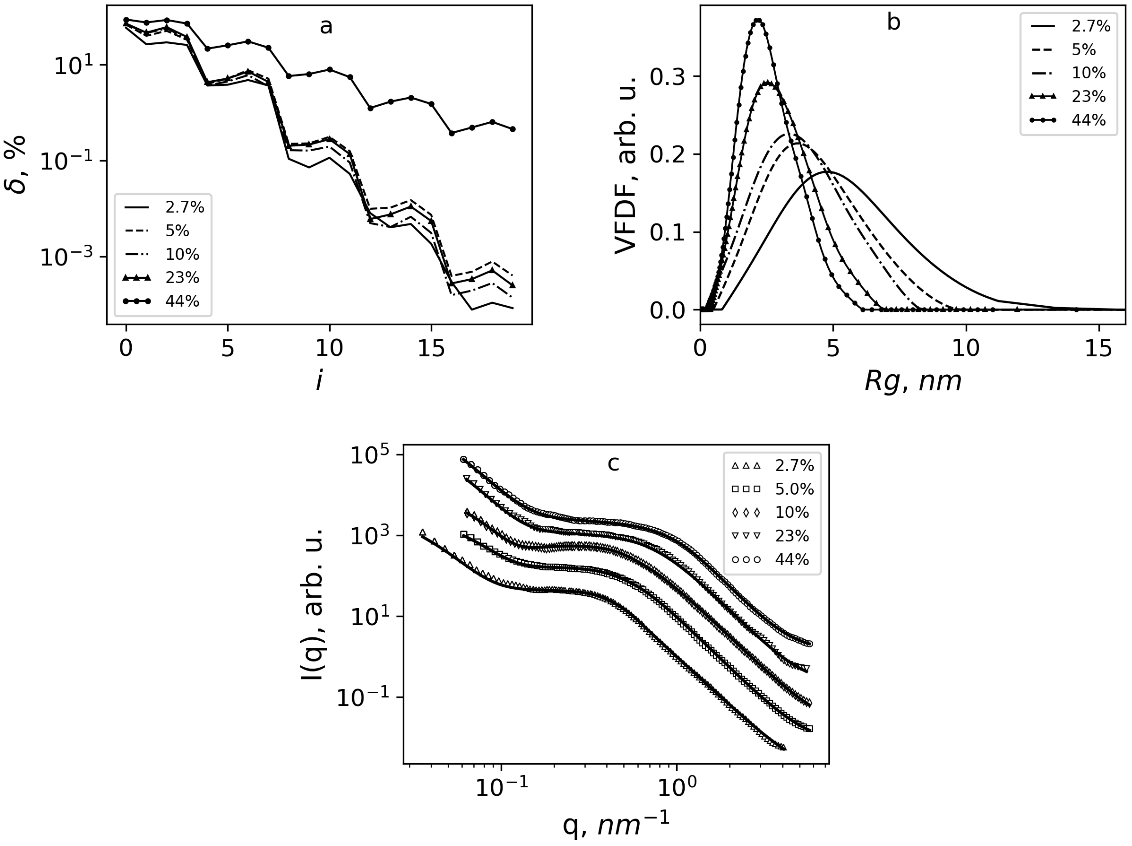

FIG. 4. Results of the application of iterative procedure in relation to SAXS of powder samples composed of ZrO_2+Y_2O_3: a) dependence of the relative difference $\delta\left(f_+^{(i-1)}, f_+^{(i)}\right)$ on the iteration number; b) VFDFs obtained using an iterative procedure; c) comparison of experimental scattering intensities and the intensities calculated on the basis of obtained VFDFs. The legend shows mass fraction of yttrium dioxide in the sample

From Fig. 4(b), it can be seen that as the yttrium oxide mass fraction in the sample goes up, the distribution maximum shifts towards lower values, while the distribution itself becomes narrower. Accordingly, as the yttrium oxide mass fraction increases, the average particle size diminishes to a significant extent, which is in line with prior results [22].

5. Conclusion

This paper proposes an iterative procedure for reconstructing volume fraction distribution function according to radii of gyration in spherical particle systems with a high fraction value φ of scattering substance surface area. The elaborated iterative procedure allows the inclusion of interference contributions into scattering intensity, which, in the case of $\varphi \geq 0.1$, significantly affects the shape of the scattering curve.

The effectiveness of this procedure was verified on the SAXS model curves for typical distribution (1) in the range $\varphi = 0.1...0.4$. The procedure convergence was confirmed by its application to experimental scattering intensities for powder samples of nanoparticles comprised of ZrO_2+Y_2O_3 with a significant difference in yttrium oxide mass fraction.

The iterative procedure suggested in this paper is used for reconstructing the distribution functions of volume fractions in a polydisperse system of particles with a spherical form. However, this procedure is likely to be effective for reconstructing the distributions of particles of other shapes (ellipsoid, cylinder, etc.) as well. The main problem here lies in the manner in which the intensity and structure factor for a polydisperse system of particles of a given form are calculated. The few works that deal with calculating structure factor for non-spherical particles [27, 28] focus solely on monodisperse systems. In line with the development of computer technology, any advancement in the field of investigating polydisperse systems consisting of non-spherical particles will probably be related to a direct simulation of scattering, using methods analogous to the one suggested in [9].

References

[1] Precious-Ayanwale A., Donohu'e-Cornejo A., et al. Review of the synthesis, characterization and application of zirconia mixed metal oxide nanoparticles. *Int. J. of Research – GRANTHAALAYAH*, 2018, **6** (8), P. 136–145.

[2] Larina L.L., Alexeeva O.V., et al. Very wide-bandgap nanostructured metal oxide materials for perovskite solar cells. *Nanosystems: Physics, Chemistry, Mathematics*, 2019, **10** (1), P. 70–74.

[3] Kablov E.N., Stolyarova V.L., et al. Thermodynamics and vaporization of ceramics based on the Y_2O_3–ZrO_2 system studied by KEMS. *J. of Alloys and Compounds*, 2019, **794**, P. 606–614.

[4] Hu C., Sun J., et al. Synthesis of nano zirconium oxide and its application in dentistry. *Nanotechnol Rev.*, 2019, **8** (1), P. 396–404.

[5] Kalinina E.G., Pikalova E.Y. Preparation and properties of stable suspensions of ZrO_2–Y_2O_3 powders with different particle sizes for electrophoretic deposition. *Inorganic Materials*, 2020, **56** (9), P. 941–948.

[6] Guinier A., Fournet G. *Small-angle Scattering of X-rays*. New-York, Wiley, 1955, 268 p.

[7] Agbabiaka A., Wiltfong M., Park C. Small Angle X-Ray Scattering Technique for the Particle Size Distribution of Nonporous Nanoparticles. *J. of Nanoparticles*, 2013, ID 640436, 11 p.

[8] Kuchko A.V., Smirnov A.V. The computation of the nanoparticles volume distribution function and the specific surface area based on the small-angle X-ray scattering indicatrix by the method of the statistical regularization. *Nanosystems: Physics, Chemistry, Mathematics*, 2012, **3** (3), P. 76–91.

[9] Smirnov A.V., Deryabin I.N., Fedorov B.A. Small-angle scattering: the Guinier technique underestimates the size of hard globular particles due to the structure-factor effect. *J. Appl. Cryst.*, 2015, **48**, P. 1089–1093.

[10] Vonk C. On two methods of determination of particle size distribution functions by means of small-angle X-ray scattering. *J. of Applied Crystallography*, 1976, **9** (6), P. 433–440.

[11] Letcher J.H., Schmidt P.W. Small Angle X Ray Scattering Determination of Particle Diameter Distributions in Polydisperse Suspensions of Spherical Particles. *J. Appl. Cryst.*, 1966, **37** (2), P. 649–655.

[12] Yan Y.D., Clarke J.H.R. In-situ determination of particle size distributions in colloids. *Advances in Colloid and Interface Science*, 1989, **29** (3,4), P. 277–318.

[13] Mori Y., Furukawa M., Hayashi T., Nakamura K. Size distribution of gold nanoparticles used by small angle X-ray scattering. *Particulate Science and Technology*, 2006, **24** (1), P. 97–103.

[14] Tyrsted C., Becker J., et al. In-Situ Synchrotron Radiation Study of Formation and Growth of Crystalline $Ce_xZr_{1-x}O_2$ Nanoparticles Synthesized in Supercritical Water. *Chem. Mater.*, 2010, **22**, P. 1814–1820.

[15] Sivtsov E.V., Kalinin A.V., et al. In Situ Preparation of Polymer Nanocomposites Based on Sols of Surface-Modified Detonation Nanodiamonds by Classical and Controlled Radical Polymerization. *Polymer Science, Series B*, 2020, **62** (6), P. 734–749.

[16] Laube J., Gjuqel A., Ottershtedt R. Zirconium oxide and way of its production (Invention RU 2 442 752 C2). Federal service of Russian Federation for intellectual property, 20.02.2012 Bull., 19 p.

[17] Pedersen J.S. Determination of Size Distributions from Small-Angle Scattering Data for Systems with Effective Hard-Sphere Interactions. *J. Appl. Cryst.*, 1994, **27**, P. 595–608.

[18] Vrij A. Mixtures of hard spheres in the Percus-Yevick approximation. Light scattering at finite angles. *J. of Chem. Phys.*, 1979, **71** (8), P. 3267–3270.

[19] Almjasheva O.V., Fedorov B.A., Smirnov A.V., Gusarov V.V. Size, morphology and structure of the particles of zirconia nanopowder obtained under hydrothermal conditions. *Nanosystems: Physics, Chemistry, Mathematics*, 2010, **1** (1), P. 26–36.

[20] Almjasheva O.V., Krasilin A.A., Gusarov V.V. Formation mechanism of core-shell nanocrystals obtained via dehydration of coprecipitated hydroxides at hydrothermal conditions. *Nanosystems: Phys. Chem. Math.*, 2018, **9** (4), P. 568–572.

[21] Kuchko A.V., Smirnov A.V. SAXSEV 2.1 cross-platform application for data analysis of small-angle x-ray scattering from polydisperse systems. *Sci. Tech. J. Inf. Technol. Mech. Opt.*, 2015, **15** (2), P. 267–274.

[22] Shuklina A.I., Smirnov A.V., et al. Structure of nanoparticles in the ZrO_2–Y_2O_3 system, as obtained under hydrothermal conditions. *Nanosystems: Physics, Chemistry, Mathematics*, 2020, **11** (6), P. 729–738.

[23] Ruland W. Small-Angle Scattering of Two-Phase Systems: Determination and Significance of Systematic Deviations from Porod's Law. *J. Appl. Cryst.*, 1971, **4**, P. 70–73.

[24] Feigin L.A., Svergun D.I. *Structure Analysis by Small-Angle X-Ray and Neutron Scattering*. New York, Plenum Press, 1987, 335 p.

[25] Teixeira J. Small-Angle Scattering by Fractal Systems. *J. Appl. Cryst.*, 1988, **21**, P. 781–785.

[26] Guinier A. La diffraction des rayons X aux très petits angles: application à l'étude de phénomènes ultramicroscopiques. *Ann. Phys.*, 1939, **11** (12), P. 161–237.

[27] Hansen S. The structure factor in small-angle scattering and the effect of deviation from spherical symmetry. *J. Appl. Cryst.*, 2011, **44**, P. 265–327.

[28] Hansen S. Monte Carlo estimation of the structure factor for hard bodies in small-angle scattering. *J. Appl. Cryst.*, 2012, **45**, P. 381–388.

Appendix

Formulae for calculating the structure factor for spherical particles with effective hard-sphere interactions.

Let $f(r)$ be a normalized distribution function of the particle amount based on their radii other than zero in the interval $R_{\min}...R_{\max}$, let the particle material unit have scattering density one, and let the scattering substance surface area volume fraction be φ. In that case, scattering intensity per system volume unit equals to

$$I(q) = \frac{6 \cdot \sum\limits_{i=1}^{6} C_i(q)}{\pi \left|F_{11}(q)F_{22}(q) - F_{12}(q)F_{21}(q)\right|^2}, \tag{A1}$$

in which case the following ancillary functions are used:

$$C_1(q) = \left\langle V^2(r)\Phi^2(qr)\right\rangle |T_1(q)|^2; \tag{A2}$$

$$C_2(q) = \left\langle (2r)^6\,\Phi^2(qr)\right\rangle |T_2(q)|^2; \tag{A3}$$

$$C_3(q) = 9\left\langle (2r)^4\,\Psi^2(qr)\right\rangle |T_3(q)|^2; \tag{A4}$$

$$C_4(q) = 2\left\langle V(r)\,(2r)^3\,\Phi^2(qr)\right\rangle \mathrm{Re}\left(T_1(q)T_2^*(q)\right); \tag{A5}$$

$$C_5 = 6\left\langle V(r)\,(2r)^2\,\Phi(qr)\,\Psi(qr)\right\rangle \mathrm{Re}\left(T_1(q)T_3^*(q)\right); \tag{A6}$$

$$C_6 = 6\left\langle (2r)^5\,\Phi(qr)\,\Psi(qr)\right\rangle \mathrm{Re}\left(T_2(q)T_3^*(q)\right); \tag{A7}$$

$$T_1(q) = F_{11}(q)F_{22}(q) - F_{12}(q)F_{21}(q); \tag{A8}$$

$$T_2(q) = F_{21}(q)\left\langle 2rV(r)\Phi(qr)\,e^{iqr}\right\rangle - F_{22}(q)\left\langle V(r)\Phi(qr)\,e^{iqr}\right\rangle; \tag{A9}$$

$$T_3(q) = F_{12}(q)\left\langle V(r)\Phi(qr)\,e^{iqr}\right\rangle - F_{11}(q)\left\langle 2rV(r)\Phi(qr)\,e^{iqr}\right\rangle; \tag{A10}$$

$$F_{11}(q) = 1 - \xi_3 + \left\langle (2r)^3\,\Phi(qr)\,e^{iqr}\right\rangle; \tag{A11}$$

$$F_{12}(q) = \left\langle (2r)^4\,\Phi(qr)\,e^{iqr}\right\rangle; \tag{A12}$$

$$F_{21}(q) = \frac{1}{2}\left(1-\xi_3\right) iq - 3\xi_2 + 3\left\langle (2r)^2\,\Psi(qr)\,e^{iqr}\right\rangle; \tag{A13}$$

$$F_{22}(q) = 1 - \xi_3 + 3\left\langle (2r)^3\,\Psi(qr)\,e^{iqr}\right\rangle; \tag{A14}$$

$$\Phi(X) = 3\frac{\sin(X) - X\cos(X)}{(X)^3}; \quad \Psi(X) = \frac{\sin(X)}{X}. \tag{A15}$$

In expressions (A2)–(A15), we use the following notation:

$$V(r) = \frac{4}{3}\pi r^3; \quad \xi_\nu = \left\langle (2r)^\nu \right\rangle. \tag{A16}$$

Let Υ be a mathematical expression. Then $\langle \Upsilon \rangle$ is as follows:

$$\langle \Upsilon \rangle = \frac{\pi}{6}\frac{\varphi}{V_m}\int\limits_{R_{\min}}^{R_{max}} (\Upsilon)\, f(r)dr, \tag{A17}$$

where

$$V_m = \int\limits_{R_{\min}}^{R_{\max}} V(r)f(r)dr. \tag{A18}$$

Formulae (A1)–(A18) represent a generalization in the case of continuous distribution based on the radii of the formulae obtained in [18] for particle systems with discrete sets of radii.

Submitted 15 December 2021; revised 7 January 2021; accepted 8 January 2021

Information about the authors:

Artem V. Kuchko – ITMO University, 49, Kronverkskiy, St. Petersburg, 197101, Russia; ORCID 0000-0003-0971-0810; artemkav@gmail.com

Alexander V. Smirnov – ITMO University, 49, Kronverkskiy, St. Petersburg, 197101, Russia; ORCID 0000-0002-2677-136X; smirnav_2@mail.ru

Conflict of interest: the authors declare no conflict of interest.

NANOSYSTEMS:
PHYSICS, CHEMISTRY, MATHEMATICS

Original article

Priyanka, Savita Gill *Nanosystems: Phys. Chem. Math.*, 2022, **13** (1), 71–77.
http://nanojournal.ifmo.ru
DOI 10.17586/2220-8054-2022-13-1-71-77

Pump photons present in a non-linear process as a witnesses of non-classicality of a system

Priyanka[a], Savita Gill[b]

University Institute of Engineering and Technology, Kurukshetra University Kurukshetra, 136119, India

[a]Chauhan7101@gmail.com, [b]Savita2015@kuk.ac.in

Corresponding author: Savita Gill, Savita2015@kuk.ac.in

ABSTRACT We have studied non-classical effects, i.e. higher order photon antibunching (HOA) and higher order sub-Poissonian photon number statistics (HOSPS) in various non-linear optical processes like second harmonic generation, fourth harmonic generation, coherent anti-Stokes Raman scattering (CARS) and coherent anti-Stokes hyper-Raman scattering (CAHRS) using short time interaction techniques. The non-classical effects directly depend on number of photons prior to interaction with non-linear medium has already been studied but we have found that non-linear processes involving equal number of pump photons have same higher order photo antibunching (HOA) and higher order sub-Poissonian photon number statistics (HOSPS) independent of the non-linear process involved.

KEYWORDS Higher order sub-Poissonian photon number statistics, higher order photon antibunching, optical processes.

FOR CITATION Priyanka, Savita Gill Pump photons present in a non-linear process as a witnesses of non-classicality of a system. *Nanosystems: Phys. Chem. Math.*, 2022, **13** (1), 71–77.

1. Introduction

Non-classical states cannot be characterized by a mixture of coherent states and these are often defined by the negative values of Glauber-Sudarshan P-functions [1,2]. In fact, there is no method for determining the P-function experimentally, except for a single proposal [3]. A number of operational criteria for witnessing non classicality have been developed [4,5]. These observers of non-classicality can be communicated as the moments of creation and annihilation operators and a non-classical property seen through a moment-based model that observes a non-classical characteristic through a lower order connection is known as a lower-order non-classical property. Higher-order non-classicality, as the name implies, refers to the non-classical characteristics revealed by higher order correlations. Higher order photon antibunching (HOA) [6], higher-order sub-Poissonian photon number statistics (HOSPS) [7,8], higher order squeezing of Hong-Mandel type [9,10] are the most often researched higher order non-classical characteristics. All of these non-classical characteristics have lower order equivalents that have been well investigated [11, 12]. Due to the successful experimental characterizations of higher-order non-classical states, much attention has been given to these states recently [13–16]. The fact that weak non-classicalities not identified by their lower order equivalents can be recognized by higher order non-classicality criteria has led to a significant number of theoretical studies as well [14, 15]. Indeed, higher order photon antibunching (HOA) and higher order squeezing (HOS) has been accounted in an opto-mechanical like system [17], finite dimensional coherent state [5], optical coupler [18], hyper-Raman process [19] and higher order sub-Poissonian photon number statistics (HOSPS) has been accounted in finite dimensional coherent state [5], photon added and subtracted squeezed coherent states [20]. Previously, research into these non-classical phenomena was mostly for academic interest [21], but their numerous applications in quantum information theory, such as optical communication [14], dense coding [22], quantum teleportation [23], and quantum cryptography [24], are now well-known. Non-classicality has been shown to be a required input for the entangled state [25]. All of the physical systems mentioned above are experimentally feasible and may be easily seen in a non- linear optics laboratory [26, 27]. Photon number statistics may be obtained experimentally using the homodyne detection technique [28, 29]. A number of new opportunities for non-linear optics have arisen due to the rapid growth of nanotechnology and nanoscience. During the last few decades, non-linear optical materials have made significant progress in laser technology and these materials have large non-linear optical properties and a fast non-linear response for various photonic applications such as pulsed laser deposition, laser ablation, optical information processing, optical communication, optical limiters and optical data storage [30–35]. Nanomaterials with large non-linear responses are useful in photocatalysis and optical limiting applications [36] and optical non-linear microscopy [37]. Materials with large third order optical non-linearity and fast response time will be required for future optical device applications [38,39]. Due to their high non-linear optical response of these nonlinear optical materials, these materials are used in fiber optic communication systems such as all digital signal restoration, routing units, de- multiplexing and multiplexing and optical storage media [39] as well as in optical switching [40]. Strong optical non-linearities observed due to the quantum confinement effects such as second and third order optical non-linearities and non-linear optical absorption that can be studied for making laser second and third harmonic generators and optical modulators [38, 39]. There has been a lot of research done on measuring third order nonlinear susceptibility χ^3 to examine optical nonlinearity of nanoparticles may be Z scan technique and degenerate four wave mixing experiments [39]. Hanamura analyzed theoretically the third order optical polarizability χ^3 and the oscillator strength in semiconductor microcrystallites [41].

The state of non-classicality of the non-linear optical system is described in segment 2 of the current study. Segment 3 will introduce a second order solution of equation of motion by means of an illustration of fourth harmonic generation process and show the presence of higher order photon antibunching (HOA) and higher order sub-Poissonian photon number statistics (HOSPS). In segment 4, we have investigated the presence of higher order non-classical effects in second harmonic generation, coherent anti-Stokes Raman scattering process (CARS) and coherent anti-Stokes hyper-Raman scattering (CAHRS) non-linear optical processes, as well as their direct association with pump photons present in the system. In section 5, we used graphs to compare the results and section 6 is devoted to the conclusion.

2. Condition of non-classicality of a non-linear optical system

2.1. Condition for higher order photon antibunching(HOA)

Lee presented the higher order photon antibunching (HOA) criteria as follows [42]:

$$R(l,p) = \frac{\langle N_x^{l-1}\rangle \langle N_x^{p+1}\rangle}{\langle N_x^{l}\rangle \langle N_x^{p}\rangle} - 1 < 0, \tag{1}$$

where number operator is represented by N.

$\left\langle N^{(k)}\right\rangle = \langle N(N-1)(N-2)\cdots(N-k+1)\rangle$ is the k^{th} factorial moment of the number operator. Integers l and p fulfilling condition $l \le p \le 1$ and x addendum indicates specific mode. $p = 1$ is picked by Ba An [43] and condition of the l^{th} order photon antibunching is reduced to

$$A_{x,l} = \frac{\langle N_x^{l+1}\rangle}{\langle N_x^{l}\rangle \langle N_x\rangle} - 1 < 0, \tag{2}$$

And:

$$\langle N_x^{l+1}\rangle < \langle N_x^{l}\rangle \langle N_x\rangle . \tag{3}$$

Physically, a state which is photon antibunched in the l^{th} order must be photon antibunched in the $(l-1)^{th}$ order. Therefore, we can simplify (3) as:

$$\langle N_x^{l+1}\rangle < \langle N_x^{l}\rangle \langle N_x\rangle < \langle N_x^{l-1}\rangle \langle N_x^{2}\rangle < \cdots < \langle N_x\rangle^{l+1},$$

and obtain condition of l^{th} order photon antibunching as:

$$d(l) = \langle N_x^{l+1}\rangle - \langle N_x\rangle^{l+1} < 0. \tag{4}$$

From equation (4), we can see that for sub-Poissonian state $d(l) < 0$. Along these lines, we can say that a single photon source utilized in quantum cryptography should fulfill the criteria given in equation (4) of higher order photon antibunching (HOA).

2.2. Criteria for higher order sub-poissonian photon number statistics (HOSPS)

Mishra and Prakash [44] provide the criteria of $(l-1)^{th}$ order higher order sub-Poissonian photon number statistics (HOSPS) is given as:

$$D(l-1) = \sum_{k=0}^{l}\sum_{i=0}^{l-k} {}^{l}C_k(-1)^k S_2(l-k,i)\langle N^i\rangle \langle N\rangle^k - \sum_{k=0}^{l}\sum_{i=0}^{l-k} {}^{l}C_k(-1)^k S_2(l-k,i)\langle N\rangle^{k+i} < 0, \tag{5}$$

where $S_2(l,k)$ is the second-order Stirling number. For $l = 3$, the condition of second order sub-Poissonian photon number statistics (HOSPS) is described as:

$$D(2) = \langle N^3\rangle + 2\langle N\rangle^3 - 3\langle N^2\rangle \langle N\rangle + 3\langle N^2\rangle - 3\langle N\rangle^2 < 0. \tag{6}$$

3. Fourth harmonic generation process

To examine higher order photon antibunching (HOA) and higher order sub-Poissonian photon number statistics (HOSPS), we used the fourth harmonic generation process, which involves absorption of four photons, each with a frequency ω_1 and the emission of one photon with frequency ω_2 where $\omega_2 = 4\omega_1$. For this process, the Hamiltonian is:

$$H = \omega_1 a^\dagger a + \omega_2 b^\dagger b + g(a^4 b^\dagger + a^{\dagger 4} b), \tag{7}$$

where $a^\dagger$ (a), $b^\dagger$ (b) are the creation (annihilation) operators and g is coupling constant. $A = a\exp i\omega_1 t$, $B = b\exp i\omega_2 t$ are the gradually varying operators at frequencies ω_1 and ω_2.

3.1. Time evolution of pump mode A

The Heisenberg equation of motion for the time evolution of operator in mode A is given as:

$$\frac{dA}{dt} = \frac{\partial A}{\partial t} + i\,[H, A]\,. \tag{8}$$

We obtain:

$$\dot{A} = -4igA^{+3}B, \tag{9}$$

and

$$\dot{B} = -igA^4. \tag{10}$$

We now expand $A\,(t)$ using Taylor series expansion and treating terms up to g^2t^2 by using short time approximation as:

$$A(t) = A - 4igtA^{\dagger 3}B + 2g^2t^2(12A^{\dagger 2}A^3N_B + 36A^{\dagger}A^2N_B + 24AN_B - A^{\dagger 3}A^4). \tag{11}$$

Using equation (11), number operator $N_A(t) = A^{\dagger}(t)A(t)$ is given as:

$$N_A(t) = A^{\dagger}A - 4igt(A^{\dagger 4}B - A^4B^{\dagger}) + 4g^2t^2(16A^{\dagger 3}A^3N_B + 72A^{\dagger 2}A^2N_B + 96A^{\dagger}AN_B + 24N_B - A^{\dagger 4}A^4). \tag{12}$$

To investigate photon antibunching, we start with a quantum state that is the product of coherent state $|\alpha\rangle$ for pump mode A and vacuum state $|0\rangle$ for stokes mode B i.e.:

$$|\psi\rangle = |\alpha\rangle_A\,|0\rangle_B\,. \tag{13}$$

Using equation (13) in equation (12), we get average value of $\langle N_A(t)\rangle_\alpha = \left\langle A^{\dagger}(t)A(t)\right\rangle$ as:

$$\langle N_A(t)\rangle_\alpha = |\alpha|^2 - 4g^2t^2\,|\alpha|^8\,, \tag{14}$$

where $A\,|\alpha\rangle = \alpha\,|\alpha\rangle$. Now, the average value of $N_A^4(t)$ is given as:

$$\left\langle N_A^4(t)\right\rangle_\alpha = \left\langle A^{\dagger 4}(t)A^4(t)\right\rangle = |\alpha|^8 - 8g^2t^2(2\,|\alpha|^{14} + 9\,|\alpha|^{12} + 12\,|\alpha|^{10} + 3\,|\alpha|^8).$$

Now, using equations (14) in equation (4), we get third order photon antibunching as

$$d_A(3)_\alpha = -24g^2t^2(3\,|\alpha|^{12} + 4\,|\alpha|^{10} + |\alpha|^8). \tag{15}$$

Equation (15) shows that fourth harmonic generation process satisfies the criteria of higher order photon antibunching.

To examine higher order photon antibunching, we used the initial state which is equal to the product of vacuum state $|0\rangle$ for pump mode A and $|\beta\rangle$ for stokes mode B i.e.:

$$|\psi\rangle = |0\rangle_A\,|\beta\rangle_B\,. \tag{16}$$

Now, taking average values of $N_A^4(t)$ in pump mode A with respect to condition (16) is given as:

$$\left\langle N_A^4(t)\right\rangle_\beta = 0. \tag{17}$$

Using equation (17) in equation (4), we obtain third order photon antibunching in mode A in relation to $|0\rangle\,|\beta\rangle$ is given as:

$$d_A(3)_\beta = 0. \tag{18}$$

Equation (18) shows that higher order photon antibunching is absent in mode A with respect to the quantum state $|0\rangle\,|\beta\rangle$.

Now, using equations (12, 13 and 16) in equation (6), we obtain:

$$D(2)_\alpha = -60g^2t^2\,|\alpha|^8\,, \tag{19}$$

$$D(2)_\beta = 0,$$

we obtain a negative value in equation (19), which indicates that higher order sub-Poissonian photon number statistics exists in mode A with respect to quantum state $|\psi\rangle = |\alpha\rangle_A\,|0\rangle_B$.

4. Non-classicality in other non-linear optical processes

We have analyzed higher order photon antibunching (HOA) and higher order sub-Poissonian photon number statistics (HOSPS) in various non-linear optical processes and all the results that we have obtained is mentioned in Table 1 and Table 2 respectively.

In Table 1 and Table 2, $*$ represents the average values are taken with regards to $|\alpha\rangle\,|0\rangle\,|0\rangle$ in mode A.

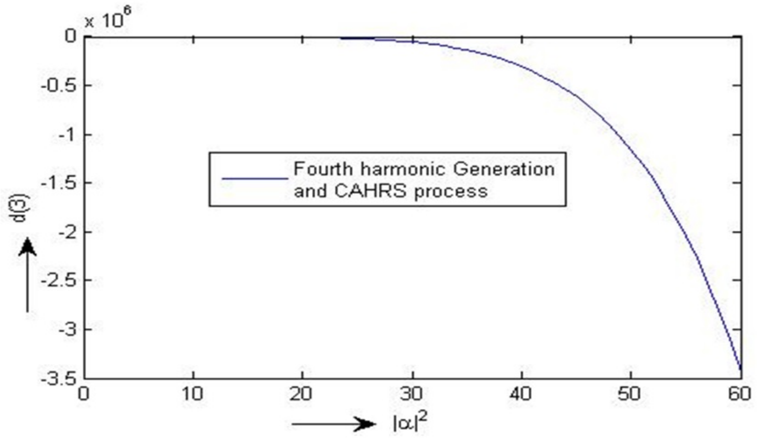

FIG. 1. The plot of third order photon antibunching $d(3)$ versus $|\alpha|^2$ in fourth harmonic generation and coherent anti-Stokes hyper-Raman scattering process (CAHRS) (taking $g^2t^2 \approx 10^{-6}$)

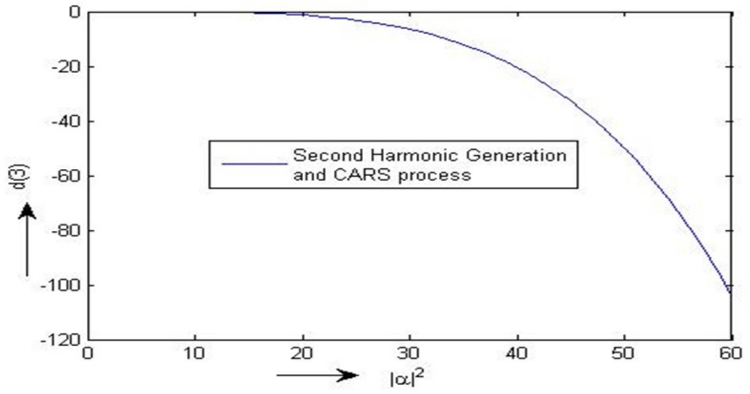

FIG. 2. The plot of third order photon antibunching $d(3)$ versus $|\alpha|^2$ in second harmonic generation and coherent anti-Stokes Raman scattering process (CARS) (taking $g^2t^2 \approx 10^{-6}$)

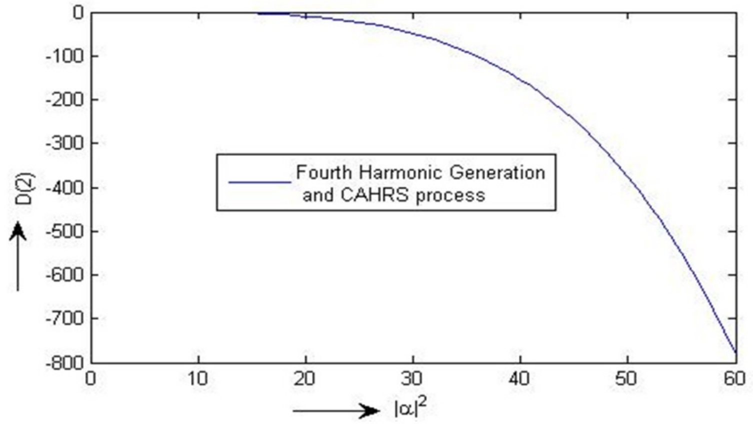

FIG. 3. The plot of higher order sub-Poissonian photon number statistics $D(2)$ versus $|\alpha|^2$ in fourth harmonic generation and coherent anti-Stokes hyper-Raman scattering process (CAHRS) (taking $g^2t^2 \approx 10^{-6}$)

TABLE 1. Results obtained for higher order photon antibunching (HOA) in non-linear optical processes

Sr. no.	Optical processes	Interaction term	Parameter $d(3)$ Expectation value w. r. t. $*$, $\lvert\alpha\rangle \lvert 0\rangle \lvert 0\rangle$
1	Second harmonic generation	$A^{\dagger 2}B$	$d(3) = -8g^2t^2 \lvert\alpha\rvert^8$
2	Coherent anti-Stokes Raman scattering (CARS) process	$A^{\dagger}BA^{\dagger}C$	$d(3) = -8g^2t^2 \lvert\alpha\rvert^8$
3	Fourth harmonic generation	$A^{\dagger 4}B$	$d(3) = -24g^2t^2(3\lvert\alpha\rvert^{12} + 4\lvert\alpha\rvert^{10} + \lvert\alpha\rvert^8)$
4	Coherent anti-Stokes hyper-Raman scattering (CAHRS) process	$A^{\dagger 2}BA^{\dagger 2}C$	$d(3) = -24g^2t^2(3\lvert\alpha\rvert^{12} + 4\lvert\alpha\rvert^{10} + \lvert\alpha\rvert^8)$

TABLE 2. Results obtained for higher order sub-Poissonian photon number statistics in non-linear optical processes

Sr. no.	Optical processes	Interaction term	Parameter $D(2)$ Expectation value w. r. t. $*$, $\lvert\alpha\rangle \lvert 0\rangle \lvert 0\rangle$
1	Second harmonic generation	$A^{\dagger 2}B$	$D(2) = -6g^2t^2(\lvert\alpha\rvert^4)$
2	Coherent anti-Stokes Raman scattering (CARS) process	$A^{\dagger}BA^{\dagger}C$	$D(2) = -6g^2t^2(\lvert\alpha\rvert^4)$
3	Fourth harmonic generation	$A^{\dagger 4}B$	$D(2) = -60g^2t^2 \lvert\alpha\rvert^8$
4	Coherent anti-Stokes hyper-Raman scattering (CAHRS) process	$A^{\dagger 2}BA^{\dagger 2}C$	$D(2) = -60g^2t^2 \lvert\alpha\rvert^8$

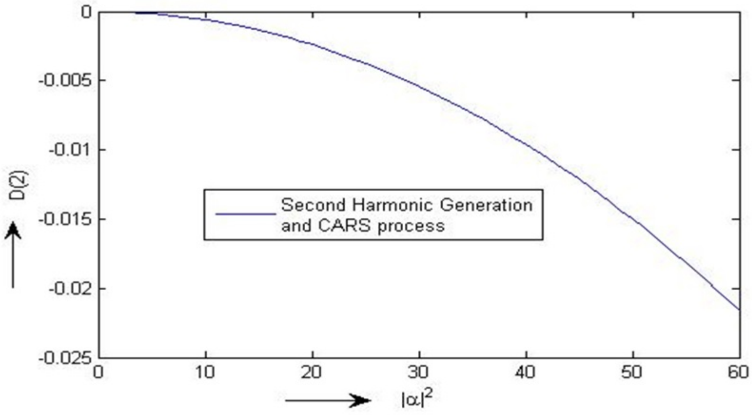

FIG. 4. The plot of higher order sub-Poissonian photon number statistics$D(2)$ versus $\lvert\alpha\rvert^2$ in second harmonic generation and coherent anti-Stokes Raman scattering process (CARS) (taking $g^2t^2 \approx 10^{-6}$)

5. Result

Tables 1 and Tables 2 illustrate the existence of higher order sub-Poissonian photon number statistics (HOSPS) and higher order photon antibunching (HOA) in different non-linear processes. If we plot a graph connecting higher order photon antibunching (HOA) say $d(3)$ and higher order sub-Poissonian photon number statistics (HOSPS) say D(2) with photon number in pump mode A i.e. $\lvert\alpha\rvert^2$, it is obvious that higher order sub-Poissonian photon number statistics (HOSPS) and higher order photon antibunching (HOA) increase non-linearly as $\lvert\alpha\rvert^2$ increases. Fig. 1 of higher order photon antibunching (HOA) and Fig. 3 of higher order sub-Poissonian photon number statistics (HOSPS) of fourth harmonic generation and coherent anti-Stokes hyper-Raman scattering (CAHRS) show the same values of higher order photon antibunching (HOA) as well as higher order sub-Poissonian photon number statistics (HOSPS). Similarly, Fig. 2 and Fig. 4 of second harmonic generation and coherent anti-Stokes Raman scattering process (CARS) also show the same values of higher order photon antibunching (HOA) as well as higher order sub-Poissonian photon number statistics (HOSPS). In all these non-linear optical processes, we have observed higher order photon antibunching (HOA) and higher order sub-Poissonian photon number statistics (HOSPS) only with respect to a quantum state which is the product of a coherent state $|\alpha\rangle$ for pump mode A and vacuum state $|0\rangle$ for Stokes mode B and signal mode C.

6. Conclusion

Higher order non-classical effects i.e. higher order photon antibunching (HOA) and higher order sub-Poissonian photon number statistics (HOSPS) in pump mode have been observed in a variety of non-linear optical processes. We have found that the non-linear processes having the same number of pump photons present prior to interaction have the same value of higher order photon antibunching and higher order sub-Poissonian photon number statistics, which we have demonstrated using examples of fourth harmonic generation with coherent anti-Stokes hyper-Raman scattering (CAHRS) and second harmonic generation with coherent anti-Stokes Raman scattering process (CARS). Further, we are obtaining the maximum value of non-classicality in fourth harmonic generation and coherent anti-Stokes hyper-Raman scattering process (CAHRS), as it has the maximum number of pump photons as compared to other non-linear optical processes which we have taken into consideration. As a result, we can conclude that non-classicality of a system can be revealed by the number of pump photons present in the system prior to interaction irrespective of the non-linear process involved. To study the higher order non-classical effects in various non-linear optical processes, we need the non-linear materials having higher order non-linear susceptibility which can be studied for making optical modulators and higher harmonic generators.

References

[1] Glauber R.J. Coherent and incoherent states of the radiation field. *Physical Review*, 1963, **131**(6), P. 2766–2788.

[2] Sudarshan E.C.G. Equivalence of semi-classical and quantum mechanical descriptions of statistical light beams. *Physical Review Letters*, 1963, **10**(7), P. 277–279.

[3] Alexanian M. Non-classicality criteria: Glauber–Sudarshan P function and Mandel parameter. *Journal of Modern Optics*, 2017, **65**(1), P. 16–22.

[4] Miranowicz A., Bartkowiak M., Wang X., Liu Y.X., Nori F. Testing non classicality in multimode fields: A unified derivation of classical inequalities. *Physical Review A*, 2010, **82**(1), 013824(1-14).

[5] Alam N., Verma A., Pathak A. Higher-order non-classicalities of finite dimensional coherent states: A comparative study. *Physics Letters A*, 2018, **382**(28), P. 1842–1851.

[6] Pathak A., Garcia M.E. Control of higher order antibunching. *Applied Physics B*, 2006, **84**(3), P. 479–484.

[7] Verma A. Study of higher order squeezing and sub-Poissonian photon statistics in generalized binomial state of light, International Conference on Photonics. *Meta materials & Plasmonics AIP Conference Proceeding*, 2019, **2136**, 050009(14).

[8] Verma A., Pathak A. Generalized structure of higher order non-classicality. *Physics Letters A*, 2010, **374**(8), P. 1009–1020.

[9] Priyanka, Gill S. Higher Order Squeezing in Pump Mode in Multi-wave Mixing Process, In book: Advances in Communication and Computational Technology. *Select Proceedings of ICACCT*, 2019, P. 149–162.

[10] Gill S. Non Classical Effect of Light in Stimulated Five Wave Mixing. *International Journal of Research and Scientific Innovation*, 2017, **4**(6), P. 90–93.

[11] Priyanka, Gill S. Study of Nonclassicality in Fifth Harmonic Generation Nonlinear Optical Process. *Nanosystems: Physics, Chemistry, Mathematics*, 2021, **12**(1), P. 65–72.

[12] Mendoza K.Z., Dey S., Hussin V. Generalized squeezed states. *Physics Letters A*, 2018, **382**(47), P. 3369–3375.

[13] Avenhaus M., Laiho K., Chekhova M.V., Silberhorn C. Accessing higher order correlations in quantum optical states by time multiplexing. *Physical Review Letters*, 2010, **104**(6), 063602(1-4).

[14] Allevi A., Olivares S., Bondani M. High-order photon-number correlations: a resource for characterization and applications of quantum states. *International Journal of Quantum Information*, 2012, **10**(08), 1241003(1-8).

[15] Allevi A., Olivares S., Bondani M. Measuring high-order photon-number correlations in experiments with multimode pulsed quantum states. *Physical Review A*, 2012, **85**(6), 063835(1-5).

[16] Peřina J., Michálek V. Haderka O. Higher-order sub-poissonian-like non classical fields: Theoretical and experimental comparison. *Physical Review A*, 2017, **96**(3), 033852(1-7).

[17] Alam N., Thapliyal K., Pathak A., Sen B., Verma A., Mandal S. Lower-and higher-order non-classicality in a Bose-condensed opto mechanical-like system and a Fabry-Perot cavity with one movable mirror: squeezing, antibunching and entanglement. arXiv preprintarXiv, 2017, 1708.03967.

[18] Thapliyal K., Pathak A., Sen B., Peřina J. Higher-order non-classicalities in a codirectional nonlinear optical coupler: quantum entanglement, squeezing, and antibunching. *Physical Review A*, 2014, 90(1), 013808(1-10).

[19] Thapliyal K., Pathak A., Sen B., Perina J. Nonclassicality in non-degenerate hyper-Raman processes. arXiv preprint arXiv, 2017, 1710.04456.

[20] Thapliyal K., Samantray N.L., Banerji J., Pathak A. Comparison of lower order and higher order non-classicality in photon added and photon subtracted squeezed coherent states. *Physics Letters A*, 2017, **381**(37), P. 3178–3187.

[21] Mollow B.R., Glauber R.J. Quantum Theory of Parametric Amplification. *Physical Review*, 1967, **160**(5), P. 1076–1096.

[22] Bennett C.H., Shor P.W., Smolin J.A., Thapliyal A.V. Entanglement Assisted Classical Capacity of Noisy Quantum Channels. *Physical Review Letters*, 1999, **83**(15), P. 3081–3084.

[23] Laurenza R., Lupo C., Lloyd S., Pirandola S. Dense coding capacity of a quantum channel. *Physical Review Research*, 2020, **2**(2), 023023(1-5).

[24] Braunstein S.L., D'Ariano G.M., Milburn G.J., Sacchi M.F. Universal Teleportation with a Twist. *Physical Review Letters*, 2000, **84**(15), P. 3486–3489.

[25] Bennett C.H., Brassard G., Mermin N.D. Quantum cryptography without Bell's theorem. *Physical Review Letters*, 1992, **68**(5), P. 557–559.

[26] Kim M.S. et. al. Entanglement by a beam splitter: Non-classicality as a prerequisite for entanglement. *Physical Review A*, 2002, **65**(3), 032323(1-7).

[27] Bachor H.A.A Guide to Experiments in Quantum Optics. Weinheim: Wiley VCH, 1998, Chapters 8 and 10.

[28] Vyas R., Wang C., Singh S. Homodyne detection for the enhancement of antibunching. *Physical Review A*, 1996, **54**(3), P. 2391–2396.

[29] Erenso D., Vyas R., Singh S. Higher order sub-Poissonian photon statistics in terms of factorial moments. *Journal of Optical Society B*, 2002, **19**(6), P. 1471–1475.

[30] Basak S., Chandrasekar R. Passive optical wave guiding organic rectangular tubes: tube cutting, controlling light propagation distance and multiple optical outputs. *Journal of Materials Chemistry C*, 2013, **2**(8), P. 1404–1408.

[31] Hu S., Melton C., Mukherjee D. A facile route for the synthesis of nanostructured oxides and hydroxides of cobalt using laser ablation synthesis in solution (LASIS). *Physical Chemistry Chemical Physics*, 2014, **16**(43), P. 24034–24044.

[32] Udayabhaskar R., Ollakkan M.S., Karthikeyan B. Preparation, optical and non-linear optical power limiting properties of Cu, CuNi nanowires. *Appled Physics Letters*, 2014, **104**(1), 013017(1-4).

[33] Emelyanov A.V., Khenkin M.V., Kazanskii A.G., Forsh P.A., Kashkarov P.K., Gecevicius, Mindaugas, Beresna, Martynas, Kazansky, Peter G. Femtosecond laser induced crystallization of hydrogenated amorphous silicon for photovoltaic applications. *Thin Solid Films*, 2014, **556**(4), P. 410–413.

[34] Tang C., Zheng Q., Zhu H., Wang L., Chen S.C., Ma E., Chen X. Two-photon absorption and optical power limiting properties of ladder-type tetra phenylene cored chromophores with different terminal groups. *Journal of Materials Chemistry C*, 2013, **1**(9), P. 1771–1780.

[35] Jiang T., Qin G., Qin W., Zhou J. Passively Q-switched erbium-doped fiber laser based on gold nanorods. *Optik*, 2014, **125**(19), P. 5789–5793.

[36] Krishnan S., Sandeep C.S.S., Philip R., et al. Two-photon assisted excited state absorption in multiferroic $YCrO_3$, nanoparticles. *Chemical Physics Letters*, 2012, **529**(5), P. 59–63.

[37] Ren P., Fan H., Wang X. Electrospun nanofibers of $ZnO/BaTiO_3$, heterostructures with enhanced photocatalytic activity. *Catalysis Communications*, 2012, **25**(8), P. 32–35.

[38] Xie R.H. *H andbook of advanced electronic and photonic materials and devices* (H.S. Nalwa edition). Academic Press, New York, 2000, **9**, P. 267–307.

[39] Xie R.H., Rao Q., Jensen L. *Encyclopedia of nanoscience and nanotechnology* (H.S. Nalwwa edition). American Scientific, Los Angeles, 2003.

[40] Stentz A.J., Boyd R. *Handbook of Photonics* (M.C. Gupta edition), CRC press, Boca Raton, 1997.

[41] Hanamura E. Rapid radiative decay and enhanced optical nonlinearity of excitons in a quantum well. *Physical Review B*, 1988, **38**(2), P. 1228–1234.

[42] Lee C.T. Higher order criteria for non-classical effects in photon statistics. *Physical Review A*. 1990, **41**(3), P. 1721–1723.

[43] An N.B. Multimode higher-order antibunching and squeezing in trio coherent states. Journal Optics B: Quantum and Semiclassical Optics, 2002, **4**(3), P. 222–227.

[44] Prakash H., Mishra D.K. Higher order sub-Poissonian photon statistics and their use in detection of Hong and Mandel squeezing and amplitude squared squeezing. *Journal of Physics B: Atomic, Molecular and Optical Physics*, 2006, **39**(9), P. 2291–2297.

Submitted 10 January 2022; revised 22 January 2022; accepted 2 February 2022

Information about the authors:

Priyanka – Department of Applied Science, University Institute of Engineering and Technology, Kurukshetra 136119, India; Chauhan7101@gmail.com

Savita Gill – Department of Applied Science, University Institute of Engineering and Technology, Kurukshetra 136119, India; Savita2015@kuk.ac.in

Conflict of interest: the authors declare no conflict of interest.

NANOSYSTEMS:
PHYSICS, CHEMISTRY, MATHEMATICS

Jeba R., Radhika S., et al. *Nanosystems: Phys. Chem. Math.*, 2022, **13** (1), 78–86.
http://nanojournal.ifmo.ru
DOI 10.17586/2220-8054-2022-13-1-78-86

Original article

Synthesis and characterization of zirconia nanorods as a photo catalyst for the degradation of methylene blue dye

R. Jeba[1,4,a], S. Radhika[2,4], C. M. Padma[3,4], X. Ascar Davix[5]

[1]Research Scholar, Women's Christian College, Tamilnadu, India
[2]Pioneer Kumaraswamy College, Tamilnadu, India
[3]Department of Physics, Women's Christian College, Tamilnadu, India
[4]Manonmaniam Sundaranar University, Abishekapatti, Tirunelveli, Tamilnadu, India
[5]Department of Electronics and Communication Engineering, R.V.R. & J.C. College of Engineering, Andhra Pradesh, India

[a]jeba170787@gmail.com

Corresponding author: R. Jeba, jeba170787@gmail.com

ABSTRACT t-ZrO_2 nano crystalline photocatalyst have been synthesized by a simple co-precipitation method. The crystal structure, morphology, size, and elemental composition of ZrO_2 nanorods were determined using XRD, SEM, EDX analysis. The optical properties and photocatalysis were analyzed using UV-Vis spectroscopy. The investigation of XRD pattern indicates tetragonal (t-ZrO_2) and monoclinic phases (m-ZrO_2) for the annealing temperatures 500 and 900 °C respectively. SEM images depicts rod like morphology. UV-Vis spectra illustrates that the synthesized samples have wide band gap. t-ZrO_2 photocatalyst degrades methylene blue dye with 80 % removal efficiency in 180 minutes.

KEYWORDS zirconium oxide (ZrO_2), co-precipitation, photocatalysis

FOR CITATION Jeba R., Radhika S., Padma C.M., Ascar Davix X. Synthesis and characterization of zirconia nanorods as a photo catalyst for the degradation of methylene blue dye. *Nanosystems: Phys. Chem. Math.*, 2022, **13** (1), 78–86.

1. Introduction

In the current decade, industrialization is rapidly increasing all over the world. The increase in industries leads to the contamination of water. The main cause for water contamination is the waste effluents from chemical, textile, medicine, manufacturing, and petroleum industries [1]. Important organic compounds which contaminate groundwater resources are dyes, pesticides, aromatic solvents. These organic compounds affect the aquatic life and human health. Most of the contaminations are removed using conventional wastewater management systems [2, 3]. Around 700,000 tons of dyes were produced annually for industrial purpose. Dyes used by the textile industry are one important factor which affects the aquatic life [4]. To prevent the contaminations of water and conserve the aquatic ecosystem, there is the need for the research of wastewater treatment options such as coagulation, flocculation, precipitation, adsorption, ion exchange and membrane processing. Advanced Oxidation Process (AOP) is one fundamental water treatment method which has been efficiently developed. AOP is performed at room temperature and normal pressure. A hydroxyl radical is created on the catalyst surface which then acts as oxidizing agent for the decontamination of water [5]. Photocatalysis is a phenomenon in which the valance band electrons are excited into the conduction band when a semiconducting material absorbs a light that is higher than its energy band gap value [27]. Various semiconductor nano metal oxides such as TiO_2, ZnO, SnO_2, have been studied for their photocatalytic ability to degrade pollutants [6]. N-type semiconductor Zirconia has also been used as a photocatalyst [7, 8]. An attempt has been made to investigate the photo degradation of methylene blue (MB) dye using zirconium oxide.

Zirconia is the most popular ceramic oxide used in a variety of applications such as engineering, science and medical fields. The important properties of zirconia are high density, high fracture toughness, high temperature capability and low thermal conductivity [9]. Because of its photochemical stability, high refractive index, large band gap, transparency in the visible and near-infrared regions of the spectrum, and low phonon energy, zirconia is the best optical medium for lanthanide ions among p-type semiconductors. It also has a low phonon energy, which reduces the likelihood of non-radiative transitions due to multiphonon relaxation [31]. Zirconia (ZrO_2) has a high bandgap energy and is a chemically stable material. It exhibits more oxygen vacancies on its surface. Since it has high ion exchange capacity and redox activities, it is used as a photocatalyst. The optical photon energy of zirconia relies on its crystalline structure. This enhances the light absorption ability and charge separation due to the surface modification, which increases the photocatalytic ability. Zirconia is polymorphic, and shows different phases at different temperatures. Also, it shows three crystal structures, namely tetragonal, monoclinic and cubic. Zirconia was used in monoclinic phase which was stable at temperature $T < 1170$ °C. The stable properties of this material are not consistent at room temperature. The phase stability mainly depends on the preparation of the material [10]. The material was prepared at various temperatures and also in three different phases [11, 12]. Tetragonal ZrO_2 was formed at 700 °C by co-precipitation method and it was formed at the same temperature by a microemulsion refined precipitation technique [13]. Only few researchers have reported on the photocatalytic activity of ZrO_2 [20]. ZrO_2 nanoparticles played a major role in the area of photocatalysis with the amalgamation of other visible light active semiconductors. ZrO_2 has negative flat band potential and wide band gap. The conduction band has the lowest potential and the valance band has the highest potential. The reduction potential of e^- in the conduction band was more negative than potentials of H_2/H_2O and CO/CO_2. Due to this, the oxidation potential of H^+ in the valance band was more positive than the potential of O_2/H_2O. This property of ZrO_2 makes it a better photocatalyst [28]. Zheng et al. synthesized Nanocrystalline ZrO_2 by the L-lysine-assisted hydrothermal method and the photocatalytic activity was studied using Rhodamine B (Rh B) as a model pollutant [21]. Olga Długosz et al. proposed ZrO_2–ZnO nanoparticles for the degradation of MB solution. Since ZnO has broad energy gap, it limits the photocatalytic property. To enhance the photocataytic efficiency, ZrO_2–ZnO nanoparticles were used [22].

In this research article, zirconia (ZrO_2) nanoparticles are synthesized by co-precipitation method under various annealing temperatures such as 500, 700, and 900 °C. The obtained nanoparticles are characterized by XRD, UV-vis, EDX and stockticker SEM analysis. Photocatalytic activity of synthesized ZrO_2 nanoparticles on the degradation of MB is analyzed. MB is a phenothiazine derivative, used for dying textiles, and it is highly toxic and carcinogenic. An oxidation process is frequently required to degrade contaminants. Thus, we have chosen MB for the degradation process [29].

2. Materials and method

Nanorods of ZrO_2 are prepared by simple co-precipitation method. An aqueous solution of zirconium oxychloride and sodium hydroxide were taken in the ratio of 0.5:2 M (8.056 g $ZrOCl_2$: 4 g NaOH /50 ml distilled water) to maintain a pH 12. Aqueous solution of zirconium oxychloride was magnetically stirred at 60 °C. NaOH solution was added dropwise to adjust to pH 12 and stirred constantly for 2 hours at 60 °C. The presence of chloride and sodium ions in the final product were controlled by filtering the obtained precipitate followed by repeatedly washing with distilled water and then finally with acetone. Thereafter the precipitate was dried at 150 °C by using a hot air oven. After drying the obtained precipitate was ground by using mortar and pestle to afford a fine powder. The ZrO_2 thus obtained was divided into three parts. One part was annealed at 500 °C, another at 700 °C, and the third part at 900 °C for 2 hours.

X-Ray Diffraction (XRD) analysis with an XPERT-PRO diffractometer was used to determine the crystallite size and proper phases that exist in the zirconia nanorods in the diffraction angle 2θ ranging from 10 to 80°. Optical properties are analyzed using UV-VIS spectrum taken from Perkin Elmer Lambda 35 spectrophotometer. The photocatalytic activity of synthesized ZrO_2 nanoparticles annealed at 500 °C on the degradation of MB was analyzed. An aqueous solution of MB (0.1 M, 50 ml) was taken and 0.2 g of the photocatalyst was suspended in that solution. The experiment was done under UV light irradiation. The continuously stirred solution was irradiated with a 50 W halogen lamp. For every 60 min, 4 ml of dye solution was taken from the system and the dye removal efficiency was analyzed by a UV-Vis spectrometer.

3. Results and discussion

UV-VIS spectrum taken from Perkin Elmer Lambda 35 spectrophotometer describes the absorbance and transmittance properties of zirconia nanorods and is also used to study the removal efficiency of the photocatalyst. Scanning Electron Microscope (SEM) images and EDAX analysis of the nano zirconia is characterized using EV018 (CARL ZEISS) and Quantax 200 with X Flash 6130 microscope.

3.1. Crystallinity, phase and structural studies

The wide band gap zirconia nanorods were synthesized using a co-precipitation method. The XRD pattern of the initial powder for zirconia nanoparticles is shown in Fig. 1 and identified amorphous state of the particle. The peaks at 32, 48, and 57 are in good accord with the standard JCPDS no. 87-2105 and are indexed as orthorhombic ZrO_2. The element is annealed at various temperatures and examined to obtain a definite structure. The X-ray diffraction pattern obtained for ZrO_2 nanoparticles annealed at 500, 700 and 900 °C are shown Fig. 2. The XRD pattern was used to identify the phase of nanoparticles and it confirmed pure tetragonal phase (JCPDS-50-1089) for zirconia annealed at 500 °C. The peaks are indexed as follows: 30.24° (011), 34.97° (002), 35.31° (110), 50.59° (112), 59.92° (013), 63.04° (202) and 74.34° (220). The average crystallite size of the sample at 500 °C was 29.74 nm.

The XRD pattern of ZrO_2 annealed at 700 °C confirms both tetragonal and monoclinic phases. The phase composition at 700 °C consists of 87 % monoclinic and 13 % tetragonal phases.

The highest peak in the pattern is indexed as tetragonal phase (JCPDS-50-1089) corresponding to the angle 30.3° (011). The remaining peaks are indexed as the monoclinic phase (JCPDS-65-1025). The major peaks of the monoclinic phase are 50.67° (122), 50.21° (220), 60.08° (302), 28.28° (111), and 59.88° (131). The average crystallite size of the sample at 700 °C is 42.5 nm.

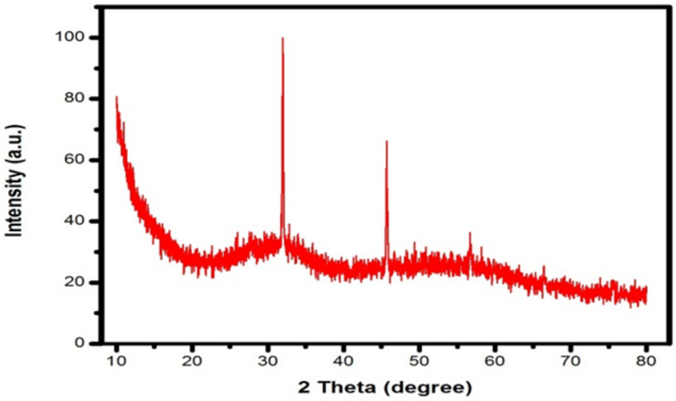

FIG. 1. XRD pattern of as prepared sample

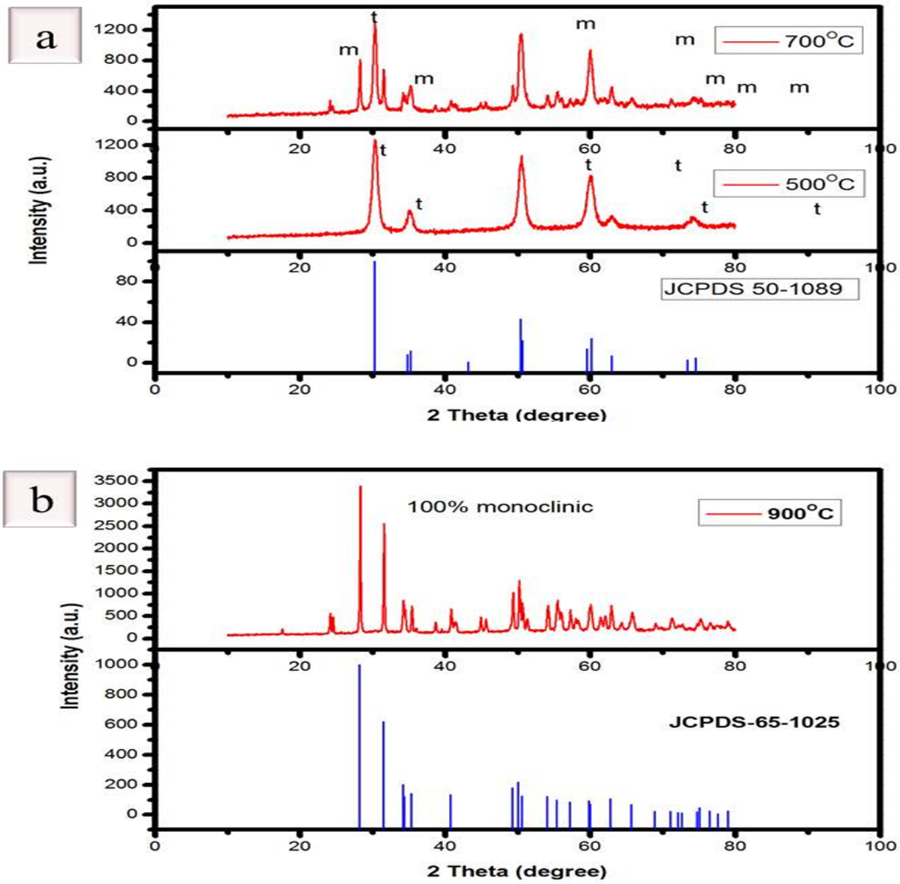

FIG. 2. XRD pattern of ZrO_2 calcined at (a) 500 °C and 700 °C, (b) 900 °C

The peaks of the XRD pattern of ZrO_2 annealed at 900 °C are indexed as monoclinic phase (JCPDS-65-1025). The major peaks of the monoclinic phase are 28.30° ($\bar{1}11$), 31.59° (111), 50.24° (220), 49.39° (022), and 34.24° (020). The average crystallite size of the sample at 900 °C is 63.84 nm. The average crystallite size,phase and energy gap parameters of ZrO_2 with various annealing temperature are listed in Table 1. The XRD patterns of all three samples reveal that the tetragonal phase is transformed into the monoclinic as the annealing temperature is increased from 500 to 900 °C. The faster phase transformation is due to the increase of calcination temperature [23, 24].

Annealing temperature has a significant role on the structural modification of the nanoparticles. It was observed that the crystallite size increased with increasing temperature. Generally, calcination decreases the lattice defects and strains; however,on the other hand, higher temperatures may cause crystallites to coalescence, which leads to an increase in the crystallite and nanoparticle sizes [26]. The average crystallite size (D) of ZrO_2 powder was calculated using Scherrer's formula, $D = \dfrac{0.9\lambda}{\beta \cos\theta}$, where, λ is the wavelength of the X-rays; θ is the Bragg's diffraction angle, and β is the full width

TABLE 1. The average crystallite size, phase and energy gap parameters of ZrO_2 with various annealing temperatures

Annealing temperature	Average Crystallite size, D (nm)	Phase	Energy gap parameters, eV	
			E_{g1}	E_{g2}
500 °C	29.74	t	4.7	4.6
700 °C	36.09 (t) 50.45 (m)	t + m	4.6	4.4
900 °C	63.84	m	4.4	4.3

at half maximum (FWHM) of the diffraction peaks (in radians) [30, 33]. The diffraction pattern shows sharp and well defined peaks, which indicate the highly crystalline nature as well as purity of the sample [14].

3.2. Optical studies

Figure 3 shows the optical absorbance spectrum of ZrO_2 at different annealing temperatures such as 500, 700, and 900 °C. The strong absorbance peak for ZrO_2 annealed at 500 and 700 °C occurs at 375.2 nm. The strong absorbance peak occurs at 278.6 nm, for the sample prepared at 900 °C. So it is noted that, the absorbance increases when the annealing temperature increases.

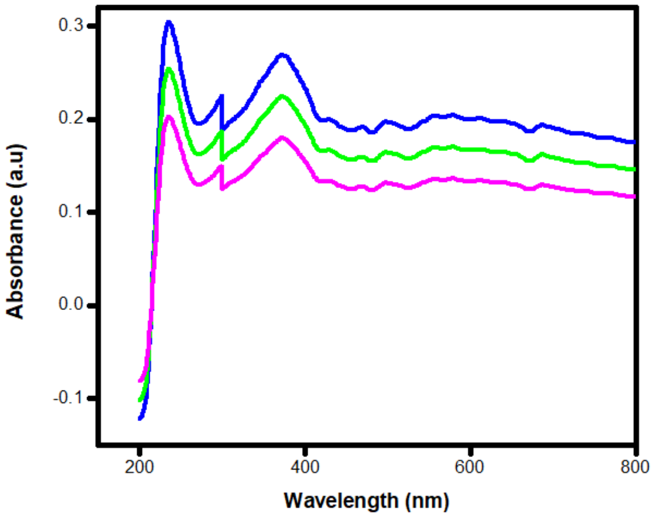

FIG. 3. Optical absorbance spectrum of ZrO_2 at different calcination temperatures

The band gap energy of the prepared samples is calculated by using Tauc relation:

$$\alpha h\nu = A(h\nu - E_g)^n, \tag{1}$$

where, $h\nu$ is the energy of photon, E_g is the band gap energy, A is the proportionality constant, n takes the value $1/2$ for direct allowed transitions and α is the absorption coefficient [15]. The absorption coefficient α is determined using the formula:

$$\alpha = \frac{2.303 \log (1/T)}{t}, \tag{2}$$

Here, T represents transmittance and t represents the thickness of sample ($t = 1$ mm) [16]. The Tauc plot is drawn to determine the band gap of ZrO_2 at different annealing temperatures and it is shown in Fig. 4. It is identified that, the variation of $(\alpha h\nu)^2$ with respect to $h\nu$ is linear which reveals the transition is a directly allowed transition. The band gap energy was calculated from the x-axis intersection point of the linear fit of the Tauc plot. The band gap energy of ZrO_2 at different annealing temperature was determined from the Tauc plot and is listed in Table 1. E_g values of the synthesized nanostructures are found from 4.3 to 4.7 eV.

The energy gap of ZrO_2 decreases with respect to an increase in the temperature. This is due to the increased crystallite size, increased inter-atomic space and surface defect such as oxygen vacancies [24]. The variation of electronic levels that arises between the conduction band and valance band is due to the presence of oxygen vacancies [25].

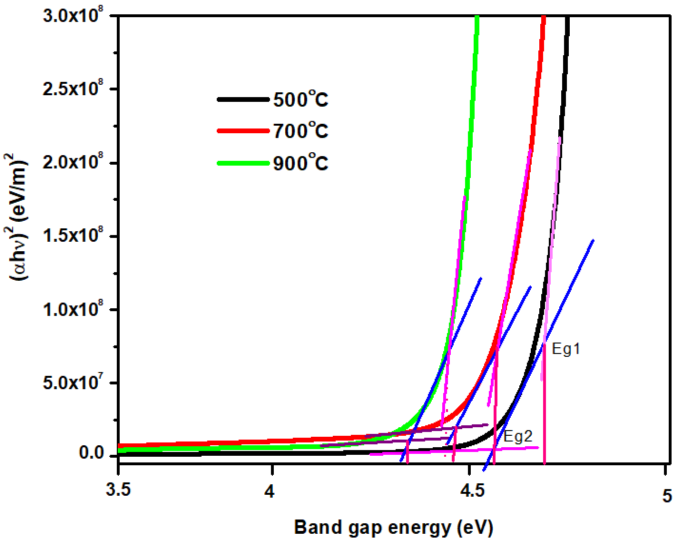

FIG. 4. Tauc's plot of ZrO_2 at different annealing temperatures to determine the band gap energy

3.3. SEM and EDX analysis

The morphology of the synthesized ZrO_2 nanoparticles at 500, 700, and 900 °C was analyzed with scanning electron microscopy (SEM) taken at different magnification scales, and is the results are shown in Fig. 5. The synthesized samples were observed to have a rod-shaped morphology. The first stage of the growth of nanorod is isotropic which has the growth of seed particles. The second stage of the growth is anisotropic which has the growth in one direction. The third stage of the growth is rod shaped particle. The approximate values of the average lengths and widths of the nanorods at 500, 700, and 900 °C are 222, 159, 102 nm and 31, 14, 17 nm respectively.

The EDX characterization depicts the elemental composition of the prepared ZrO_2 nanoparticles at 500, 700, and 900 °C. The EDX characterization spectrum is shown in Fig. 6. High intense peak was identified for zirconium (Zr) and oxygen (O) elements. These results are also in agreement with the SEM-EDX mapping images shown in Fig. 7. Furthermore, these images confirm that Zr and O elements are homogeneously dispersed.

3.4. Photocatalytic performance

The photocatalytic performance of the prepared catalyst ZrO_2 was experimentally determined by the degradation of MB organic dye. The optical absorbance spectra of the degradation of MB dye using ZrO_2 nanoparticles annealed at 500 °C is shown in Fig. 8. An aqueous solution of MB (0.1 M, 50 ml) was taken and 0.2 g of photocatalyst zirconia was added. The experiment was done under UV irradiation at 350 nm. The solution is exposed to halogen lamp of 50 W with continuous stirring. For every 60 min, 4 ml of dye solution is taken from the system and the degradation percentage is analyzed by UV-Vis spectrophotometer. From the absorbance spectrum, the strong peak is identified at 663.25 nm which is the absorption wavelength of MB dye. The following equation provides the removal efficiency (E) of MB degradation:

$$E = \frac{C_0 - C}{C_0} \times 100\,\%, \tag{3}$$

where C_0 is the initial concentration of dye and C is the concentration of MB after UV irradiation. It was observed that, 53 % of MB dye degraded after 1 hour and 80 % of MB dye was degraded after 3 hours. This is mainly due to high crystallinity nature of t-ZrO_2 prepared at 500 °C, small crystallite size and well defined morphology and surface properties. The normalized residual concentration of MB dye is estimated using:

$$\frac{C_t}{C_0} = \frac{A_t}{A_0},$$

where C_0 and C_t are the initial and residual concentration of MB dye, A_t and A_0 are the absorbance intensity at time t and at time $t = 0$ obtained from UV-absorbance spectrum [17].

The growth of the rod shaped particle is greater in one direction with respect to the growth of the particle in other dimensions [18]. Since, the morphology of the prepared nanoparticle is rod shape; the surface area of the particle is high. The high surface area provides more active sites for the reaction of photodegradation [19]. Due to this property, the efficiency of the degradation of MB is high for zirconia even though it has wide band gap. The decomposition of MB dye by ZrO_2 with respect time is shown in Fig. 9. In addition to particle size, phase composition, and optical characteristics, there may be other parameters that influence photocatalytic activity [32].

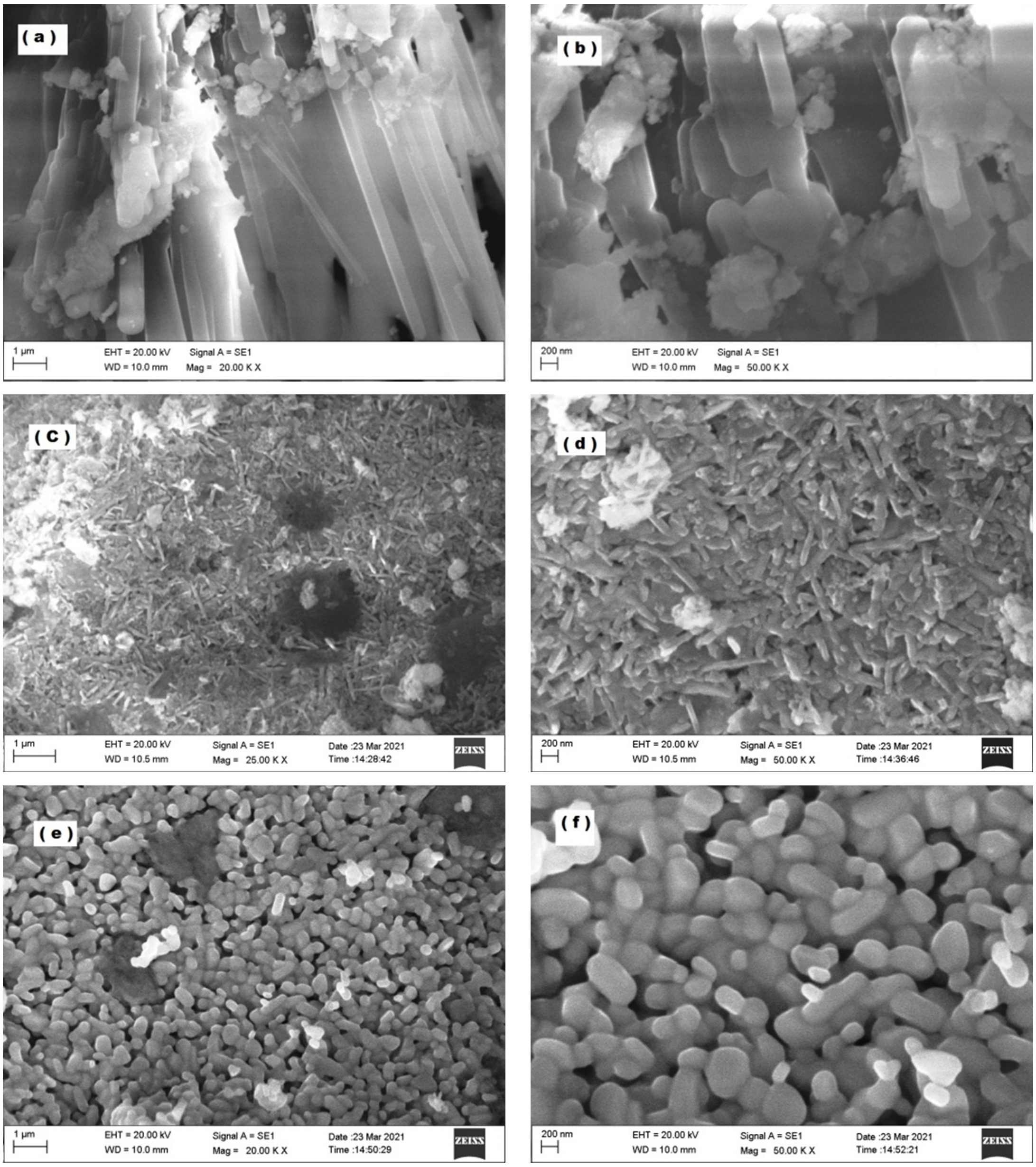

FIG. 5. SEM image of ZrO_2 at (a), (b) 500 °C, (c), (d) 700 °C and (e), (f) 900 °C

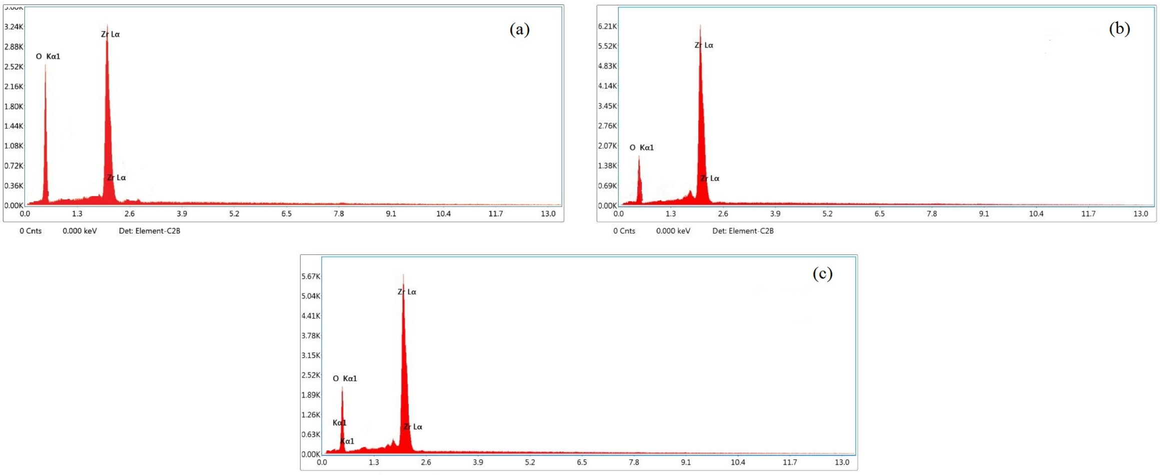

FIG. 6. EDX characterization spectra of ZrO_2 at (a) 500 °C, (b) 700 °C, and (c) 900 °C

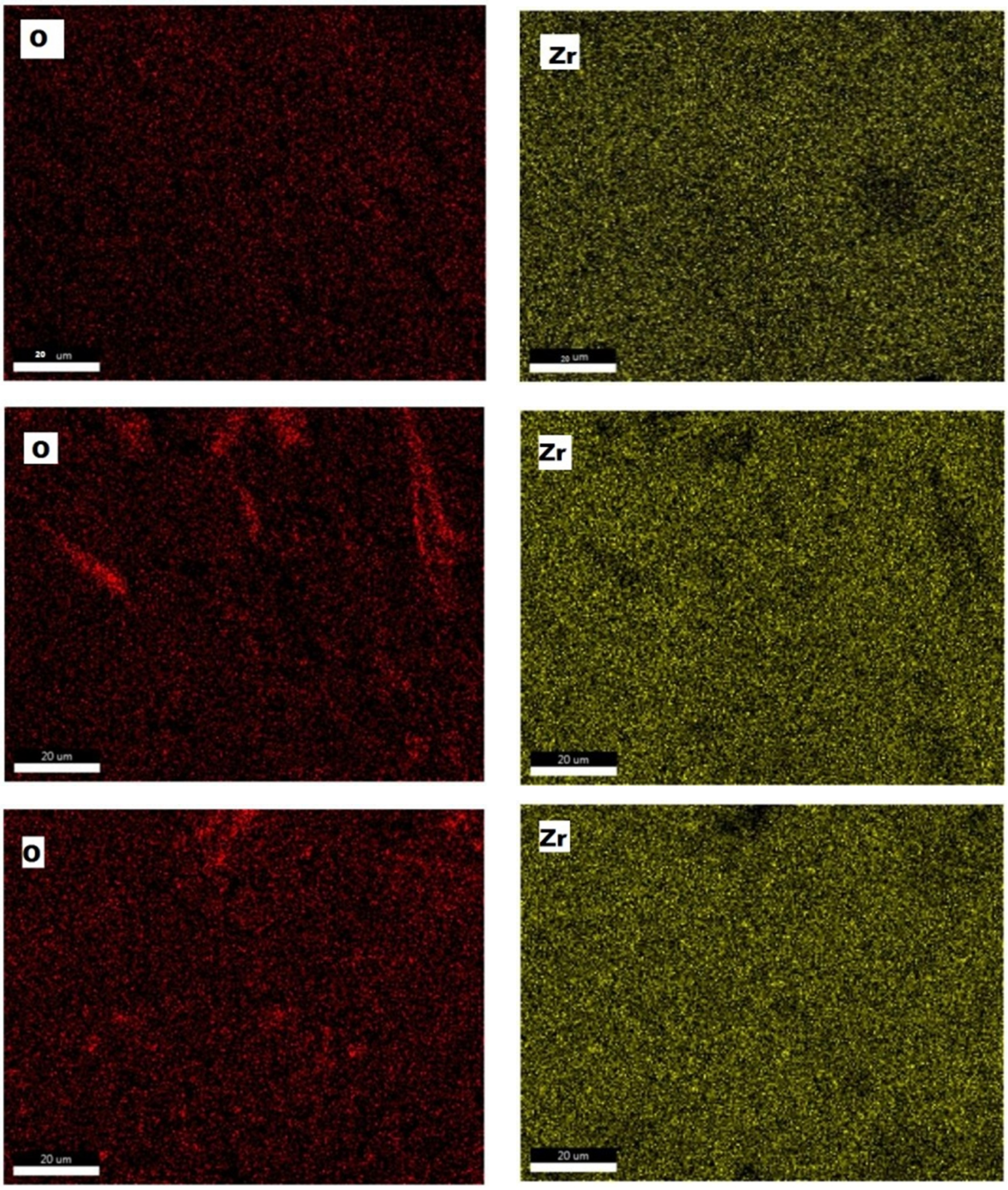

FIG. 7. EDX mapping of ZrO_2 at (a) 500 °C, (b) 700 °C and (c) 900 °C

4. Conclusion

Zirconium oxide nanorods have been successfully synthesized by a co-precipitation method under various annealing temperatures such as 500, 700, 900 °C. XRD analysis confirmed the tetragonal phase (t-ZrO_2) at 500 °C. Both the tetragonal and monoclinic phases were present when annealed at 700 °C. The pure monoclinic phase (m-ZrO_2) was identified at 900 °C. The crystallite size increased at higher annealing temperatures. The band gap energy was calculated from UV-Vis absorption spectrum and it was found to decrease with increases in annealing temperature. Rod shaped morphology was observed in SEM images, ans therefore, the particles had high surface area. This enhances the removal efficiency of the photocatalyst. The elemental composition of the synthesized nanoparticles was found using EDX analysis. The nanoparticles synthesized at 500 °C provide small crystallite size and high crystallinity and rod shaped morphology and therefore used as photocatalyst for degradation of MB dye. This photocatalyst degrades 80 % of MB dye in 180 minutes under UV irradiation.

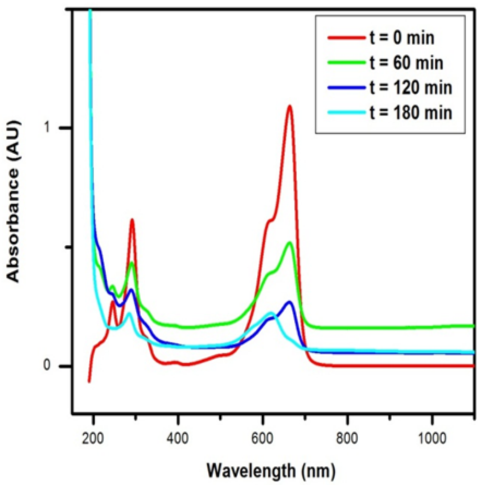

FIG. 8. Optical absorbance spectra of MB dye using ZrO$_2$ at 500 °C

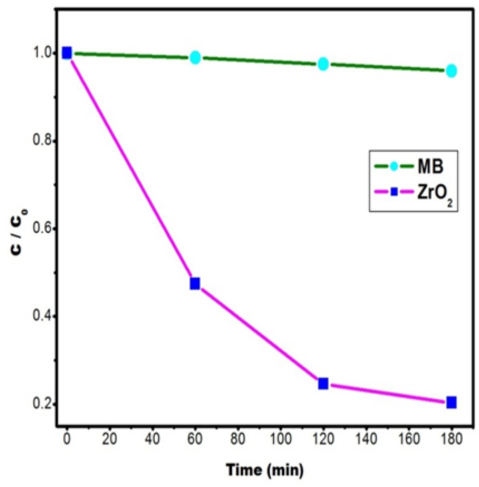

FIG. 9. Removal efficiency of ZrO$_2$

References

[1] Mahy J.G., Lambert S.D., et al. Ambient temperature ZrO$_2$-doped TiO$_2$ crystalline photocatalysts: Highly efficient powders and films for water depollution. *Materials Today Energy*, 2019, **13**, P. 312–322.

[2] Sugi S., Usha Rajalakshmi P., Shanthi J. Photocatalytic Degradation efficiency of Cu$_x$Zn$_{1-x}$O Composite. *Optik*, 2017, **131**, P. 406–413.

[3] Scholz N. Setting Criteria on Endocrine Disruptors: Follow-Up to the General Court Judgment. Brief. From Eur. Parliam., 27 April 2016, P. 1–10.

[4] Ratnayake S.P., Mantilaka M.M.M.G.P.G., et al. Carbon quantum dots-decorated nano-zirconia: A highly efficient photocatalyst. *Applied Catalysis A: General*, 2019, **570**, P. 23–30.

[5] Oturan M.A., Aaron J.J. Advanced oxidation processes in water/wastewater treatment: principles and applications. A review. *Critical Reviews in Environmental Science and Technology*, 2014, **44** (23), P. 2577–2641.

[6] Wang J., Gu H. Novel metal nanomaterials and their catalytic applications. *Molecules*, 2015, **20** (9), P. 17070–17092.

[7] Kirsch B.L., Tolbert S.H. Stabilization of Isolated Hydrous Amorphous and Tetragonal Zirconia Nanoparticles through the Formation of a Passivating Alumina Shell. *Adv. Funct. Mater.*, 2003, **13**, P. 281–288.

[8] Rashad M.M., Baioumy H.M. Effect of thermal treatment on the crystal structure and morphology of zirconia nanopowders produced by three different routes. *J. Mater. Process. Technol.*, 2008, **195**, P. 178–185.

[9] Ward D.A., Ko E.I. Synthesis and structural transformation of zirconia aerogels. *Chem. Mater.*, 1993, **5**, P. 956–969.

[10] Trice R.W., Su Y.J., Mawdsley J.R., Faber K.T. Effect of heat treatment on phase stability, microstructure, and thermal conductivity of plasma-sprayed YSZ. *J. Mater. Sci.*, 2002, **37**, P. 2359–2365.

[11] Neppolian B., Wang Q., Yamashita H., Choi H. Synthesis and characterization of ZrO$_2$–TiO$_2$ binary oxide semiconductor nanoparticles: Application and interparticle electron transfer process. *Appl. Catal. A: Gen.*, 2007, **333**, P. 264–271.

[12] Wu C., Zhao X., et al. Gas-phase photo-oxidations of organic compoundsover different forms of zirconia. *J. Mol. Catal. A: Chem.*, 2005, **229**, P. 233–239.

[13] Rajababu C. Influence of calcination temperature on structural, optical, dielectric properties of nano zirconium oxide. *Optik*, 2016, **127** (11), P. 4889–4893.

[14] Besky Job C., Shabu R., Paul Raj S. Growth, structural, optical, and photo conductivity studies of potassium tetra fluoro antimonite. *Optik*, 2016, **127** (8), P. 3783–3787.

[15] Radhika S., Padma C.M., Ramalingom S., Chithambara Thanu T. Growth, optical, thermal, mechanical and dielectric studies of potassium sulphate crystals doped with urea. *Archives of Physics Research*, 2013, **4** (1), P. 49–59.

[16] Sadeghzadeh-Attar A. Efficient photocatalytic degradation of methylene blue dye by SnO$_2$ nanotubes synthesized at different calcination temperatures. *Solar Energy Materials and Solar Cells*, 2018, **183**, P. 16–24.

[17] Sheeba J.R., Radhika S., Padma C.M. Photo catalytic degradation of Methylene Blue Dye by Cu doped SnO$_2$ Nano Crystals. *Wutan Huatan Jisuan Jishu*, 2020, **16** (9), P. 66–76.

[18] Bilal A., Sachin K., Sumeet K., Animesh K. Ojha. Shape Induced (spherical, sheets and rods) Optical and Magnetic Properties of CdS Nanostructures with Enhanced Photocatalytic Activity for Photodegradation of Methylene Blue Dye under Ultra-violet Irradiation. *J. of Alloys and Compounds*, 2016, **679**, P. 324–334.

[19] Vijaya Sankar K., Ashok M. Significantly enhanced photo catalytic activities of PbBi$_2$Nb$_2$O$_9$(Bulk)/TiO$_2$(Nano) hetero structured composites for methylene blue dye degradation under visible light. *Materials Chemistry and Physics*, 2020, **244**, 122659.

[20] Venkata Reddy Ch., Bathula Babu, Neelakanta Reddy I, Jaesool Shim. Synthesis and Characterization of Pure tetragonal ZrO$_2$ Nano Particles with enhanced Photocatalytic activity. *Ceramics International*, 2018, **44** (6), P. 6940–6948.

[21] He Zheng, Kaiyu Liu, Huaqiang Cao, Xinrong Zhang. l-Lysine-Assisted Synthesis of ZrO$_2$ Nanocrystals and Their Application in Photocatalysis. *J. Phys. Chem. C*, 2009, **113** (42), P. 18259–18263.

[22] Długosz O., Szostak K., Banach M. Photocatalytic properties of zirconium oxide–zinc oxide nanoparticles synthesised using microwave irradiation. *Applied Nanoscience*, 2020, **10**, P. 941–954.

[23] Prasad K., Pinjari D.V., Pandit A.B., Mhaskea S.T. Synthesis of zirconium dioxide by ultrasound assisted precipitation: Effect of calcination temperature. *Ultrasonics Sonochemistry*, 2011, **18** (5), P. 1128–1137.

[24] Horti N.C., Kamatagi M.D., et al. Structural and optical properties of zirconium oxide (ZrO$_2$) nanoparticles: effect of calcination temperature. *Nano Express*, 2020, **1** (1), 010022.

[25] Berlin J., Sujathalekshmy S., et al. Effect of Mn doping on the structural and optical properties of ZrO_2 thin films prepared by sol–gel method. *Thin Solid Films*, 2014, **550**, P. 199–205.

[26] Shirsath S.E., Kadam R.H., et al. Effect of sintering temperature and the particle size on the structural and magnetic properties of nanocrystalline $Li_{0.5}Fe_{2.5}O_4$. *J. of Magnetism and Magnetic Materials*, 2011, **323** (23), P. 3104–3108.

[27] Baytar O., Sahin O., Kilicvuran H., Horoz S. Synthesis, structural, optical and photocatalytic properties of Fe-alloyed CdZnS nanoparticles. *J. of Materials Science: Materials in Electronics*, 2017, **29** (6), P. 4564–4568.

[28] Sayama K., Arakawa H. Photocatalytic Decomposition of Water and Photocatalytic Reduction of Carbon Dioxide over ZrO_2 Catalyst. *The J. of Physical Chemistry*, 1993, **97** (3), P. 531–533.

[29] Vasiljevic Z., Dojcinovic M.P., et al. Photocatalytic degradation of methylene blue under natural sunlight using iron titanate nanoparticles prepared by a modified sol–gel method. *R. Soc. Open Sci.*, 2020, **7** (9), 200708.

[30] Langford J.I., Wilson A.J.C. Scherrer after sixty years: A survey and some new results in the determination of crystallite size. *J. Appl. Cryst.*, 1978, **11**, P. 102–113.

[31] Bugrov A.N., Smyslov R.Yu., et al. Phosphors with different morphology, formed under hydrothermal conditions on the basis of ZrO_2:Eu^{3+} nanocrystallites. *Nanosystems: Phys., Chem., Math.*, 2019, **10** (6), P. 654–665.

[32] Kolesnik I.V., Lebedev V.A., Garshev A.V. Optical properties and photocatalytic activity of nanocrystalline TiO_2 doped by 3d-metal ions. *Nanosystems: Phys., Chem., Math.*, 2018, **9** (3), P. 401–409.

[33] Lele S., Anantharaman T.R. Influence of crystallite shape on particle size broadening of Debye-Scherrer reflections. *Proc. Indian Acad. Sci.*, 1966, **64**, P. 261–274.

Submitted 9 June 2021; revised 6 October 2021; accepted 1 February 2022

Information about the authors:

Rengaswamy Jeba – Research Scholar, Reg. No. 18223282132002, Women's Christian College, Tamilnadu, India-629001; Manonmaniam Sundaranar University, Abishekapatti, Tirunelveli, Tamilnadu – 627012, India;
ORCID 0000-0002-5156-0628; jeba170787@gmail.com

Sathasivam Radhika – Department of Physics, Pioneer Kumaraswamy College, Tamilnadu – 629003, India; Manonmaniam Sundaranar University, Abishekapatti, Tirunelveli, Tamilnadu-627012, India; radhisatha@yahoo.com

Chellaia Muthammal Padma – Department of Physics, Women's Christian College, Tamilnadu – 629001, India; Manonmaniam Sundaranar University, Abishekapatti, Tirunelveli, Tamilnadu – 627012, India; padmajeyaraj19@gmail.com

Xavier Durai Ascar Davix – Department of Electronics and Communication Engineering, R.V.R. & J.C. College of Engineering, Andhra Pradesh – 522019, India; ORCID 0000-0002-6795-7865; davixascar@gmail.com

Conflict of interest: the authors declare no conflict of interest.

NANOSYSTEMS:
PHYSICS, CHEMISTRY, MATHEMATICS

Original article

Sokolova A.N., Proskurina O.V., et al. *Nanosystems: Phys. Chem. Math.*, 2022, **13** (1), 87–95.
http://nanojournal.ifmo.ru
DOI 10.17586/2220-8054-2022-13-1-87-95

Photocatalytic properties of composites based on $\mathbf{Y_{1-x}Bi_xFeO_3}$ $(\mathbf{0 \le x \le 0.15})$ nanocrystalline solid solutions with a hexagonal structure

Anastasiya N. Sokolova[1,2,a], Olga V. Proskurina[1,2,b], Dmitry P. Danilovich[1,c], Victor V. Gusarov[2,d]

[1]St. Petersburg State Institute of Technology, 190013 St. Petersburg, Russia

[2]Ioffe Institute, 194021 St. Petersburg, Russia

[a]sok5552@mail.ru, [b]proskurinaov@mail.ru, [c]dmitrydanilovich@gmail.com, [d]victor.v.gusarov@gmail.com

Corresponding author: Anastasiya N. Sokolova, sok5552@mail.ru

ABSTRACT Nanopowders of $Y_{1-x}Bi_xFeO_3$ ($x = 0$, 0.05, 0.10, 0.15) solid solutions were obtained by coprecipitation of hydroxides with simultaneous sonication and subsequent thermal treatment of the precipitate in air at 800 °C for 1 min. in the annealing-quenching mode. The results of X-ray phase analysis showed the formation of nanocrystalline solid solutions with a structure of hexagonal yttrium orthoferrite. The average crystallite size increases from 4 to 10 nm with the increasing bismuth content in the solid solution. The influence of Y^{3+} substitution for Bi^{3+} in yttrium orthoferrite on the photocatalytic activity of $Y_{1-x}Bi_xFeO_3$ nanopowders during the Fenton-like degradation of methyl violet under the visible light irradiation has been studied. The maximum reaction rate constant of 0.0197 min^{-1} was shown by the $YFeO_3$ nanopowder, which has the smallest crystallite size of ∼4 nm.

KEYWORDS coprecipitation, yttrium orthoferrite, heat treatment, nanoparticles, photocatalyst, Fenton-like reactions

ACKNOWLEDGEMENTS X-ray diffraction studies and elemental analyses of samples were performed employing the equipment of the Engineering Center of the St. Petersburg State Institute of Technology (Technical University). The research was supported by the Russian Science Foundation Grant 20-63-47016.

FOR CITATION Sokolova A.N., Proskurina O.V., Danilovich D.P., Gusarov V.V. Photocatalytic properties of composites based on $\mathbf{Y_{1-x}Bi_xFeO_3}$ $(\mathbf{0 \le x \le 0.15})$ nanocrystalline solid solutions with a hexagonal structure. *Nanosystems: Phys. Chem. Math.*, 2022, **13** (1), 87–95.

1. Introduction

Recently, yttrium orthoferrite $YFeO_3$ has become of interest to researchers due to the broadening of the fields of its practical applications. It can be used as a basis of a functional material in gas sensitive sensors, in magnetic devices, as a catalyst, a photocatalyst in particular [1–3]. Most studies have focused on yttrium orthoferrite with an orthorhombic structure [4, 5]. The metastable modification of yttrium orthoferrite with a hexagonal structure has been studied much less [6–9].

Hexagonal structured nanocrystalline yttrium orthoferrite can be obtained using various soft chemistry methods, such as hydrothermal, microwave synthesis, sol-gel, co-precipitation followed by thermal treatment, and solution combustion. These methods make it possible to control the structure, size of particles and crystallites, and their morphology, which determine the functional properties of yttrium orthoferrite-based materials [10–14].

The possibility of yttrium orthoferrite-based solid solutions formation, their structural features, and properties are even less studied. At the same time, many orthoferrites have a set of functional properties that are important for application. These compounds include, in particular, bismuth orthoferrite [15–19]. There are publications [20–23] devoted to the study of solid solutions based on the Bi-doped $YFeO_3$, but all these articles describe only the samples with an orthorhombic structure.

One of the promising directions for using orthoferrite-based nanopowders is their application for purifying polluted aqueous media thanks to their high photocatalytic activity [6, 24–30].

Due to the above reasons, it is of interest to study the synthesis of $Y_{1-x}Bi_xFeO_3$ nanocrystalline solid solutions with a hexagonal structure and to determine their photocatalytic properties.

2. Experimental

2.1. $Y_{1-x}Bi_xFeO_3$ synthesis

Nanocrystalline $Y_{1-x}Bi_xFeO_3$ $(0 \le x \le 0.15)$ solid solutions were synthesized in several stages. $Bi(NO_3)_3{\cdot}5H_2O$, $Y(NO_3)_3{\cdot}6H_2O$, $Fe(NO_3)_3{\cdot}9H_2O$ of p.a. purity grade without additional purification were used as initial reagents. Salts were weighted in proportions in order to obtain of 1 g of yttrium-bismuth ferrite and then sequentially dissolved in 2 ml of 6 M aq. HNO_3 aqueous solution with stirring and heating. Magnetic stirring was carried out for 15 min. Separately, 40 ml of 4M aqueous NaOH was prepared.

Solutions of nitrates and alkali were mixed by the reverse precipitation with simultaneous magnetic stirring under sonication (with a power of 630 W and a frequency of 23 kHz), pouring the nitrate solution into the alkali solution with a syringe in a thin stream for 1 min.

The coprecipitated metal hydroxides were rinsed with distilled water until neutral pH value and dried at 80 °C for 10 h.

The samples were thermally treated in the annealing-quenching mode in a tube furnace preheated to 800 °C. The platinum crucible containing a sample was placed in the oven for 1 min, after which the sample was taken out and spilled onto a metal plate for rapid cooling.

2.2. Characterization

X-ray diffraction patterns were recorded on a Rigaku SmartLab 3 diffractometer (Rigaku, Japan) operating in Bragg-Brentano geometry and equipped with an X-ray tube with a copper anode. Radiation filtration (Cu-K_α duplicate X-ray line) was carried out using a nickel K_β filter. The measurements were carried out in the range 2θ = 10 – 70° with a 0.01° step, at a rate of 0.5°/min. Quantitative X-ray phase analysis and determination of the cell parameters of all samples were carried out using α-Al_2O_3 powder as an internal standard and shooting in the range 2θ = 10 – 120°. The average crystallite size was determined by the Halder-Wagner method using the SmartLab Studio II software package from Rigaku.

The size distribution of crystallites and distribution parameters were determined by the method of fundamental parameters in approximation to the log-normal distribution model, using the SmartLab Studio II software package.

The elemental analysis of the samples was determined using an FEI Quanta 200 scanning electron microscope with an attachment for energy dispersive microanalysis.

IR spectra were obtained on an FSM-1202 IR Fourier spectrometer (Russia).

The photocatalytic activity of samples in the process of photo Fenton-like oxidation of methyl violet (MV) in the presence of hydrogen peroxide (H_2O_2) in the 400–700 nm wavelength range was studied.

The photocatalytic activity of the heat-treated $Y_{1-x}Bi_xFeO_3$ nanopowders was studied in the process of Fenton-like oxidation of MV in the presence of hydrogen peroxide (H_2O_2) in the 400–700 nm wavelength range. The dye concentration was determined on a Shimadzu UV1600 spectrophotometer (Japan).

The light-mediated Fenton-like oxidation of methyl violet was carried out in 50 ml beakers using a magnetic stirrer and two 100 W Xe lamps with a UV-light filter ($\lambda \geq 420$ nm). The experimental system was placed in an isolated box, which made it possible to thermostat the reaction solutions and avoid exposure to external radiation. In all experiments, 25 ml of a solution was prepared to contain the exact amount of $Y_{1-x}Bi_xFeO_3$ catalyst (previously sonicated for 30 min.), methylene violet and hydrogen peroxide.

3. Results and discussion

The elemental analysis results for the samples are presented in Table 1.

It can be seen from the data in the table that all the samples have a slight excess of iron in comparison with the total amount of yttrium and bismuth, and a slight excess of bismuth with respect to yttrium in the samples with the amount of bismuth specified for the synthesis at $x = 0.05$ and 0.15. Taking into account the error of the method, the samples' compositions correspond to the nominal one. Later in this article, all samples will be designated in accordance with the nominal amount of bismuth in $Y_{1-x}Bi_xFeO_3$, i.e. sample 1 – $x = 0$, sample 2 – $x = 0.05$, sample 3 – $x = 0.10$, and sample 4 – $x = 0.15$.

TABLE 1. Elemental analysis of the initial samples

Sample	Nominal composition		EDX data	
	$YO_{1.5}$: $BiO_{1.5}$: $FeO_{1.5}$	$YO_{1.5}$: $BiO_{1.5}$	$YO_{1.5}$: $BiO_{1.5}$: $FeO_{1.5}$	$YO_{1.5}$: $BiO_{1.5}$
1	1 : 0 : 1	–	0.96 : 0 : 1	–
2	0.95 : 0.05 : 1	0.95 : 0.05	0.92 : 0.06 : 1	0.93 : 0.07
3	0.90 : 0.10 : 1	0.90 : 0.10	0.90 : 0.09 : 1	0.90 : 0.10
4	0.85 : 0.15 : 1	0.85 : 0.15	0.83 : 0.13 : 1	0.84 : 0.16

The conditions for the thermal treatment of coprecipitated hydroxides were chosen in order to obtain nanocrystals of the minimum size in all the investigated samples. The $Y_{0.95}Bi_{0.05}FeO_3$ composition was selected for the study. The crystallization temperature of pure bismuth orthoferrite is much lower than that of pure yttrium orthoferrite (~490 °C [31] compared to ~800 °C [32]). An increase in the amount of bismuth in a sample leads to a decrease in the crystallization temperature, and the crystalline phase in samples with a larger amount of bismuth will be observed already at lower temperatures, whereas the samples with a smaller amount of bismuth will still remain X-ray amorphous.

Figure 1 presents the X-ray diffraction patterns of $Y_{0.95}Bi_{0.05}FeO_3$ samples obtained under different thermal treatment conditions. At 750 °C, a sample remains X-ray amorphous, as well as when the heating time is reduced to 0.5 min. at 800 °C. With an increase in temperature up to 850 °C (with a heating duration of 1 min.), crystalline phase peaks corresponding to hexagonal yttrium orthoferrite [ICDD 00-048-0529] are observed in a sample, but with crystallites of larger size compared to the sample heated at 800 °C.

Thus, the thermal treatment conditions of 800 °C and 1 min duration were chosen.

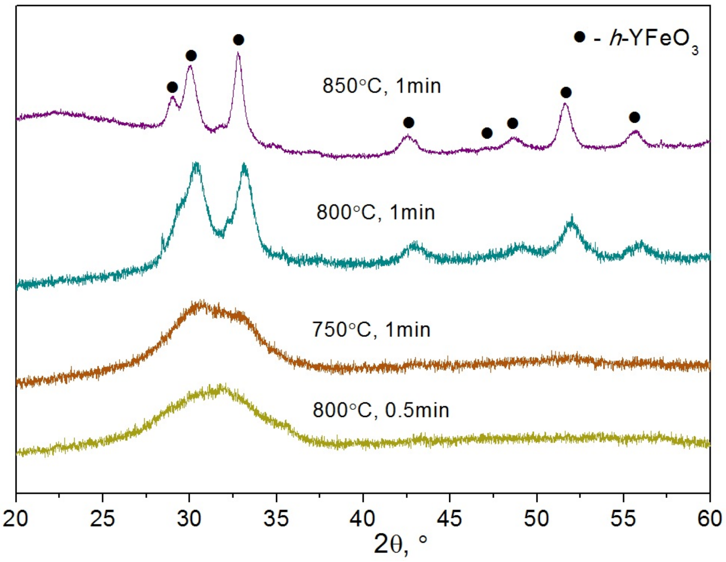

FIG. 1. X-ray diffraction patterns of an $Y_{0.95}Bi_{0.05}FeO_3$ sample thermally treated under different conditions

X-ray diffraction patterns of $Y_{1-x}Bi_xFeO_3$ ($0 \leq x \leq 0.15$) samples heated for 1 min. at 800 °C are shown in Fig. 2 in the 2θ=10–70° angle range. All samples contain peaks corresponding to the hexagonal phase of yttrium orthoferrite h-$YFeO_3$ [PDF 00-048-0529]. Samples 3 and 4 demonstrated the appearance of peaks of an impurity phase corresponding to c-$Y_3Fe_5O_{12}$ cubic garnet [JCPDS 00 – 0033-0693]. The formation of an iron-rich phase can be explained by some compositional inhomogeneity in the coprecipitated hydroxides despite the sonication during synthesis aimed at minimizing the spatial separation of the solid solution components.

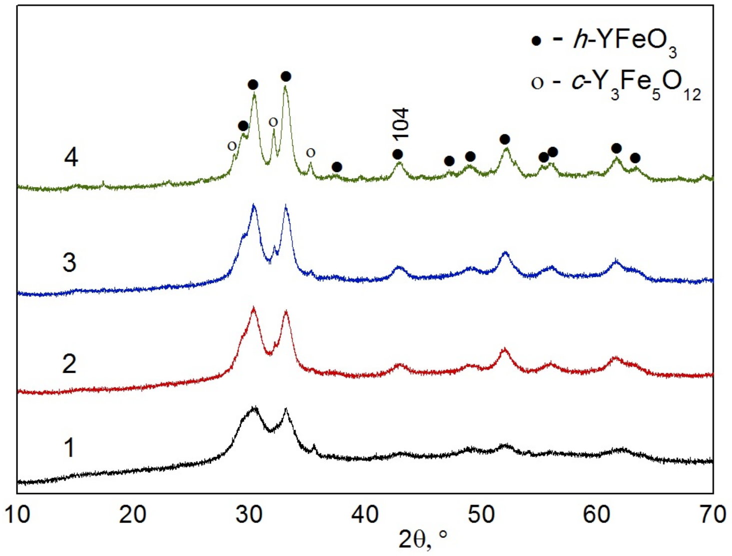

FIG. 2. X-ray diffraction patterns of $Y_{1-x}Bi_xFeO_3$ samples (sample 1 – $x = 0$, sample 2 – $x = 0.05$, sample 3 – $x = 0.10$, and sample 4 – $x = 0.15$)

Figure 3 shows the dependence of the cell parameters of a phase based on a hexagonal yttrium ferrite. The cell parameters increase depending on the composition of the sample, which provides evidence for the incorporation of bismuth into the crystal lattice of hexagonal yttrium orthoferrite and the formation of an $\mathrm{Y}_{1-x}\mathrm{Bi}_x\mathrm{FeO}_3$ solid solution.

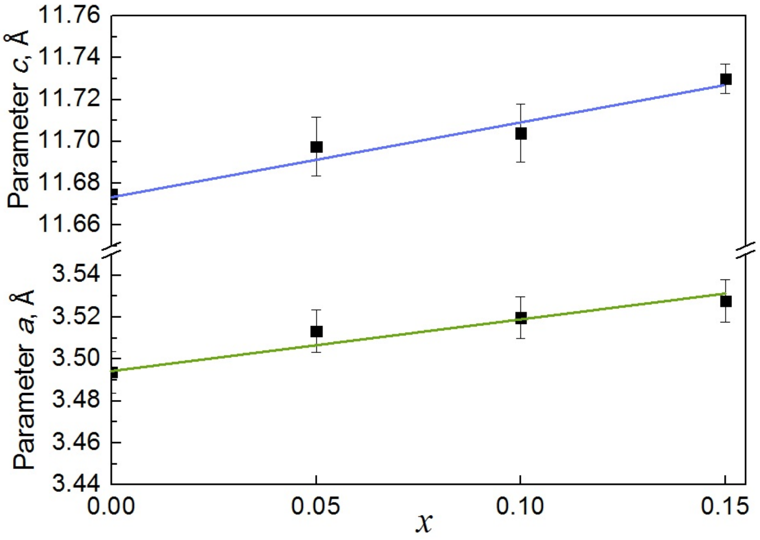

FIG. 3. Dependence of cell parameters of hexagonal $\mathrm{Y}_{1-x}\mathrm{Bi}_x\mathrm{FeO}_3$ on samples composition

The ratio of the phases mass fractions in the samples heated for 1 min. at 800 °C, is shown in Fig. 4. An increase in the amount of bismuth in a sample contributes to an increase in the amount of the $\mathrm{Y}_{1-x}\mathrm{Bi}_x\mathrm{FeO}_3$ hexagonal solid solution and a decrease in the amorphous phase fraction. This can be explained by the fact that an increase in the amount of bismuth leads to a decrease in the solid solution crystallization temperature, and the sample with $x = 0.15$ becomes more crystallized than other samples.

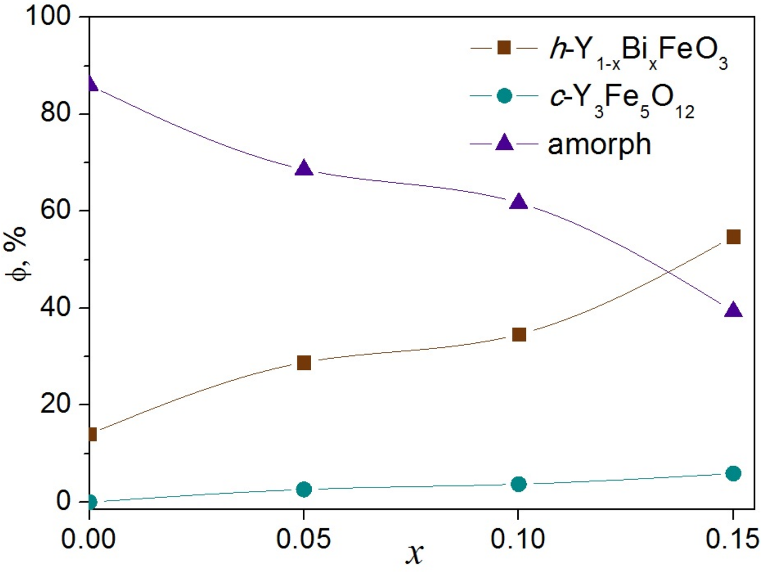

FIG. 4. Dependence of the phases mass content (φ) on the samples composition

It was determined by different methods that average sizes of crystallites of the hexagonal $\mathrm{Y}_{1-x}\mathrm{Bi}_x\mathrm{FeO}_3$ phase significantly differ (Fig. 5). In [33], the influence of the method for determining the size of crystallites on their values was analyzed. For instance, the mode obtained from the size distribution of crystallites for the peak 104 (Fig. 6) almost coincides with the crystallite sizes calculated by the Halder-Wagner method for all the peaks. The obtained results allow one to conclude that an increase in the bismuth content in the $\mathrm{Y}_{1-x}\mathrm{Bi}_x\mathrm{FeO}_3$ solid solution leads to an increase in the crystallite size from ~4 to ~9 nm.

An analysis of the crystallites' size distribution for samples with different compositions (Fig. 6) shows that an increase in the amount of bismuth in the $\mathrm{Y}_{1-x}\mathrm{Bi}_x\mathrm{FeO}_3$ phase leads to a narrowing of the crystallite size distribution compared

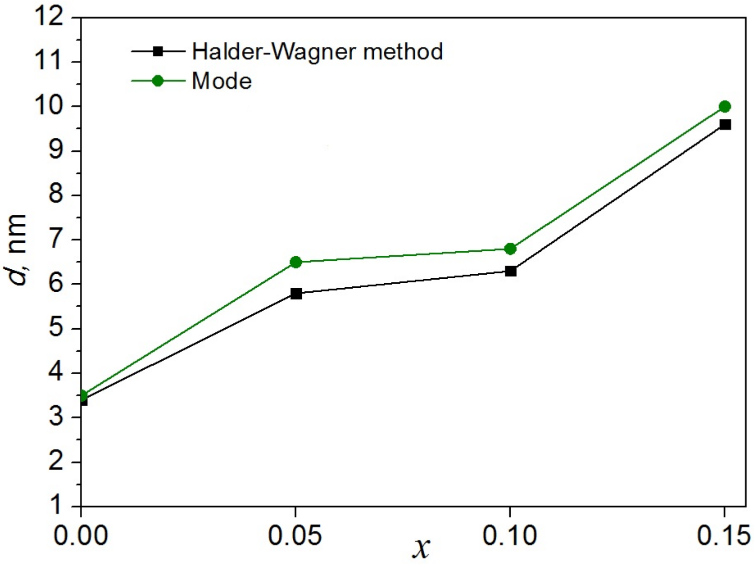

FIG. 5. Crystallite sizes determined from the distribution data in Fig. 6, as well as by the Halder-Wagner method for all the peaks of the $Y_{1-x}Bi_xFeO_3$ phase

to hexagonal yttrium ferrite. It is noteworthy that the maximum value of the distribution is limited by the crystallite size of about 15 nm, which confirms the conclusion made in [9] about the ultimate crystallite size of the hexagonal phase of yttrium ferrite, after which, the metastable hexagonal phase transits into the stable orthorhombic one. The conclusion from [9] is also valid for $Y_{1-x}Bi_xFeO_3$ solid solutions.

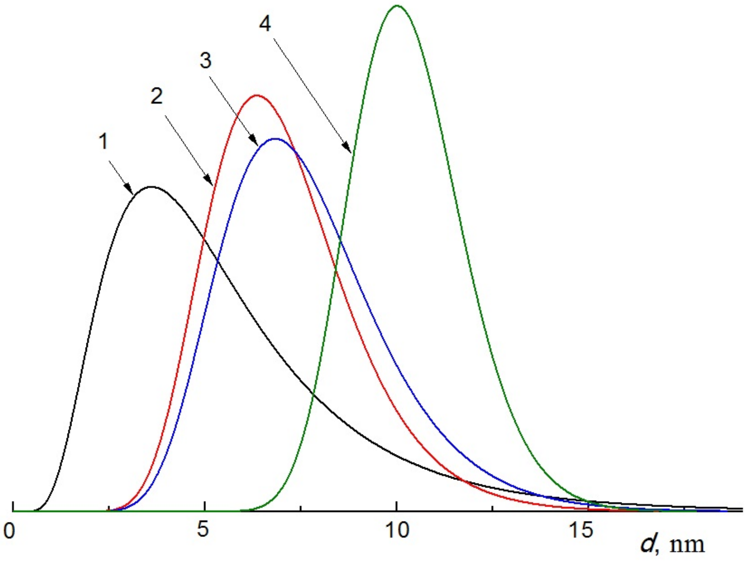

FIG. 6. Size distribution of crystallites determined from the peak 104 in samples of $Y_{1-x}Bi_xFeO_3$ (sample 1 – $x = 0$, sample 2 – $x = 0.05$, sample 3 – $x = 0.10$ and sample 4 – $x = 0.15$)

The IR spectroscopy data for samples with different composition are presented in Fig. 7: before heat treatment (Fig. 7a), and after thermal treatment at 800 °C for 1 min. (Fig. 7b). The variation in the composition of $Y_{1-x}Bi_xFeO_3$ solid solutions under study has practically no effect on the shape of the IR spectra within the same series. The spectra of both series, before and after thermal treatment, have several identical bands. The broad band of 3430 cm^{-1} and the band of 1620 cm^{-1} indicate the presence of H_2O molecules in samples, since they contain an amorphous phase both before and after heating; however, these bands become less expressed after thermal treatment at 800 °C. Before heating, the IR spectra of the samples (Fig. 7a) contained bands at 845, 1078, 1370, and 1520 cm^{-1}, which can be attributed to C–O oscillations in yttrium carbonate $Y_2(CO_3)_3$ [34]. After heat treatment, the IR spectra of the samples (Fig. 7b) contain bands at 1370 and 1520 cm^{-1} of lower intensity, which can be attributed to C–O oscillations in yttrium oxycarbonate $Y_2O_2CO_3$ [34].

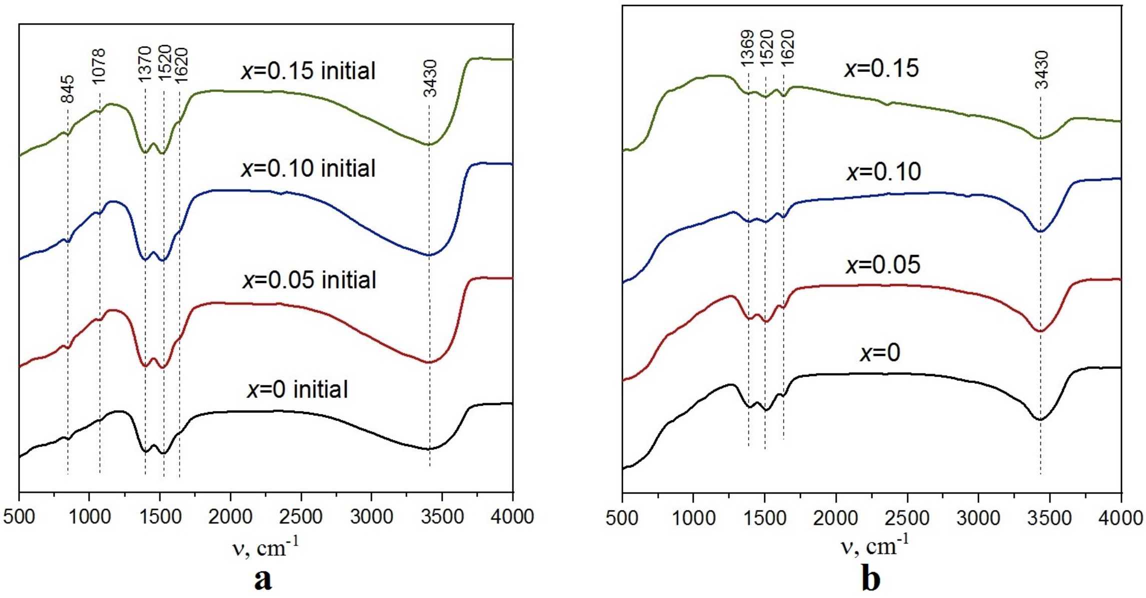

FIG. 7. IR spectra of $Y_{1-x}Bi_xFeO_3$ samples (sample 1 – $x = 0$, sample 2 – $x = 0.05$, sample 3 – $x = 0.10$, and sample 4 – $x = 0.15$) before heat treatment (a) and after heat treatment (b)

Before starting the photocatalysis experiment, the $Y_{1-x}Bi_xFeO_3$ catalysts were tested for the adsorption capacity without a light source. To determine the most active catalyst among samples 1, 2, 3, and 4, solutions were prepared to contain 10 ml of a colloidal solution of the corresponding $Y_{1-x}Bi_xFeO_3$ nanopowder (C = 0.5 g/L), 0.6 ml of a methyl violet solution (C = 1 g/L), 4 ml of hydrogen peroxide (C = 1 mol/l), and 10.4 ml of distilled water. Before the photocatalysis experiment, the solutions were stirred for 15 min. in the dark to establish the adsorption equilibrium. The degree of adsorption q (mg/g) was calculated for each sample according to the equation:

$$q = \frac{(C_0 - C) \cdot V}{g},$$

where C_0 is the initial concentration of the dye, C is the final concentration of the dye after its adsorption, V is the reaction volume of the mixture, and g is the mass of the catalyst in the solution.

The degree of adsorption for each of the samples is shown in Fig. 8.

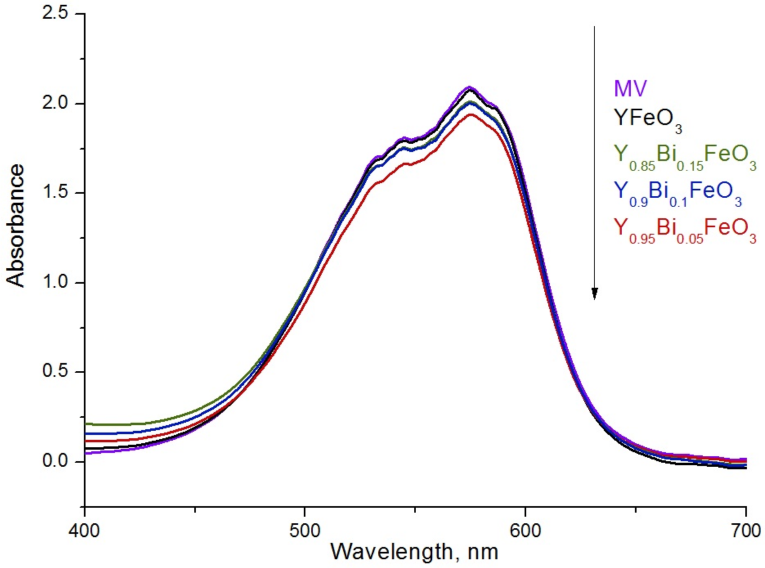

FIG. 8. The spectra of MV absorption in the presence of $Y_{1-x}Bi_xFeO_3$ without exposure to light

According to the obtained experimental data, the adsorption capacity of the samples decreases in the series $Y_{0.95}Bi_{0.05}FeO_3 > Y_{0.9}Bi_{0.1}FeO_3 > Y_{0.85}Bi_{0.15}FeO_3 > YFeO_3$.

Then, the obtained $Y_{1-x}Bi_xFeO_3$ samples were studied in the process of Fenton-like oxidation of methyl violet under the action of visible light (Fig. 9).

The resulting solutions were irradiated with visible light for 15 min. with continuous stirring. After this time, 5 ml samples were taken from these solutions to evaluate the concentration of the dye. The methyl violet removal efficiency was calculated using the formula:

$$\text{Degradation efficiency} = \frac{C_0 - C}{C_0} \cdot 100\%,$$

where C_0 is the initial dye concentration, C is the final dye concentration after Fenton-like oxidation.

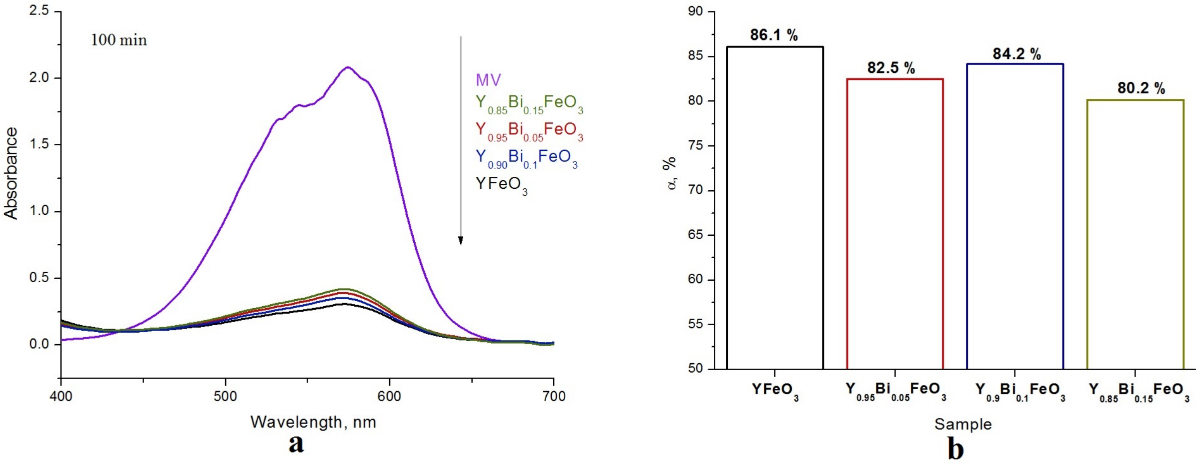

FIG. 9. The spectra of MV absorption in the presence of $Y_{1-x}Bi_xFeO_3$ in the 400–700 nm wavelength range (a), dye removal efficiency for samples 1, 2, 3, 4 (b)

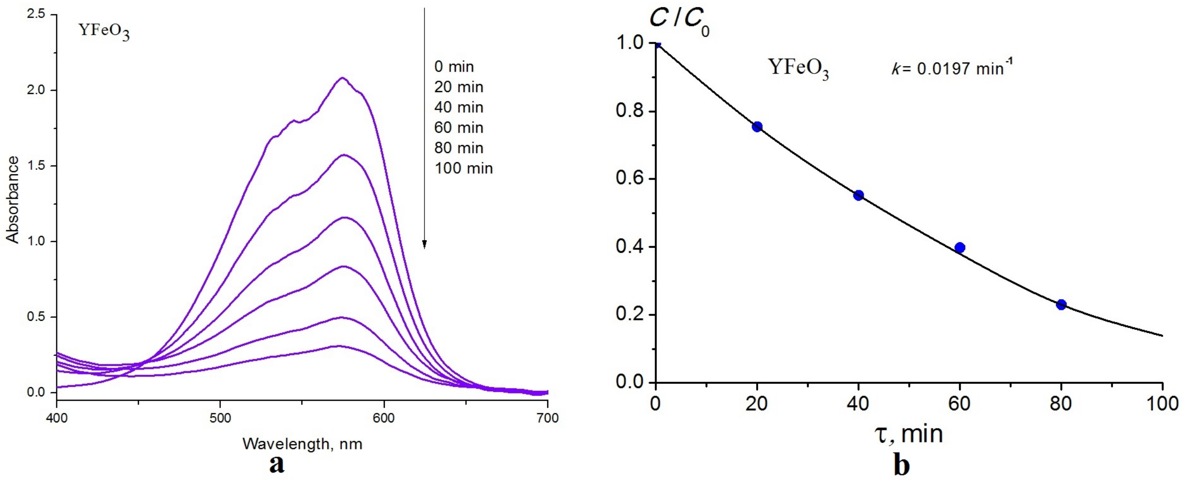

FIG. 10. The spectra of MV absorption in the presence of $YFeO_3$ in the 400–700 nm wavelength range depending on the duration of irradiation (a) and the kinetic curve for $YFeO_3$ sample (b)

Depending on the amount of bismuth in the samples, the catalytic ability of the samples changes in the following order: $YFeO_3 > Y_{0.9}Bi_{0.1}FeO_3 > Y_{0.95}Bi_{0.05}FeO_3 > Y_{0.85}Bi_{0.15}FeO_3$. However, the obtained data cannot lead to the conclusion that doping with bismuth worsens the catalytic ability of yttrium orthoferrite, since it can also be affected by particle morphology, crystallite size, and other factors. With a decrease in the heating temperature and the formation of smaller crystallites, the effect of bismuth doping can possibly be different.

Since the results of these tests showed $YFeO_3$ nanopowders to be the most active, an additional series of experiments with them was performed to determine the kinetics of methyl violet removal.

To study the kinetic parameters of the photo-Fenton-like oxidation of methyl violet, 25 ml of a solution containing 1.2 ml of MV (0.0464 g/L in 25 ml), 12.5 ml of a $YFeO_3$ suspension, 6 ml of H_2O_2, and 4.1 ml of H_2O were prepared. With constant stirring, the solution was irradiated for 100 minutes, with sampling every 20 minutes, to obtain the dependence of the dye removal efficiency on the duration of irradiation.

The results the kinetics studies of the photocatalytic oxidation of MV in the presence of $YFeO_3$ nanoparticles are shown in Fig. 10. With an increase in the duration of the reaction solution irradiation, a regular decrease in the relative concentration of the dye was observed (Fig. 10b). The rate constant of this process was calculated based on the linearization of the kinetic dependence in logarithmic coordinates, and was found to be 0.0197 min^{-1}, which is almost 4 times greater than for similar $YbFeO_3$-based photocatalysts [27]. The corresponding change in the MV adsorption spectra depending on the exposure time is shown in Fig. 10a.

The obtained results allow considering the produced nanopowders as promising photocatalysts for the oxidation of organic water pollutants.

4. Conclusion

Nanocrystalline samples of $Y_{1-x}Bi_xFeO_3$ ($x = 0$, 0.05, 0.10, 0.15) solid solutions with a hexagonal structure were obtained by co-precipitation of magnetically stirred yttrium, bismuth and iron hydroxides with simultaneous sonication, and subsequent thermal treatment of the rinsed and dried samples at 800 °C for 1 min. The average crystallite size increases from $\sim$4 to $\sim$10 nm with the increasing bismuth content in the solid solution. The maximum size distribution of crystallites for all samples is limited to $\sim$15 nm, which leads to a conclusion about the ultimate size of yttrium ferrite crystallites in the metastable hexagonal phase, after which, it transitions to a stable orthorhombic phase. The photocatalytic activity of the obtained nanopowders of $Y_{1-x}Bi_xFeO_3$ solid solutions was studied in the Fenton-like oxidation of methyl violet. A higher catalytic activity was demonstrated by a sample of undoped yttrium ferrite. The obtained nanopowders can be considered as promising photocatalysts for the oxidation of organic water pollutants.

References

[1] Ahmad T., Lone I.H., Ansari S.G., Ahmed J., Ahamad T., Alshehri S.M. Multifunctional properties and applications of yttrium ferrite nanoparticles prepared by citrate precursor route. *Materials and Design*, 2017, **126**, P. 331–338.

[2] Shang M., Zhang C., Zhang T., Yuan L., Ge L., Yuan H., Feng S. The multiferroic perovskite $YFeO_3$. *Applied physics letters*, 2013, **102**(6), P. 062903.

[3] Cheong S.W., Mostovoy M. Multiferroics: a magnetic twist for ferroelectricity. *Nature Materials*, 2007, **6**(1), P. 13–20.

[4] Zhang R., Wang X., Yu C., Liu J, Yao J., Kang X., Xing X., Xiong S. Preparation of Multiferroic $YFeO_3$ Nanofibers and the Photocatalytic Activity under Visible Irradiation. *Integrated Ferroelectrics*, 2020, **206**(1), P. 105–111.

[5] Popkov V.I., Almjasheva O.V., Semenova A.S., Kellerman D.G., Nevedomskiy V.N., Gusarov V.V. Magnetic properties of $YFeO_3$ nanocrystals obtained by different soft-chemical methods. *Journal of Materials Science: Materials in Electronics*, 2017, **28**(10), P. 7163–7170.

[6] Ismael M., Elhaddad E., Taffa D.H., Wark M. Synthesis of Phase Pure Hexagonal $YFeO_3$ Perovskite as Efficient Visible Light Active Photocatalyst. *Catalysts*, 2017, **7**(11), P. 326–338.

[7] Popkov V.I., Almjasheva O.V., Gusarov V.V. The Investigation of the Structure Control Possibility of Nanocrystalline Yttrium Orthoferrite in Its Synthesis from Amorphous Powders. *Russian Journal of Applied Chemistry*, 2014, **87**(10), P. 1417–1421.

[8] Popkov V.I., Almjasheva O.V., Panchuk V.V., Semenov V.G., Gusarov V.V. The Role of Pre-Nucleus States in Formation of Nanocrystalline Yttrium Orthoferrite. *Doklady Chemistry*, 2016, **471**(2), P. 356–359.

[9] Popkov V.I., Almjasheva O.V., Nevedomskiy V.N., Panchuk V.V., Semenov V.G., Gusarov V.V. Effect of spatial constraints on the phase evolution of $YFeO_3$-based nanopowders under heat treatment of glycine-nitrate combustion products. *Ceramics International*, 2018, **44**(17), P. 20906–20912.

[10] Li Y., Ma Y., Iiu W., Wang Z., Liu H., Wang X., Wei H., Zeng S., Cheng G.J. A promising inorganic $YFeO_3$ pigments with high near-infrared reflectance and infrared emission. *Solar Energy*, 2021, **226**(3), P. 180–191.

[11] Sui Y., Lu F., Liu X., Zhang Y., Sun X., Liu C. A novel hexagonal $YFeO_3$ 3D nanomaterial with room temperature ferromagnetic properties prepared by self-assembling method. *Results in Materials*, 2021, **10**(2), P. 100186.

[12] Wu L., Yu J.C., Zhang L., Wang X., Li S. Selective self-propagating combustion synthesis of hexagonal and orthorhombic nanocrystalline yttrium iron oxide. *Journal of Solid State Chemistry*, 2004, **177**(10), P. 3666–3674.

[13] Zhang R.-L., Chen C.-L., Jin K.-X., Niu L.-W., Xing H., Luo B.-c. Dielectric behavior of hexagonal and orthorhombic $YFeO_3$ prepared by modified sol-gel method. *Journal of Electroceramics*, 2014, **32**(2–3), P. 187–191.

[14] Shen H., Xu J., Jin M., Jiang G. Influence of manganese on the structure and magnetic properties of $YFeO_3$ nanocrystal. *Ceramics International*, 2012, **38**(2), P. 1473–1477.

[15] Lomanova N.A., Tomkovich M.V., Danilovich D.P., Osipov A.V., Panchuk V.V., Semenov V.G., Pleshakov I.V., Volkov M.P., Gusarov V.V. Magnetic Characteristics of Nanocrystalline $BiFeO_3$-Based Materials Prepared by Solution Combustion Synthesis. *Inorganic Materials*, 2020, **56**(12), P. 1271–1277.

[16] Maleki H., Zakeri M., Fathi R. Experimental study of the effect of yttrium on the structural, thermal, and magnetic properties of $BiFeO_3$. *Applied Physics A*, 2018, **124**(11), 728.

[17] Medina L.M.S., Jorge G.A., Negri R.M. Structural, dielectric and magnetic properties of $Bi_{1-x}Y_xFeO_3$ ($0 \leq x \leq 0.2$) obtained by acid–base co-precipitation. *Journal of Alloys and Compounds*, 2014, **592**, P. 306–312.

[18] Ilić N.I., Bobić J.D., Stojadinović B.S., Džunuzović A.S., Vijatović Petrović M.M., Dohčević-Mitrović Z.D., Stojavinoć B.D. Improving of the electrical and magnetic properties of $BiFeO_3$ by doping with yttrium. *Materials Research Bulletin*, 2016, **77**, P. 60–69.

[19] Tomina E.V., Perov N.S., Mittova I.Y., Alekhina Y.A., Stekleneva O.V., Kurkin N.A. Microwave synthesis and magnetic properties of bismuth ferrite nanopowder doped with cobalt. *Russian Chemical Bulletin*, 2020, **69**(5), P. 941–946.

[20] Naveen K., Kumar N., Rani S., Mandal T., Gaur A., Babu P.D., Siruguri V., Maji P. K., Kanungo S., Paul A.K. Investigation of multiferroic behaviour at room temperature in Bi-induced orthoferrite: combined experimental and first principles studies. *Bulletin of Materials Science*, 2020, **43**(1), 196.

[21] Suthar L., Bhadala F., Kumari P., Roy M. Structural, morphological, magnetic and spectral studies of Bi^{3+} substituted $YFeO_3$ Nano-powders: Obtained by sol-gel synthesis. *Journal of Electroceramics*, 2020, **44**(4), P. 195–202.

[22] Rosales-González O., Jesús S.D., Pedro-García F., Cortés-Escobedo C.A., Ramírez-Cardona M., Bolarín-Miró A.M. Enhanced Multiferroic Properties of $YFeO_3$ by Doping with Bi^{3+}. *Materials*, 2019, **12**(13), 2054.

[23] Suthar L., Bhadala F., Roy M. The impact of Bi^{3+} substitution for Y^{3+} cation on structural, topographical, electrical and thermal behaviour of $YFeO_3$. *Ceramics International*, 2019, **45**(16), P. 20891–20899.

[24] Liu Y.-H., Kuo Y.-S., Liu W.-C., Chou W.-L. Photoelectrocatalytic activity of perovskite $YFeO_3$/carbon fiber composite electrode under visible light irradiation for organic wastewater treatment. *Journal of the Taiwan Institute of Chemical Engineers*, 2021, **128**, P. 227–236.

[25] Luo W., Zhu L., Wang N., Tang H., Cao M., She Y. Efficient removal of organic pollutants with magnetic nanoscaled $BiFeO_3$ as a reusable heterogeneous Fenton-like catalyst. *Environmental Science and Technology*, 2010, **44**(5), P. 1786–1791.

[26] Ju L., Chen Z., Fang L., Dong W., Zheng F., Shen M. Sol-gel synthesis and photo-Fenton-like catalytic activity of $EuFeO_3$ nanoparticles. *Journal of the American Ceramic Society*, 2011, **94**(10), P. 3418–3424.

[27] Tikhanova S.M., Lebedev L.A., Martinson K.D., Chebanenko M.I., Buryanenko I.V., Semenov V.G., Nevedomskiy V.N., Popkov V.I. Synthesis of novel heterojunction h-$YbFeO_3$/o-$YbFeO_3$ photocatalyst with enhanced Fenton-like activity under visible-light. *New Journal of Chemistry*, 2021, **45**(3) P. 1541–1550.

[28] Zhang Y., Yang J., Xu J., Gao Q., Hong Z.. Controllable synthesis of hexagonal and orthorhombic $YFeO_3$ and their visible-light photocatalytic activities. *Materials Letters*, 2012, **81**, P. 1–4.

[29] Tang P., Sun H., Chen H., Cao F. Hydrothermal Processing-Assisted Synthesis of Nanocrystalline $YFeO_3$ and its Visible-Light Photocatalytic Activity. *Current Nanoscience*, 2012, **8**(1), P. 64–67.

[30] Seroglazova A.S., Lebedev L.A., Chebanenko M.I., Sklyarova A.S., Buryanenko I.V., Semenov V.G., Popkov V.I. Ox/Red-controllable combustion synthesis of foam-like $PrFeO_3$ nanopowders for effective photo-Fenton degradation of methyl violet. *Advanced Powder Technology*, 2022, **33**(2), P. 103398.

[31] Proskurina O.V., Sokolova A.N., Sirotkin A.A., Abiev R.Sh., Gusarov V.V. Role of Hydroxide Precipitation Conditions in the Formation of Nanocrystalline $BiFeO_3$. *Russian Journal of Inorganic Chemistry*, 2021, **66**(2), P. 163–169.

[32] Wang M., Wang T., Song S.-H., Ravi M., Liu R.-C., Ji S.-S. Effect of calcination temperature on structural, magnetic and optical properties of multiferroic $YFeO_3$ nanopowders synthesized by a low temperature solid-state reaction. *Ceramics International*, 2017, **43**(13), P. 10270–10276.

[33] Proskurina O.V., Abiev R.S., Danilovich D.P., Panchuk V.V., Semenov V.G., Nevedomsky V.N., Gusarov V.V. Formation of nanocrystalline $BiFeO_3$ during heat treatment of hydroxides co-precipitated in an impinging-jets microreactor. *Chemical Engineering and Processing - Process Intensification*, 2019, **143**(7), P. 107598.

[34] Popkov V.I., Almjasheva O.V., Schmidt M.P., Izotova S.G., Gusarov V.V. Features ofnanosized $YFeO_3$ formation under heat treatment of glycine-nitrate combustion products. *Russian Journal of Inorganic Chemistry*, 2015, **60**(10), P. 1193–1198.

Submitted 11 November 2021; accepted 5 December 2021

Information about the authors:

Anastasiya N. Sokolova – St. Petersburg State Institute of Technology, 26, Moskovsky Pr., St. Petersburg, 190013, Russia; Ioffe Institute, Politekhnicheskaya St. 26, St. Petersburg, 194021, Russia; sok5552@mail.ru

Olga V. Proskurina – St. Petersburg State Institute of Technology, 26, Moskovsky Pr., St. Petersburg, 190013, Russia; Ioffe Institute, Politekhnicheskaya St. 26, St. Petersburg, 194021, Russia; proskurinaov@mail.ru

Dmitry P. Danilovich – St. Petersburg State Institute of Technology, 26, Moskovsky Pr., St. Petersburg, 190013, Russia; dmitrydanilovich@gmail.com

Victor V. Gusarov – Ioffe Institute, Politekhnicheskaya St. 26, St. Petersburg, 194021, Russia; victor.v.gusarov@gmail.com

Conflict of interest: the authors declare no conflict of interest.

NANOSYSTEMS:
PHYSICS, CHEMISTRY, MATHEMATICS

Original article

Popov A.L., Kolmanovich D.D., et al. *Nanosystems: Phys. Chem. Math.*, 2022, **13** (1), 96–103.
http://nanojournal.ifmo.ru
DOI 10.17586/2220-8054-2022-13-1-96-103

Synthesis and biocompatibility study of ceria-mildronate nanocomposite *in vitro*

A. L. Popov[1,a], D. D. Kolmanovich[1,b], N. R. Popova[1,c], S. S. Sorokina[1,d], O. S. Ivanova[2,e], N. N. Chukavin[1,3,f], A. B. Shcherbakov[4,g], T. O. Kozlova[2,h], S. A. Kalashnikova[5,j], V. K. Ivanov[2,k]

[1]Institute of Theoretical and Experimental Biophysics of the Russian Academy of Sciences, 142290, Russia
[2]Kurnakov Institute of General and Inorganic Chemistry of the Russian Academy of Sciences, 119991, Russia
[3]Moscow Region State University, 141014, Moscow, Russia
[4]Zabolotny Institute of Microbiology and Virology, Kyiv D0368, Ukraine
[5]40th City clinical hospital, Ekaterinburg, 620102, Russia

[a]antonpopovleonid@gmail.com, [b]kdd100996@mail.ru, [c]nellipopovaran@gmail.com,
[d]sorokinasvetlana.iteb@gmail.com, [e]runetta05@mail.ru, [f]chukavinnik@gmail.com,
[g]ceroform@gmail.com, [h]tasiok@mail.ru, [j]kalashnikova.sana@mail.ru, [k]van@igic.ras.ru

Corresponding author: A. L. Popov, antonpopovleonid@gmail.com

PACS 68.65.-k, 81.20.-n, 82.70. Dd, 87.80.-y

ABSTRACT Nanoscale cerium dioxide (CeO_2, nanoceria) possesses notable redox activity, which is actively used in advanced biomedical applications. The low toxicity, high biocompatibility and antioxidant activity of nanoceria make it a new generation nanozyme with a unique activity. Combination of nanoceria with various biologically active substances results in organic-inorganic nanocomposites possessing enhanced activity. Here, we synthesized a novel organic-inorganic hybrid material (Mil-CeO_2) based on 2-(2-carboxylatoethyl)-1,1,1-trimethylhydrazinium and nanoceria, which has an ultra-small particle size, high antioxidant activity and pronounced biological activity. The analysis of cytotoxicity of the composite did not reveal any negative effects on the NCTC L929 mouse fibroblasts at concentrations below 10 mM. It was shown that the nanocomposite did not cause morphological changes in cells, or lead to cell death and mitochondrial membrane potential disruption, while maintaining viability in mouse fibroblasts *in vitro*. Additionally, we showed that Mil-CeO_2 is capable of protecting cells from hydrogen peroxide (H_2O_2)-induced or radiation-induced oxidative stress.

KEYWORDS cerium oxide nanoparticles, nanoceria, 2- (2-carboxylatoethyl) -1,1,1-trimethylhydrazinium, toxicity, nanocomposite

ACKNOWLEDGEMENTS The work was supported by the Russian Science Foundation (project 20-74-00086). The research was carried out using the equipment of MSU Shared Research Equipment Center “Technologies for obtaining new nanostructured materials and their complex study” and purchased by MSU in the frame of the Equipment Renovation Program (National Project ”Science”) and in the frame of the MSU Program of Development.

FOR CITATION Popov A.L., Kolmanovich D.D., Popova N.R., Sorokina S.S., Ivanova O.S., Chukavin N.N., Shcherbakov A.B., Kozlova T.O., Kalashnikova S.A., Ivanov V.K. Synthesis and biocompatibility study of ceria-mildronate nanocomposite *in vitro*. *Nanosystems: Phys. Chem. Math.*, 2022, **13** (1), 96–103.

1. Introduction

Cerium oxide nanoparticles (CNPs) are considered as the most versatile inorganic antioxidant [1–3]. CNPs redox activity is probably due to a high degree of oxygen nonstoichiometry, which is due to the presence of defects in the crystal lattice of CeO_2 nanoparticles [4–7]. Cerium oxide nanoparticles are capable of inactivating a wide range of reactive oxygen species (ROS) and free radicals [8–11], preventing the development of intracellular oxidative stress *in vitro* [12, 13] and *in vivo* [14–16]. It is also well known that cerium oxide nanoparticles mimic the activity of endogenous enzymes such as superoxide dismutase (SOD) [17–19] and catalase [20]. Cerium oxide nanoparticles are considered as a promising anticancer [21–23], antibacterial [24–26] and antiviral [27–29] agent as well as a promising inorganic antioxidant for diverse biomedical applications [30–32].

We have previously shown that cerium dioxide nanoparticles demonstrate a synergistic effect with well-known anticancer drugs or another therapeutic substances, enhancing their effect [33–36]. In particular, it has been shown that the panthenol-cerium dioxide complex protects testicular epithelial cells (ST cells) from oxidative stress caused by hydrogen peroxide or UV radiation [37]. Similarly, conjugation with cerium dioxide affects the cytotoxicity and photocytotoxicity of curcumin, depending on the cell type, being more toxic for cancer cells. The nanoceria-curcumin conjugate demonstrated highly selective cytotoxicity under oxidative stress conditions induced by UVA/UVC irradiation or H_2O_2, causing a dramatic inhibition of metabolic activity of cancer cells and protecting normal cells from these damaging factors [38]. The combination of recombinant TNF-alpha with cerium dioxide nanoparticles has been shown to provide a stronger and more stable cytotoxic effect in Hep-2 and A-549 tumor cell lines [39]. Thus, the design and study of hybrid cerium-containing nanocomposites could be a promising tool for creating advanced functional materials with a therapeutic activity exceeding that of the individual components (synergism).

There are a large number of promising drugs that could act as a synergistic agent for cerium dioxide nanoparticles. One possible candidate is meldonium, which is a small, highly hydrophilic molecule that has no affinity for plasma proteins. Upon administration, the maximum plasma concentration of meldonium is reached after about 1 hour, and its half-life depends on the dosage, treatment time and pharmaceutical form. Meldonium is metabolized mainly in the liver by gamma-butyrobetaine hydroxylase (BBOX) to form dimethylamine, 2-hydroxymethyl-2-(hydroxymethylamino) propane-1,3-diol, 3–amino-4-(hydroxymethylmethylamino). The latter metabolite can be converted to succinic acid, the main metabolite found in plasma. Mildronate is regarded as a mitochondria-targeted drug as it easily penetrates into mitochondria and enters the metabolic cycle [40, 41]. Mitochondrial damage can activate free radical processes and lead to the initiation of apoptosis, as well as disruption of mitochondrial oxidative phosphorylation, damage to the endoplasmic reticulum and changes in gene activity [42–44]. Mitochondria are the main site of ROS formation in the cell. There are several factors that determine ROS generation in mitochondria: the presence of different metabolic intermediates, hypo/hyperoxia, an increase in the concentration of NADH or membrane mitochondrial potential (MMP). Thus, the development and study of a new mitochondria-targeted biologically active nanocomposites is an urgent task. To summarize, the ceria-mildronate composite can be considered as a promising substance for inhibiting the oxidative stress and increasing the cell metabolic status.

2. Materials and methods

2.1. Synthesis and characterization of nanocomposite

The ceria-mildronate composite (CeO_2-Mil) was synthesized in two stages. Initially, cerium (III) trimeldonate solution was obtained by mixing 500 mg sodium mildronate (3.48 mM) with cerium chloride ($CeCl_3 \cdot 7H_2O$) in a molar ratio of 3:1 with thorough stirring. Next, we synthesized nanoscale cerium dioxide composite with meldonium (CeO_2-Mil) by precipitation using NaOH (1 M). The composite was separated by decantation and then centrifuged at 10,000 rpm and washed three times with MQ water. CeO_2-Mil composite sol was sonicated for 1 hour before using. The hydrodynamic diameter and the ζ- potential values were measured using a Zetasizer Nano ZS analyzer (Malvern Instruments Ltd., UK). High-resolution transmission electron microscopy (HR-TEM) analysis was performed using a Libra 200 MC microscope (Zeiss, Germany). TEM images were recorded by a CCD camera (Gatan, USA) with a matrix size of 4096×4096 pixels.

2.2. Cell culture

The analysis of cytotoxicity and bioactivity was carried out using NCTC clone L929 cell culture from the Institute of Cell Biophysics collection; NCTC clone L929 fibroblasts were obtained from the subcutaneous connective tissue of C3H/An mice. The cells were seeded in 96-well plates at a density of $2*10^4$ per cm^2 in DMEM/F12 medium (1:1) supplemented with 10% fetal bovine serum (FBS) and 100 U/ml penicillin/streptomycin solution. Cells were cultivated under 5% CO_2 at 37°C.

2.3. MTT assay

Cell viability was assessed using the MTT test. The cells were seeded in 96-well plates and cultivated for 24 hours. 6 h after cell seeding, the culture medium was replaced with a medium containing CeO_2-Mil nanocomposite at various concentrations (0.05-11 mM). Cells with the medium, but without CeO_2-Mil nanocomposite, were used as a control. 24 h after the introduction of the nanocomposite, the medium in wells was replaced with a medium containing 3-4,5-dimethylthiazol-2-yl-2,5-diphenyltetrazole (5 mg/ml). The optical density of the formed formazan was determined at a wavelength of λ=540 nm using a BIO-RAD model 680 photometer.

2.4. Live/Dead assay

To assess the ratio of living/dead cells in culture, we used the L-7007 LIVE/DEAD BacLight Bacterial Viability Kit (Invitrogen) containing SYTO 9 (stains all cells, λ=485/498 nm) and propidium iodide (stains the nuclei of dead cells, λ=535/617 nm) dyes. Cell staining was performed by replacing the culture medium with a dye mixture (5 μM). Observation of morphology and fluorescent staining was carried out on an Axiovert 200 inverted microscope (Carl Zeiss). Microphotography was performed using a Power Shot A620 digital camera (Canon). Stained cells were counted using the Image J software.

2.5. Mitochondrial membrane potential (MMP level) analysis

The MMP level was assessed using tetramethyl rhodamine, TMRE (Thermo Fisher Scientific, USA). TMRE is a positively charged red-orange dye that penetrates cells and accumulates readily in active mitochondria due to their negative membrane potential. Depolarized or inactive mitochondria have a reduced membrane potential and are unable to accumulate TMRE. The TMRE excitation peak is 488 nm, the emission peak is 575 nm. The preparation of the working solution with the dye was carried out in Hanks solution, upon the addition of the prepared solution to the cells, cultivation was carried out for 15 minutes. Before the study itself, using microscopic methods, the solution with the dye was replaced with the Hanks solution. The work was carried out under sterile conditions in a laminar flow hood. For the study, we used an Axiovert 200 Zeiss inverted fluorescence microscope. Then, the level of fluorescence intensity was calculated using ImageJ.

2.6. Fluorescent staining of cell nuclear with Hoechst 33342 dye

Cells were cultured in 96-well plates, as described above. After 24 hours of culturing with nanocomposite, the cells were washed with HBSS, prior to 20 min staining with Hoechst 33342 (5 μM). Images of stained cells were captured by a fluorescence microscope Zeiss Axiovert 200.

2.7. Oxidative stress model *in vitro*

The protective action of CeO_2-Mil nanocomposite was analyzed using two experimental models of oxidative stress: single dose X-ray irradiation (15 Gy) or hydrogen peroxide treatment (1 mM for 30 minutes). Cell viability analysis was performed using MTT test after 24 hours for hydrogen peroxide treatment and after 72 hours for X-ray irradiation, respectively.

2.8. Statistical analysis

Data are presented as standard deviation from the mean value. The significance of differences between experimental groups was assessed by the Mann-Whitney U-test.

3. Results and discussion

The synthesis of CeO_2-Mil nanocomposite was carried out according to the scheme shown in Fig. 1a. The hydrodynamic radius of the nanocomposite upon dilution in water was approximately 15–20 nm (Fig. 1b). The zeta potential of the particles when diluted in distilled water was $+23\pm3.2$ mV. According to TEM data, the particle size of the nanocomposite was 4–5 nm (Fig. 1c). The synthesized CeO_2-Mil nanocomposite demonstrated good colloidal stability and can be stored for at least 7 days without any signs of sedimentation.

It is well known that cerium oxide nanoparticles coated by biocompatible ligands are not toxic to mammalian cells *in vitro* and *in vivo*, even at high concentrations [45–47]. For example, citrate-stabilized cerium oxide nanoparticles do not cause toxic effects in the culture of mouse embryonic fibroblasts, while maintaining a high level of their migratory, proliferative and metabolic activity [48]. In turn, dextran-stabilized gadolinium-doped cerium oxide nanoparticles have demonstrated selective toxicity against cancer cells [49]. Nevertheless, each new synthesis scheme for CeO_2 nanoparticles preparation and stabilization requires a comprehensive analysis of cytotoxicity to analyze the prospects for biomedical use.

The cytotoxicity of the CeO_2-Mil nanocomposite was analyzed using mouse fibroblasts cell line NCTC L929 (Fig. 2). The CeO_2-Mil nanocomposite was shown to have no toxic effect and provided a high level of metabolic activity at the concentrations below 1 mM. It should be noted that cerium (III) chloride in high concentrations (above 1 mM) was toxic for mouse fibroblasts, while this was not the case for CeO_2-Mil nanocomposite. Additionally, an assessment of the toxicity of mildronate and cerium chloride at the same concentrations was carried out. Analysis of the ratio of live and dead cells using the differential staining method has shown that the CeO_2-Mil nanocomposite does not cause cell death at all studied concentrations (0.05–11 mM), retaining the native morphology and phenotypic features characteristic of fibroblasts (Fig. 3b).

Mitochondria are redox-sensitive organelles [50]. The mitochondrial disruption is accompanied by the changes in the membrane potential and alterations to the oxidation–reduction potential of the mitochondria. Previously, it was shown that nanoceria could depolarize mitochondrial membrane of human colon cancer cells [51]. In the current study, it was revealed that preliminary incubation of NCTC L929 with CeO_2-Mil nanocomposite did not lead to any changes in the MMP in any of the concentrations thus confirming the high biocompatibility of the nanocomposite (Fig. 3c)

The results of Ce-Mil nanocomposite protective effects study are presented in Fig. 4. The radioprotective action of Ce-Mil nanocomposite was analyzed after X-ray exposure. Earlier, we have demonstrated radioprotective action of cerium oxide nanoparticles using mouse fibroblasts upon X-ray irradiation [52]. The optimal dose for NCTC L929 cell culture irradiation was selected at 15 Gy. The dose of radiation and cultivation time after irradiation were chosen on the basis of preliminary experiments. Live/Dead and MTT assays were performed 72 hours after X-ray irradiation. It was shown that the CeO_2-Mil nanocomposite after X-ray radiation exposure (15 Gy) showed protective action only at the highest concentration (0.5 mM), which ensured the preservation of cell viability by about 25% compared to the irradiated control.

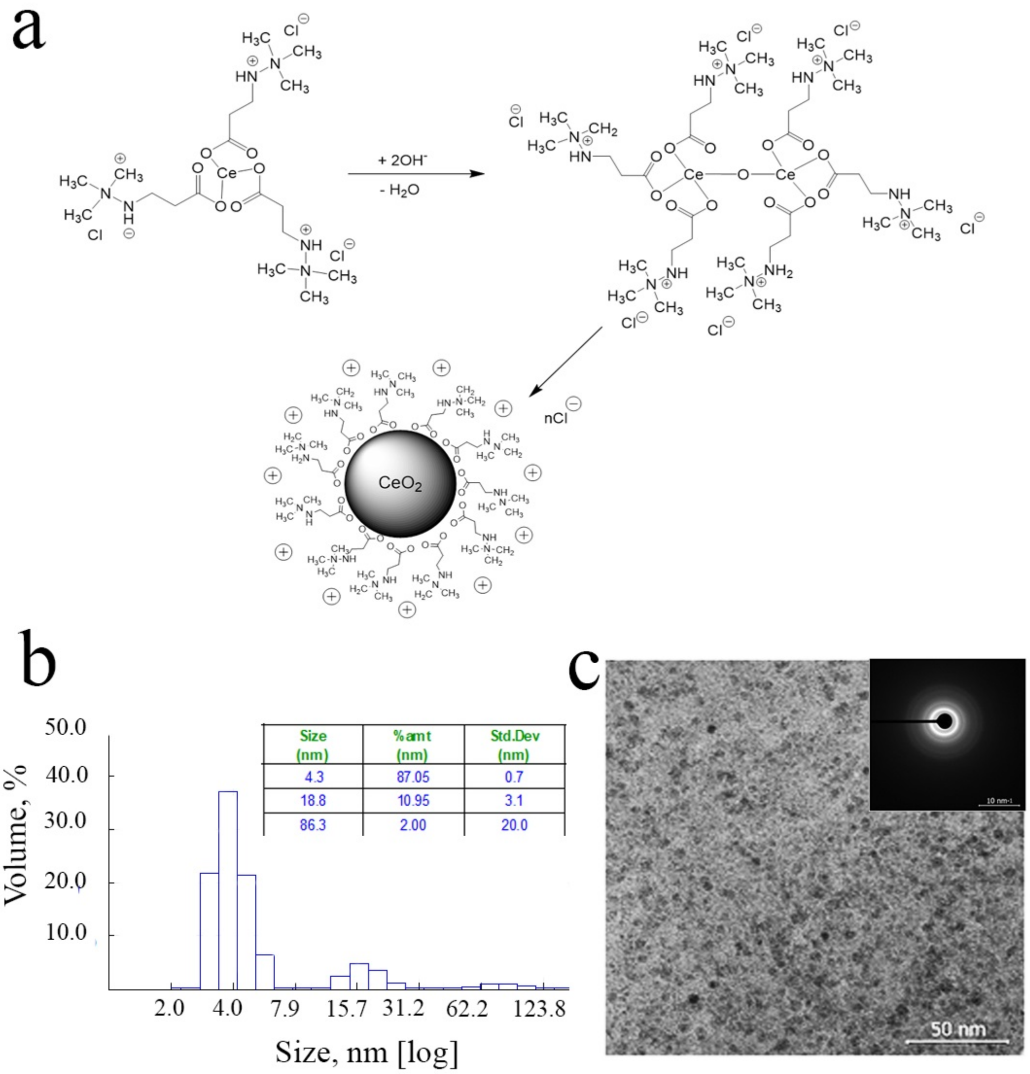

Size (nm)	%amt (nm)	Std.Dev (nm)
4.3	87.05	0.7
18.8	10.95	3.1
86.3	2.00	20.0

FIG. 1. Synthesis scheme and the structure of the CeO_2-Mil nanocomposite (a), dynamic light scattering in MQ water (b) and transmission electron microscopy (c)

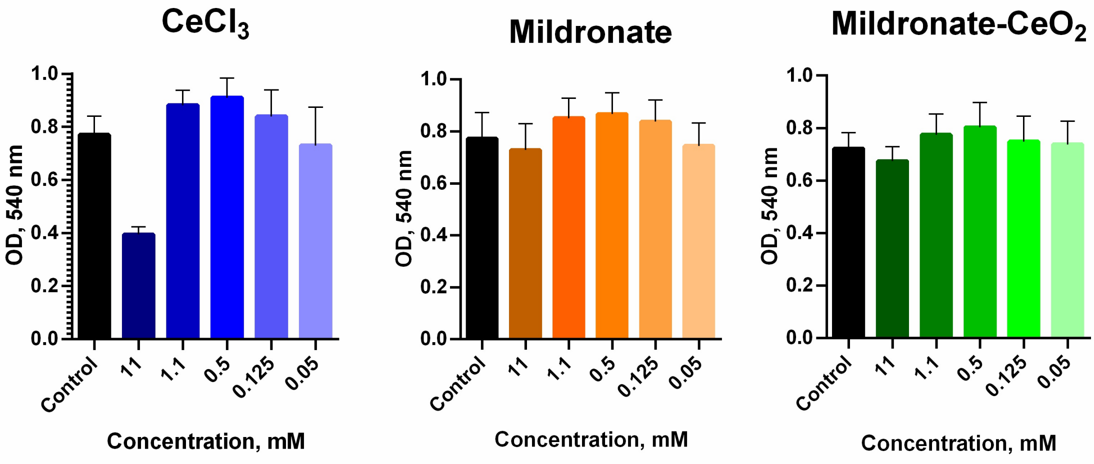

FIG. 2. Cytotoxicity analysis by the MTT test of CeO_2-Mil nanocomposite using NCTC L929 cell line (24 hours after incubation)

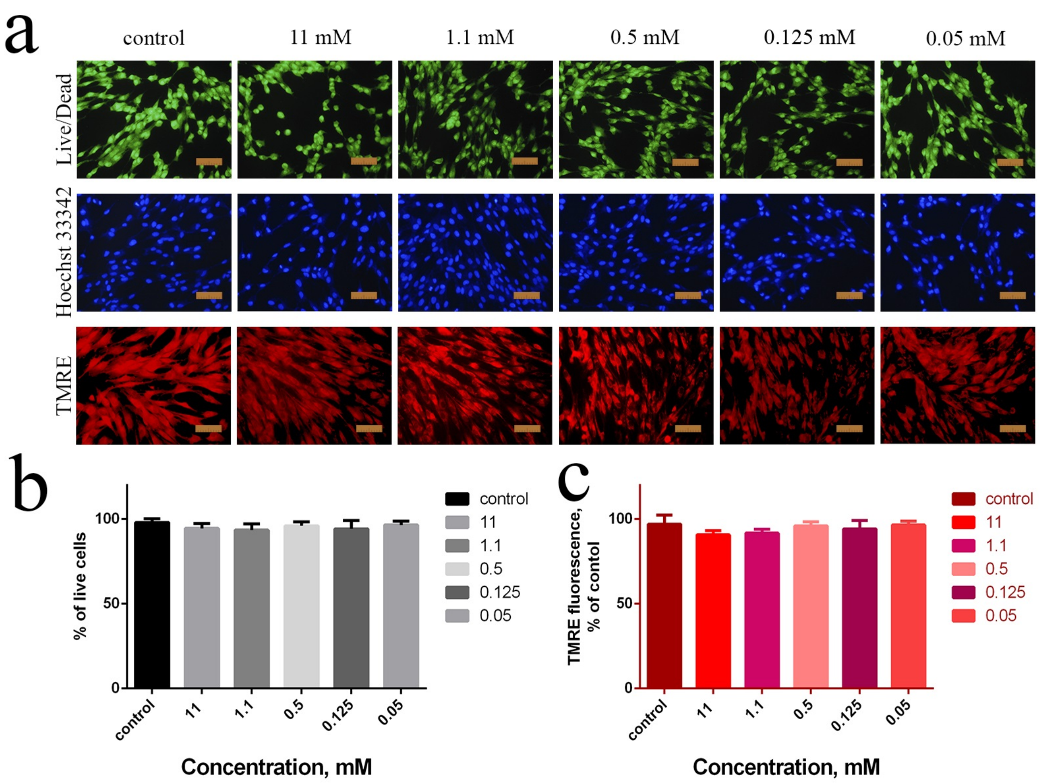

FIG. 3. Microphotographs of NCTC L929 mouse fibroblasts 24 hours after incubation with CeO_2-Mil nanocomposite (0.05–11 mM) dyed with SYTO9/PI (top line), Hoechst 33342 (middle line) and TMRE (bottom line) (a). Quantitative analysis of live/dead assay (b) and MMP level (c)

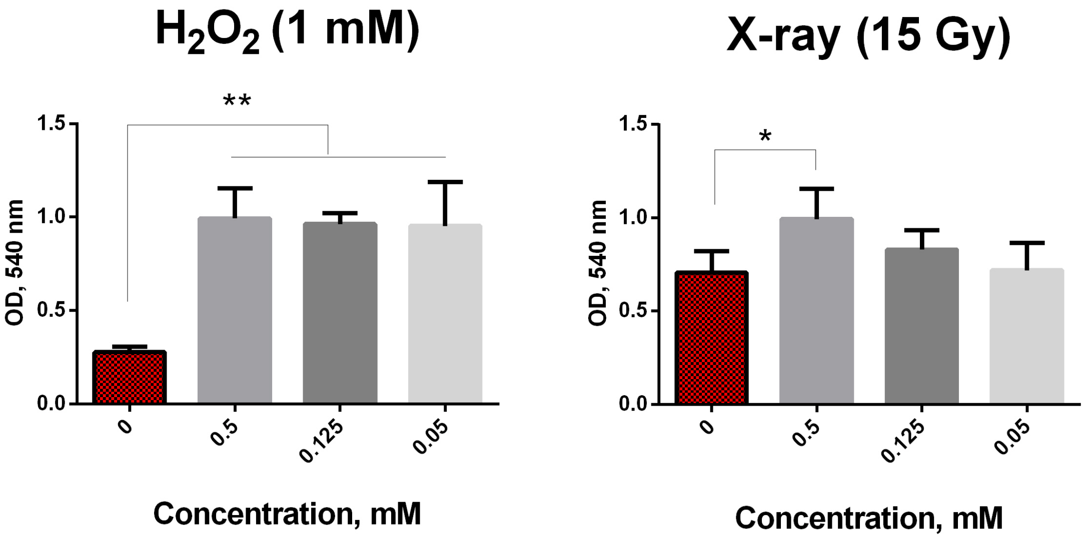

FIG. 4. Protective effect of CeO_2-Mil nanocomposite (0.05–0.5 mM) on NCTC L929 cell line under oxidative stress conditions induced by H_2O_2 treatment (left) and X-ray irradiation (right) as assessed using MTT assay. The cells were pretreated with a CeO_2-Mil nanocomposite in different concentrations (0.05–0.5 mM) and then exposed to X-ray irradiation (15 Gy) or treated with hydrogen peroxide (1 mM for 30 min). Data are presented at mean ±SD, * $p \leq 0.05\%$, ** $p \leq 0.001\%$

Lower concentrations of CeO_2-Mil nanocomposite (0.125–0.05 mM) did not provide a radioprotective effect. Meanwhile, the protective effect of CeO_2-Mil nanocomposite upon H_2O_2 treatment was observed in all the studied nanocomposite concentrations (0.05–0.5 mM) maintaining a high level of NCTC L929 cell viability close to the control values.

The protective action of the CeO_2-Mil nanocomposite under H_2O_2 induced oxidative stress can be explained by the pronounced catalase-like activity of the cerium oxide nanoparticles. We assume that the CeO_2-Mil nanocomposite, after being introduced into the cell culture, is localized not only in the cytoplasm of the cell, but is also partially adsorbed on the outer surface of cell membranes, which makes it possible to effectively decompose hydrogen peroxide in the selected concentration range (0.05–0.5 mM). At the same time, upon X-ray exposure, oxidative stress and the corresponding damaging factors develop through the water radiolysis inside and outside the cell. When exposed to X-rays, hydroxyl and superoxide radicals are first formed, which can dismutate to hydrogen peroxide. At the same time, it is well known that under acidic conditions, cerium oxide nanoparticles lose their catalase-mimetic activity while maintaining their SOD-mimetic ability, which leads to the accumulation of H_2O_2, being more toxic than superoxides, resulting in the selective radiation-induced cytotoxicity in relation to transformed cells [53]. Cerium oxide nanoparticles possess pronounced antioxidant properties and thus they can inactivate almost all types of ROS and free radicals formed as a result of radiation-induced water radiolysis, including the superoxide anion [54, 55] and hydroxyl radicals [56, 57]. Radiation-induced damage also develops in mitochondria, which is expressed in damage to mitochondrial DNA, uncoupling of the respiratory chain due to the development of oxidative stress, and a drop in the mitochondrial membrane potential [58–60]. Thus, the use of mitochondria-targeted radioprotectors based on cerium oxide can be considered as a promising strategy for protecting healthy surrounding tissue during radiation therapy.

References

[1] Singh S. Cerium oxide based nanozymes: Redox phenomenon at biointerfaces. *Biointerphases*, 2016, **11**(4), P. 04B202.

[2] Saifi M.A., Seal S., Godugu C. Nanoceria, the versatile nanoparticles: Promising biomedical applications. *J. Control Release*, 2021, **338**, P. 164–189.

[3] Lord M.S., Berret J.F., Singh S., Vinu A., Karakoti A.S. Redox Active Cerium Oxide Nanoparticles: Current Status and Burning Issues. *Small*, 2021, **17**(51), P. e2102342.

[4] Ivanov V.K., Baranchikov A.E., Ivanova Polezhaeva O.S., Kopitsa G.P., Tretyakov Y.D. Oxygen nonstoichiometry of nanocrystalline ceria. *Russian Journal of Inorganic Chemistry*, 2010, **55**(3), P. 325–327.

[5] Seminko V., Maksimchuk P., Grygorova G., Okrushko E., Avrunin O., Semenets V., Malyukin Y. Mechanism and Dynamics of Fast Redox Cycling in Cerium Oxide Nanoparticles at High Oxidant Concentration. *J. Phys. Chem. C*, 2021, **125**(8), P. 4743–4749.

[6] Malyukin Y., Maksimchuk P., Seminko V., Okrushko E., Spivak N. Limitations of Self-Regenerative Antioxidant Ability of Nanoceria Imposed by Oxygen Diffusion. *J. Phys. Chem. C*, 2018, **122**(28), P. 16406–16411.

[7] Malyukin Y., Klochkov V., Maksimchuk P., Seminko V., Spivak N. Oscillations of Cerium Oxidation State Driven by Oxygen Diffusion in Colloidal Nanoceria (CeO_{2-x}). *Nanoscale Res Lett*, 2017, **12**, P. 566.

[8] Shekunova T.O., Lapkina L.A., Shcherbakov A.B., Meshkov I.N., Ivanov V.K., Tsivadze A.Yu., Gorbunova Y.G. Deactivation of singlet oxygen by cerium oxide nanoparticles. *Journal of Photochemistry and Photobiology A: Chemistry*, 2019, **382**, P. 111925.

[9] Xue Y., Luan Q., Yang D., Yao X., Zhou K. Direct evidence for hydroxyl radical scavenging activity of cerium oxide nanoparticles. *J. Phys. Chem. C*, 2011, **115**, P. 4433–4438.

[10] Plakhova T., Romanchuk A., Butorin S., Konyukhova A., Egorov A., Shiryaev A., Baranchikov A., Dorovatovskii P., Huthwelker T., Gerber E., Bauters S., Sozarukova M., Scheinost A., Ivanov V., Kalmykov S., Kvashnina K. Towards the surface hydroxyl species in CeO_2 nanoparticles. *Nanoscale*, 2019, **11**(39), P. 18142–18149.

[11] Das S., Dowding J.M., Klump K.E., McGinnis J.F., Self W., Seal S. Cerium oxide nanoparticles: applications and prospects in nanomedicine. *Nanomedicine*, 2013, **8**, P. 1483–1508.

[12] Bhushan B., Gopinath P. Antioxidant nanozyme: a facile synthesis and evaluation of the reactive oxygen species scavenging potential of nanoceria encapsulated albumin nanoparticles. *J Mater Chem B*, 2015, **3**(24), P. 4843–4852.

[13] Pagliari F., Mandoli C., Forte G., Magnani E., Pagliari S., Nardone G., Licoccia S., Minieri M., Di Nardo P., Traversa E. Cerium Oxide Nanoparticles Protect Cardiac Progenitor Cells from Oxidative Stress. *ACS Nano*, 2012, **6**(5), P. 3767–3775.

[14] Hirst S.M., Karakoti A., Singh S., Self W., Tyler R., Seal S., Reilly C.M. Bio-distribution and in vivo antioxidant effects of cerium oxide nanoparticles in mice. *Envirom Toxicology*, 2013, **28**(2), P. 107–118.

[15] Popov A.L., Zaichkina S.I., Popova N.R., Rozanova O.M., Romanchenko S.P., Ivanova O.S., Smirnov A.A., Mironova E.V., Selezneva I.I., Ivanov V.K. Radioprotective effects of ultra-small citrate-stabilized cerium oxide nanoparticles. *RSC Advances*, 2016, **6**, P. 106141–106149.

[16] Inbaraj S.B., Chen B.H. An overview on recent in vivo biological application of cerium oxide nanoparticles. *Asian J Pharm Sci*, 2020, **15**(5), P. 558–575.

[17] Heckert E.G., Karakoti A.S., Seal S., Self W.T. The role of cerium redox state in the SOD mimetic activity of nanoceria. *Biomaterials*, 2008, **29**(18), P. 2705-9.

[18] Zhao H., Zhang R., Yan X., Fan K. Superoxide dismutase nanozymes: an emerging star for anti-oxidation. *J. Mater. Chem. B*, 2021, **9**, P. 6939–6957.

[19] Heckert E.G., Karakoti A.S., Seal S., Self W.T. The role of cerium redox state in the SOD mimetic activity of nanoceria. *Biomater*, 2008, **29**, P. 2705–2709.

[20] Baldim V., Bedioui F., Mignet N., Margaill I., Berret J.-F. The enzyme-like catalytic activity of cerium oxide nanoparticles and its dependency on Ce^{3+} surface area concentration. *Nanoscale*, 2018, **10**, P. 6971–6980.

[21] Shcherbakov A., Zholobak N., Spivak N., Ivanov V. Advances and prospects of using nanocrystalline ceria in cancer theranostics. *Russian Journal of Inorganic Chemistry*, 2014, **59**(13), P. 1556–1575.

[22] Zeng L., Cheng H., Dai Y., Su Z., Wang C., Lei L., Lin D., Li X., Chen H., Fan K., Shi S. In Vivo Regenerable Cerium Oxide Nanozyme-Loaded pH/$H_{(2)}O_{(2)}$-Responsive Nanovesicle for Tumor-Targeted Photothermal and Photodynamic Therapies. *ACS Appl Mater Interfaces*, 2021, **13**(1), P. 233–244.

[23] Nourmohammadi E., Khoshdel-Sarkarizi H., Nedaeinia R., Darroudi M., Kazemi Oskuee R. Cerium oxide nanoparticles: A promising tool for the treatment of fibrosarcoma in-vivo. *Mater Sci Eng C Mater Biol Appl*, 2020, **109**, P. 110533.

[24] Qi M., Li W., Zheng X., Li X., Sun Y., Wang Y., Li C., Wang L. Cerium and Its Oxidant-Based Nanomaterials for Antibacterial Applications: A State-of-the-Art Review. *Front. Mater.*, 2020, **7**.

[25] Zamani K., Allah-Bakhshi N., Akhavan F., Yousefi M., Golmoradi R., Ramezani M., Bach H., Razavi S., Irajian G.R., Gerami M., Pakdin-Parizi A., Tafrihi M., Ramezani F. Antibacterial effect of cerium oxide nanoparticle against Pseudomonas aeruginosa. *BMC Biotechnol*, 2021, **21**(1), P. 68.

[26] Pop O.L., Mesaros A., Vodnar D.C., Suharoschi R., Tăbăran F., Mageruşan L., Tódor I.S., Diaconeasa Z., Balint A., Ciontea L., Socaciu C. Cerium Oxide Nanoparticles and Their Efficient Antibacterial Application In Vitro against Gram-Positive and Gram-Negative Pathogens. *Nanomaterials (Basel)*, 2020, **10**(8), P. 1614.

[27] Shydlovska O., Kharchenko E., Osenniy I., Spivak M., Shcherbakov A., Zholobak N. Nanoparticles of cerium dioxide – an effective antiviral agent and adjuvant of biologically active molecules. *ScienceRise Biological Science*, 2018, **1**(10).

[28] Neal C.J., Fox C.R., Sakthivel T.S., Kumar U., Fu Y., Drake C., Parks G.D. Seal S. Metal-Mediated Nanoscale Cerium Oxide Inactivates Human Coronavirus and Rhinovirus by Surface Disruption. *ACS Nano*, 2021, **15**(9), P. 14544–14556.

[29] Mohamed H.E.A, Afridi S., Khalil A.T, Ali M.., Zohra T, Akhtar R., Ikram A., Shinwari Z.K., Maaza M. Promising antiviral, antimicrobial and therapeutic properties of green nanoceria. *Nanomedicine (Lond)*, 2020, **15**(5), P. 467–488.

[30] Shcherbakov A.B., Zholobak N.M., Ivanov V.K. Biological, biomedical and pharmaceutical applications of cerium oxide. *Cerium Oxide (CeO?): Synthesis, Properties and Applications*, 2020, P. 279–358.

[31] Shcherbakov A., Reukov V., Yakimansky A., Krasnopeeva E., Ivanova O., Popov A., Ivanov V. CeO_2 Nanoparticle-Containing Polymers for Biomedical Applications: A Review. *Polymers*, 2021, **13**(6), P. 924.

[32] Yang B., Chen Y., Shi J. Reactive Oxygen Species (ROS)-Based Nanomedicine. *Chem Rev*, 2019, **119**(8), P. 4881-4985.

[33] Krysanov E., Demidova T., Ivanova O., Ordzhonikidze K., Shcherbakov A., Ivanov V. Synergetic action of ceria nanoparticles and doxorubicin on the early development of two fish species, Danio rerio and Puntius tetrazona. *Nanosystems: Physics, Chemistry, Mathematics*, 2019, **10**(3), P. 289–302.

[34] Xu C., Lin Y., Wang J., Wu L., Wei W., Ren J., Qu X. Nanoceria-triggered synergetic drug release based on CeO_2-capped mesoporous silica host-guest interactions and switchable enzymatic activity and cellular effects of CeO_2 *Adv Healthc Mater.*, 2013, **2**(12), P. 1591-9.

[35] Liu X., Liu J., Chen S., Xie Y., Fan Q., Zhou J., Bao J., Wei T., Dai Z. Dual-path modulation of hydrogen peroxide to ameliorate hypoxia for enhancing photodynamic/starvation synergistic therapy. *J Mater Chem B*, 2020, **8**(43), P. 9933–9942.

[36] Barkam S., Das S., Saraf S., McCormack R., Richardson D., Atencio L., Moosavifazel V., Seal S. The change in antioxidant properties of dextran-coated redox active nanoparticles due to synergetic photoreduction-oxidation. *Chemistry*, 2015, **21**(36), P. 12646-56.

[37] Zholobak N. M., Shcherbakov A. B., Bogorad-Kobelska A. S., Ivanova O. S., Baranchikov A. Ye., Spivak N. Ya., Ivanov V. K. Panthenol-stabilized cerium dioxide nanoparticles for cosmeceutic formulations against ROS-induced and UV-induced damage. *J Photochem Photobiol B*, 2014, **130**, P. 102–108.

[38] Zholobak N.M., Shcherbakov A.B., Ivanova O.S., Reukov V., Baranchikov A.E., Ivanov V.K. Nanoceria-curcumin conjugate: synthesis and selective cytotoxicity against cancer cells under oxidative stress conditions. *J. Photochem. Photobiol. B*, 2020, **209**, P. 111921.

[39] Shydlovska O., Kharchenko E., Zholobak N., Shcherbakov A., Marynin A., Ivanova O., Baranchikov A., Ivanov V. Cerium oxide nanoparticles increase the cytotoxicity of TNF-alpha in vitro. *Nanosystems: Phys. Chem. Math.*, 2018, **9**(4), P. 537–543.

[40] Pupure J., Fernandes M. A. S., Santos M. S., Moreno A. J. M., Kalvinsh I., Klusa V., Oliveira C. R. Mitochondria as the target for mildronate's protective effects in azidothymidine (AZT)-induced toxicity of isolated rat liver mitochondria. *Cell Biochem Funct*, 2008, **26**, P. 620–631.

[41] Pupure J., Isajevs S., Skapare E., Rumaks J., Svirskis S., Svirina D., Kalvinsh I., Klusa V. Neuroprotective properties of mildronate, a mitochondria-targeted small molecule. *Neurosci Lett*, 2010, **470**(2), P. 100–105.

[42] Wang C., Youle R.J. The Role of Mitochondria in Apoptosis. *Annu Rev Genet*, 2009, **43**, P. 95–118.

[43] Lin M.T., Beal M.F. Mitochondrial dysfunction and oxidative stress in neurodegenerative diseases. *Nature*, 2006, **443**(7113), P. 787–795.

[44] Luo Y., Ma J., Lu W. The Significance of Mitochondrial Dysfunction in Cancer. *Int J Mol Sci*, 2020, **21**(16), P. 5598.

[45] Asati A., Santra S., Kaittanis C., Perez J.M. Surface-Charge-Dependent Cell Localization and Cytotoxicity of Cerium Oxide Nanoparticles. *ACS Nano*, 2010, **4**(9), P. 5321–5331.

[46] Ma Y., Li P., Zhao L., Liu J., Yu J., Huang Y., Zhu Y., Li Z., Zhao R., Hua S., Zhu Y., Zhang Z. Size-Dependent Cytotoxicity and Reactive Oxygen Species of Cerium Oxide Nanoparticles in Human Retinal Pigment Epithelia Cells. *Int J Nanomedicine*, 2021, **16**, P. 5333–5341.

[47] García-Salvador A., Katsumiti A., Rojas E., Aristimuño C., Betanzos M., Martínez-Moro M., Moya S.E., Goñi-de-Cerio F. A Complete In Vitro Toxicological Assessment of the Biological Effects of Cerium Oxide Nanoparticles: From Acute Toxicity to Multi-Dose Subchronic Cytotoxicity Study. *Nanomaterials (Basel)*, 2021, **11**(6), P. 1577.

[48] Popov A.L., Popova N.R., Selezneva I.I., Akkizov A.Y., Ivanov V.K. Cerium oxide nanoparticles stimulate proliferation of primary mouse embryonic fibroblasts *in vitro*. *Materials Science and Engineering C*, 2016, **68**, P. 406–413.

[49] Popov A., Abakumov M., Savintseva I., Ermakov A., Popova N., Ivanova O., Kolmanovich D., Baranchikov A., Ivanov V. Biocompatible dextran-coated gadolinium-doped cerium oxide nanoparticles as MRI contrast agents with high T1 relaxivity and selective cytotoxicity to cancer cells. *J. Mater. Chem. B*, 2021, **9**, P. 6586–6599.

[50] Xiong S., Mu T., Wang G., Jiang X. Mitochondria-mediated apoptosis in mammals. *Protein Cell*, 2014, **5** P. 737–749.

[51] Jana S.K., Banerjee P., Das S., Seal S. Chaudhury K. Redox-active nanoceria depolarize mitochondrial membrane of human colon cancer cells. *J. Nanopart. Res.*, 2014, **16**, P. 2441.

[52] Xu P.T., Maidment B.W., Antonic V., Jackson I.L., Das S., Zodda A., Zhang X., Seal S., Vujaskovic Z. Cerium Oxide Nanoparticles: A Potential Medical Countermeasure to Mitigate Radiation-Induced Lung Injury in CBA/J Mice. *Radiat Res*, 2016, **185**(5), P. 516–526.

[53] Perez J.M., Asati A., Nath S., Kaittanis C. Synthesis of Biocompatible Dextran-Coated Nanoceria with pH-Dependent Antioxidant Properties. *Small*, 2008, **4**(5), P. 552–556.

[54] Akhtar M.J., Ahamed M., Alhadlaq H. Anti-Inflammatory CeO_2 Nanoparticles Prevented Cytotoxicity Due to Exogenous Nitric Oxide Donors via Induction Rather Than Inhibition of Superoxide/Nitric Oxide in HUVE Cells. *Molecules*, 2021, **26**(17), P. 5416.

[55] Akhtar M.J., Ahamed M., Alhadlaq H. Anti-Inflammatory CeO_2 Nanoparticles Prevented Cytotoxicity Due to Exogenous Nitric Oxide Donors via Induction Rather Than Inhibition of Superoxide/Nitric Oxide in HUVE Cells. *Molecules*, 2021, **26**(17), P. 5416.

[56] Zou S., Zhu X., Zhang L., Guo F., Zhang M., Tan Y., Gong A., Fang Z., Ju H., Wu C., Du F. Biomineralization-Inspired Synthesis of Cerium-Doped Carbonaceous Nanoparticles for Highly Hydroxyl Radical Scavenging Activity. *Nanoscale Res Lett*, 2018, **13**(1), P. 76.

[57] Zhai J.H., Wu Y., Wang X.Y., Cao Y., Xu K., Xu L., Guo Y. Antioxidation of Cerium Oxide Nanoparticles to Several Series of Oxidative Damage Related to Type II Diabetes Mellitus In Vitro. *Med Sci Monit.*, 2016, **22**, P. 3792–3797.

[58] Leach J.K., Van Tuyle G., Lin P. S., Schmidt-Ullrich R., Mikkelsen R.B. Ionizing radiation-induced, mitochondria-dependent generation of reactive oxygen/nitrogen. *Cancer Res*, 2001, **61**(10), P. 3894–3901.

[59] Averbeck D., Rodriguez-Lafrasse C. Role of Mitochondria in Radiation Responses: Epigenetic, Metabolic, and Signaling Impacts. *Int J Mol Sci.*,2021, **22**(20), P. 11047.

[60] Murray V., Hardie M.E., Gautam S.D. Comparison of Different Methods to Determine the DNA Sequence Preference of Ionising Radiation-Induced DNA Damage. *Genes (Basel)*, 2019, **11**(1), P. 8.

Submitted 11 January 2022; accepted 31 January 2022

Information about the authors:

A. L. Popov – Institute of Theoretical and Experimental Biophysics of the Russian Academy of Sciences, Institutskaya str., 3, Pushchino, 142290, Russia; antonpopovleonid@gmail.com

D. D. Kolmanovich – Institute of Theoretical and Experimental Biophysics of the Russian Academy of Sciences, Institutskaya str., 3, Pushchino, 142290, Russia; kdd100996@mail.ru

N. R. Popova – Institute of Theoretical and Experimental Biophysics of the Russian Academy of Sciences, Institutskaya str., 3, Pushchino, 142290, Russia; nellipopovaran@gmail.com

S. S. Sorokina – Institute of Theoretical and Experimental Biophysics of the Russian Academy of Sciences, Institutskaya str., 3, Pushchino, 142290, Russia; sorokinasvetlana.iteb@gmail.com

O. S. Ivanova – Kurnakov Institute of General and Inorganic Chemistry of the Russian Academy of Sciences, Leninskiy prosp., 31, Moscow, 119991, Russia; runetta05@mail.ru

N. N. Chukavin – Institute of Theoretical and Experimental Biophysics of the Russian Academy of Sciences, Institutskaya str., 3, Pushchino, 142290, Russia; Moscow Region State University, 141014 Moscow, Russia; chukavinnik@gmail.com

A. B. Shcherbakov – Zabolotny Institute of Microbiology and Virology, National Academy of Sciences of Ukraine, Kyiv D0368, Ukraine; ceroform@gmail.com

T. O. Kozlova – Kurnakov Institute of General and Inorganic Chemistry of the Russian Academy of Sciences, Leninskiy prosp., 31, Moscow, 119991, Russia; tasiok@mail.ru

S. A. Kalashnikova – 40th City clinical hospital, Volgogradskaya st., 189, Yekaterinburg, 620102, Russia; kalashnikova.sana@mail.ru

V. K. Ivanov – Kurnakov Institute of General and Inorganic Chemistry of the Russian Academy of Sciences, Leninskiy prosp., 31, Moscow, 119991, Russia; van@igic.ras.ru

Conflict of interest: the authors declare no conflict of interest.

NANOSYSTEMS:
PHYSICS, CHEMISTRY, MATHEMATICS

Original article

Miditana S.R., Tirukkovalluri S.R., Raju I.M. *Nanosystems: Phys. Chem. Math.*, 2022, **13** (1), 104–114.
http://nanojournal.ifmo.ru
DOI 10.17586/2220-8054-2022-13-1-104-114

Synthesis and antibacterial activity of transition metal (Ni/Mn) co-doped TiO_2 nanophotocatalyst on different pathogens under visible light irradiation

Sankara Rao Miditana[1,2,a], Siva Rao Tirukkovalluri[2,b], Imandi Manga Raju[2,c]

[1]Government Degree College, Puttur, Chittoor, Andhra Pradesh – 517583, India
[2]Andhra University, Visakhapatnam, Andhra Pradesh – 530003, India

[a]sraom90@gmail.com, [b]sivaraoau@gmail.com, [c]mangorchem@gmail.com

Corresponding author: Sankara Rao Miditana, sraom90@gmail.com

ABSTRACT Visible light driven photocatalytically active mesoporous nanomaterials plays an indispensable role for antibacterial activity in low light applications. In this work, nanomaterials were handily prepared by varying the dopant concentrations from 0.25 to 1.0 Wt % using sol-gel method. All the prepared samples were characterized by Powdered X-ray diffraction (XRD), Scanning electron microscope-energy dispersive X-ray spectroscopy (SEM-EDS), Fourier transform infrared spectroscopy (FTIR), Ultraviolet-visible diffuse reflectance spectroscopy (UV/Vis-DRS), Transmission electron microscopy (TEM) and Brauner–Emmett–Teller (BET). The characterization results revealed that a photocatalytically active phase i.e.; anatase and rutile mixed phase was observed for co-doped catalyst samples. Due to substitutional doping of Mn and Ni by replacing Ti, the frequency shift of Ti–O–Ti in the catalyst samples was observed by FTIR. Further the catalyst shows roughmorphology, irregular particle shape with less particle size having high surface area, and reduced band gap energy. The photocatalytically active materials antibacterial activity was discerned by using *Sphingomonas paucimobilis* and *Pseudomonas fluorescence*. The result of antibacterial activity shows that among all nanocatalysts, NMT2 catalyst shows optimum zone of inhibition at 25.1 ± 0.2 mm for *Sphingomonas paucimobilis* and 18.1 ± 0.2 mm for *Pseudomonas fluorescence* compared to standard (chloramphenicol) value at 24.1 ± 0.1 mm and 23.1 ± 0.05 mm at 100 μg/mL respectively.

KEYWORDS nanomaterials, photocatalysis, Ni/Mn–TiO_2, antibacterial activity, agar-well diffusion method

FOR CITATION Miditana S.R., Tirukkovalluri S.R., Raju I.M. Synthesis and antibacterial activity of transition metal (Ni/Mn) co-doped TiO_2 nanophotocatalyst on different pathogens under visible light irradiation. *Nanosystems: Phys. Chem. Math.*, 2022, **13** (1), 104–114.

1. Introduction

TiO_2 is an acquainted photocatalyst with non-toxicity, inexpensive, accessible, etc. In addition, TiO_2 photocatalyst has the functions of photoelectric transfer, desideration, sterilization and surface self-cleaning. So, it is used to enhance the environment extensively in the air purification and sewage treatment [1–3]. It exists in three crystalline structures: anatase, rutile and brookite. Anatase and rutile belong to the large bandgap semiconductors with bandgap energies of 3.2 and 3.0 eV, respectively [4]. However, because of its wide forbidden band gap, it excites the electron from valance band to conduction band by UV light, which is available only 4 – 5 % in the solar light. Co-doping of transition metals into the TiO_2 lattice enhances the photocatalytic action by reducing the bandgap in between VB and CB [5]. An appended benefit of transition metal doping like Mn, Cr, Ni, Cu is to improve the trapping of electron to inhibit the e^+/h^- recombination during irradiation of light [6, 7]. "Transition metal doped TiO_2 nanoparticles demonstrated that Ni or Mn doped TiO_2 possess better absorption ability of visible light and Ni/Mn either substitutes Ti^{4+} site or embeds in the vacancy of TiO_2 lattice" [8].

In the present investigation, among all the transition metals manganese and nickel were selected for the synthesis of Mn–Ni co-doped TiO_2 using the sol-gel method. These metals are preferred because the presence of the t_{2g} orbital of d is very close to the conduction band of TiO_2 by which the absorption is shifted to visible region [9, 10]. Manganese has the greatest potential in permitting significant optical absorption in the visible region through the combined effects of a narrow bandgap and the introduction of intermediate bands within forbidden gap [9]. In the Mn–Ni co-doped TiO_2, Mn^{2+} and Ni^{2+} ions replaced the Ti^{4+} in TiO_2 lattice because ionic radii of Ti^{4+} (0.068 nm) is similar to that of Mn^{2+} (0.078 nm) and Ni^{2+} (0.072 nm) [11]. On the other hand, the introduction of Ni ions into the TiO_2 lattice can form heterojunctions between n-type TiO_2 and p-type Ni oxide dopant. The presence of p-n junctions can promote the segregation of electron-hole pairs through the electric junction field and facilitate the interfacial charge transfer [12]. There are numerous methods for producing titania nanoparticles, such as sol-gel process, electrochemical coating, hydrothermal process, flame aerosol process, micro emulsion method, thermolysis, chemical vapor deposition, etc. [13]. Among all these methods, the sol-gel method is often employed and it offers advantages such as precise control over the stoichiometry, low temperature synthesis, high crystallinity and high purity [14].

In the present work, metal ion (Ni, Mn) doped TiO_2 samples were prepared by calcination and their antibacterial activity was studied by measuring zone of inhibition forgram negative pathogens like *Sphingomonas paucimobilis* and *Pseudomonas fluorescence*. *Sphingomonas paucimobilis* (MTCC-6363) has a single polar flagellum with slow motility. It is usually found in soil and water, hospitals and various types of clinical specimens, including respiratory therapy items, humidifiers, water, air, bedside water bottles, sinks, and temperature probes. This organism causes blood stream infections, leg ulcers, and urinary tract infections in humans [15]. *Pseudomonas fluorescence* (MTCC-1688) constitutes large domain of prokaryotic microorganisms. Typically, a few micrometers in length, the bacteria have a number of shapes, ranging from spheres to rods and spirals. *Pseudomonas fluorescence* flourishes in hospital environments and is a particular problem in this environment, since it is the second-most common infection in hospitalized patients [16].

2. Experimental

2.1. Materials

All the chemicals used in the synthesis process were reagent grade and used without further purification. n-butyl tetra orthotitanate ($Ti(OBu)_4$), manganese nitrate ($[Mn(NO_3)_2]\cdot 6H_2O$) and nickel nitrate ($[Ni(NO_3)_2]\cdot 6H_2O$) were obtained from E-Merck, Germany and used as a precursors for titanium, manganese and nickel for preparing undoped TiO_2 and co-doped TiO_2 catalysts respectively.

2.2. Synthesis of nanocatalyst

Manganese and nickel co-doped nanotitania was synthesized by the sol-gel method [17, 18]. In this process, n-butyl tetra orthotitanate (20 mL) was added to 40 mL of ethanol and acidified with 3.2 mL of nitric acid (concentrated HNO_3) taken in a 150 mL pyrex glass beaker (solution-A) and stirred for 15 min. In another beaker, the required weight (as per the dopant weight percentage) of Mn and Ni from its precursors with respect to titania were taken and added 40 mL of ethanol and then 7.2 mL of deionized water for hydrolysis (solution-B). Then solution-B was added to solution-A drop wise under vigorous stirring. After complete addition of solution-B, a colloidal suspension formed and was stirred continuously for 90 min and aged for 48 h. The obtained gel was dried in an oven at 70 °C, ground in a mortar and calcined at 450 °C for about 5 h in a muffle furnace. Finally, it was cooled and ground to an homogeneous powder. Following the above procedure, different Mn & Ni co-doped catalysts were prepared by varying weight percentages of Mn & Ni (0.25 – 1.0 Wt %) as shown in Table 1. For preparation of undoped TiO_2, the above procedure is followed without addition of nickel and manganese precursors.

TABLE 1. Name assigned to different weight percentages of co-doped TiO_2 catalyst samples

S. No	Dopant (Transition metal) weight percentages in TiO_2(Wt %)	Name assigned to co-doped TiO_2 Catalyst
1	1.00 Mn 0.25 Ni	NMT1
2	0.25 Mn 1.00 Ni	NMT2
3	0.50 Mn 0.50 Ni	NMT3
4	0.25 Mn 0.75 Ni	NMT4
5	0.75 Mn 0.25 Ni	NMT5
6	Nil	undoped TiO_2

2.3. Experimental techniques used for characterization of the catalysts

The crystalline structure of photocatalysts were determined by powder X-ray diffraction (XRD) spectra taken (PAN Analytical) using anode Cu-WL 1 ($\lambda = 1.5406$ nm) radiation with a nickel filter. The applied current and voltage were 40 mA and 40 kV respectively. The average crystallite size of anatase was determined according to the Scherrer equation using full width at half maximum (FWHM) data of the selected peak. The surface area and porosity measurements were carried out with a micrometrics, Gemini VII surface area analyzer. The nitrogen adsorption/desorption isotherms were recorded 2 – 3 times to obtain reproducible results and reported by BJH surface/volume mesopore analysis. The micro pore volume was calculated using the Frenkel–Halsey–Hill isotherm equation. Each sample was degassed at 300 °C for 2 h. The size and shape of the catalyst were recorded with TEM using JEOL/JEM 2100, operated at 200 kV. The morphology and elemental composition of the catalyst were characterized using scanning electron microscope (SEM)

(ZEISS-SUPRA 55 VP) equipped with an energy dispersive X-ray (EDX) spectrophotometer and operated at 20 kV. FT-IR analyses were performed on a FT-IR spectrometer (Nicolet Avatar360). The Diffuse reflectance spectra (DRS) of the catalyst samples were recorded with a Shimadzu 3600 UV-Visible-DRS Spectrophotometer equipped with an integrating sphere diffuse reflectance accessory, using $BaSO_4$ as reference scatter. Powder samples were loaded into a quartz cell and spectra were recorded in the range of 200 – 900 nm.

2.4. Experimental set up for the antibacterial activity study of photocatalyst

Antibacterial activity study of NMT-2 was carried out by the agar-well diffusion method [19] against bacterial strain namely *Sphingomonas paucimobilis* and *Pseudomonas fluorescence* of Gram-negative pathogens. The nutrient agar (High media – India) dissolved in water was distributed in 100 mL conical flask and sterilized in autoclave at 121 °C 15 lbp for 15 min. After autoclaving, the media was poured into sterilized petri plates which were then swabbed by using L-shaped glass rod with 100 μL of 24 h mature broth of the bacterial strain culture. The wells were made sterile by cork-borer. Wells are created in two different petri plates in the first plate undoped TiO_2 another plates NMT-2 sample solution injected (100, 300 and 400 μg/mL) into the wells. The TiO_2 nanoparticles were dispersed in sterile water and it was used as a negative control and simultaneously the standard antibiotic chloramphenicol (100 μg/mL) as positive control were tested against the bacterial pathogen, then the plates were incubated 24 h at 37 °C. The zone inhibition of every well measured in millimeters.

3. Results and discussion

3.1. X-ray diffraction studies (XRD)

Figure 1 shows crystallinity and structural properties of manganese and nickel co-doped TiO_2 of different phases in the XRD patterns of the samples obtained after calcination at 450 °C. All diffraction lines are relatively strong, which indicating a high crystallinity for all samples. Further, the peak positions and relative intensities of the diffraction lines match with standard diffraction data for different TiO_2 phases, i.e. anatase and rutile for NMT1, NMT2, NMT3. The anatase phase was confirmed with the Joint Committee on Powder Diffraction Standard (JCPDS) file no. 21-1272. The peaks at $2\theta = 25.28$, 37.81, and 48.05 corresponded to the (101), (004), and (200) planes of anatase, while the peaks at $2\theta = 27.29$, 44.10 and 54.32, corresponded to the (110), (101) and (220) planes of rutile structure with the JCPDS file no. 21-1276. The existence of rutile in the nanomaterial was readily discernible from its (110) diffraction peak located at 2θ of 27.29° in the XRD pattern, because no overlapping of this peak with any other peaks from anatase occurred. Anatase phase can also be easily identified from its (101) peak located at 2θ of 25.3°, as this peak doesn't overlap with any other peaks of rutile. This result clearly demonstrates that rutile and anatase coexisted in the samples NMT1 – NMT3. The percentage ratio of anatase/rutile was found to be 86:14 estimated using Rietveld refinement method. Further, the samples NMT4, NMT5 and undoped TiO_2 shows anatase phase only. The X-ray diffraction patterns of anatase TiO_2 nanoparticles exhibited broad peaks, indicating small sizes of the nanoparticles at 450 °C calcination temperature while the sharp peaks indicated large nanoparticle sizes. The average crystallite sizes of the samples were determined by the Debye–Scherrer equation using high intensity of anatase (101) and rutile (110) diffraction peaks, the results were shown in Table 2. The XRD patterns of the samples exhibited similar diffraction peaks, indicating that the obtained samples were the TiO_2 nanomaterial consisting of anatase and rutile nanoparticles.

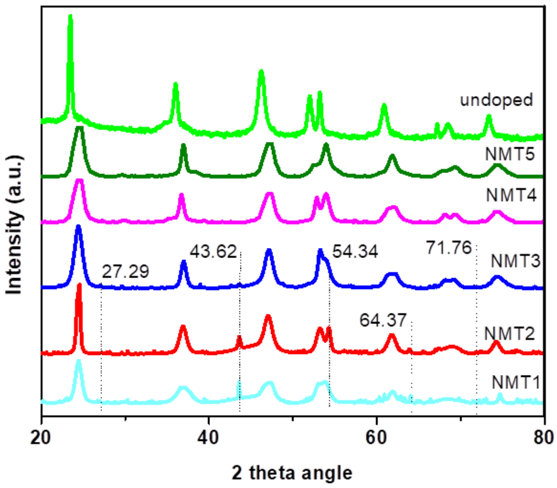

FIG. 1. XRD patterns of undoped and co-doped NMT catalysts

TABLE 2. The results of crystallite size (XRD), band gap (UV-Vis-DRS) and BET surface area

S.No	Catalyst	Crystallite size (nm)	Band gap energy (eV)	BET surface area analysis		
				Surface area (m^2/g)	Pore volume (cm^3/g)	Pore size (nm)
1	NMT1	7.35	2.74	113.41	0.22	7.3
2	NMT2	6.5	2.70	135.70	0.22	6.2
3	NMT3	7.31	2.78	114.06	0.22	7.3
4	NMT4	7.9	2.84	106.81	0.20	8.2
5	NMT5	8.50	3.0	88.87	0.20	9.3
6	undoped	18.3	3.20	64.09	0.21	10

3.2. Scanning electron microscopy & Energy dispersive spectroscopy (SEM-EDX)

The morphology and particle size of the catalyst, which play very important roles in its photocatalytic activity [20], were examined by the SEM. Fig. 2 shows that the SEM micrograph of the as prepared undoped TiO_2 and NMT2 nanocatalysts. In the Fig. 2(a) undoped TiO_2 clearly revealed large particle size and Fig. 2(b) co-doped TiO_2 shows small particle size, which leads to high surface area, well correlated with BET results. The morphology has different shapes of grains with irregular boundaries. Images of undoped TiO_2 (Fig. 2(a)) show randomly shaped and aggregated particles. HRSEM of 1.00 wt% of Ni and 0.25 wt% of Mn–TiO_2 (Fig. 2(b)) shows irregular tiny clusters composed of large numbers of nanoparticles with lower aggregation and better distribution. From the SEM images it can be inferred that aggregation is decreased greatly due to co-doping. The elemental composition of the prepared catalyst determined by the EDX detector was attached to a SEM shown in Fig. 2(c). EDX analysis revealed that the presence of Ti,O, Ni and Mn elements. No impurities related to precursor molecules were detected.

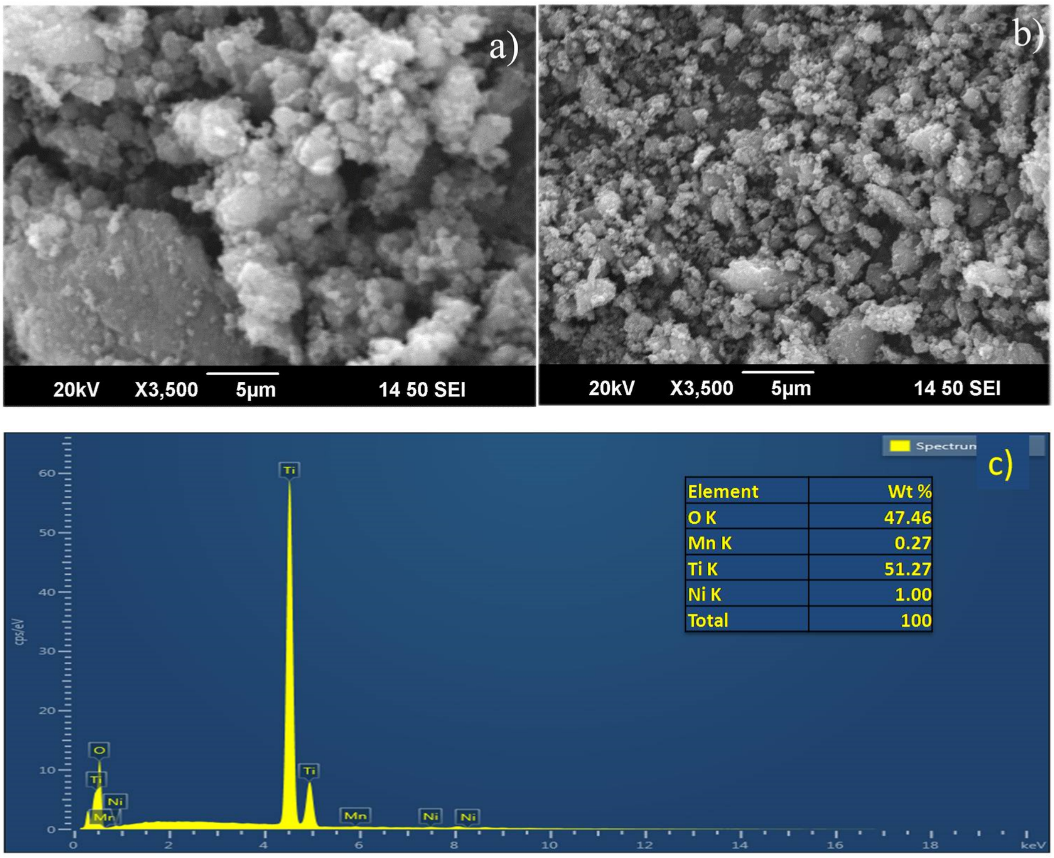

Element	Wt %
O K	47.46
Mn K	0.27
Ti K	51.27
Ni K	1.00
Total	100

FIG. 2. SEM images of a) undoped TiO_2 and b) NMT2; c) EDX spectra of NMT2

3.3. Transmission electron microscopy (TEM)

The particle size distribution was obtained by measuring the diameter of particles from representative TEM images. The TEM micrographs of undoped and co-doped (NMT2) TiO_2 samples are shown in Fig. 3(a) and (b). From the images it is noticed that the particle size of NMT2 is smaller compared to undoped TiO_2. The Fig. 3(c) shows the catalyst particles lattice fringes with d spacing 0.33 nm corresponding to 101 plane of anatase TiO_2. The diffraction rings are observed (Fig. 3(d)) for co-doped (NMT2) TiO_2 catalyst from SAED pattern clearly reveals that no structural change of anatase TiO_2 was found; the planes are (101), (004), (200) and (211). Fig. 3(e) shows that the average size of the prepared nanoparticle is 6.5 nm, which was calculated from the Gaussian fitting of the size Histogram [20, 21]. These results confirmed that the co-doping of Ni and Mn reduces the particle size of TiO_2.

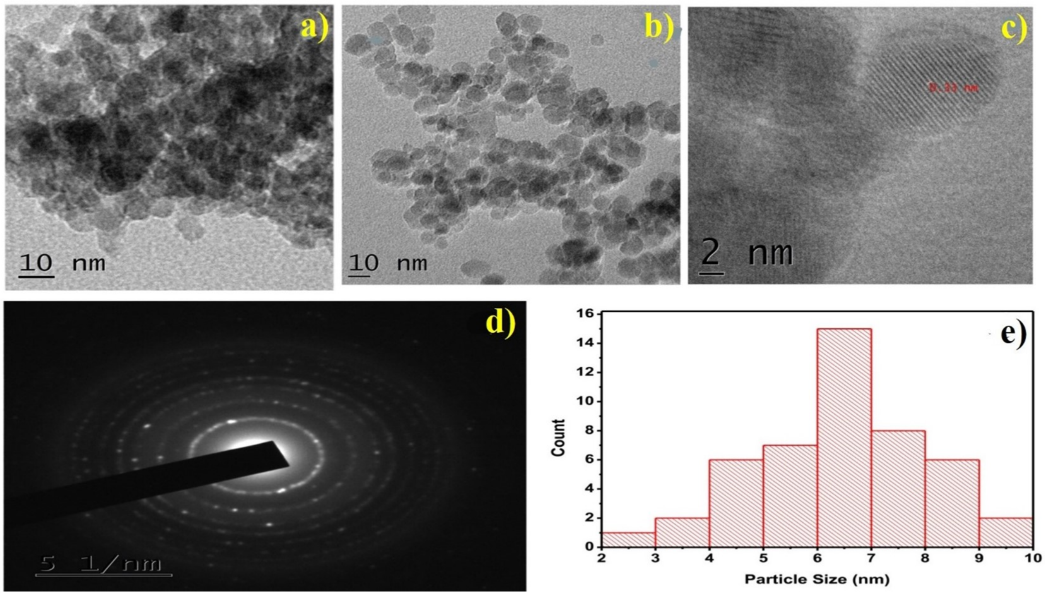

FIG. 3. TEM images of a) undoped TiO_2; b) NMT2; c) NMT2 showing lattice fringes; d) SAED pattern of NMT2; e) NMT2 particle size distribution

3.4. Fourier Transform – Infra Red Spectroscopy (FT-IR)

Undoped and Ni^{2+}, Mn^{2+} co-doped TiO_2 nanomaterials were identified by FT-IR spectra and were given in Fig. 4. The bands appeared around at 3012, 3464, and 1620 – 1635 cm^{-1} [22] corresponding to stretching vibrations of OH belongs to Ti–OH on the surface and bending vibrations of adsorbed H–OH molecule. The strong absorption band around 569 cm^{-1} is due to stretching vibrations of Ti–O–Ti and Ti–O band in undoped TiO_2 which is in good agreement with previous studies [23]. From Fig. 4(b) it is seen that after co-doping of Ni and Mn into TiO_2 lattice the stretching vibrations of skeletal Ti–O–Ti shifted to 569 to 605 cm^{-1} indicating that Ni and Mn had been co-doped into the TiO_2 lattice by substituting titanium [24]. Further, the increased band intensity located at 1020 cm^{-1} for co-doped TiO_2 indicated that Ni and Mn are co-doped into TiO_2 lattice.

3.5. Ultraviolet-visible diffuse reflectance spectroscopic studies (UV-Vis-DRS)

The diffused reflectance spectra (DRS) of undoped and Ni, Mn co-doped TiO_2 samples shown in Fig. 5 indicate that the absorption of the electromagnetic spectrum appeared at the visible region ($\sim$ 400 – 800 nm). NMTs (Ni and Mn co-doped samples) showed remarkable decreases in band gap and extension of absorption edge towards visible light wavelength (red shift). This is may be due to the formation of an extra energy level above the valance band by Ni 2p leading to narrowing the band gap of TiO_2 [25]. This shift is associated with the doping as well as the formation of stable rutile phase of TiO_2 as illustrated in XRD. The inherent reason for the red shift in the band gap is due to the change of the sp-d exchange interactions between the band electrons and the localized d-electrons of the Ni^{2+} ions [26].

The manganese ions incorporated into TiO_2 lattice distort the surrounding environment which affects the conduction band of TiO_2 through the interaction with Ti-3d orbitals which helps to suppress the recombination of electron hole pairs and extended the optical response [27]. Furthermore, this was supported by the calculated band gap energies of all the synthesized samples from the reflectance spectra using the Kubelka–Monk formalism and Tauc plot method [28] shown in Fig. 5(b). The undoped TiO_2 exhibited a band gap of 3.2 eV, which is comparable with the literature value [29] and the co-doped TiO_2 sample showing the band gap ranging from 2.7 to 3.01 eV. Among all the co-doped samples, NMT2 exhibited the lowest band gap energy (2.70 eV). Thus, the results indicated that all the co-doped samples are visible light-active and enhance the photocatalytic degradation efficiency due to the formation of more number of photo generated

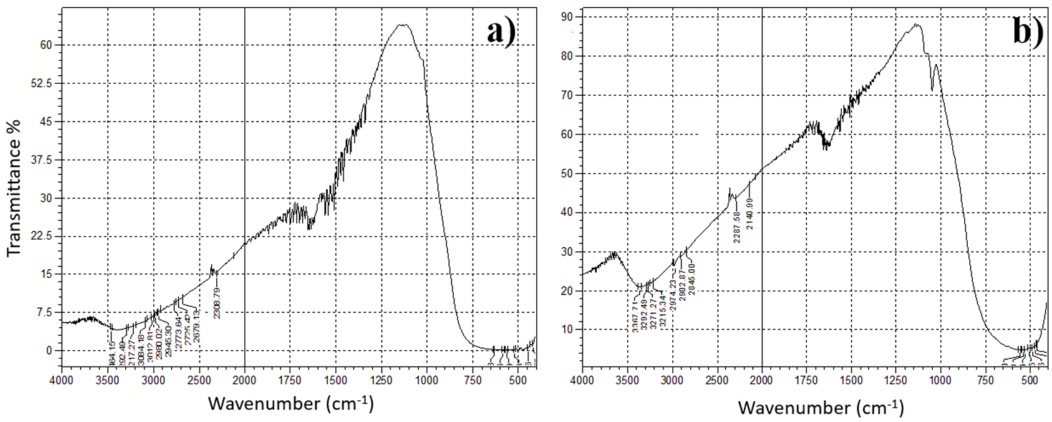

FIG. 4. FT-IR spectra of a) undoped TiO_2; b) NMT2

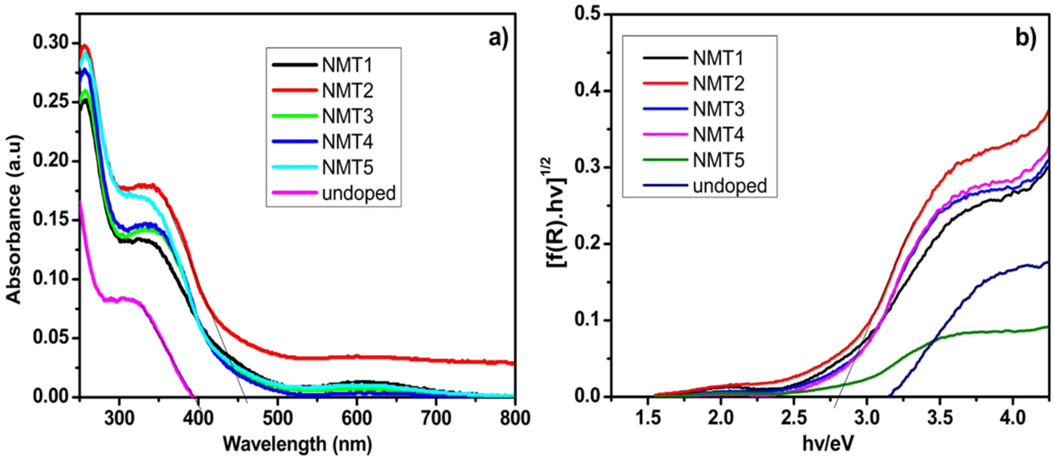

FIG. 5. (a) The DRS spectra of undoped and co-doped TiO_2 with different Wt% of Mn and Ni; (b) Tauc plots of the square root of the Kubelka–Munk function determining band gap energy values

electron/hole pairs. Further, when compared the band gap values of Mn and Ni single doped TiO_2 catalysts (which are obtained from literature value), the band gap of NMT2 catalyst is reduced and the values are given in Table 3 [30, 31].

TABLE 3. The comparative band gap values of Mn and Ni single doped and Mn and Ni co-doped TiO_2

S.No	Doping elements	Catalysts band gap energy (eV)	Reference No.
1	Mn	2.95	28
2	Ni	2.99	29
3	Undoped TiO_2	3.2	27
4	Mn and Ni	2.70	Present work

3.6. Brauner–Emmett–Teller (BET)

The specific surface area and porosity of the undoped TiO_2 and NMT2 were investigated by using the N_2 adsorption and desorption isotherms as shown in Fig. 6(a). All the isotherms of samples revealed the stepwise adsorption and desorption branch of type IV curves, indicating the presence of mesoporous material having a three-dimensional (3D) intersection according to IUPAC classification. A hysteresis loop with a stepwise adsorption and desorption branch is observed at wide range of pressure (P/P_0), and the surface area of NMT2 mesoporous TiO_2 calcined at 450 °C is 135.70 m^2/g as shown in Fig. 6(a). The undoped TiO_2 surface area is 64 m^2/g as shown in Fig. 6(a). This result indicates that the synthesized material has wider mesoporous structure. To analyze pore size and pore volume, the plots of the pore size distribution are investigated by desorption branch of the BJH method as shown in Fig. 6(b). The average pore diameter of mesoporous TiO_2 calcined at 450 °C is 6.2 nm with relatively narrow pore size distribution. The pore volume of mesoporous TiO_2 is 0.22 cm^3/g. However, for undoped TiO_2, a 10 nm pore size distribution is observed and 0.21 cm^3/g pore volume is also counted. Such physical properties of large surface area and high crystallinity with nano crystalline aggregated make a material a good candidate for high photocatalytic activity. This increased surface area may favor the adsorption of the more number of dye molecules on the surface of the catalyst, which enhances the degradation efficiency of the catalyst.

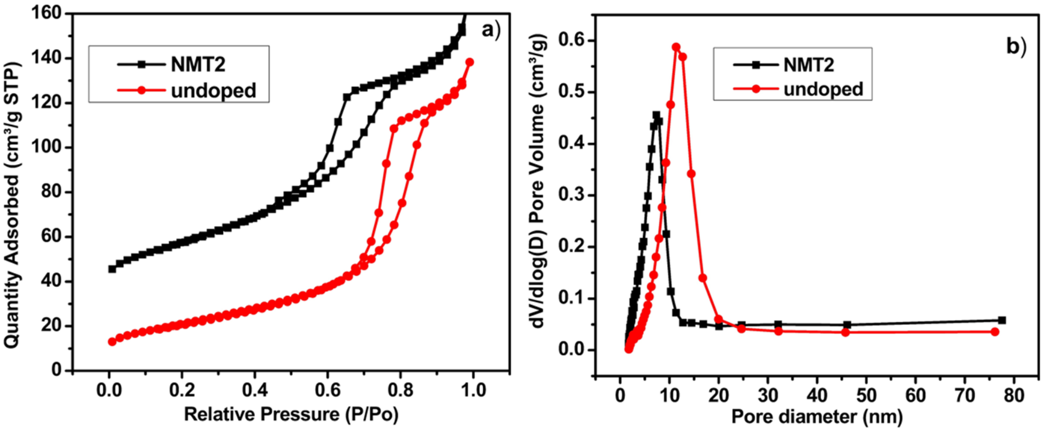

FIG. 6. (a) The N_2 adsorption–desorption isotherms and (b) pore diameter distribution curves of NMT2 co-doped TiO_2

4. Evaluation of antibacterial activity of Ni and Mn co-doped TiO_2 on *Sphingomonas paucimobilis* and *Pseudomonas fluorescence*

4.1. Antibacterial activity of NMT2 catalyst against *Sphingomonas paucimobilis*

The antibacterial activity of co-doped TiO_2 nanoparticles were carried out by the agar-well diffusion method against *Sphingomonas paucimobilis* (MTCC-6363) at different concentrations of undoped and co-doped TiO_2 (NMT2) nanoparticles ranging from 100, 300, 400 μg/mL and control (chloramphenicol – 100 μg/mL). Performance standards for antimicrobial susceptibility tests were conducted [32]. The antibacterial petri plates are shown in Fig. 7(a) – undoped TiO_2 and Fig. 7(b) – co-doped TiO_2. TiO_2 petri plates showed the bacterial growth zone diameters; and from those, the results are presented in Table 4. From the table, the value represented the zone of inhibition of bacterial growth for *Sphingomonas paucimobilis* at 400 μg/mL was 25.1 ± 0.2 mm. These results showed that 400 μg/mL is the best concentration for the zone of inhibition of bacterial growth compared with standard reference (chloramphenicol) and undoped TiO_2. Further, we have calculated T-test values for three replicates of each bacterium by using SPSS software and the values are given in Table 5.

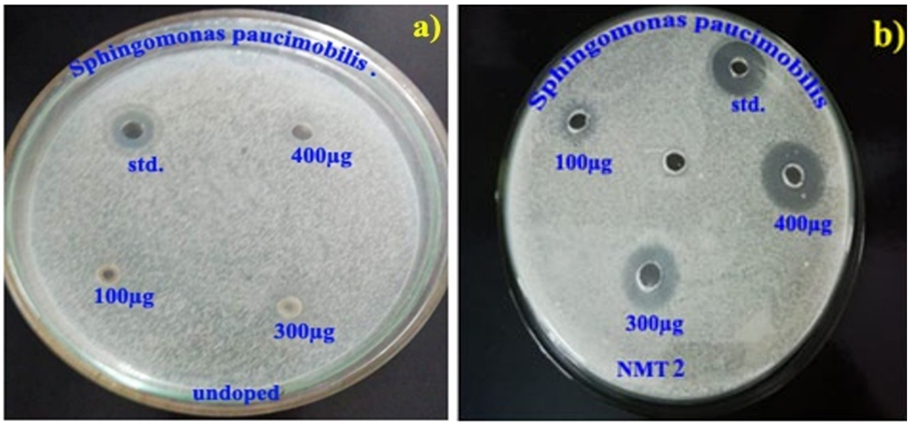

FIG. 7. Zone of inhibition of *Sphingomonas paucimobilis* by (a) Undoped TiO_2 and (b) NMT2 Catalyst

TABLE 4. Agar-well diffusion of undoped and co-doped TiO_2 nanoparticles (NMT2) on *Sphingomonas paucimobilis* (MTCC-6363)

S.No	Catalyst	Organism	Zone of inhibition (mm)			
			100 μg/mL	300 μg/mL	400 μg/mL	Standard (Chloramphenicol) 100 μg/mL
1	(NMT-2)	*Sphingomonas paucimobilis* (MTCC-6363)	14.3 ± 0.25	20.2 ± 0.26	25.1 ± 0.2	24.1 ± 0.1
2	Undoped TiO_2	*Sphingomonas paucimobilis* (MTCC-6363)	—	—	—	24.1 ± 0.1

TABLE 5. Determination of mean of three replicates for zone of inhibition of *Sphingomonas paucimobilis*(MTCC-6363) with NMT2 nanocatalyst

Parameter	100 μg/mL	300 μg/mL	400 μg/mL	100 μg/mL (Standard)
Mean	14.30	19.03	25.90	24.1
SD	0.25	0.25	0.15	0.05
T-test	96.71	70.25	151.81*	434.74
P value	0.00	0.00	0.00	0.00

Mean of three replicates ± Standard deviation

$*P < 0.05$ was consider as significant difference

4.2. Antibacterial activity of NMT2 catalyst on *Pseudomonas fluorescence* (MTCC-1688)

The antibacterial activity of co-doped TiO_2 nanoparticles were carried out by the agar-well diffusion method against *Pseudomonas fluorescence* (MTCC-1688) at different concentrations of undoped and co-doped TiO_2 (NMT2) nanoparticles ranging from 100, 300, 400 μg/mL and control (chloramphenicol – 100 μg/mL). The antibacterial petri plates are shown in Fig. 8(a) – undoped TiO_2 and Fig. 8(b) – co-doped TiO_2. As before, the TiO_2 petri plates showed the bacterial growth zone diameters, and the results are presented in Table 6. In this table, the values represented the zone of inhibition of bacterial growth for *Pseudomonas fluorescence* (MTCC-1688). At 400 μg/mL, this value was 18.1 ± 0.2 mm. These results showed that 400 μg/mL was the best concentration for the zone of inhibition of bacterial growth compared with standard (chloramphenicol) and undoped TiO_2. Further, we have calculated T-test values for three replicates of each bacterium by using SPSS software and the values are given in Table 7. This zone of inhibition of bacterial growth with the catalyst may be due to exposure of catalyst with the visible light formation of e^-/h^+ pairs which can acts as a strong oxidizing agent and the excited electron can reacts with adsorbed oxygen and converted to reactive oxygen species (e.g., super oxide radicals which in turns produces OH). Then these e^-/h^+ and OH both can be acts as oxidizing agents which can degrade the protein coat of bacteria, leading to the inhibition of the growth of the organism during the catalysis.

TABLE 6. Agar-well diffusion of undoped and co-doped TiO_2 nanoparticles (NMT2) on *Pseudomonas fluorescence* (MTCC-1688)

S. No	Catalyst	Organism	Zone of inhibition (mm) (Mean of three replicates ± SD)			
			100 μg/mL	300 μg/mL	400 μg/mL	Standard (Chloramphenicol) 100 μg/mL
1	NMT2	*Pseudomonas fluorescens* (MTCC-1688)	5.8 ± 0.43	12.6 ± 0.25	18.1 ± 0.17	23.1 ± 0.05
2	Undoped TiO_2	*Pseudomonas fluorescens* (MTCC-1688)	—	—	—	23.1 ± 0.05

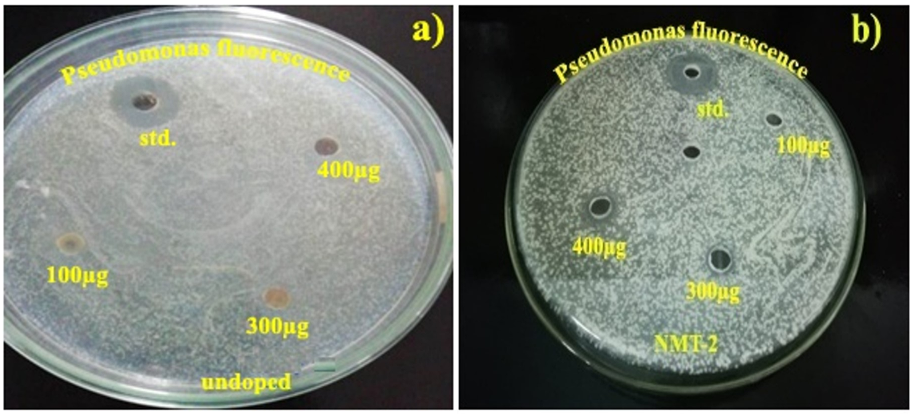

FIG. 8. Zone of inhibition of *Pseudomonas fluorescence (MTCC-1688)* by a) Undoped TiO_2; b) NMT2 Catalyst

TABLE 7. Determination of mean of three replicates for zone of inhibition of *Pseudomonas fluorescence* (MTCC-1688) with NMT2 nanocatalyst

Parameter	100 μg/mL	300 μg/mL	400 μg/mL	100 μg/mL (Standard)
Mean	5.30	12.03	18.10	23.16
SD	0.25	0.25	0.05	0.05
T-test	96.71	70.25	151.81*	434.74
P value	0.00	0.00	0.00	0.00

Mean of three replicates ± Standard deviation

*$P < 0.05$ was consider as significant difference

In this case, hydroxyl radicals were released by the photocatalyst when irradiated by visible light. The bactericidal effect of co-doped TiO_2 has generally been attributed to the decomposition of bacterial outer membranes by reactive oxygen species (ROS), primarily hydroxyl radicals (OH), which leads to phospholipid peroxidation and ultimately cell death. Hence the generated hydroxyl radicals acted as powerful oxidizing agents which may be reacting with peptidoglycan (poly-N-acetylglucoseamine and N-acetylmuramic acid) of the bacterial outer cell wall. This promotes the disruption of cell respiration leading to the destruction of bacteria.

4.3. Photocatalytic mechanism for photodegradation of bacteria

The reactive catalyst particles play a key role in the production of hydroxyl radicals ($HO^{\bullet}$) leading to antibacterial activity. The photocatalytic mechanism by co-doped TiO_2 is briefly represented as follows.

The following steps are the prime steps for formation of $^{\bullet}OH$. Its formation is an important step in the photocatalytic degradation of pollutants and the antibacterial activity of photocatalyst. When co-doped TiO_2 nano powder is irradiated with visible light, the electrons are excited to the conduction band, leaving behind the holes in the valence band. The recombination of the generated electrons and holes must be prevented for effective utilization of the catalyst. Thus, generated electrons are captured by the doped dopant ions preventing their recombination:

$$\mathrm{TiO_2} + h\nu \longrightarrow \mathrm{TiO_2(h^+)} + \mathrm{TiO_2(e^-)}.$$

The holes react with surface bound hydroxyl groups or with water adsorbed on the surface of TiO_2 to produce hydroxyl radicals and hydrogen ions:

$$\mathrm{TiO_2(h^+)} + \mathrm{H_2O} \longrightarrow \mathrm{TiO_2} + \mathrm{HO^{\bullet}} + \mathrm{H^+},$$

$$\mathrm{TiO_2(h^+)} + \mathrm{HO^-} \longrightarrow \mathrm{TiO_2} + \mathrm{HO^{\bullet}}.$$

The electrons are transferred to adsorbed oxygen producing superoxide anion:

$$\mathrm{TiO_2(e^-)} + \mathrm{O_2} \longrightarrow \mathrm{TiO_2} + \mathrm{O_2^{\bullet -}}.$$

These superoxide anions further react with adsorbed water molecules producing peroxide radicals and hydroxyl ions:

$$\mathrm{TiO_2(e^-)} + \mathrm{O_2^{\bullet -}} + \mathrm{H_2O} \longrightarrow \mathrm{TiO_2} + \mathrm{HO_2^{\bullet}} + \mathrm{HO^-}.$$

The peroxide radicals combine with H^+ resulting in the formation of hydroxyl radicals and hydroxyl ions. Hydrogen peroxide is formed as an intermediate product:

$$\mathrm{TiO_2(e^-) + HO_2^{\bullet} + H^+ \longrightarrow TiO_2 + H_2O_2,}$$

$$\mathrm{TiO_2(e^-) + H_2O_2 \longrightarrow TiO_2 + HO^{\bullet} + HO^-.}$$

Holes oxidize these hydroxyl ions to hydroxyl radicals. Thus, all the species facilitate the formation of $HO^{\bullet}$. The strong oxidizing $HO^{\bullet}$ reacts with the outer part peptidoglycan of bacteria and degrade it.

$$\text{Bacteria} + \mathrm{HO^{\bullet}} \longrightarrow \text{Products.}$$

Thus, the formation of hydroxyl radicals and their role in photocatalytic activity plays an essential role in the degradation mechanism.

5. Conclusions

In the current work, nanocatalysts are synthesized by sol-gel method and these are calcined at 450 °C. These samples are characterized by various techniques. Co-doping of transition metal into TiO_2 lattice ceases the electron-hole recombination and reduces the bandgap. Moreover, co-doped TiO_2 nanomaterials exhibit excellent antibacterial performance. The XRD results reveals that the anatase and rutile mixed phase was observed for the co-doped samples. FTIR stretching frequencies confirmed the shifting of absorption band of TiO_2 from UV to visible region. SEM-EDS shows morphology and composition of the photocatalyst. UV-vis-DRS, TEM and BET reported bandgap, particle size and surface area respectively. These photocatalytically active materials antibacterial activities were deduced by using *Sphingomonas paucimobilis* and *Pseudomonas fluorescence*. The results show that among all the nanocatalysts, NMT2 catalyst shows optimum zone of inhibition at 25.1 ± 0.2 mm for *Sphingomonas paucimobilis* and 18.1 ± 0.2 mm for *Pseudomonas fluorescence* compared to standard (chloramphenicol) value at 24.1 ± 0.1 mm and 23.1 ± 0.05 mm at 100 μg/mL respectively.

References

[1] Fujishima A., Kobayakawa K., Honda K. Electrochemical photolysis of water at a semiconductor electrode. *Nature*, 1972, **238**, P. 37–38.

[2] Mital G.S., Tripathi M. A review on the synthesis of TiO_2 nanoparticles by solution route. *Central European J. of Chemistry*, 2021, **10** (2), P. 279–294.

[3] Fujishima A., Rao T.N., Tryle D. Titanium Dioxide photocatalysis. *J. of photochemistry and photobiology C: photochemistry reviews*, 2000, **1**, P. 1–21.

[4] Vassilios B., Danae V., Dimitrios K., George K. Modified TiO_2 based photocatalysts for improved air and health quality. *J. of Materiomics*, 2017, **3** (1), P. 3–16.

[5] Ashahi R., Morikawa T. Visible–light photocatalysis in Nitogen-doped Titanium oxides. *Science*, 2001, **293**, P. 269–271.

[6] Umar K., Aris A., et al. Synthesis of visible light active doped TiO_2 for the degradation of organic pollutants—methylene blue and glyphosate. *J. of Analytical Science and Technology*, 2016, **7**, 29.

[7] Jing D., Zhang Y., Guo L. Study on the synthesis of Ni doped mesoporous TiO_2 and its photocatalytic activity for hydrogen evolution in aqueous methanol solution. *Chemical Physics Letters*, 2005, **415**, P. 74–78.

[8] Miditana S.R., Tirukkovalluri S.R., Alim A.S., Imandi M.R. Photocatalytic degradation of allura red by Mn–Ni co-doped nanotitania under visible light irradiation. *IJITEE*, 2019, **8**, P. 650–657.

[9] Zhao C.F., Song L., et al. Electronic, optical and photocatalytic behavior of Mn, N doped and codoped TiO_2: Experiment and simulation. *J. of Solid State Chemistry*, 2016, **235**, P. 160–168.

[10] Pelaez M., Nicholas T.N., et al. A review on the visible light active titanium dioxide photocatalysts for environmental applications. *Applied Catalysis B: Environmental*, 2012, **125**, P. 331–349.

[11] Shifu C., Sujuani Z., Wei W.Z. Preparation and activity evaluation of p–n junction photocatalyst NiO/TiO_2. *J. of Hazardous Materials*, 2008, **55**, P. 320–326.

[12] Wilke K., Breuer H.D. The influence of transition metal doping on the physical and photocatalytic properties of titania. *J. of Photochemistry and Photobiology A: Chemistry*, 1999, **121**, P. 49–53.

[13] Tavakoli A., Sohrabi M., Kargariandii Ali. A Review of Methods for Synthesis of Nanostructured Metals with Emphasis on Iron Compounds. *Chemical Papers*, 2007, **61**, P. 151–170.

[14] Rafiq M.A., Ikram M., Nafees M., Ali S. Structural, optical and magnetic study of Nidoped TiO_2 nanoparticles synthesized by solgel method. *Int. Nano Letters*, 2018, 8, **8**, P. 1–8.

[15] Boyan B., James H., Judicael P. Principles of assessing bacterial susceptibility to antibiotics using the agar diffusion method. *J. of Antimicrobial Chemotherapy*, 2008, **61** (6), 1295.

[16] Cappucino J.G., Sherman N. Microbiology, A Laboratory Mannual. 6th Ed., Pearson Education (Singapore) Ltd, 2004, **4**, 199.

[17] Avasarala B.K., Raoi T.S., Sridher B. Enhanced photocatalytic activity of beryllium doped titania in visible light on the degradation of methyl orange dye. *Int. J. of Materials Research*, 2010, **101**, P. 1–7.

[18] Alim S.A., Rao T.S., et al. Fabrication of visible light driven nano structured Copper, Boron codoped TiO_2 for photocatalytic removal of Lissamine Green B. *J. of Saudi Chemical Societies*, 2019, **23**, P. 92–103.

[19] Liu G., Wang K., Zhou Z. Influence of doping on antibacterial effect of TiO_2 nanoparticles. *Materials Science Forum*, 2006, **510–511**, P. 86–89.

[20] Gharibshahi E., Saion E. Influence of dose on particle size and optical properties of colloidal platinum nanoparticles. *Int. J. of Molecular Sciences*, 2012, **13**, P. 14723–14741.

[21] Taranjeeti K., Abhishek S., Amrit P.T. Wanchoo R.K. Utilization of solar energy for the degradation of carbendazim and propiconazole Fe doped TiO_2. *Solari Energy*, 2016, **125**, P. 65–76.

[22] Zhongping Y., Fanghou J., et al. Microporous Ni-doped TiO_2 film photocatalyst by plasma electrolytic oxidation. *Applied Materials Science*, 2010, **2**, P. 2617–2622.

[23] Sharotri N., Sud D. Aigreener approach to synthesize visible light responsive nanoporous S-doped TiO_2 with enhanced photocatalytic activity. *New J. of Chemistry*, 2015, **39**, P. 217–223.

[24] Othmana I., Mohamed R. Ibrahem F. Study of photocatalytic oxidation of indigo carmine dye on Mn supported TiO_2. *J. of Photochemistry and Photobiology A: Chemistry*, 2007, **189**, P. 80–85.

[25] Jensen S., Kilin S.D. Electronic properties of Ni-doped TiO_2 anatase. *J. of Physics: Condensed Matter*, 2015, **27**, P. 1–13.

[26] Shah S.M., Hussain S.M.H. Effect of carrier concentration on the optical band gap of TiO_2 nanoparticles. *Materials & Design*, 2016, **96**, P. 64–72.

[27] Wang Y., Zhang R., Liangliang J., Lin L.S. First principles study on transition metal-doped anatase TiO_2. *Nanoscale Research Letters*, 2014, **9**, P. 35–46.

[28] Chang S., Chien-yao H., Pin-haniand L., Chang T. Preparation of phosphate Zr doped TiO_2 exhibiting high photocatalytic activity through calcination of ligand-capped nanocrystals. *Applied Catalysis B: Environmental*, 2009, **90**, P. 233–241.

[29] Christian D., Osorio S.M.P., et al. TiO_2 anatase with a bandgap in the visible region. *Nano Letters*, 2014, **14**, P. 6533–6538.

[30] Chauhan R., Kumar R., Chaudhary A.P. Structural and photocatalytic studies of Mn doped TiO_2 nanoiparticles. *Spectrochemica Acta Part A: Molecular and Biomolecular Spectroscopy*, 2012, **98**, P. 256–264.

[31] Bhatia V., Dhir A. Transition metal doped TiO_2 mediated photocatalytic degradation of anti-inflammatory drug under solar irradiations. *J. of Environmental Chemical Engineering*, 2016, **4**, P. 1267–1273.

[32] Jayaseelan C., Rahuman A.A., et al. Biological approach to synthesize TiO_2 nanoparticles using aeromonas hydrophilia and its antibacterial activity. *Spectrochimica Acta Part A: Molecular and Biomolecular Spectroscopy*, 2013, **107**, P. 82–89.

Submitted 13 June 2021; revised 15 November 2021; accepted 30 December 2021

Information about the authors:

Sankara Rao Miditana – Department of Chemistry, Government Degree College, Puttur, Chittoor, Andhra Pradesh – 517583, India; Department of Inorganic & Analytical Chemistry, A.U. College of Science & Technology, Andhra University, Visakhapatnam, Andhra Pradesh – 530003, India; ORCID 0000-0001-7988-9022; sraom90@gmail.com

Siva Rao Tirukkovalluri – Department of Inorganic & Analytical Chemistry, A.U. College of Science & Technology, Andhra University, Visakhapatnam, Andhra Pradesh – 530003, India; ORCID 0000-0001-5156-1885; sivaraoau@gmail.com

Imandi Manga Raju – Department of Inorganic & Analytical Chemistry, A.U. College of Science & Technology, Andhra University, Visakhapatnam, Andhra Pradesh – 530003, India; ORCID 0000-0002-6291-601X; mangorchem@gmail.com

Conflict of interest: the authors declare no conflict of interest.

NANOSYSTEMS:
PHYSICS, CHEMISTRY, MATHEMATICS

Doronin F.A., Evdokimov A.G., et al. *Nanosystems: Phys. Chem. Math.*, 2022, **13** (1), 115–127.
http://nanojournal.ifmo.ru
DOI 10.17586/2220-8054-2022-13-1-115-127

Original article

A new approach to function-structure modeling of the surface modified polymers

Fedor A. Doronin[1,a], Andrey G. Evdokimov[1,b], Yury V. Rudyak[1,c], Georgy O. Rytikov[1,2,d],
Irina P. Taranets[1,e], Viktor G. Nazarov[1,f]

[1]Moscow Polytechnic University, Moscow, Russia
[2]State university of management, Moscow, Russia

[a]f.a.doronin@mospolytech.ru, [b]evdokag@gmail.com, [c]rudyak@mail.ru, [d]gr-yandex@yandex.ru,
[e]qwerty818@mail.ru, [f]110505n@gmail.com

Corresponding author: Fedor A. Doronin, f.a.doronin@mospolytech.ru

PACS 87.15.Aa

ABSTRACT We introduce a novel approach to function-structure modeling of the polymer materials. It's based on mathematical and statistical processing of the images obtained by scanning electron microscopy (SEM) of the corresponding surfaces. We studied the correlation-rotational anisotropy, the degrees of planar and contour heterogeneity and the morphological spectra of the SEM images to characterize the function-structure relationships quantitatively. The introduced quantitative characteristics will allow to rationalize the choice of chemical compositions of the modifying gas mixtures (for example, helium-fluorine-oxygen) that provide the maximum possible wetting edge angles for the materials under consideration with reference polar and non-polar liquids.

KEYWORDS oxyfluorination, scanning electron microscopy, modification, morphology, correlation, polymer substrate

ACKNOWLEDGEMENTS This work was carried out with the financial support of the Ministry of science and higher education of the Russian Federation (State assignment “Structure and properties of polymer materials obtained with the use of systems of methods of chemically, thermally and / or mechanically induced surface and volume modification”, topic number FZRR-2020-0024, code 0699-2020-0024).

FOR CITATION Doronin F.A., Evdokimov A.G., Rudyak Yu.V., Rytikov G.O., Taranets I.P., Nazarov V.G. A new approach to function-structure modeling of the surface modified polymers. *Nanosystems: Phys. Chem. Math.*, 2022, **13** (1), 115–127.

1. Introduction

Surface modification of the polymers is a well-known method for altering their physical, chemical and functional characteristics [1–3]. Classifying the methods of the surface modification by the aggregate state of the modifier, we can conditionally distinguish solid-, liquid- and gas-phase approaches to the surface treatment [4–6]. There are also a number of additional activation techniques: mechanical, thermal, electro- and optical methods [7–11]. In particular, gas-phase oxyfluorination allows the formation of heterogeneous coatings with different chemical and morphological design and thus with a wide range of controlled set of physical, chemical and, as a result, functional surface properties. This is possible due to the synergetic cooperation of the optimal gas mixture composition and the external factors (temperature, pressure) acting during the processing [12–18] on the surface of commonly used polymers (such as low-density polyethylene (LDPE), polypropylene (PP), polyethyleneterephthalate (PET), etc.). Considering the development trends in the direction of “personalized” production of polymers and their compositions for the private scientific-technical and production tasks using surface, bulk, additive and combined modification techniques [19–23], adjusting the ratio of (for example, in the case of oxyfluorination) the gas mixture components that provides the functional-operational properties specifications for the manufactured polymer products becomes more complicated. It is obvious that the set of polymer properties formed in the process of modification occurs both due to changes in their chemical composition and structure and due to micro- and nanotexturing of the corresponding surfaces [24–28]. In particular, under the manufacturing of the polymer-based composite materials with reduced platelet adhesion (for medical purposes), it was shown that the plasma-chemical treatment, the sulfation or the fluorination can provide a radical reduction in the thrombocyte activation and in the platelet adhesion to the modified LDPE-surface [29]. Micro- and nanotextures formed on the polymer surface during the modification affect surface parameters such as friction coefficients, wettability (hydrophilicity/hydrophobicity) and adhesion [30–34]. One of the main high-precision tools for polymer surface morphology (in the mode of secondary electrons scattering) and chemical composition (in the mode of energy-dispersion analysis) studying is scanning electron microscopy (SEM) [35, 36] that provides an ultimate spatial resolution of the generated images in range from 1 to 10 nm. However, along with the high technical capabilities of the scanning electron microscope, it can not be considered as a "reference" and fully reliable way to study surfaces because, when adjusting the contrast and brightness, the microscope-operators are often guided by their own subjective visual perception of the analyzed image. And moreover, as a rule, they try to visualize the exotic features (artifacts) of the studied surface and pay insufficient attention to the quantitative analysis of the background textures that, in most cases, determine the macro- and nanoscopic properties of the studied objects [37–39]. It is obvious that shooting the same object under various conditions can lead to completely different conclusions about the true morphology and structure of its surface (Fig. 1).

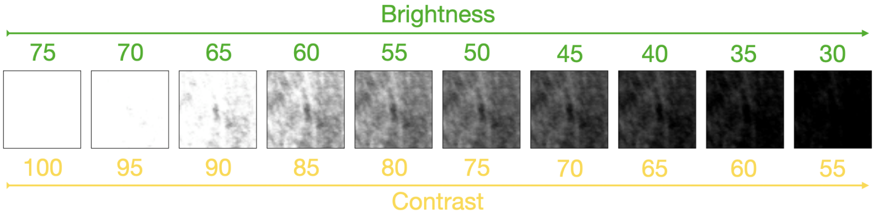

FIG. 1. The SEM image [40] of the same LDPE-film at different values of image brightness and contrast

Visual analysis of the SEM-image pictures with 75, 70 and 30 % of brightness shows that the film of low-density polyethylene (LDPE) is homogeneous and does not have an explicit texture. However, pictures with brightness levels from 65 to 45 % demonstrate the presence of a well-developed, most likely, multi-modal system of morphological inhomogeneities. Similar problems of obtained results interpretation are usually encountered in medicine under the visual analysis of ultrasound studies, x-rays and optical images in order to diagnose and monitor the dynamics of various diseases [41–46].

The most modern analytical devices designed to study the surfaces of polymers and other materials have specialized software and hardware complexes (set-top boxes), which include digital tools for the formed surface images processing. In particular, atomic force microscopes can form three-dimensional surface images and provide information about the average values of a number of quantitative roughness characteristics (Ra, Rq, Sm, etc. [47–51]). Thus, in [52], the morphology and roughness parameters of fluorinated films of polyvinylchloride (PVC) and polyethyleneterephthalate (PET) were investigated using atomic force microscopy (Fig. 2).

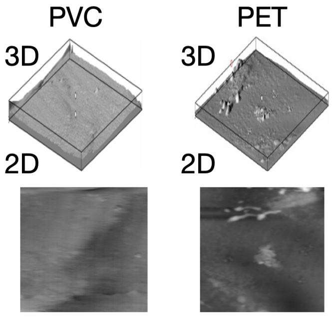

Polymer	R_a, nm	R_q, nm	R_z, nm	Rmax, nm	S_m, nm	S, nm	D_a,°	D_q,°	L_o, nm
PVC	2,9	2,3	10,1	15,8	147,8	41,1	4,4	5,9	1,005
PET	2,6	2,1	4,4	11,4	261,0	54,7	2,2	2,9	1,001

FIG. 2. The AFM-images of the surface fragments of the fluorinated PVC- and PET-films [52]

It can be seen that the undulation of the surface of the fluorinated PVC-sample is formed by single nanoscale "protrusions" ($R_a \sim 3$ nm) and extended "folds", the characteristic transverse dimensions of which ($S \sim 40$ nm) are significantly inferior to the longitudinal ones ($S_m \sim 150$ nm). Both "folds" ($S \sim 50$ nm and $S_m \sim 260$ nm) and single "protrusions" ($R_a \sim 3$ nm) are also observed on the surface of the PET-sample. The Pearson correlation coefficient calculated for the two presented sets of nanorelief characteristics is ~ 0.997, which indicates the textural homogeneity (high degree of similarity of surface nanotextures) of the films under consideration. But the values of the free surface energy of the modified PET- and PVC-samples differ and are 90 [53] and 50 [54] mN/m respectively, which is probably due to the chemical nature of the materials under discussion. Another important example for understanding the considering problem is presented in [55]. Fig. 3 shows three SEM-images of the surfaces fragments of different LDPE-films produced under the same industrial technology.

Taking into account the widely known large dispersion of the contact angle of wetting values for the chemically identical samples ($\pm 10^\circ$), easily visually observable morphological features of the textures (Fig. 3) can make a significant

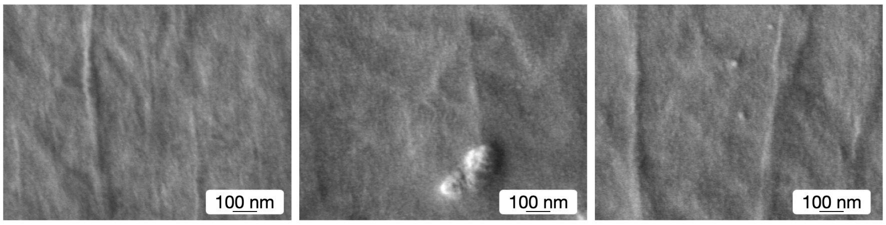

FIG. 3. The SEM-images of the surface fragments of unmodified (initial) LDPE-films [55]

contribution to the formation of free surface energy values, which in particular, determines the characteristics of the surface wetting. But when predicting the main macroscopic physical and chemical properties of chemically identical polymer matrices, it is necessary to focus on the textural characteristics of such areas where the single macroscopic defects (microcracks, microcrystals of third-party substances, fibers, etc.) are not observed. Thus, it is important to choose a rational zone for nanoscopic (SEM, AFM, EDS, etc.) analysis, since most of the studied polymer substrates are characterized by a certain level of initial defects which is not associated with modifying external influences. In connection with the above, to effectively design and predict the properties of the modified materials based on the quantitative analysis of their surfaces SEM-images it is necessary: – to conduct the additional studies of the of polymer films' chemical structure that can be performed, for example, with the scanning electron microscopy in the mode of the EDS-analysis; – to develope more sensitive techniques for the specification of the digital nanorelief models' parameters that would allow us to statistically reliably distinguish the samples with different physical and chemical properties. Thus, the quantitative analysis of images of polymer surfaces (in particular, SEM-images) becomes extremely important, first, in order to reduce the dependence of the observation results on the operators of measuring complexes, and, second, in order to provide the possibility of introducing quantitative measures, criteria and techniques that allow comparing nanotextures of the surfaces (in particular, for the fluoropolymers) previously observed under approximately the same conditions [56]. The original concepts and techniques for applying some possible solutions to the problem of quantitative description and modeling of polymer film surface structures are presented in [57].

In the framework of the present paper, two algorithms of computer analysis were developed for the texture deficiency of the polymeric substrates surfaces (for example, LDPE). The algorithms are based on the quantitative determination of the characteristic size of the morphological spectrum localization region and of the rotational anisotropy degrees of the characteristic functions of the corresponding SEM-images digital heterogeneities. Based on the information about the features of the nanorelief surfaces of LDPE-samples, a retrospective assessment of the optimality of the chemical compositions of the modifying mixture used in their gas-phase treatment with the oxyfluorination technique.

2. Material and methods

Some polymer material surface modification methods (e.g., fluorination, sulfonation, corona discharge treatment, etc.) were considered in [58, 59]. The most impressive achievement is that of the surface superhydrophilicity for a number of initially hydrophobic polymers that was demonstrated in [59] as a consequence of the oxyfluorination – the gas-phase modification of the samples by mixtures of helium, fluorine and oxygen. The surface oxyfluorination of the LDPE-films (NPO Plastik, Russia) was performed in a 500 ml stainless steel reactor with preliminary and subsequent vacuuming according to the method [59] at four concentrations of gas mixture components: 1) $7\%F_2/10\%O_2/83\%He$; 2) $10\%F_2/6\%O_2/84\%He$; 3) $11\%F_2/4\%O_2/85\%He$; 4) $15\%F_2/{\sim}0.5\%O_2/84.5\%He$ (the ~ 0.5 % concentration of O_2 is due to its content in industrially diluted F_2). The processing times for the LDPE-films were 5, 30 and 180 minutes. The morphological changes of the LDPE-films surfaces before and after the modification were monitored using the autoemission scanning electron microscope JSM 7500-F ("JEOL", Japan) operated at an accelerating voltage of 10 kV. The achieved spatial resolution was $\sim$ 1 nm. To reduce the level of static charge and to prevent the destruction of dielectrics under the action of an electron beam, a pre-sputtering layer of platinum ($\sim$ 8 nm thickness) was superimposed on the samples' surfaces. In Fig. 4 the results of the morphological structure investigation for the LDPE-films surfaces (3 series for each modification mode) with the scanning electron microscopy in the mode of secondary electron scattering are shown.

The visual analysis of the presented SEM images suggests that the largest number of nanoobjects (light spots) of approximately the same size (1 – 10 nm) formed during the oxyfluorination is observed at a certain optimal ratio of fluorine and oxygen concentrations in the modifying gas mixture. It is also clearly visible that the particular implementations of the LDPE-films surfaces' textures differ significantly from each other. However, the physico-chemical properties of the discussed surfaces (the wettability, the permeability, the sorption capacity, the work of adhesion, etc.) are the same for all private implementations obtained under the same conditions of the oxyfluorination, and they significantly depend on the composition of the modifying gas mixture due to the dissimilar values of the modified LDPE-films' free surface energies derived under the different oxyfluorination modes. The quantitative estimation of free surface energy value can,

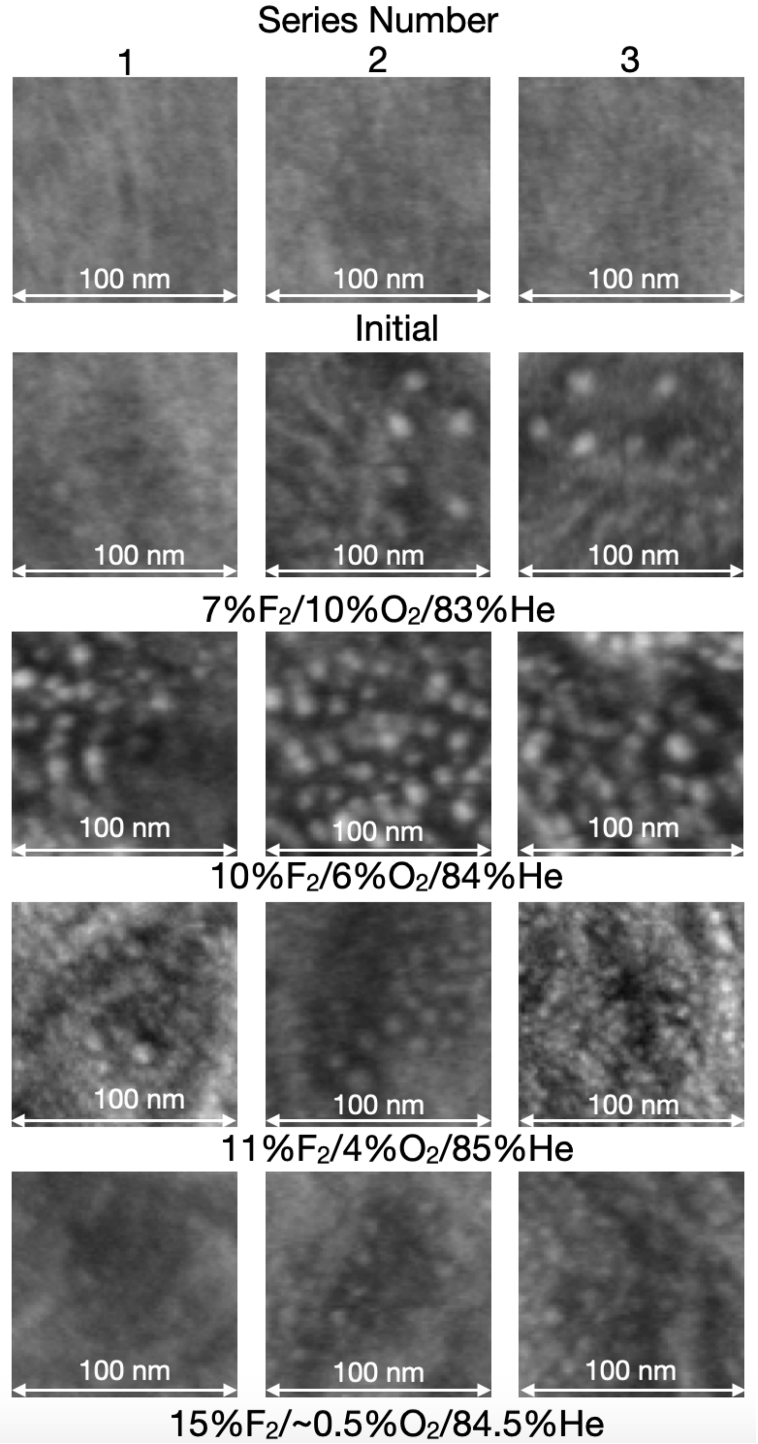

FIG. 4. The SEM-images of the oxyfluorinated LDPE samples (the characteristic size (square side) of the analyzed regions $\sim$ 100 nm)

in particular, be carried out on the basis of direct macroscopic measurements of the wetting edge angles with reference polar (distilled water) and less-polar (ethylene glycol) liquids. The determination of the LDPE films edge wetting angle with the distilled water and the ethylene glycol “before” and “after” the modification procedures was carried out on an upgraded laboratory stand for high-speed micro-photography of the wetting process in the photo/video fixation mode [56]. The obtained results are shown in Table 1.

Thus, there is a need for internally-consistent quantitative characterization of the textures of both individual LDPE-samples and the corresponding series as a whole. This requires implementation of a rational parameterization and the design of such a texture simulation approach that, on one hand, differs the individual samples from each other, and on another, gives the common model to the series.

TABLE 1. The edge wetting angles for the LDPE-substrates oxyfluorinated under the various modification modes

Free Surface Energy, mJ/m^2	Θ_w, °	Θ_e, °	He, %	F_2, %	O_2, %
27 ± 3	78 ± 8	63 ± 6	—	—	—
46 ± 5	54 ± 5	22 ± 2	83 ± 1	7.0 ± 0.5	10.0 ± 0.5
44 ± 4	57 ± 6	28 ± 3	84 ± 1	10.0 ± 0.5	6.0 ± 0.5
46 ± 5	54 ± 5	32 ± 3	85 ± 1	11.0 ± 0.5	4.0 ± 0.5
41 ± 4	67 ± 7	34 ± 3	84.5 ± 0.5	15.0 ± 0.5	0.5 ± 0.5

3. Results and the discussion

3.1. The correlation-rotational anisotropy of the polymer surfaces SEM-images

The probability that a random defect will take the form of an object that has a symmetry is quite small. Such defects usually attract researchers' attention and the theory of their genesis, formation and potential practical applications appears quickly. As it was shown in the "Introduction" section, when predicting the properties of macroscopically homogeneous polymer films, it is necessary to focus on the "defect-free" or "low-defect" areas of the surfaces. It is evident that any initial images show areas that are more or less optically homogeneous. The more that a secondary image (formed by rotating the initial one to an arbitrary angle) differs from the primary one, the more optically heterogeneous it is. Thus, any observed defects demonstrate a high level of the rotational optical anisotropy, which does not allow us to consider such areas as representative in further analysis. While the "defect-free" and the "low-defect" zones provide a relatively high level of rotational correlation and a low level of rotational anisotropy. The modified LDPE-samples do not contain obvious macroscopic defects (Fig. 4), but the mesoscopic defects can be masked as regular inhomogeneities of the nanorelief. So it was necessary to develop an algorithm for automatic selection for further analysis of areas that are characterized by the greatest observed structural homogeneity. The post-rejection of the samples with the microcracks, agglomerates of foreign particles, fibers and etc. will significantly improve the quality of the analytic data obtained by the researchers from measuring devices characterized by (potentially) nanoscopic resolution in the future. A scanning electron microscope operating in the mode of secondary electron scattering is usually used as a nanorelief visualizer. The characteristic geometric dimensions of the vertical inhomogeneities of the studied textures can be associated with the polymer film surfaces images pixels' brightnesses expressed in relative units (nanorelief indices) in accordance with the device intrinsic algoritms. Thus, the quantitative SEM-image analysis allows us to create the digital models of the investigated surfaces that can be used to carry out the structural and functional properties forecasting (in particular, for the oxyfluorinated polymers) in the future. Fifteen primary digital images were generated from the corresponding SEM-images by tabulating the values of the corresponding pixels' brightnesses (five series of three digital images each). Using the standard rotation transformations of the coordinate system, 9 secondary images were obtained from the primary digital images (the rotation was performed in the range from 0° to 90° with a step of 10°). By averaging the numerical values of the corresponding pixel brightness, five statistical digital models of the studied surfaces were formed. For each of them the maximum and minimum values of the nanorelief indexes were found. Their dependences on the fluorine and oxygen concentrations are shown in Fig. 5. Based on the results obtained (Fig. 6), it can be assumed that the presence of significant changes in the functional properties of the modified LDPE-films could be observed when a gas mixture was $\sim$ 13%F_2/$\sim$ 3%O_2/$\sim$ 84%He. At the specified concentrations of active components of the modifying mixture, local extremes of the minimum and maximum values of the corresponding nanorelief indices are observed.

3.2. The digital morphological heterogeneity of the polymer surfaces SEM-images

It was shown in [57] that for characterization of the surfaces' digital images it is possible to use several quantitative measures describing different aspects of forming pictures pixels' brightnesses inhomogeneities. In particular, it was found that the efficient parameters are:

– the "planar heterogeneity" $\sigma = S/S_0$, where S – the total area of flat shapes with a brightness less than the "threshold" value A_0; the S_0 – the area of the entire image. To calculate σ, the "threshold" A_0 takes in turn all natural values from the interval [0; 255] from minimum brightness to maximum brightness.

– the "contour heterogeneity" $\lambda = L/L_0$, where L – the total length of the perimeter of the above figures – normalized by the perimeter L_0 of the entire image. λ is calculated similarly to σ with A_0 taking values from the interval [0; 255].

The authors create the algorithm (presented in Fig. 6(a)) for the constructing of image heterogeneities functional dependencies on the "threshold" pixels brightness A_0. Using the developed computer application that implements the above algorithm routinely the functions of planar and contour heterogeneities for the unmodified (initial) LDPE-films

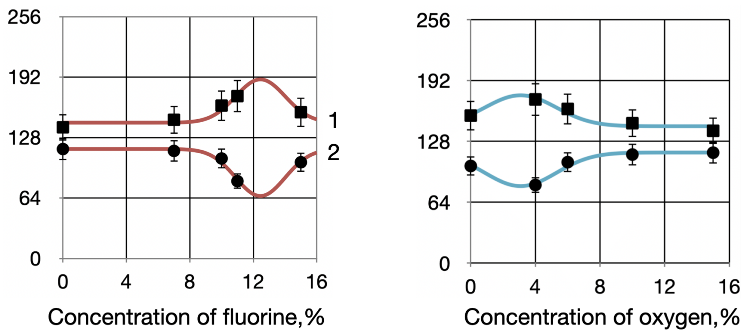

FIG. 5. The dependences of the maximum-1,3 and the minimum-2,4 values of the nanorelief indexes of the modified LDPE-samples' surfaces on the mass concentration of fluorine-1,2 and oxygen-3,4 in the modifying gas mixture

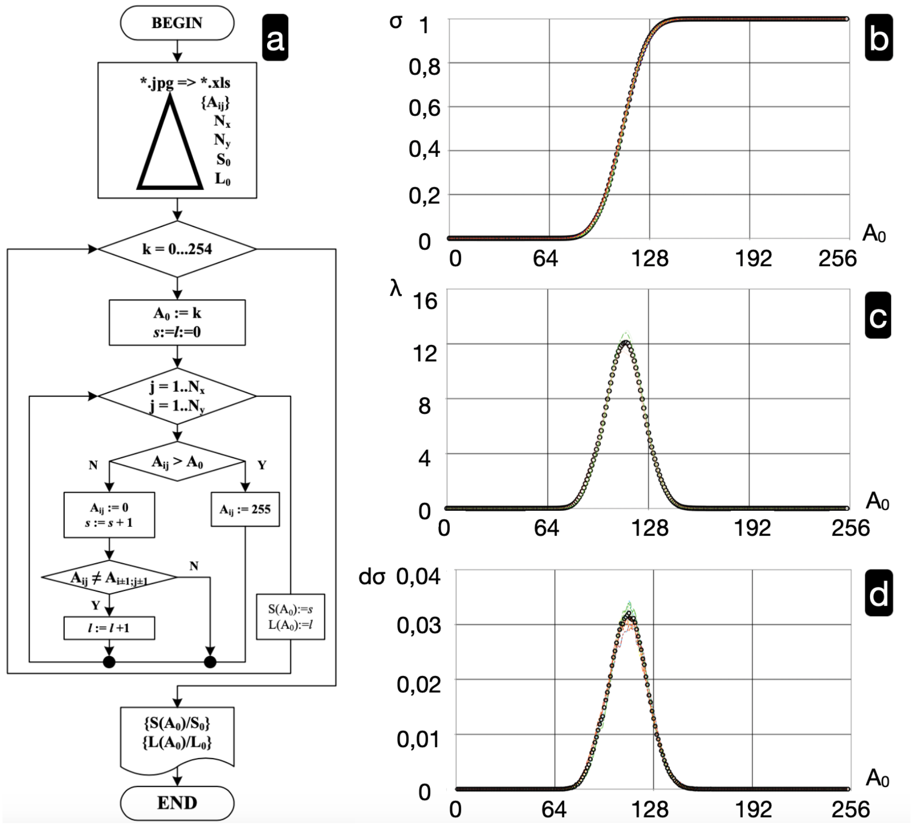

FIG. 6. The flowchart of the core algorithm for the degrees of planar and contour digital image heterogeneities calculating (a) and the plots of the planar (b), contour (c) and "differential" planar – (d) heterogeneities computed under the unmodified LDPE-films SEM-images quantitative analysis.

were obtained. To confirm the rotational anisotropy absence for the discussed SEM-image the necessary calculations were performed for ten images, nine of which there were obtained by rotating the original one in the horizontal plane at angles of 10° to 90° degrees in increments of 10°. The derived dependencies are shown in (Fig. 6(d and c)). The differential function of planar heterogeneity was also calculated. Its information-logical meaning is the increment of the planar heterogeneity function associated with a change in the brightness threshold level by one increment point (Fig. 6(d)). The calculation of Pearson coefficient value for the contour and the differential planar heterogeneities showed that they correlate at a level of more then 0.99.

The detailed analysis of the correlation-rotational anisotropy, performed by Pearson correlation coefficients calculating for the images with 10° rotations, shows that the highest degree of anisotropy is evident for the planar heterogeneity function presented in the differential form (Fig. 7).

Thus, the proposed quantitative SEM-images characteristics and, as a result, the morphological inhomogeneities of the corresponding surfaces demonstrate a high level of correlation-rotational stability ($R_{xy} > 0.995$). For the most

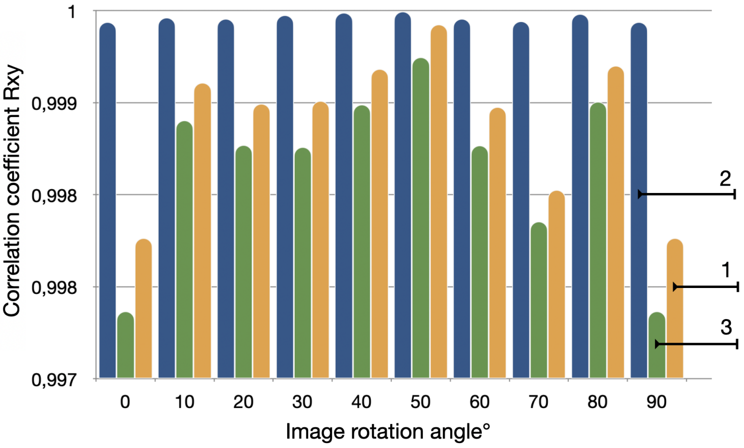

FIG. 7. The comparative analysis of the correlation-rotational anisotropy of the contour (1), integral (2) and differential (3) planar heterogeneities calculated for the unmodified LDPE-films digital SEM-images

effective identification of structural differences, the differential form of the planar heterogeneity characteristic function should be used:

$$d\sigma(A_0) = \frac{\partial\sigma(A_0)}{\partial A_0} \cdot dA_0. \tag{1}$$

3.3. The differential planar heterogeneity and the chemical composition of the modifying gas mixture

The planar heterogeneity characteristic functions (in differential form) were constructed for all LDPE-films surfaces SEM-images and are shown in Fig. 4. For this purpose the digital images were additionally subjected to the standardization procedure (bringing to the same average pixel brightness level) after which the characteristic function of planar heterogeneity was averaged over three developed samples series. The standardization reduces the results' dependences on the operator's subjective perception of the observed images. The averaging over of the results' characteristic function increases the statistical reliability of the research results. Based on the integral characteristics obtained by this technique, the differential ones (presented in Fig. 8) were also calculated.

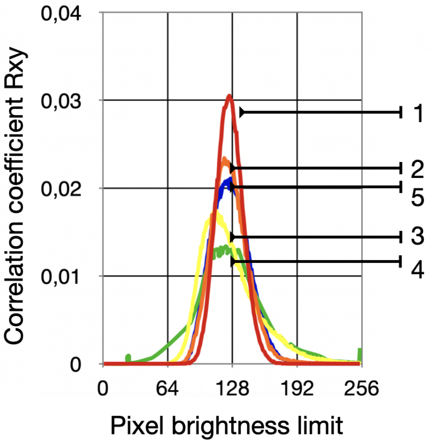

FIG. 8. The differential planar heterogeneities characteristic functions for the standardized digital LDPE-samples surfaces SEM-images corresponding to respective compositions of modifying gas mixtures: curve 1 – initial, curve 2 – 7% F_2/10% O_2/83% He, curve 3 – 10% F_2/6% O_2/84% He, curve 4 – 11% F_2/4% O_2/85% He, curve 5 – 15% F_2/$\sim$ 0.5% O_2/$\sim$ 84.5% He

Comparison of the relationship between the maxima of the differential planar heterogeneity functions and the edge angles of wetting with water and ethylene glycol for the samples' surfaces (Fig. 9) with the concentrations of fluorine and oxygen in the modifying gas mixture indirectly confirms the previously formulated assumption that there is an "optimal" formulation for the volume fractions of fluorine and oxygen in [8; 12] and [3; 7] mass % ranges respectively.

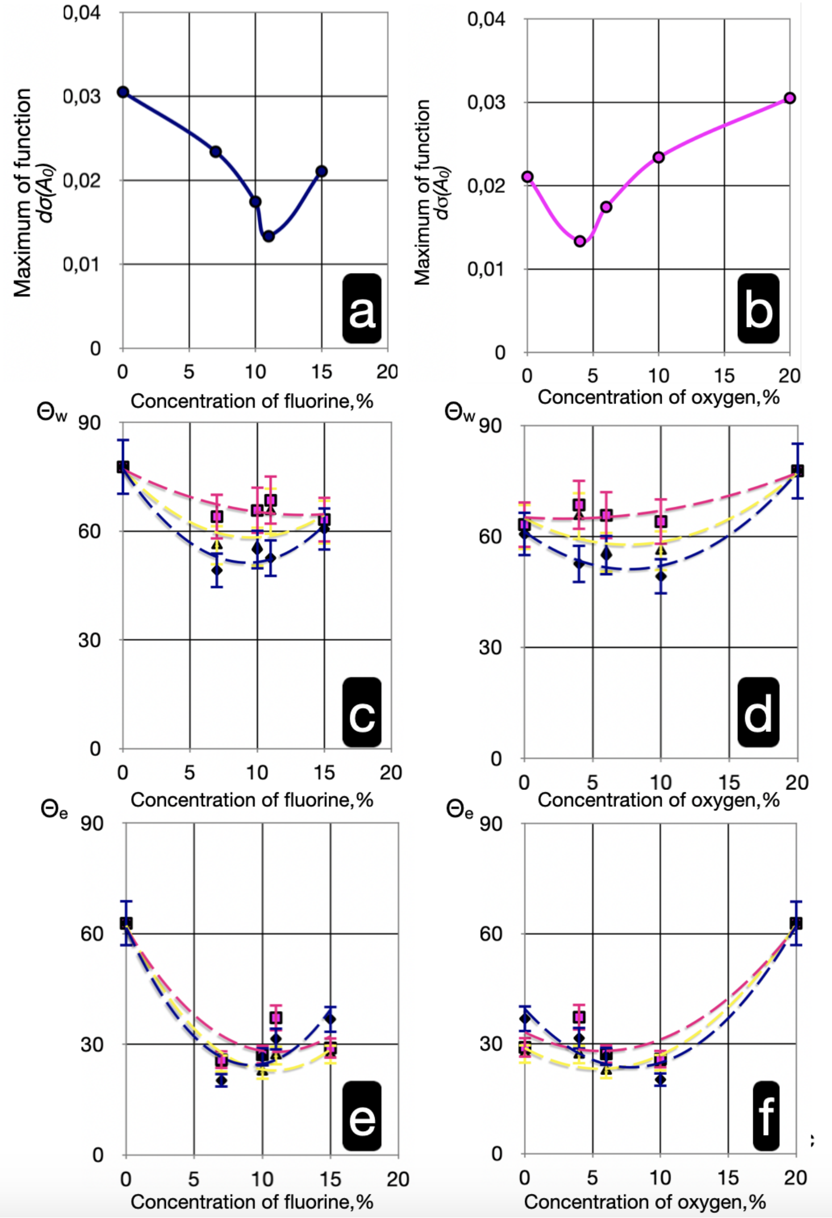

FIG. 9. The dependences of the maxima of the differential planar heterogeneity functions (a, b) and the edge angles of wetting with water (c, d) and ethylene glycol (e, f) of the initial and the oxyfluorinated LDPE-films on the concentrations of fluorine and oxygen in the modifying gas mixture

3.4. The morphological spectra and the compounds of the modifying mixtures

The algorithm for the LDPE-film surfaces SEM-images morphological spectra amplitudes calculating is implemented practically and represented in Fig. 10.

It can be seen that the most delocalized of the considered is the spectrum that characterizes the LDPE-film modified with a mixture of 85%He/11%F_2/4%O_2. A joint analysis of the degree of morphological spectrum delocalization and the concentrations of modifying gas mixtures components also shows the probable presence of maxima in the degree of delocalization at concentrations of fluorine and oxygen of ~ 11 % and ~ 5 % respectively (Fig. 11).

The degree of morphological spectrum delocalization (~ 0.16) seems to characterize surfaces perceived as "smooth" even when considered by SEM-method. If we consider the surface of the polymer film before the modification it will be characterized by some "natural" level of textural heterogeneity. In cases with exceedingly intensive surface modification, which occur with the use of excessive concentrations of active components (fluorine and/or oxygen), the morphologically transformed surface layers of the polymer "block" (or perhaps significantly reduced), the possibility exists for further penetration of reagents deep into the material. So the surface remains texturally as "smooth" as it was before the modification, and only at well-defined concentrations of active reagents on the modified surface will it be possible to observe a noticeable nanorelief structure formation. It is likely that at these concentrations the minimum values of wetting edge

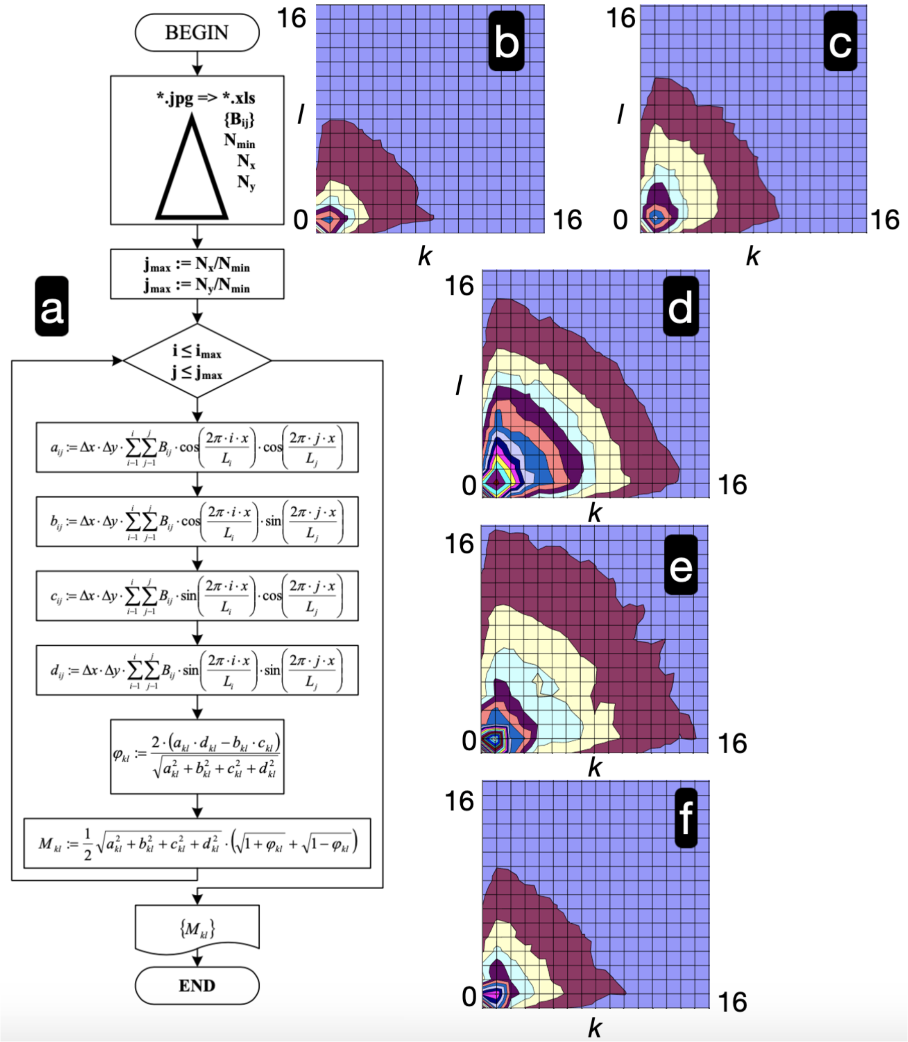

FIG. 10. The flowchart of the core algorithm for the morphological spectra amplitude calculating (a), the regions of SEM-images morphological spectra localizations for the original (b) and the oxyfluorinated (c–f) LDPE-films. The compounds of the modifying gas mixtures: 7%F_2/10%O_2/83%He (c); 10%F_2/6%O_2/84%He (d); 11%F_2/4%O_2/85%He (e); 15%F_2/$\sim$ 0.5% O_2/$\sim$ 84.5%He (f)

angles, the highest degree of delocalization of the morphological spectrum, and the minimum values of the maxima of the differential planar heterogeneity functions are observed.

The set of the obtained experimental data was subjected to correlation analysis. All data and the complete pair correlation coefficient matrices are presented in Tables 2 and 3 respectively.

TABLE 2. The averaged values of the edge wetting angles with the distilled water and ethylene glycol for the LDPE films surfaces modified with different concentrations of fluorine and oxygen gas mixtures, the indices of the nanorelief and the degrees of the morphological spectra delocalization and the differential planar heterogeneity functions corresponding maxima

Θ_w	Θ_e	C_{F2}, %	C_{O2}, %	$i_{\min}$	$i_{\max}$	$P(M_{kl} > 0.5)$	$\max(d_\sigma(A_0))$
63 ± 6	40 ± 4	15.0 ± 0.5	0.5 ± 0.5	96 ± 1	158 ± 1	0.15 ± 0.02	0.021 ± 0.002
60 ± 6	29 ± 3	11.0 ± 0.5	4.0 ± 0.5	88 ± 1	170 ± 1	0.38 ± 0.04	0.013 ± 0.001
58 ± 6	27 ± 3	10.0 ± 0.5	6.0 ± 0.5	100 ± 1	160 ± 1	0.25 ± 0.03	0.018 ± 0.002
59 ± 6	28 ± 3	7.0 ± 0.5	10.0 ± 0.5	118 ± 1	136 ± 1	0.17 ± 0.02	0.024 ± 0.002
75 ± 8	63 ± 6	0.0 ± 0.5	14.0 ± 0.5	120 ± 1	136 ± 1	0.14 ± 0.02	0.031 ± 0.003

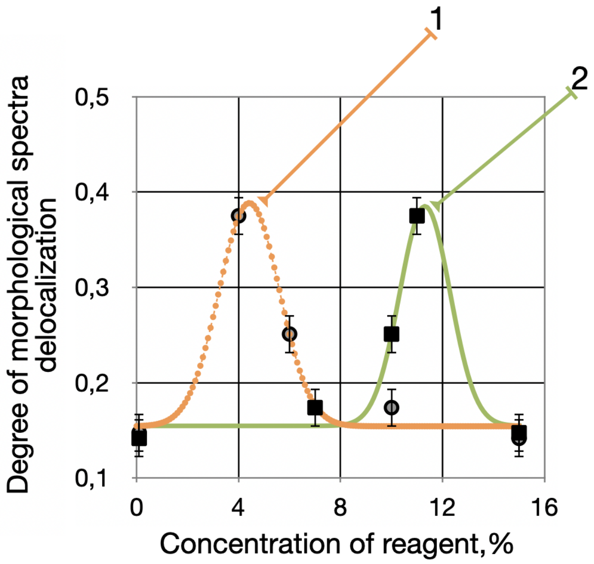

FIG. 11. The dependences of the morphological spectra delocalizations degree for oxyfluorinated LDPE-films on the oxygen (1) and fluorine (2) concentrations in the modifying gas mixture. The experimental results are represented with the dots. The curve lines approximations are the Gauss functions.

TABLE 3. The complete pair correlations coefficients matrix

r_{XY}	Θ_w	Θ_e	$C_{F2}, \%$	$C_{O2}, \%$	$i_{\min}$	$i_{\max}$	$P(M_{kl} > 0.5)$	$\max(d_\sigma(A_0))$
Θ_w	1	0.99	−0.71	0.59	0.52	−0.56	−0.50	0.78
Θ_e	0.99	1	−0.65	0.53	0.51	−0.55	−0.56	0.79
$C_{F2}, \%$	−0.71	−0.65	1	−0.98	−0.81	0.76	0.33	−0.76
$C_{O2}, \%$	0.59	0.53	−0.98	1	0.88	−0.82	−0.36	0.75
$i_{\min}$	0.52	0.51	−0.81	0.88	1	−0.99	−0.73	0.90
$i_{\max}$	−0.56	−0.55	0.76	−0.82	−0.99	1	0.79	−0.93
$P(M_{kl} > 0.5)$	−0.50	−0.56	0.33	−0.36	−0.73	0.79	1	−0.86
$\max(d_\sigma(A_0))$	0.78	0.79	−0.76	0.75	0.90	−0.93	−0.86	1

If, while keeping the value of the multiple correlation coefficient high $R \geq 0.95$, we minimize the multicollinearity of the factors considered as independent then the optimized correlation model in matrix form, characterized by the value $R \cong 0.96$, will take the form shown in Table 4.

Excluding the factor "degree of delocalization of the morphological spectrum" from the consideration leads to a drop in the multiple correlations coefficient value to the level of $R \cong 0.80$ but simplifies the matrix correlation model to the presented in Table 5 type.

TABLE 4. The optimized pair correlations coefficients matrix characterized by an acceptable level of multiple correlation $R \cong 0.96$

r_{XY}	Θ_w	$C_{F2}, \%$	$P(M_{kl} > 0.5)$	$\max(d_\sigma(A_0))$
Θ_w	1	−0.71	−0.50	0.78
$C_{F2}. \%$	−0.71	1	0.33	−0.76
$P(M_{kl} > 0.5)$	−0.50	0.33	1	−0.86
$\max(d_\sigma(A_0))$	0.78	−0.76	−0.86	1

TABLE 5. The optimized pair correlations coefficients matrix characterized by an insufficiently high level of multiple correlation $R \cong 0.80$

r_{XY}	Θ_w	$C_{F2}, \%$	$\max(d_\sigma(A_0))$
Θ_w	1	−0.71	0.78
$C_{F2}, \%$	−0.71	1	−0.76
$\max(d_\sigma(A_0))$	0.78	−0.76	1

As a result of the correlation analysis, it was found that the wetting edge angles with the distilled water and the ethylene glycol (because of a high degree of partial correlations of these factors) correlate with the maximum values of the differential planar heterogeneity functions and are inversely correlated with both the concentrations of fluorine in the modifying gas mixture and the degrees of the corresponding SEM-images' morphological spectra delocalizations.

Thus, the nature of the dependences of the nanorelief indices, the maxima of differential and contour planar heterogeneities, the degrees of the morphological spectra delocalizations, and the modified LDPE-films surfaces edge wetting angles on the concentrations of fluorine and oxygen in the modifying gas mixture indicate the presence of its optimal chemical composition ($\sim$ 11% F_2 and $\sim$ 5% O_2 at $\sim$ 84% Ne) which provides the minimum wetting edge angle values and, as a result, the maximum free surface energy for the oxyfluorinated LDPE-films – 46 mJ/m^2.

4. Conclusions

The visual analysis of the same SEM-image fragment of the low-density polyethylene (LDPE) film surface allows us to establish a significant influence of the image brightness and contrast onto the conclusions about the corresponding nanorelief degree of uniformity.

We have quantitatively analyzed standard characteristics (undulation, roughness, etc.) of the nanorelief surfaces obtained by means of atomic force microscopy (AFM) for the polyvinylchloride (PVC) and the polyethyleneterephthalate (PET) films. The results demonstrate that sufficiently high degree of their textural homogeneity does not prevent them from having significantly different values of free surface energy.

On the other hand, when considering several samples of LDPE-films, the significant differences in the local textures of the studied fragments have a minimal effect on the functional properties of the investigated material.

Thus, we've concluded that the creation of new methods for quantitative analysis of the polymer surfaces' images becomes important, both in order to reduce the influence of the measurement setup operator and to provide the possibility for introducing quantitative measures, criteria and techniques that could allow the effective describing/simulating and predicting of some new materials' properties.

The case objects of our research were the LDPE-films with modified surfaces. We've used the oxyfluorination modification technique – the treatment of the samples' surfaces with gaseous mixtures of helium, fluorine and oxygen under the different concentrations of chemically active reagents. The significant morphological transformations of the experimental samples' surface layers were confirmed by changes in their functional characteristics (the edge angles of wetting with polar and non-polar liquids) and were observed "visually" when using SEM.

Using the example of the oxyfluorinated LDPE-films a new approach to function-structural modeling of the polymer materials surfaces' nanotextures has been developed. It simultaneously provides the ability to identify the belonging to a series for each particular sample implementation and links the quantitative structural characteristics for a series of samples with the common physical and chemical properties of the material under study.

The use of the introduced quantitative structural characteristics of the modified polymers surfaces SEM images allows for a rational choice of chemical compositions of modifying (for example, helium-fluorine-oxygen) gas mixtures that provide the maximum possible edge wetting angles for the materials under consideration with the reference polar and non-polar liquids. It was found that the minimum values of the edge angles of wetting with water and ethylene glycol under the modification of LDPE-films by the oxyfluorination technique are achieved at volume concentrations of $12(\pm 1)\%(F_2)$ and $4(\pm 1)\%(O_2)$ in the modifying gas mixture. It was also shown that at these concentrations (within the limits of statistical error) the extreme values of morphological heterogeneity indicators (the maxima of the morphological spectra delocalization degrees and the minima of the dependencies of the differential planar heterogeneity characteristic functions maximum values from the fluorine and oxygen concentrations) are reached simultaneously. It was shown that the concentrations of the modifying mixture active reagents and a number of structural characteristics of the surfaces' nanotextures correlate.

We studied the relationships between the values of the wetting edge angles, the concentrations of the modifying mixture active reagents, the degree of delocalization of the morphological spectrum, and the maximum values of the differential digital planar heterogeneity functions. The edge angles of wetting were found using distilled water and ethylene glycol, which correlate with the maximum values of the differential planar heterogeneity functions and anticorrelate with both the concentrations of fluorine in the modifying gas mixture and the degrees of morphological spectra delocalization of the corresponding SEM-images. The flowcharts of using algorithms and the results of multi-factor correlation analysis are presented.

References

[1] Zhang X., Shi F., et al. Superhydrophobic surfaces: From structural control to functional application. *J. Mater. Chem.*, 2008, **18**, P. 621–633.

[2] Cui N.Y., Brown N.M.D. Modification of the surface properties of a polypropylene (PP) film using an air dielectric barrier discharge plasma. *Appl. Surf. Sci.*, 2002, **189** (1–2), P. 31–38.

[3] Peyroux J., Dubois M., et al. Surface modification of low-density polyethylene packaging film via direct fluorination. *Surf. Coatings Technol.*, 2016, **292**, P. 144–154.

[4] Luo M.L., Zhao J.Q., Tang W., Pu C.S. Hydrophilic modification of poly(ether sulfone) ultrafiltration membrane surface by self-assembly of TiO_2 nanoparticles. *Appl. Surf. Sci.*, 2005, **249** (1–4), P. 76–84.

[5] Long X., He L., et al. Surface modification of polypropylene non-woven fabric for improving its hydrophilicity. *Surf. Eng.*, 2018, **34** (11), P. 818–824.

[6] Kahradeh K.H., Saievar-Iranizad E., Bayat A. Electrophoretically deposited carbon micro and nanospheres thin films as superhydrophobic coatings. *Surf. Coatings Technol.*, 2017, **319**, P. 318–325.

[7] Guruvenket S., Rao G.M., Komath M., Raichur A.M. Plasma surface modification of polystyrene and polyethylene. *Appl. Surf. Sci.*, 2004, **236** (1–4), P. 278–284.

[8] Beyer M.K., Clausen-Schaumann H. Mechanochemistry: The mechanical activation of covalent bonds. *Chem. Rev.*, 2005, **105** (8), P. 2921–2948.

[9] Bora U., Sharma P., et al. Photochemical activation of a polycarbonate surface for covalent immobilization of a protein ligand. *Talanta*, 2006, **70** (3), P. 624–629.

[10] Bezbradica D., Jugović B., et al. Electrochemically synthesized polyaniline as support for lipase immobilization. *J. Mol. Catal. B Enzym.*, 2011, **70** (1–2), P. 55–60.

[11] Dryakhlov V.O., Nikitina M.Y., et al. Effect of parameters of the corona discharge treatment of the surface of polyacrylonitrile membranes on the separation efficiency of oil-in-water emulsions. *Surf. Eng. Appl. Electrochem.*, 2015, **51**, P. 406–411.

[12] Sarani A., Nikiforov A.Y., et al. Surface modification of polypropylene with an atmospheric pressure plasma jet sustained in argon and an argon/water vapour mixture. *Appl. Surf. Sci.*, 2011, **257** (20), P. 8737–8741.

[13] Kharitonov A.P., Taege R., et al. Direct fluorination - Useful tool to enhance commercial properties of polymer articles. *J. Fluor. Chem.*, 2005, **126** (2), P. 251–263.

[14] Shadpour H., Musyimi H., Chen J., Soper S.A. Physiochemical properties of various polymer substrates and their effects on microchip electrophoresis performance. *J. Chromatogr. A*, 2006, **1111** (2), P. 238–251.

[15] Sonnier R., Leroy E., et al. Polyethylene/ground tyre rubber blends: Influence of particle morphology and oxidation on mechanical properties. *Polym. Test.*, 2007, **26** (2), P. 274–281.

[16] Xiao K.Q., Zhang L.C., Zarudi I. Mechanical and rheological properties of carbon nanotube-reinforced polyethylene composites. *Compos. Sci. Technol.*, 2007, **67** (2), P. 177–182.

[17] Sailaja R.R.N., Deepthi M.V. Mechanical and thermal properties of compatibilized composites of polyethylene and esterified lignin. *Mater. Des.*, 2010, **31** (9), P. 4369–4379.

[18] Sabatini V., Cattò C., et al. Protective features, durability and biodegration study of acrylic and methacrylic fluorinated polymer coatings for marble protection. *Prog. Org. Coatings*, 2018, **114**, P. 47–57.

[19] Riccardi C., Barni R., et al. Surface modification of poly(ethylene terephthalate) fibers induced by radio frequency air plasma treatment. *Appl. Surf. Sci.*, 2003, **211** (1–4), P. 386–397.

[20] Luzinov I., Minko S., Tsukruk V.V. Adaptive and responsive surfaces through controlled reorganization of interfacial polymer layers. *Prog. Polym. Sci.*, 2004, **29** (7), P. 635–698.

[21] Goddard J.M., Hotchkiss J.H. Polymer surface modification for the attachment of bioactive compounds. *Prog. Polym. Sci.*, 2007, **32** (7), P. 698–725.

[22] Zhao C., Xue J., Ran F., Sun S. Modification of polyethersulfone membranes – A review of methods. *Prog. Mater. Sci.*, 2013, **58** (1), P. 76–150.

[23] ul Haq A., Boyd A., et al. Corona Discharge-Induced Functional Surfaces of Polycarbonate and Cyclic Olefins Substrates. *Surf. Coatings Technol.*, 2019, **362**, P. 185–190.

[24] Burmeister F., Badowsky W., et al. Colloid monolayer lithography–A flexible approach for nanostructuring of surfaces. *Appl. Surf. Sci.*, 1999, **144–145**, P. 461–466.

[25] Asua J.M. Miniemulsion polymerization. *Prog. Polym. Sci.*, 2002, **27** (7), P. 1283–1346.

[26] Wei G., Ma P.X. Structure and properties of nano-hydroxyapatite/polymer composite scaffolds for bone tissue engineering. *Biomaterials*, 2004, **25** (19), P. 4749–4757.

[27] Park H.B., Jung C.H., et al. Polymers with cavities tuned for fast selective transport of small molecules and ions. *Science*, 2007, **318** (5848), P. 254–258.

[28] Zaitsev A., Lacoste A., et al. Nanotexturing of plasma-polymer thin films using argon plasma treatment. *Surf. Coatings Technol.*, 2017, **330**, P. 196–203.

[29] Isaev E.A., Pervukhin D.V., et al. Platelet adhesion quantification to fluorinated polyethylene from the structural caracteristics of its surface. *Math. Biol. Bioinforma.*, 2019, **14** (2), P. 420–429.

[30] Yang Z., Wang L., et al. Superhydrophobic epoxy coating modified by fluorographene used for anti-corrosion and self-cleaning. *Appl. Surf. Sci.*, 2017, **401**, P. 146–155.

[31] Feng L., Li S., et al. Super-hydrophobic surfaces: From natural to artificial. *Adv. Mater.*, 2002, **14** (24), P. 1857–1860.

[32] Liu Y., Schaefer J.A. The sliding friction of thermoplastic polymer composites tested at low speeds. *Wear*, 2006, **261** (5–6), P. 568–577.

[33] Stuart M.A.C., Huck W.T.S., et al. Emerging applications of stimuli-responsive polymer materials. *Nat. Mater.*, 2010, **9**, P. 101–113.

[34] Nunez E.E., Gheisari R., Polycarpou A.A. Tribology review of blended bulk polymers and their coatings for high-load bearing applications. *Tribol. Int.*, 2019, **129**, P. 92–111.

[35] Egerton R.F., Li P., Malac M. Radiation damage in the TEM and SEM. *Micron*, 2004, **35** (6), P. 399–409.

[36] Efimov A.E., Tonevitsky A.G., Dittrich M., Matsko N.B. Atomic force microscope (AFM) combined with the ultramicrotome: A novel device for the serial section tomography and AFM/TEM complementary structural analysis of biological and polymer samples. *J. Microsc.*, 2007, **226** (3), P. 207–216.

[37] Vernitskaya T.V. Polypyrrole: a conducting polymer; its synthesis, properties and applications. *Russ. Chem. Rev.*, 1997, **66** (5), P. 443–457.

[38] Chu P.K., Li L. Characterization of amorphous and nanocrystalline carbon films. *Mater. Chem. Phys.*, 2006, **96** (2–3), P. 253–277.

[39] Misyura S.Y., Kuznetsov G. V., et al. The influence of the surface microtexture on wettability properties and drop evaporation. *Surf. Coatings Technol.*, 2019, **375**, P. 458–467.

[40] Rytikov G.O., Doronin F.A., et al. The automating of the quantitative analysis and characterization of the polymer based films surfaces SEM-images. *J. Phys. Conf. Ser.*, 2020, **1546**, 012027.

[41] Sarvazyan A.P., Rudenko O.V., et al. Shear wave elasticity imaging: A new ultrasonic technology of medical diagnostics. *Ultrasound Med. Biol.*, 1998, **24** (9), P. 1419–1435.

[42] Zuccaro G., Gladkova N., et al. Optical coherence tomography of the esophagus and proximal stomach in health and disease. *Am. J. Gastroenterol.*, 2001, **96** (9), P. 2633–2639.

[43] Li Q. Recent progress in computer-aided diagnosis of lung nodules on thin-section CT. *Comput. Med. Imaging Graph.*, 2007, **31** (4–5), P. 248–257.

[44] Ren H., Park K.C., et al. Early detection of carcinoma in situ of the bladder: A comparative study of white light cystoscopy, narrow band imaging, 5-ALA fluorescence cystoscopy and 3-dimensional optical coherence tomography. *J. Urol.*, 2012, **187** (3), P. 1063–1070.

[45] Taruttis A., Ntziachristos V. Translational optical imaging. *Am. J. Roentgenol.*, 2012, **199**, P. 263–271.

[46] Domenyuk D.A., Zelensky V.A., et al. Application of Laboratory and X-Ray Gentral Studies un Early Diagnostics of Metabolic Disturbances of Bone Tissue in Children with Autoimmune Diabetes Mellitus. *Entomol. Appl. Sci. Lett.*, 2018, **5** (4), P. 1–12.

[47] García R., Pérez R. Dynamic atomic force microscopy methods. *Surf. Sci. Rep.*, 2002, **47** (6–8), P. 197–301.

[48] Butt H.J., Cappella B., Kappl M. Force measurements with the atomic force microscope: Technique, interpretation and applications. *Surf. Sci. Rep.*, 2005, **59** (1–6), P. 1–152.

[49] Paredes J.I., Villar-Rodil S., et al. Atomic force and scanning tunneling microscopy imaging of graphene nanosheets derived from graphite oxide. *Langmuir*, 2009, **25** (10), P. 5957–5968.

[50] Haase K., Pelling A.E. Investigating cell mechanics with atomic force microscopy. *J. R. Soc. Interface*, 2015, **12** (104).

[51] Liu X., Song D., et al. Nanopore structure of deep-burial coals explored by AFM. *Fuel*, 2019, **246**, P. 9–17.

[52] Nazarov V.G., Stolyarov V.P., Evlampieva L.A., Fokin A.V. Heterophase fluorination of polymers. *Dokl. Phys. Chem.*, 1996, **350** (5), P. 639–641.

[53] Kharitonov A.P., Simbirtseva G.V., et al. Enhanced anti-graffiti or adhesion properties of polymers using versatile combination of fluorination and polymer grafting. *Prog. Org. Coatings.*, 2015, **88**, P. 127–136.

[54] Nazarov V.G. Surface characteristics of modified polymeric materials, *Kolloidn. Zhurnal*, 1997, **59** (2), P. 206–211.

[55] Nazarov V.G., Stolyarov V.P. Modified polymer substrates for the formation of submicron particle ensembles from colloidal solution. *Colloid J.*, 2016, **78**, P. 75–82.

[56] Nazarov V.G., Stolyarov V.P., et al. Heterogeneous fluorine-containing surface macro-, micro- and nanostructures in polymer films and their applications. *Polym. Sci. – Ser. A*, 2013, **55**, P. 652–665.

[57] Drozdov S.A., Nazarov V.G., et al. The polymer composites' morphological structure simulation. *Nanosystems: Phys., Chem., Math.*, 2017, **8** (1), P. 137–145.

[58] Nazarov V.G., Stolyarov V.P., et al. Comparison of the Effects of Some Modification Methods on the Characteristics of Ultrahigh-Molecular-Weight Polyethylene and Composites on Its Basis. *Polym. Sci. – Ser. A*, 2019, **61**, P. 325–333.

[59] Nazarov V.G., Doronin F.A., et al. Oxyfluorination-Controlled Variations in the Wettability of Polymer Film Surfaces. *Colloid J.*, 2019, **81**, P. 146–157.

Submitted 30 September 2021; accepted 1 February 2022

Information about the authors:

Fedor A. Doronin – Moscow Polytechnic University, 38 B. Semenovskya str., Moscow 107023, Russia; ORCID 0000-0002-0407-060X; f.a.doronin@mospolytech.ru

Andrey G. Evdokimov – Moscow Polytechnic University, 38 B. Semenovskya str., Moscow 107023, Russia;
ORCID 0000-0002-8124-9187; evdokag@gmail.com

Yury V. Rudyak – Moscow Polytechnic University, 38 B. Semenovskya str., Moscow 107023, Russia; ORCID 0000-0001-7886-0455; rudyak@mail.ru

Georgy O. Rytikov – Moscow Polytechnic University, 38 B. Semenovskya str., Moscow 107023, Russia; State university of management, 99 Ryazansky prospekt, Moscow 109542, Russia; ORCID 0000-0001-5521-8662; gr-yandex@yandex.ru

Irina P. Taranets – Moscow Polytechnic University, 38 B. Semenovskya str., Moscow 107023, Russia; qwerty818@mail.ru

Viktor G. Nazarov – Moscow Polytechnic University, 38 B. Semenovskya str., Moscow 107023, Russia; ORCID 0000-0002-7243-9739; 110505n@gmail.com

Conflict of interest: the authors declare no conflict of interest.

NANOSYSTEMS:

PHYSICS, CHEMISTRY, MATHEMATICS

INFORMATION FOR AUTHORS

The journal publishes research articles and reviews, and also short scientific papers (letters) which are unpublished and have not been accepted for publication in other magazines. Articles should be submitted in English. All articles are reviewed, then if necessary come back to the author to completion.

The journal is indexed in Web of Science Core Collection (Emerging Sources Citation Index), Chemical Abstract Service of the American Chemical Society, Zentralblatt MATH and in Russian Scientific Citation Index.

Author should submit the following materials:

1. Article file in English, containing article title, the initials and the surname of the authors, Institute (University), postal address, the electronic address, the summary, keywords, MSC or PACS index, article text, the list of references.
2. Files with illustrations, files with tables.
3. The covering letter in English containing the article information (article name, MSC or PACS index, keywords, the summary, the literature) and about all authors (the surname, names, the full name of places of work, the mailing address with the postal code, contact phone number with a city code, the electronic address).
4. The expert judgement on possibility of publication of the article in open press (for authors from Russia).

Authors can submit a paper and the corresponding files to the following addresses: nanojournal.ifmo@gmail.com, popov1955@gmail.com.

Text requirements

Articles should be prepared with using of text editors MS Word or LaTex (preferable). It is necessary to submit source file (LaTex) and a pdf copy. In the name of files the English alphabet is used. The recommended size of short communications (letters) is 4-6 pages, research articles– 6-15 pages, reviews – 30 pages.

Recommendations for text in MS Word:

Formulas should be written using Math Type. Figures and tables with captions should be inserted in the text. Additionally, authors present separate files for all figures and Word files of tables.

Recommendations for text in LaTex:

Please, use standard LaTex without macros and additional style files. The list of references should be included in the main LaTex file. Source LaTex file of the paper with the corresponding pdf file and files of figures should be submitted.

References in the article text are given in square brackets. The list of references should be prepared in accordance with the following samples:

[1] Surname N. *Book Title*. Nauka Publishing House, Saint Petersburg, 2000, 281 pp.
[2] Surname N., Surname N. Paper title. *Journal Name*, 2010, **1** (5), P. 17-23.
[3] Surname N., Surname N. Lecture title. In: Abstracts/Proceedings of the Conference, Place and Date, 2000, P. 17-23.
[4] Surname N., Surname N. Paper title, 2000, URL: http://books.ifmo.ru/ntv.
[5] Surname N., Surname N. Patent Name. Patent No. 11111, 2010, Bul. No. 33, 5 pp.
[6] Surname N., Surname N. Thesis Title. Thesis for full doctor degree in math. and physics, Saint Petersburg, 2000, 105 pp.

Requirements to illustrations

Illustrations should be submitted as separate black-and-white files. Formats of files – jpeg, eps, tiff.

NANOSYSTEMS:

PHYSICS, CHEMISTRY, MATHEMATICS

Журнал зарегистрирован
Федеральной службой по надзору в сфере связи, информационных технологий и массовых коммуникаций
(свидетельство ПИ № ФС 77 - 49048 от 22.03.2012 г.)
ISSN 2220-8054

Учредитель: федеральное государственное автономное образовательное учреждение высшего образования
«Санкт-Петербургский национальный исследовательский университет информационных технологий, механики и оптики»

Издатель: федеральное государственное автономное образовательное учреждение высшего образования
«Санкт-Петербургский национальный исследовательский университет информационных технологий, механики и оптики»

Отпечатано в Учреждении «Университетские телекоммуникации»
Адрес: 197101, Санкт-Петербург, Кронверкский пр., 49

Подписка на журнал НФХМ
На второе полугодие 2022 года подписка осуществляется через
ОАО «АРЗИ», подписной индекс Э57385